27
25 to NTIS
4/6/76

ORNL/TM-5147

Equilibrium, Confinement and Stability of Runaway Electrons in Tokamaks

Donald Atchison Spong

MASTER

OAK RIDGE NATIONAL LABORATORY

OPERATED BY UNION CARBIDE CORPORATION FOR THE ENERGY RESEARCH AND DEVELOPMENT ADMINISTRATION

DISTRIBUTION OF THIS DOCUMENT IS UNLIMITED

Printed in the United States of America. Available from
National Technical Information Service
U.S. Department of Commerce
5285 Port Royal Road, Springfield, Virginia 22161
Price: Printed Copy $8.00; Microfiche $2.25

ORNL/TM-5147

Contract No. W-7405-eng-26

Thermonuclear Division

EQUILIBRIUM, CONFINEMENT AND STABILITY OF RUNAWAY ELECTRONS IN TOKAMAKS

Donald Atchison Spong

Submitted as a dissertation to the Graduate School
of The University of Michigan in partial fulfillment
of the requirements for the degree of Doctor of
Philosophy of Nuclear Engineering.

MARCH 1976

NOTICE This document contains information of a preliminary nature and was prepared primarily for internal use at the Oak Ridge National Laboratory. It is subject to revision or correction and therefore does not represent a final report.

OAK RIDGE NATIONAL LABORATORY
Oak Ridge, Tennessee 37830
operated by
UNION CARBIDE CORPORATION
for the
ENERGY RESEARCH AND DEVELOPMENT ADMINISTRATION

ACKNOWLEDGMENTS

This work was initiated in the summer of 1972 at Oak Ridge National Laboratory while the author was working with John F. Clarke in the ORMAK group of the Thermonuclear Division. His continued interest and comments throughout the course of this project have been greatly appreciated.

The author would also like to express his sincere gratitude to his advisor, Professor Terry Kammash. His constant support and encouragement in this long endeavor and excellent advice have been essential.

In addition, Dr. Heinz Knoepfel of the Laboratorio Gas Ionizzati (Euratom-CNEN), Frascati, Italy, has provided valuable guidance and stimulation in relating much of this work to the comprehensive experimental measurements of runaway characteristics which he and Stewart Zweben of Cornell University have made on the ORMAK device at Oak Ridge.

Worthwhile interaction and criticism is further acknowledged from numerous members of the Thermonuclear Division of the Oak Ridge National Laboratory. Conversations with Drs. O. C. Eldridge, J. A. Rome, J. D. Callen, R. A. Dory, and many others have been extremely helpful.

Finally, much credit is due to Barbara Jackson for her patient and painstaking typing of this manuscript.

The financial support for the author's graduate work has been provided by a U. S. Atomic Energy Commission Special Fellowship and by an ORAU Graduate Participantship. Two summer positions at Oak Ridge National Laboratory are also acknowledged. Support for attending professional meetings and computer time has been provided by the U. S. Energy Research and Development Administration under contract with the University of Michigan and Union Carbide Corporation.

TABLE OF CONTENTS

LIST OF ILLUSTRATIONS

LIST OF APPENDICES

ABSTRACT

EQUILIBRIUM, CONFINEMENT, AND STABILITY OF RUNAWAY ELECTRONS IN TOKAMAKS

by

Donald Atchison Spong

When an electric field is applied to a plasma, a certain fraction of electrons in the high energy tail of the distribution may be freely accelerated. These are normally known as runaway electrons and their presence has been well-documented in various plasma devices. In this work, some of the ramifications of the runaway population in tokamak experiments will be investigated. Consideration is given both to the normal operating regime of tokamaks where only a small fraction of high energy runaways are present and to the strong runaway regime where runaways are thought to carry a significant portion of the toroidal current. In particular, the areas to be examined are the modeling of strong runaway discharges, single particle orbit characteristics of runaways, macroscopic beam-plasma equilibria, and stability against kink modes.

A simple one-dimensional, time-dependent model has been constructed in relation to strong runaway discharges. This assumes that a negligible plasma conduction current is present and that an accelerating beam of runaways carries most of the current. A parameter study is made of several of the early ORMAK strong runaway discharges using this model. Reasonable fits to the experimental data are obtained.

Single particle orbits are analyzed in relation to both the strong runaway regime and the weak regime. The effects of $\vec{E}\times\vec{B}$ drifts are first considered in strong runaway discharges and are found to lead to a slow inward shrinkage of the beam -- which is quite small for present-day experiments. Orbits are next treated for high energy electrons in the weak regime both analytically and numerically; cases are examined where the runaways are just beginning to intersect the plasma limiter. This is of relevance to the hard X-ray dumps which have been seen on tokamaks and quantitative agreement is obtained with ORMAK data. The transformation of the final runaway orbit (as it is lost from the discharge) back to its position at an earlier time is also treated. Understanding this effect is of importance in possible diagnostic uses of hard X-ray dumps (e.g. for examining the initial plasma breakdown, subsequent electric field profile, etc.)

Macroscopic beam-plasma equilibria are treated assuming a pressureless relativistic beam with inertia and using an ideal MHD approximation for the plasma. This area is of importance to strong runaway discharges where anomalous outward shifts have been seen in the beam-plasma column position. It may also be of significance to high power neutral injection and alpha particle production in tokamaks where large momentum flows can be present. The basic equilibrium equation is derived and mathematical limitations on its solution are given. Some sample numerical calculations are presented and compared with the existing analytic theories. The beam-plasma column shift is found to be somewhat less in the numerical solutions than is predicted by the analytic expressions. Beta poloidal limitations are treated by use of a simple toroidal force balance.

The stability of a toroidal relativistic beam against kink perturbations is examined using several models. First, a sheared velocity, two region beam is considered using an ideal, pressureless MHD model for the background plasma. The beam is assumed to be rigid, i.e. it displaces without distortion. Then, the plasma model is extended so that its range of validity includes frequencies which are not small relative to the ion gyrofrequency and the beam is treated using both fluid and the Vlasov-kinetic models. Growth rates are numerically calculated for a fixed boundary beam-plasma model.

CHAPTER I

INTRODUCTION

I.1 Introductory Comments and Classification of Tokamak Runaway Regimes

The production of superthermal electrons when an electric field is applied to an ionized gas has been the subject of numerous investigations, both theoretical and experimental, since the beginning of controlled nuclear fusion and plasma physics research. Starting with the early work on plasma betatrons nearly seventeen years ago and continuing up to the present series of tokamak experiments, runaways have been a recurrent and familiar phenomenon. Their presence has been received both with welcome -- as in the plasma betatron -- due to their suggested potential use for plasma heating and confinement (as well as accelerator applications), and with foreboding -- as in the tokamak and stellarator -- due to the, at times, substantial amount of energy which they can carry out of the plasma region and onto the walls and limiter of the device. Even in the presently projected reactor tokamaks, runaways continue to be a source of some concern due to the longer discharge pulse lengths and better confinement of high energy particles. Their presence could have some distinct and unanticipated consequences on the operation of these devices.

The fundamental reason for the existence of runaway electrons is related to the decrease in the Coulomb collision frequency with increasing energy; thus, for any value of applied electric field there is a certain energy above which electrons will be freely accelerated.

This effect was first identified in 1925 by Wilson [1] (inventor of the cloud chamber) and subsequently examined by Eddington [2] in 1926 and Giovanelli [3] in 1949.

In the tokamak device [4,5], the initial plasma breakdown and Joule heating are achieved by an induced electric field; this field is further necessary to maintain a toroidal plasma current which is required for overall equilibrium and particle confinement. The production of runaway electrons may occur throughout the discharge, but is expected to be enhanced when the electric field is large and the plasma density low, i.e. in the early phase of the discharge. The existing evidence on tokamaks, and in particular on the ORMAK device [6,7,8], tends to indicate that the most persistent and energetic component of runaways are, in fact, born during the initial plasma breakdown. However, a lower energy epithermal component of runaways have also been observed [9,10,11]; these are thought to be continuously generated and lost throughout the discharge [9]. The loss mechanisms are not yet quantitatively well understood, but have been attributed to magnetic island formation due to helical current perturbations of MHD instabilities [11,12] and diffusion in toroidal field ripples.

The motivations for examining runaways in tokamaks are various. Perhaps the most basic is related to a concern over whether they will be of importance in larger fusion-grade tokamaks. At present, the exact conditions which lead to enhanced runaway production are only empirically known and useful theoretical predictions are not available. Secondly, runaways can provide a sensitive probe of field perturbations, MHD instabilities, and the confinement quality of high energy particles in tokamak discharges. It is of particular interest to note that the momentum of a runaway with energy in the MeV range is of the same order as that of typical fast ions which are produced via neutral injection. Thus, the runaway single particle confinement characteristics (to be examined in Chapter III) reflect those of the fast ions. In the same vein, the equilibrium properties of runaway-dominated discharges (covered in Chapter IV) may have certain parallels with those of tokamak discharges heated by energetic neutral injection where toroidal momentum flows may be built up. A final motivation for examining runaways in tokamaks is related to the concept of forming an intense toroidal relativistic beam to provide confinement and/or plasma heating. In the author's opinion, there are a number of possible difficulties with this scheme such as: synchrotron radiation losses, β limits, poorly-confined orbits at the edge of the current channel, micro and macro-instabilities (examined in Chapter V). Runaway-dominated discharges in tokamaks appear to provide an attainable means of testing such a concept to determine its advantages and disadvantages. The work to follow has been motivated by the above considerations and specifically by the experimental measurements which have been reported. A classification and review of this experimental work will be given next.

Several distinct runaway regimes on tokamaks may be identified depending on the extent to which runaways are present, their energy, and confinement quality. These will be described below and in this work will be categorized as the weak, continuous, and strong runaway regimes.

The weak runaway regime is present during a normal, stable tokamak discharge and is characterized by a very low density of runaways

($\sim 10^7$ cm^{-3}), most of which are produced during the first 5-10 msec. They can, however, attain high energies -- in the 7-12 MeV range in ORMAK type B discharges [8] -- due to the fact that they seem to occur near the outside of the plasma region where the maximum volt-seconds of acceleration are experienced. In the type B discharges, these particles are observed to remain well-confined up to the end (lifetimes are of the order of 50-80 msec) when their drift orbits begin intersecting the limiter. This subject will be covered in more detail in Chapter III. In ORMAK type A discharges, runaways are dumped near the beginning due to the early large inward displacement of the plasma column and the relatively higher MHD activity.

The continuous runaway regime has perhaps been studied the most on the Princeton ST device [9] where runaway conditions were not as favorable during the initial discharge breakdown as on ORMAK. In this case runaways are generated within the central region of plasma, but are rapidly lost before they can attain high energies. Their energies typically range from 50 keV to 1 MeV. This runaway population can have very adverse effects on the energy confinement properties of tokamaks; their loss prevents the full Ohmic field energy from usefully heating the plasma. The mechanism for loss of these runaways, as mentioned above, is thought to be related to the large magnetic island structures and ergodic field lines which result from the presence of magnetic shear and deviations from axisymmetry (e.g., due to helical MHD perturbations, field ripples, shell cuts, field errors, etc.). X-ray measurements on ORMAK which show strong correlations between 50 keV X-ray bursts and MHD activity are particularly suggestive of this mechanism [13].

It may be noted that the presence of an epithermal continuous runaway component during the weak regime cannot, at present, necessarily be ruled out. The hard X-ray diagnostics which have been used on ORMAK to examine the high energy (8-12 MeV) runaways are insensitive to the lower energy component ($\leq$ 2 MeV). It may well be that an epithermal population of runaways exists in the central plasma region where island widths are large and loss rates high while runaways near the outer edge of the plasma have longer confinement times and thus greater energies (due to the lower poloidal field perturbations at the higher q surfaces).

The strong runaway regime is characterized by much higher runaway densities (10^9-10^{11} cm^{-3}) and by a substantial fraction of the total current being carried by runaways. There is at present no good means of measuring how much current is carried by high energy electrons in this regime, but rough estimates may be made from the intensity of hard bremsstrahlung produced when the runaways intersect the limiter and by examining the equilibrium properties of the discharge.

This regime is well known for its occurrence during the initial start-up phase of most tokamak experiments; however, by properly choosing the impurity content and initial preionization, it can be intentionally produced in subsequent operation as well [14,15]. The energies of the runaways have been measured in the 1-7 MeV range on ORMAK. A parameter modeling [7] of a typical strong runaway discharge will be presented in Chapter II. It is assumed there that the bulk of runaways are created early in the discharge and that this occurs within a localized region which is determined by the topology of flux surfaces early in the discharge. Strong runaway discharges have been observed on the ORMAK [7,14], T-6 [15], TM-3 [16], and TFR [17] devices.

An interesting fusion application of runaway-dominated discharges has been suggested recently [18,19,20]. This concept involves generation of a runaway beam in an initially low density plasma followed by acceleration and partial decay into a higher density plasma. This is closely related to the earlier plasma betatron concept [21,22,23] and also to more recent research into injection of a diode-generated relativistic electron beam into a torus [24,25] or racetrack [26]. The runaway method has an advantage over the latter approach in that the relativistic beam is generated in situ, thus avoiding the difficult problems of injecting charged particles across magnetic field lines. Techniques which have been suggested for external injection involve either a momentary disruption of the magnetic surfaces at the instant of injection [26] or a reliance on single particle drifts to carry the beam into the plasma region [25,27]. Possible advantages of a toroidal relativistic beam relative to Ohmic heating are: the long lifetimes of high energy electrons, leading to the potential of a steady-state toroidal current, somewhat more rapid heating rates and altered macroscopic stability properties.

The heating rates associated with a toroidal relativistic beam have yet to be fully experimentally verified; however, due to the potentially long confinement times of relativistic electrons in toroidal plasmas (50-60 msec for well-confined runaways in ORMAK, corresponding to a total path length of about 10^7 meters for collisional interaction) even the energy transfer from classical Coulomb collisions [28] can give appreciable energy loss for certain ranges of energy and plasma density. Recent density puff experiments [29] on ORMAK indicate that with just a twofold plasma density increase, mechanisms are present for completely slowing down 10 MeV runaways within less than about 10 msec. A long series of experiments have been conducted [30-35] involving plasma heating in linear devices by relativistic beams. Nonclassical mechanisms such as return current heating and microscopic electron-electron two stream instabilities are thought to be of importance in the observed beam-plasma interactions. The experimental results indicate that for relativistic beams of density $n_b = 10^{10}$-10^{11} cm^{-3} injected into plasmas with n_p in the range 10^{13}-10^{14} cm^{-3}, energy is transferred from the beam to plasma at efficiencies of about 1% to 4% per meter of path length [27].

The macroscopic stability properties of toroidal relativistic beams will be examined in some detail in Chapter V; interest in this area is motivated by the observed abnormally low amplitude of MHD activity in runaway-dominated discharges [14,15] as compared to normal tokamak discharges. Also, the parameter study to be discussed in Chapter II indicates the possibility that q (the Kruskal-Shafranov stability factor) attained values less than unity internal to the plasma without noticeable instability for a typical ORMAK runaway-dominated discharge. Speculation on this possibility has also been made in regard to runaway-dominated discharges on the T-6 experiment [15].

I.2 Review of Experimental Results on Runaways and Relation to the Theory

The theory to be developed in this work is primarily motivated in relation to the weak and strong runaway discharge regimes. In both cases the presence of a runaway component has been associated with a number of characteristic and readily observable effects. Depending on the energy density of runaways, these indications vary over a wide spectrum ranging from a slight increase in hard X-ray level to the large-scale melting of limiters and burning of holes in vacuum vessel walls (as in the TFR device). In this section some of the features which distinguish the weak and strong runaway regimes will be reviewed.

In the case of weak runaway discharges, the most direct indication of runaways is in the large intensities of hard (up to 12 MeV) bremsstrahlung X-rays which are produced. This factor has been utilized as a diagnostic tool particularly in the ORMAK runaway work and also in the Princeton ST and TFR experiments. Both plasma (free-free) [9] and wall (thick target) [8] bremsstrahlung components have been identified; however, the wall bremsstrahlung is typically many orders of magnitude more intense than that from the plasma. Since runaways are essentially collisionless particles, their transport from plasma to wall can be explained largely on the basis of classical single particle orbits [9]; these will be examined for ORMAK parameters in Chapter III. For the weak runaway regime, it is expected that particle loss due to field ripples, magnetic islands, etc. plays a relatively minor role (as compared to the continuous runaway regime); otherwise, the runaways which are produced early in the discharge would be lost much faster and at substantially lower energies than what is experimentally observed.

About the only other indication of runaways which has been measured during the weak regime is enhanced microwave emission. This has been studied on the Cleo [36], TFR [17], and ATC [37] devices. The enhancement over classical synchrotron radiation is attributed to the presence of an anisotropic superthermal electron population and the resulting velocity space instabilities. In the author's opinion, this diagnostic has not yet been developed to the degree that the hard X-ray method has; however, it certainly has the potential of providing information on the runaway electron distribution function and the nature of the beam-plasma interactions which may be present.

Strong runaway discharges [7,14,15,16,17] are distinguished by such features as: intense hard X-ray fluxes, anomalous large outward equilibrium shifts, positive voltage spikes correlated with current dumps, enhanced microwave emission, and an abnormally low amplitude of MHD (Mirnov) signals which show no poloidal mode rotation. These discharges have recently been observed on ORMAK [7,14], the T-6 [15], TM-3 [16] and TFR [17] devices; discharges of a similar nature were also studied in early work in stellarators.

On the T-6 device [15] strong runaway discharges exhibited instabilities in the form of relaxation oscillations. These resulted in positive spikes in the toroidal loop voltage which correlated with similar discontinuities in nearly all of the other measured discharge characteristics. The instability occurred only when the mean electron density was below a value of $2.5 - 5 \times 10^{12}$ cm^{-3}. Measurements of $\beta_\perp$ from diamagnetic loops indicated that at the moment the instability developed, energy was transferred from the longitudinal motion of the runaway beam into transverse plasma energy.

Measurements of the electron density profile on the T-6 runaway experiments indicated that early in time a hollowed-out profile was present which persisted 2-3 times longer than the hollow initial density profile in a normal, non-runaway discharge. At the point where the instability developed, the density profile flattened out and became bell-shaped. Also, the center of the electron density distribution was shifted further out from the torus axis than in a normal discharge. The latter fact was attributed to one of two possibilities; either the runaways formed a localized beam within the discharge, leading to a large internal inductance (which would increase the outward plasma shift) or the $\beta_{\parallel} = 8\pi\gamma n_b m_0 c^2/B_\theta^2(a)$ of the runaways was substantial enough to contribute to the outward shift. The latter explanation was deemed to be the more reasonable since it resulted in a mean energy of 500-700 keV and density between 10^{10} and 10^{11} cm^{-3} whereas the former resulted in a beam radius of 5-6 cm. If all the observed toroidal current were carried within a 5-6 cm region, this would have resulted in a q value less than unity at the edge of the beam.

Methods for converting runaway discharges into normal ones were investigated on the T-6 experiments. These included: adding inhomogeneity to the toroidal field, varying the preionization, and changing the filling pressure. A 20% $\Delta B/B$ ripple in the toroidal field was found to substantially reduce the hard X-rays and convert the discharge characteristics to those of the normal case. Better preionization and higher filling pressures also decreased the intensity of runaways.

In experiments on the TM-3 device [16], the relation between runaways and disruptive instabilities was examined. It was found that increases in hard X-rays could be correlated with disruptive events at low density and large values of q. Bolometric measurements made during the instabilities indicated that nearly all the plasma Ohmic energy was carried by a runaway component. Characteristic electromagnetic radiation was measured at the lower hybrid, ion plasma, and lower frequencies with the onset of the instability. Diamagnetic signals also indicated that rapid transverse plasma heating occurred at the disruptive events; this was interpreted as being due to a slowing of the runaway component from either a lower hybrid beam-plasma interaction or Buneman instability.

Strong runaway discharges on the ORMAK device were quite common during the initial operation of the experiment [7]. These will be examined in some detail in Chapter II; they were characterized by much higher currents than the T-6 experiments - up to 140 kA. Positive voltage spikes were also observed which correlated with current dumps of up to 20% of the total current and large outward shifts in the equilibrium position (7-8 cm). Due to the higher current levels, the equilibrium shifts could not be accounted for entirely by an enhancement in $\beta_{\parallel}$ due to the runaways. The remaining discrepancy was attributed to ℓ_i, the internal inductance, which is large if the runaways form a beam within the plasma channel. Following these early runaway-dominated discharges, examination of the limiter revealed a melted area on the outside quadrant and fracture caused by uneven thermal expansion.

A parameter study of some typical shots out of this series is given in Chapter II. The conclusion is that a beam-like current distribution is required to fit the experimental data; this implies a q profile which goes substantially below unity near the center of the discharge.

A more recent series of runaway discharges [14] were also conducted on ORMAK at lower current levels (50-70 kA) in an attempt to avoid machine damage. These exhibited small voltage spikes and only slight dumps in toroidal current ($\lesssim$ 1 kA). A systematic attempt was made through adjustment of the vertical field to keep these discharges centered. Inferred values of $\beta_p + \ell_i/2$ were quite large; values of 2-3 were typical at the maximum current level, but as high as 6-8 were attained during the current decay. When the vertical field was properly adjusted to maintain equilibrium, the current decay was quite slow, lasting up to 50-60 msec after the end of the voltage pulse in some cases. The maximum energy measured by bremsstrahlung was 5-6 MeV. A very low amplitude was observed on the MHD probe signals and no poloidal mode rotation was seen. Also signals from the pin diode array indicated relatively little activity interior to the plasma except for periodic spikes at about every 3-5 msec which correlated with spikes in the MHD probe signal. The plasma thermal energy, as measured by a radiometer probe, was quite low. Electromagnetic emission was not studied on either these or the early series of ORMAK runaway discharges.

Runaways on the TFR device [17] played a rather ominous role, leading to the piercing of holes in the vacumm liner. Runaway-dominated discharges were only obtained at low density operation ($n_e \lesssim 10^{13}$ cm^{-3}) and had a characteristic energy of 6 MeV. Examination of the plasma electromagnetic emission revealed that radiation at the electron cyclotron harmonics was correlated with hard X-ray bursts from runaways. The interpretation given for the impact zones on the liner was that cold electrons trapped in the local magnetic mirrors (due to field ripples) were being heated near the electron cyclotron resonance by a beam-plasma interaction between the stream of runaways and the background plasma. These impacts were later verified to be in the direction of electron drifts by reversing the direction of the toroidal field.

Electron cyclotron emission has also been studied in both normal and runaway-dominated discharges on the Cleo device [36]. A clear correlation was observed between the intensity and spectral distribution of the emission and the amount of high energy electrons present. Up to an order of magnitude more emitted power was measured in runaway discharges than in normal discharges. In the former case, a broad peak in the intensity was found near $\omega \simeq 3.3\omega_{ce}$ whereas in the latter a narrow peak occurred at $\omega = 2\omega_{ce}$.

As can be seen from the previous review of runaway experiments on the various machines, a wide variety of interesting experimental effects have been identified. To develop an adequate theoretical framework which could be related in detail to all such observations is far beyond the scope of the present work. However, an attempt is made here to examine a few of the areas which are relevant to understanding the role of runaways in tokamaks - particularly in the weak and strong runaway regimes.

The ensuing work will proceed along the following lines.

In Chapter II a one dimensional, time-dependent model is presented of a strong runaway discharge in which the toroidal current is carried by an accelerating beam of runaways and negligible plasma conduction current is present. Predictions of this calculation are then compared directly with several typical ORMAK runaway-dominated discharges from the early operation phase of this experiment. Chapter III deals with the single particle orbits of high energy runaways in tokamaks. Both numerical and analytic theory is presented for parameters characteristic of the ORMAK experiment. These calculations are particularly pertinent in interpreting the gradual dumps of runaways for which detailed measurements have been made by Knoepfel and Zweben [42] during ORMAK type B discharges. Toroidal equilibrium is treated in Chapter IV for the case where a centrifugal force term is included in the plasma force balance, as would be appropriate for an energetic beam. This is of relevance to strong runaway discharges where anomalous outward equilibrium shifts and large values of $\beta_p + \ell_i/2$ are observed. Finally, in Chapter V the stability theory of a toroidal runaway beam-plasma configuration against helical modes is examined. The approach taken is to examine several physical mechanisms which might account for the peculiar stability properties of runaway-dominated discharges. As may be recalled from the preceding review of the experiments, there are some definite indications either of instabilities or loss of equilibrium (i.e. voltage spikes, current jumps, etc.); however, there have also been hints from such measurements as MHD magnetic probes and from the parameter study of Chapter III that runaway discharges may be macroscopically somewhat more stable than conventional discharges. The mechanisms investigated here include:

velocity shear in the runaway beam, effects of the longitudinal dynamics of the relativistic electrons, influence of the high drift frequency of the runaways around flux surfaces (of the order of the ion cyclotron frequency), and introduction of toroidal drifts. As both the theory [43,44] and experiments [14,15,16] on the gross stability properties of runaway-dominated discharges are somewhat in their infancy, a serious quantitative comparison is, at present, not possible. However, certain qualitative features of the results of Chapter V may be of relevance; these include large growth rates near the rational magnetic surfaces ($\sim v_A/a$) and regions of stability at $q < 1$ when the runaway electron drift frequency ($= c/R_0q$) becomes large relative to frequencies characteristic of MHD ($\omega << \Omega_{ci}$).

CHAPTER II

One-Dimensional, Time-Dependent Modeling of ORMAK Runaway-Dominated Discharges

Large intensities of MeV range bremsstrahlung X-rays produced by relativistic electrons impacting the wall and limiter of the ORMAK device were observed in the early operation of this experiment. In the following, a model is presented and applied to typical data from several of these discharges. The classical production rate of runaways for typical ORMAK parameters is first examined as a function of the impurity content and degree of plasma ionization. Experimentally, it has been observed on a number of machines that runaways tend to be enhanced in discharges where poor vacuum, high impurity conditions are present. Next, the initial formation of the runaway beam is studied, taking into account the effect of magnetic field errors. The remaining part of the model is then the self-consistent acceleration of the runaway beam in an applied electric field. From this calculation, the toroidal current is obtained as a function of time and compared with experimental data.

II.1. Runaway Production Rates

The kinetic theory of runaway production in an ionized gas subject to an applied electric field has been examined by numerous authors including Giovanelli [3], Harrison [45,46], Dreicer [47], Kruskal and Bernstein [48-50], Gurevich [51-53], Lebedev [54], Kulsrud, et al. [55], and Connor and Hastie [56]. With the exception of Kulsrud, et al. (who numerically solve the Fokker-Planck equation), these calculations typically begin with the electron Fokker-Planck equation and then divide velocity space into various regions in order to obtain an analytic solution. In all cases, an infinite, homogeneous, quasi-steady-state plasma is assumed; collective effects are neglected; no magnetic field is present; and a nearly Maxwellian distribution (without trapped particles) is used. These calculations also apply only when the applied electric field is weak relative to the critical runaway field ($E \ll E_c$). This critical field is usually defined as follows. When a field E is applied to an ionized gas, there will be a certain fraction of electrons in the tail of the distribution which, due to the inverse velocity squared dependence of the dynamic friction force, will be collisionally decoupled from the bulk of the plasma and can freely accelerate. The crossover point in the distribution function from collisional electrons to those which are freely accelerating occurs at a critical velocity, v_c, when the electric field force just balances the dynamic friction force. The critical electric field is defined as that field for which the critical velocity equals the thermal velocity.

The first extensive examination of runaway production was done by Dreicer [47] (1960) in a series of two papers. He first treated a fully ionized gas in static electric and magnetic fields using hydrodynamic equations. He found that the relative drift velocity between electrons and ions was not maintained at a steady-state value by collisions, but increased in time. At the critical field, the increase was rapid enough such that the drift velocity exceeded the thermal velocity within one mean free collision time. In a second paper the problem was treated using kinetic equations and dividing velocity space into two regions: one at low velocities dominated by collisions, and a higher velocity runaway region where the electric field force predominates. It was assumed that electrons would be rapidly depleted out of the high velocity region by electric field acceleration. Runaway rates were calculated by examining the diffusion rate of electrons from the low velocity region to the higher velocity region.

Kruskal and Bernstein [48-50] next treated the runaway problem and found it necessary to divide velocity space up into three and five regions for Lorentz and Maxwellian models, respectively, in order to obtain convergent solutions of the Fokker-Planck equation. Theirs represents the most mathematically rigorous treatment and involves no ad hoc assumptions. However, the final result for runaway flux was obtained up to a function of the electric field strength times an undetermined constant which could only be evaluated by a numerical integration.

Gurevich [51-53] and Lebedev [54] also examined the classical runaway flux for a weak electric field and were able to obtain closed-form answers. In similarity to Dreicer, they also divided velocity space into only two regions, but used an improved representation for the distribution function near the runaway regime. Gurevich pointed out that close to the critical velocity the distribution function deviates substantially from a Maxwellian and becomes highly directional along the electric field. In this regime, a series expansion in $\mu-1$ (μ is the cosine of the angle between $\vec{v}$ and the electric field) was employed, i.e.

$$f\,(\vec{v},u) = \Phi_0\,(v) + (\mu-1)\,\Phi_1\,(v) + (\mu-1)^2\,\Phi_2\,(v) + \ldots \qquad \text{II-1}$$

Substituting this into the Fokker-Planck equation, the unknown coefficients up to Φ_1 were determined iteratively. This was accomplished by first setting Φ_1 to zero, solving for Φ_0, then setting $\Phi_2 = 0$, solving for Φ_1, etc. The distribution function was then matched onto a Maxwellian at the thermal velocity in order to determine the normalization factor.

Runaway fluxes were determined by integrating over the right-half of velocity space (in the direction of runaway) resulting in the following expression.

$$S = \frac{2}{\sqrt{\pi}} N_e \nu_{eo} \left(\frac{E}{E_c}\right)^{1/2} \left\{ \exp - \frac{E_c}{4E} - 2 \frac{E_c}{E}^{1/2} \right\} \qquad \text{II-2}$$

where
$$E_c = 4\pi e^3 \frac{\left[N_e \ln \frac{mv_c^2 D}{e^2} + N_n Z \ln \frac{\overline{mv^2}}{\bar{\varepsilon}} \right]^2}{kT_e N_e \ln \frac{mv_c^2 D}{e^2} + \frac{\varepsilon_i \bar{d}}{2} N_n Z \ln \frac{\overline{mv^2}}{\bar{\varepsilon}}} \qquad \text{II-3}$$

N_e = electron density

N_n = neutral density

D = Debye length

m = electron mass

Z = atomic number

$\overline{mv^2}$ = $\tilde{\sim}$ 0.3 to 0.4 mv_c^2

$\bar{\varepsilon}$ = average excitation energy

= 15 ev for hydrogen

ε_i = ionization energy

ν_{eo} = mean collision frequency for an electron

$$= \frac{N_e \ln \Lambda}{3.5 \times 10^5 \, T_e^{3/2}}$$

$\ln \Lambda$ = Coulomb logarithm

The above equations are for the case of an arbitrary degree of plasma ionization. The critical velocity is determined by balancing the electric field acceleration force and the retarding force due to collisions with neutrals and plasma electrons. It is given by

$$F(v_c) + mv_c \nu_e (v_c) = eE. \qquad \text{II-4}$$

where $F(v_c)$ = effective retarding force on an electron moving with a velocity v_c in a gas of density N_n

$$= \frac{4\pi e^4 N_n Z}{mv_c^2} \ln \frac{mv_c^2}{\varepsilon}$$

$\nu_e(v_c)$ = collision frequency of an electron of velocity v_c with other plasma electrons

$$= \frac{4\pi e^4 N_e}{m^2 v_c^3} \ln \frac{mv_c^2 D}{e^2}$$

Lebedev [54] followed a procedure similar to Gurevich's, but noted that Gurevich's distribution function was really only valid for velocities below v_c due to the iterative procedure employed in obtaining the functions $\Phi_0(v)$ and $\Phi_1(v)$. Lebedev employed an improved method and solved for Φ_0, Φ_1, Φ_2 by using an expansion in the small parameter $^E/E_c$. His expression for runaway flux is given by the following, and differs from Gurevich's by only the pre-exponential factor.

$$S = 2^{1/3} \pi^{-1/2} N_e \nu_{eo} \left(\frac{E_c}{E}\right)^{1/4} \exp \left\{- \frac{E_c}{4E} - \left(2 \frac{E_c}{E}\right)^{1/2} - \frac{1}{2}\right\} \qquad \text{II-5}$$

Kulsrud, et al. [55] numerically solved the Fokker-Planck equation for runaway rates and compared their results with previous calculations. They found that their work agreed most nearly with that of Kruskal and

Bernstein (provided the undetermined multiplicative constant was chosen to agree with the numerical result at a specific electric field). Lebedev's calculation was also close; however, Dreicer's runaway rate was about two orders of magnitude higher than that of Kulsrud, et al. and Gurevich's was low by a factor of about 3-4.

Conner and Hastie [56] have also recently considered relativistic corrections to runaway rates. They note that if the applied electric field is sufficiently weak, then the critical runaway velocity will become of the order of the speed of light. At this point, a relativistically correct collision integral must be used; they use one given by Klimontovich [57]. The fact that v_{crit} cannot exceed the speed of light results in a value of $E/E_{crit} = (kT_e/m_ec^2)$ below which no runaways may be produced. They also found that significant corrections to the calculation of Kruskal and Bernstein enter in when $E/E_{crit} < \sqrt{kT_e/m_ec^2}$.

For the parameter modeling of ORMAK discharges, the calculation of Lebedev has been found most appropriate. The corrections found by Connor and Hastie begin to be of importance during the steady-state phase of the ORMAK discharge and for reactor regime tokamaks; however, in the early part of the ORMAK discharge, when most of the runaways are thought to be produced, $E/E_{crit} > \sqrt{kT_e/m_ec^2}$ so that relativistic corrections to runaway rates are fairly minor.

Since in ORMAK, as in most tokamaks, the plasma parameters during the early breakdown of the discharge have not been well-diagnosed, several approximations had to be made in computing runaway rates. First, the resistivity was computed using the measured current and voltage;

temperature was then obtained using Spitzer's formula with an anomaly factor of four (which was typical of the early ORMAK discharges). The neutral density was modeled by assuming an initial value and then depleting this in proportion to the rising plasma density such that total number of particles was conserved. Other parameters varied were the impurity content and the penetration time of the Ohmic heating field.

A typical voltage, current, and density plot is given in Fig.II-1 for a capacitor-driven runaway discharge and for a nonrunaway discharge in Fig. II-2. The major difference between these two shots was in the direction of the Ohmic heating field; reasons for this dependence will be examined in the next section. Substituting data from the runaway discharge into equation II-5 results in the fluxes which are seen in Figs. II-3 and II-4. In Fig. II-3, the runaway rate is plotted against time for different values of Z. For simplicity, it is assumed here that the average number of electrons per neutral atom and the effective ion charge of the plasma ions are the same number, Z. Thus, the values of Z indicated in Fig. II-3 are used both in equations II-3 and II-4 in calculating E_c and v_c and also in the Spitzer resistivity in calculating the plasma temperature using the measured voltage and current. It is known that the ORMAK runaway discharges had a high level of impurity and thus a high Z; however, early in the discharge Z was probably at its lowest value. Treating Z as a parameter, it is noted that an increase tends to lower the initial peak in the runaway rate and to create a second peak later on in the discharge. The lowering of the initial peak can be readily explained by equation II-3 where increasing Z leads to an increase

ORNL DWG. 73-3697

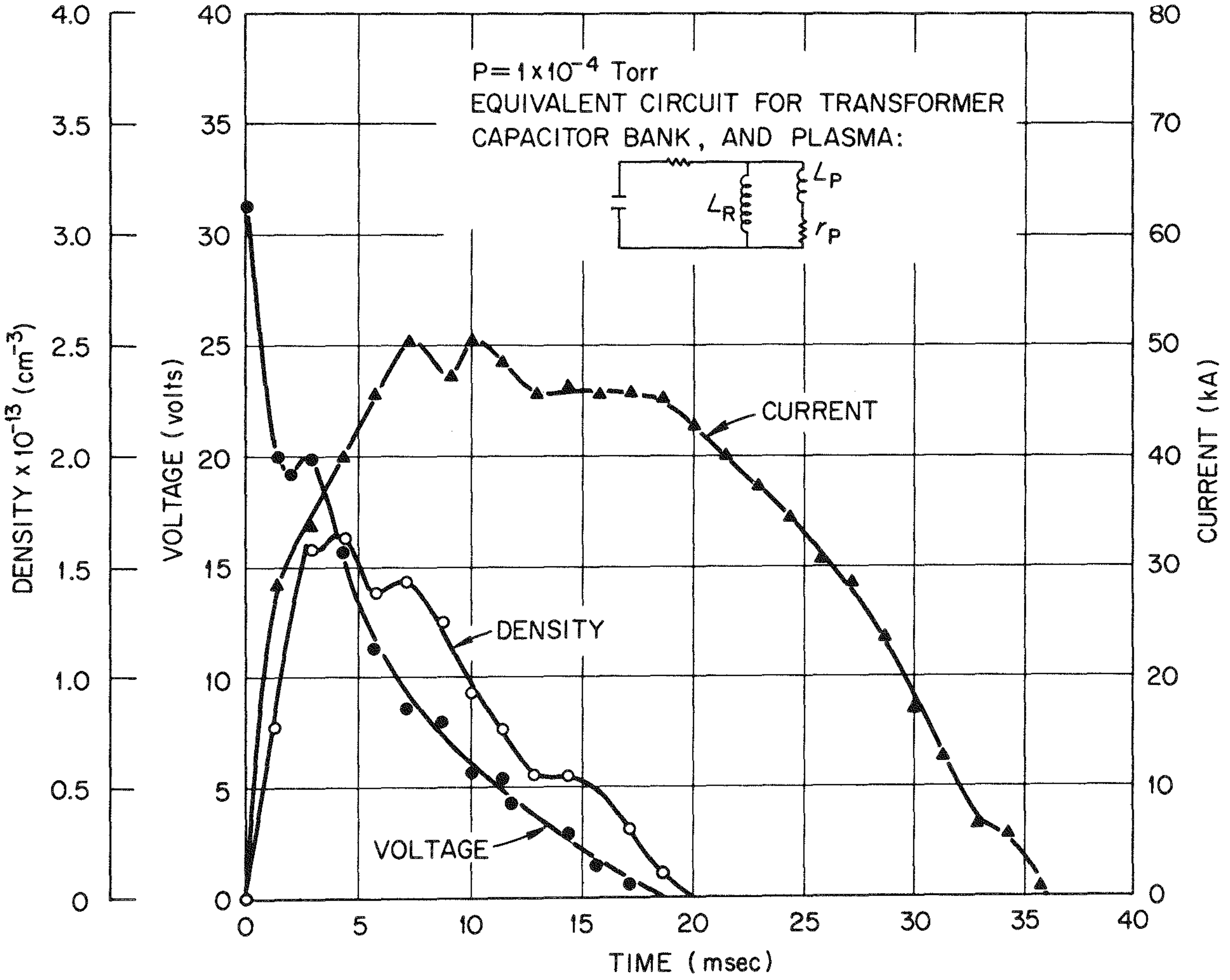

FIGURE II-1

ORMAK Parameters vs. Time for a Typical Runaway Discharge (Capacitor Power Supply).

ORNL DWG. 73-3698

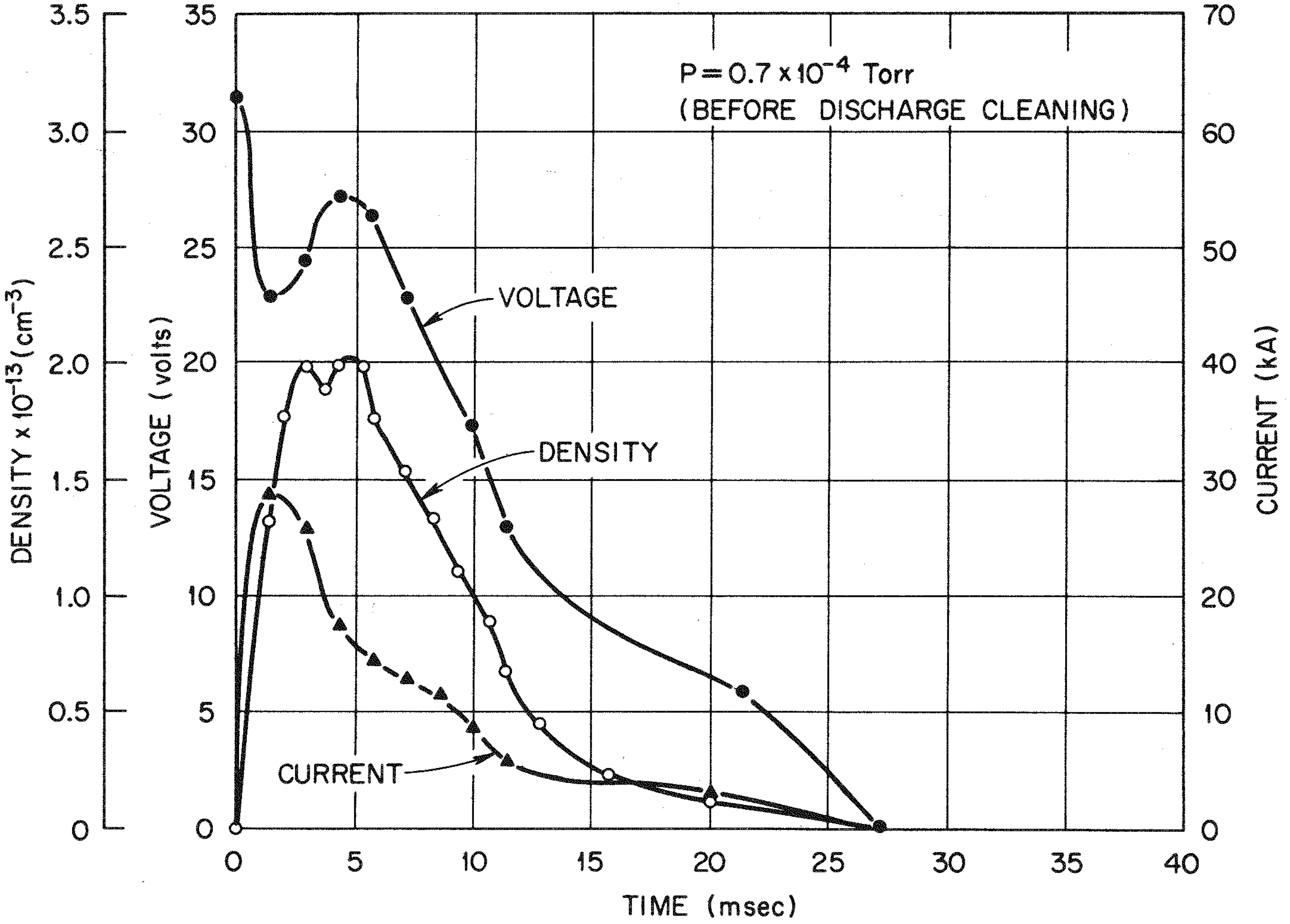

FIGURE II-2

ORMAK Parameters vs. Time for a Typical Non-Runaway Discharge (Capacitor Power Supply).

ORNL DWG. 75-12794

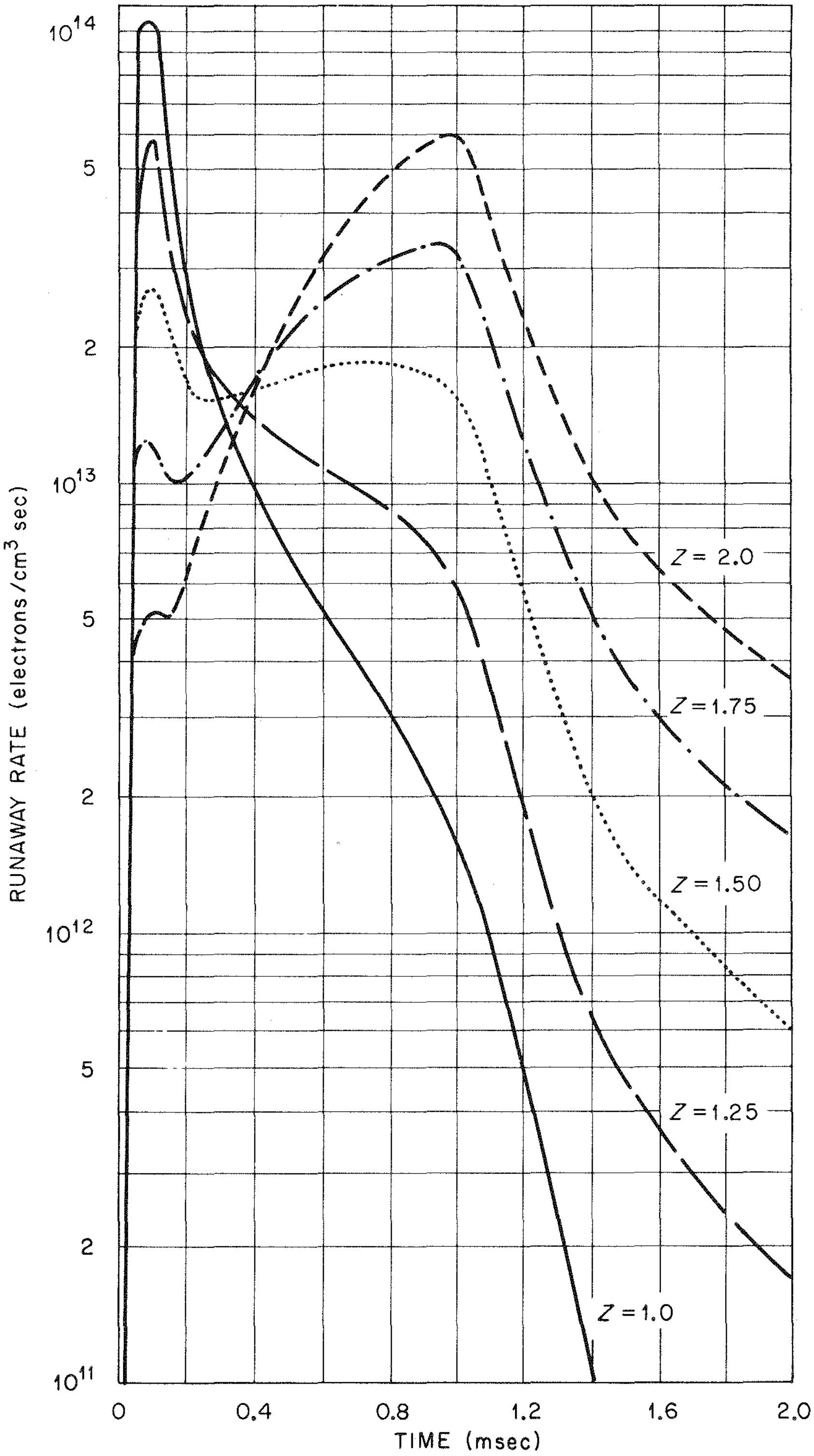

FIGURE II-3

Runaway Rate as a Function of Z and Time for an Initial Neutral Density of 5.5×10^{12} cm^{-3} and a 0.1 msec Rise Time in the Applied Electric Field.

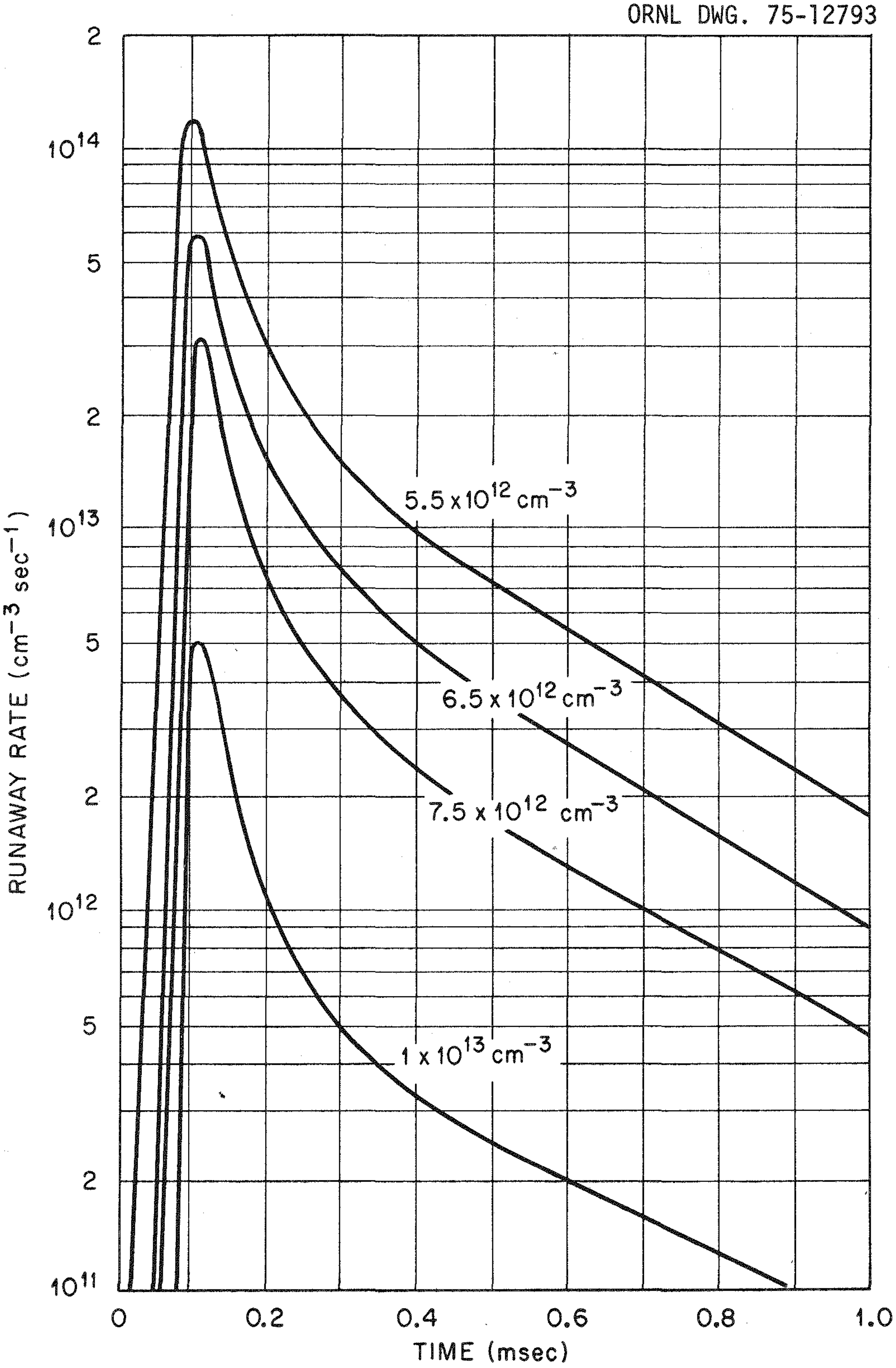

FIGURE II-4

Runaway Rate as a Function of Time and Initial Neutral Density for 0.1 msec Rise Time in the Applied Electric Field and Z=1.

in E_c. Moreover, from equation II-4, the critical velocity v_c also depends on Z, but since it enters the calculation of E_c only through the logarithmic terms, this dependence is relatively weak. The second peak which appears later on in the discharge is not related to the effect of Z on E_c. At the time when this occurs, the neutral density will have dropped (according to the model used here) to zero, thus removing completely the dependence of E_c on Z. The appearance of this peak has, however, to do with the effect of Z on the plasma temperature. An increase in Z will result in an increase in the computed temperatures which, in turn, lowers E_c and causes the second peak in the runaway rate to appear.

In Fig. II-4, the runaway rate is plotted versus time for various values of another parameter which could not be measured, i.e. the neutral density. The values of this parameter which are shown represent the initial neutral density and it is assumed that the densities decrease as the plasma density increases. An estimate of $\sim 10^{13}$ cm^{-3} for the initial neutral density is obtained from the pressure and temperature of the fill gas before the discharge. Increasing the neutral density results in a decrease in the runaway production since, according to equations II-3 and II-4, this leads to an increase in both v_c and E_c. Physically, this reduction in runaway production occurs because inelastic collisions with neutrals provide an additional mechanism for electron energy loss.

Another parameter which is introduced in the present calculation is the initial rise time of the induced electric field in the plasma. The voltage measured experimentally is the total external voltage around the torus and consists of resistive and inductive components. At early times in the discharge, the voltage applied to the plasma rises rapidly; the time constant is a characteristic of the liner-plasma-transformer circuit, i.e. the flux change which induces the Ohmic heating field must soak through the conducting liner and initially low temperature preionized plasma. Since the electrical characteristics of the liner-plasma-power supply circuit are not well known early in the discharge, this time constant is treated as a parameter. For Figs. II-3 and II-4, a value of 0.1 msec is used, and lowering this value results in more runaways. This is comparable to the time constant which is calculated by using the Spitzer resistivity and assuming that the initial preionized plasma in ORMAK has a temperature of 2 eV.

II.2 Initial Formation of the Beam and Effect of Field Errors on Beam Size

The early ORMAK discharges exhibited a striking dependence on the direction of the applied electric field. It was observed that a much lower level of runaway was present if the Ohmic heating field and toroidal magnetic field were parallel than if they were antiparallel. This effect was analyzed by Rome [6] who was able to relate it to the lack of closure of flux surfaces in the first few milliseconds of the discharge for the parallel case. When the two fields are antiparallel, flux surfaces can be closed within a certain volume in the discharge, but intersect the wall outside that volume.

As was indicated in the previous section, runaway production is favored during the early part of the discharge. Since these runaways are at nonrelativistic energies for the first few milliseconds, they tend to be closely tied to the poloidal flux surfaces and any disruption in these surfaces will lead to loss of the runaway population. At slightly later times the toroidal plasma current increases rapidly and closes the flux surfaces. However, by this time the plasma density has risen to a higher value while the Ohmic heating field has become lower; thus, runaway production is less favorable.

As mentioned above, when the toroidal magnetic field and induced electric field are antiparallel, runaways are expected to have well-confined orbits only within a certain volume of the discharge at early times. This consideration motivated the modeling of the runaways as a finite beam whose size was determined by the initial topology of the flux surfaces. In order to make a quantitative estimate of this size, the following expression for the flux function, as derived by Rome [6], was employed:

$$\psi(x,y) = \frac{N_L \mu_0 I_L b}{4\pi^2 R_0} \ln \left\{ \frac{(x-r_L-a)^2 + y^2}{(x-r_L+a)^2 + y^2} \right\} - \frac{\mu_0 I_p}{4\pi r_p^2} (x^2 + y^2) \qquad \text{II-6}$$

where N_L = number of toroidal field coils

I_L = current in the error coil

R_0 = major radius

a,b = width and length of error coils

r_L = location of error coil loop centers

The coordinate system is shown in Ref. 6. The beam size is obtained by first setting y=0 (since ψ is symmetric in y) and $x = -r_p$ (limiter radius). Calculating ψ at this point then gives the value of flux for which the outer edge of the plasma is just intersecting the limiter. Solving for a second value of x where the flux takes on the same value gives the inside location of the flux surface - x axis intersection. The difference between these two locations then gives the size of the beam. In Fig. II-5, the radius of the closed flux surface region is plotted as a function of time for the discharge parameters of Fig. II-1. This shows that after about 0.5 millisecond the entire plasma volume ($r_p = 23.5$ cm) should be well contained.

II.3 Acceleration of Runaways in Applied Ohmic Heating Field

The free acceleration of runaways is now examined using the familiar relativistic equation of motion. Although the results of Fig. II-3 for Z > 1 indicate that the peak in the runaway rate may be shifted to a later time as Z increases, it will be assumed here for simplicity that all runaways are born at a single time, t_0, early in the discharge with a negligible initial velocity. We shall also assume that the runaway current flows only in the ϕ-direction and is localized inside a beam of radius a. The force equation then gives the following

$$\frac{d}{dt}\,(\gamma m_0 \vec{v}) \;=\; -e\vec{E} \;=\; \frac{e}{c}\,\frac{\partial \vec{A}}{\partial t} \qquad \text{II-7}$$

where $\vec{A}$ is the vector potential, m_0 is the electron rest mass and γ is the usual relativistic parameter. II-7 is readily integrated to yield the velocity given below.

$$\beta \;=\; \frac{v}{c} \;=\; \frac{A}{\sqrt{1+A^2}} \qquad \text{II-8}$$

where $A \equiv \frac{e}{m_0 c}\;[A_\phi(t,\vec{R}) - A_\phi\,(t_0,\vec{R})\,]$

Note that A_ϕ consists of two parts: one from the flux change in the transformer core and the other from the beam-induced flux change.

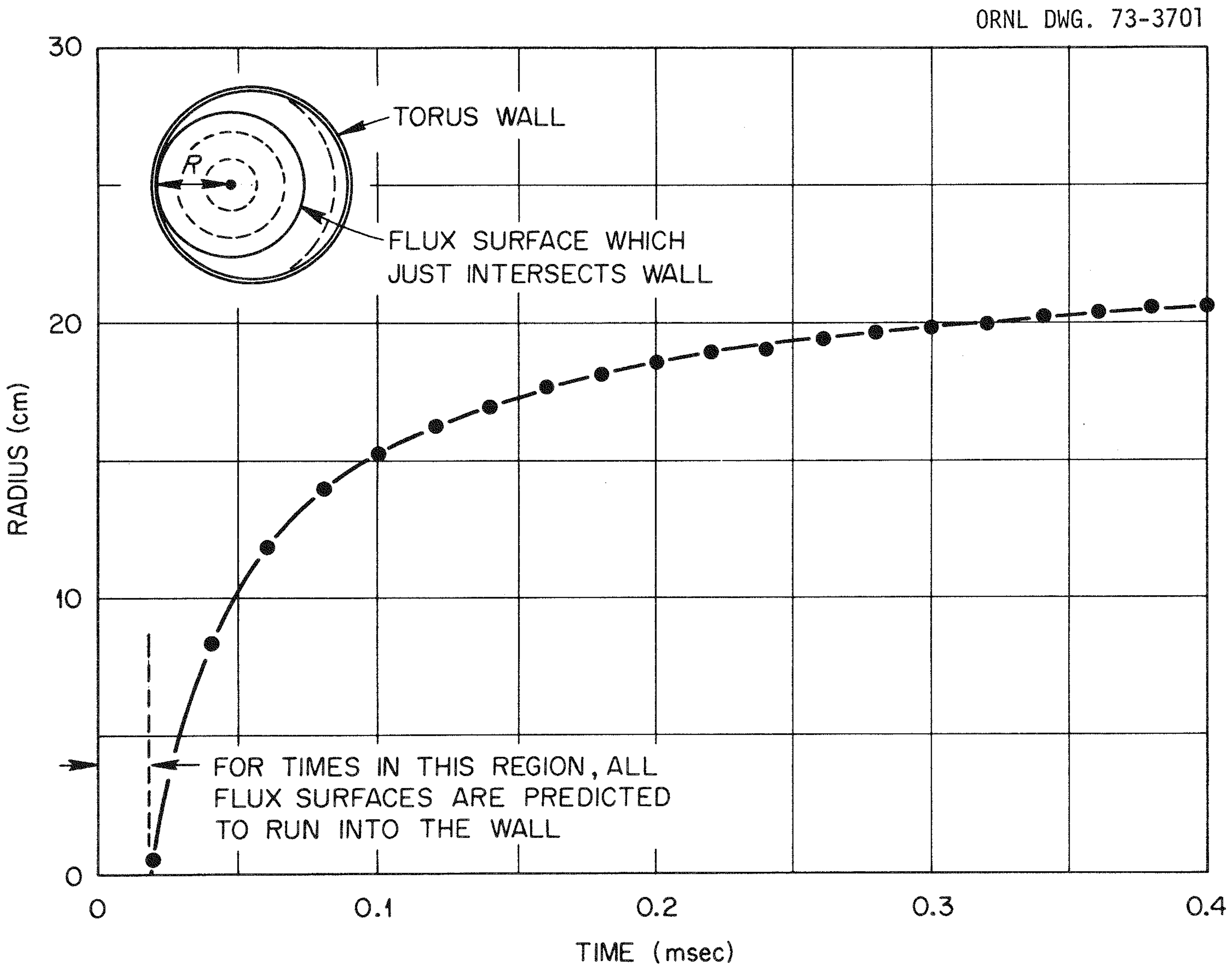

FIGURE II-5

Radius of Flux Surface which Intersects Torus Wall vs. Time.

$$A_\phi(t,\vec{R}) = A_\phi(t_0,\vec{R}) - \frac{1}{2\pi R}\int_{t_0}^{t} \varepsilon(t')dt' - \int_{t_0}^{t} E_\phi^B(t',\vec{R})dt' \qquad \text{II-9}$$

where $\varepsilon(t)$ = emf produced by the transformer core flux change

$E_\phi^B(t,\vec{R})$ = beam induced field

Since A_ϕ at $t=t_0$ is solely due to the transformer flux change, the spatial dependence of $A_\phi(t_0,\vec{R})$ is proportional to R^{-1}.

The ϕ-component of Ampere's law may be written as follows in terms of the dimensionless vector potential A.

$$\frac{m_0 c}{e}\left\{\frac{\partial^2 A}{\partial Z^2} + \frac{\partial}{\partial R}\frac{1}{R}\frac{\partial}{\partial R}(RA)\right\} = \mu_0 J_\phi \qquad \text{II-10}$$

Here axisymmetry has been assumed so that all derivatives with respect to ϕ are zero. The R,ϕ,Z coordinate system is illustrated in Fig. II-6. The toroidal current density carried by the runaways is simply $en_R v_R$ (n_R = runaway density, v_R = runaway velocity).

$$J_\phi = en_R c\beta = en_R c \frac{A}{\sqrt{1+A^2}} \qquad \text{II-11}$$

Substituting II-11 into II-10 and defining ω_{PR} as the plasma frequency for the runaway component results in the partial differential equation given below

$$\frac{\partial}{\partial R}\frac{1}{R}\frac{\partial}{\partial R}(RA) + \frac{\partial^2 A}{\partial Z^2} = \left(\frac{\omega_{PR}}{c}\right)^2 \frac{A}{\sqrt{1+A^2}} \qquad \text{II-12}$$

To order the above equation with respect to inverse aspect ratio, it is convenient to use a new coordinate system defined by the following.

$$R = R_0 + r\cos\theta \qquad \text{II-13}$$

ORNL DWG. 75-12797

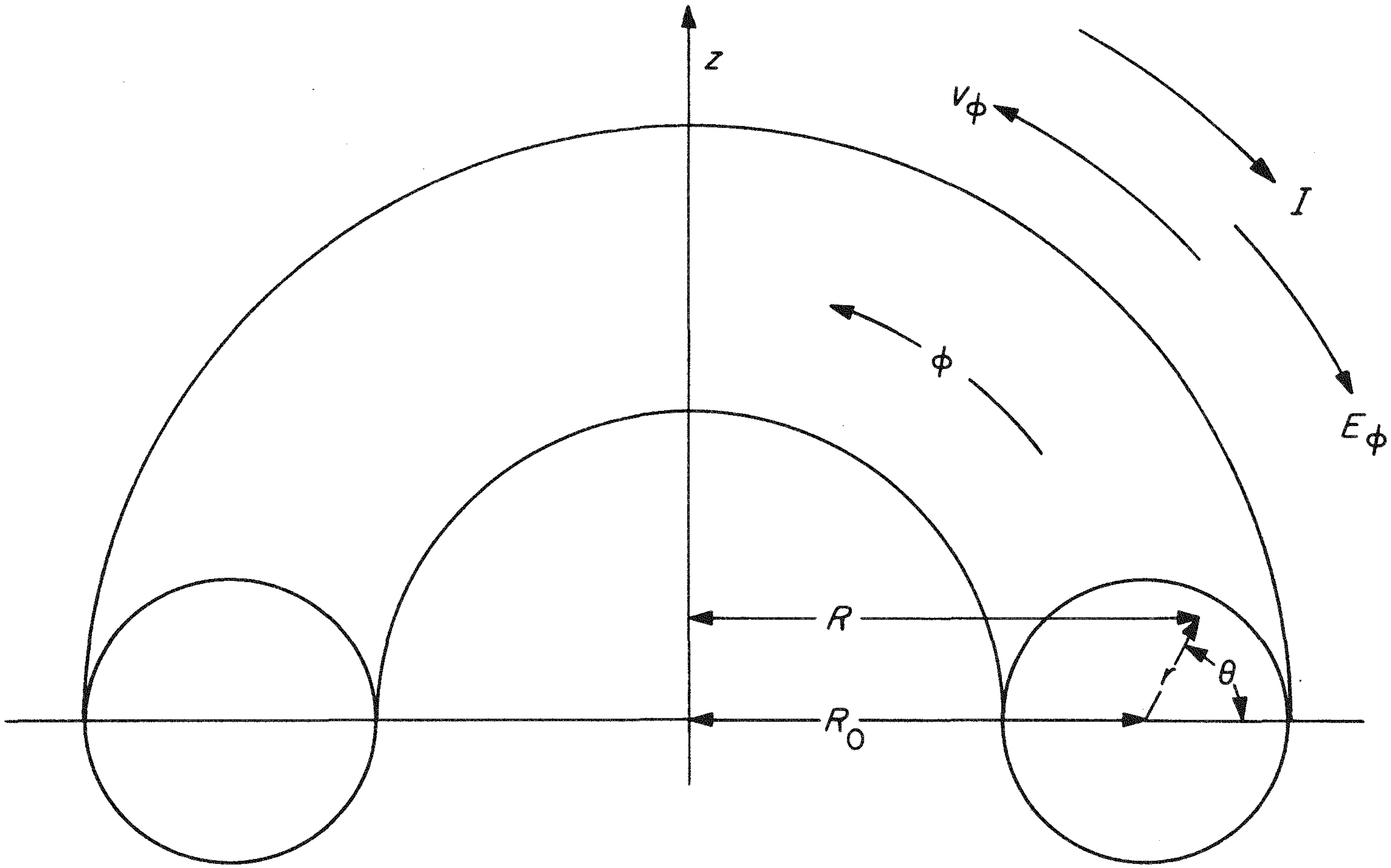

FIGURE II-6

Cylindrical and Quasi-Toroidal Coordinate Systems.

$Z = r \sin\theta$

This r,θ,ϕ coordinate system is also indicated in Fig. II-6 and its metric is $(1,r,R)$. Transforming equation II-12 into this system results in the equation below.

$$\frac{1}{rR}\left\{\frac{\partial}{\partial r}\, rR\,\frac{\partial A}{\partial r} + \frac{\partial}{\partial\theta}\,\frac{R}{r}\,\frac{\partial A}{\partial\theta}\right\} + \frac{A}{R^2} - \frac{k^2A}{\sqrt{1+A^2}} = 0 \qquad \text{II-14}$$

where $k^2 = \omega_{pr}^2/c^2$

Expanding II-14 in powers of $\varepsilon = r/R_0$ gives:

$$\frac{1}{r}\,(1-\varepsilon\cos\theta)\left\{\frac{\partial}{\partial r}\, r\,(1+\varepsilon\cos\theta)\,\frac{\partial A}{\partial r} + \frac{1}{r}\,\frac{\partial}{\partial\theta}\,(1+\varepsilon\cos\theta)\,\frac{\partial A}{\partial\theta}\right\}$$

$$- \frac{A}{R_0^{\,2}}\,(1-2\,\varepsilon\cos\theta) - \frac{k^2A}{\sqrt{1+A^2}} = 0 \qquad \text{II-15}$$

Keeping only terms to zero order in ε and assuming symmetry in the poloidal direction equation II-15 reduces to:

$$\frac{1}{r}\,\frac{\partial}{\partial r}\, r\,\frac{\partial A}{\partial r} - \frac{A}{R_0^{\,2}} - \frac{k^2A}{\sqrt{1+A^2}} = 0 \qquad \text{II-16}$$

This nonlinear equation can be readily solved in the two limits $A \gg 1$ and $A \ll 1$. In view of equation II-8, these regions correspond to $v \simeq c$ and $v \ll c$, respectively. It is expected that the limit $A \ll 1$ would hold during the early stages of acceleration while the opposite limit would apply at later times. In addition to these temporal variations, there are spatial variations in the speed of the electrons. Since the runaway beam is highly conductive, electrons near the center will be relatively well shielded from the electric field while those on the outer flux surfaces will feel the full force of acceleration.

In view of this, the $A \ll 1$ limit will be applicable near the center while the outside of the beam will approach the $A \gg 1$ limit after enough time has elapsed to bring these outer electrons to relativistic energies. The solutions of equation II-16 may be written as given below.

$$\begin{aligned} A(r,t) &= C_0(t)\; I_0(kr) && A \ll 1 \\ A(r,t) &= -(kR_0)^2 + C_1(t)\; I_0(r/R_0) && A \gg 1 \end{aligned} \qquad \text{II-17}$$

where I_0 is the modified Bessel function of zero order. The time dependent constants C_0 and C_1 are determined by the boundary value of the external field (i.e. the measured minus the beam and plasma inductive components) at the beam radius. This is given as follows:

$$\frac{\partial A_\phi}{\partial t} = -\frac{1}{2\pi R_0}\left\{\varepsilon - \mu_0 R_0 \dot{I}\, \ln \frac{b}{a}\right\} \qquad \text{II-18}$$

Integrating II-18, the boundary conditions may be expressed as follows:

$$A\Big|_{r=a} = \frac{e}{2\pi m_0 c R_0}\left\{\int_{t_0}^{t} \varepsilon(t')dt' - \mu_0 I \ln \frac{b}{a}\right\} \qquad \text{II-19}$$

The second condition used in determining C_0 and C_1 comes from the assumption that the solutions II-17 must match at some radial position r^* inside the beam where $A \simeq 1$. The result is two transcendental equations for r^*: one that applies to those early times before the outer electrons in the beam have reached relativistic energies (the $A \ll 1$ limit) and another that applies to those later times when the outer electrons have already attained relativistic energies. The time t^* at which this transition occurs is determined by the equation given below.

$$\frac{kaI_1(ka)\ln\frac{b}{a}}{I_0(ka)} - \frac{e}{2\pi m_0 c R_0}\int_{t_0}^{t^*}\varepsilon(t')dt' + 1 = 0 \qquad \text{II-20}$$

The quantity t^* is defined to be the time at which $r^*=a$, i.e. for $t<t^*$ the $A\ll 1$ solution applies inside the beam while for $t>t^*$ the $A\ll 1$ solution is used for $0<r<r^*$ and the $A\gg 1$ solution for $r^*<r<a$. The two transcendental equations for r^* referred to earlier are given by the following:

$$\frac{e}{2\pi R_0 m_0 c} I_0(kr^*)\int_{t_0}^{t^*}\varepsilon(t')dt' = I_0(ka) + kaI_1(ka)\ln\frac{b}{a} \qquad \text{II-21}$$

(for $t<t^*$)

$$r^*k\, I_1(kr^*)\ln\frac{b}{a} + \frac{I_0(a/R_0)}{I_0(r^*/R_0)}\left[1+(kR_0)^2\right]$$

$$= \frac{e}{2\pi R_0 m_0 c}\int_{t_0}^{t^*}\varepsilon(t')dt' + (kR_0)^2 - \frac{k^2}{2}(a^2 - r^{*2})\ln\frac{b}{a} \qquad \text{II-22}$$

(for $t>t^*$)

Once the radius r^* is determined as a function of time, then $A(r,t)$ may be readily obtained from equation II-17 with the constants C_0 and C_1 given as below.

$$C_0(t) = [I_0(kr^*)]^{-1} \qquad \text{II-23}$$

$$C_1(t) = \frac{1+(kR_0)^2}{I_0(r^*/R_0)} \qquad \text{II-24}$$

Using equation II-8 to relate A to the local electron velocity, the current density in the beam may be integrated over the cross-sectional area to obtain the total runaway current as a function of time.

$$I(t) = 2\pi n_R ec\int_0^a \beta(r)\, r\, dr \qquad \text{II-25}$$

$$= 2\pi n_R ec \int_0^a \frac{A\,r\,dr}{\sqrt{1+A^2}}$$

For $r < r^*$ (the $A<<1$ region), this integral can be calculated by using equation II-16 with the A/R_0^2 term neglected. In the $A>>1$ region, a convenient approximation is that $A\,(1+A^2)^{-1/2} \simeq 1$. These considerations result in the toroidal current given below.

$$I(t) = 2\pi n_R ec \left\{ \frac{r^*}{k^2} \left.\frac{\partial A}{\partial r}\right|_{r=r^*} + 1/2\,(a^2 - r^{*2}) \right\} \qquad \text{II-26}$$

Using the solutions in equations II-17, II-23 and II-24 give the following currents.

$$I(t) = \frac{2\pi n_R ec}{k^2} \frac{ka\, I_1(ka)}{I_0(kr^*)} \qquad t < t^* \qquad \text{II-27}$$

$$I(t) = \frac{2\pi n_R ec}{k^2} \left[r^*k \frac{I_1(kr^*)}{I_0(kr^*)} + \frac{k^2}{2} (a^2 - r^{*2}) \right] \quad t > t^* \qquad \text{II-28}$$

Besides total toroidal currents, a final quantity of interest in this model is the energy (or relativistic γ) as a function of time.

$$\gamma = (1 - \beta^2)^{-1/2} \qquad \text{II-29}$$

Using equation II-8, this becomes the following:

$$\gamma = \sqrt{1+A^2} \qquad \text{II-30}$$

II.4 Comparison of Theory with Experiment

Comparison of the above theory with experiment can only be made through a parameter survey since no direct information is available on the size of the beam or the total runaway density. As was discussed in

Section II.1, calculations have been made of runaway density; however, this depends sensitively on factors such as the initial plasma impurity level, degree of ionization and penetration time of the Ohmic heating field. Estimates can also be made of the beam size based on the belief that the radius is determined from the effect of magnetic field errors on the early evolution of the flux surfaces. The runaway beam radius should, in principle, correspond to the radius of the flux surface which just intersects the torus wall at the time when the peak runaway production occurs. However, the effect of field errors on flux surfaces has been calculated only approximately by averaging over the flux surfaces. When beam sizes predicted by this approach are used in the runaway current calculation, the results only agreed with experimental values to within an order of magnitude. For the above reasons, the beam radius and runaway density were left as parameters in the calculation.

Calculations of runaway beam currents have been performed using the methods developed in Section II.3 for a range of beam radii and runaway densities. Data has been used from both the capacitor-driven case (Figs. II-1, II-2) and the battery-driven case (Fig. II-7). Runaways are all assumed to be produced at $t_0=0$. It is also assumed in these calculations that nearly all the observed current is carried by runaways. This assumption may be justified by the data presented in Figs. II-1 and II-2. As mentioned above, Rome's analysis of field errors [6] indicates that for the electric field direction in the Fig. II-2 discharge, the flux surfaces run into the wall early in the discharge, thus removing runaways. However, in Fig. II-1 the flux surfaces are closed and runaways may be freely accelerated. This led then to the

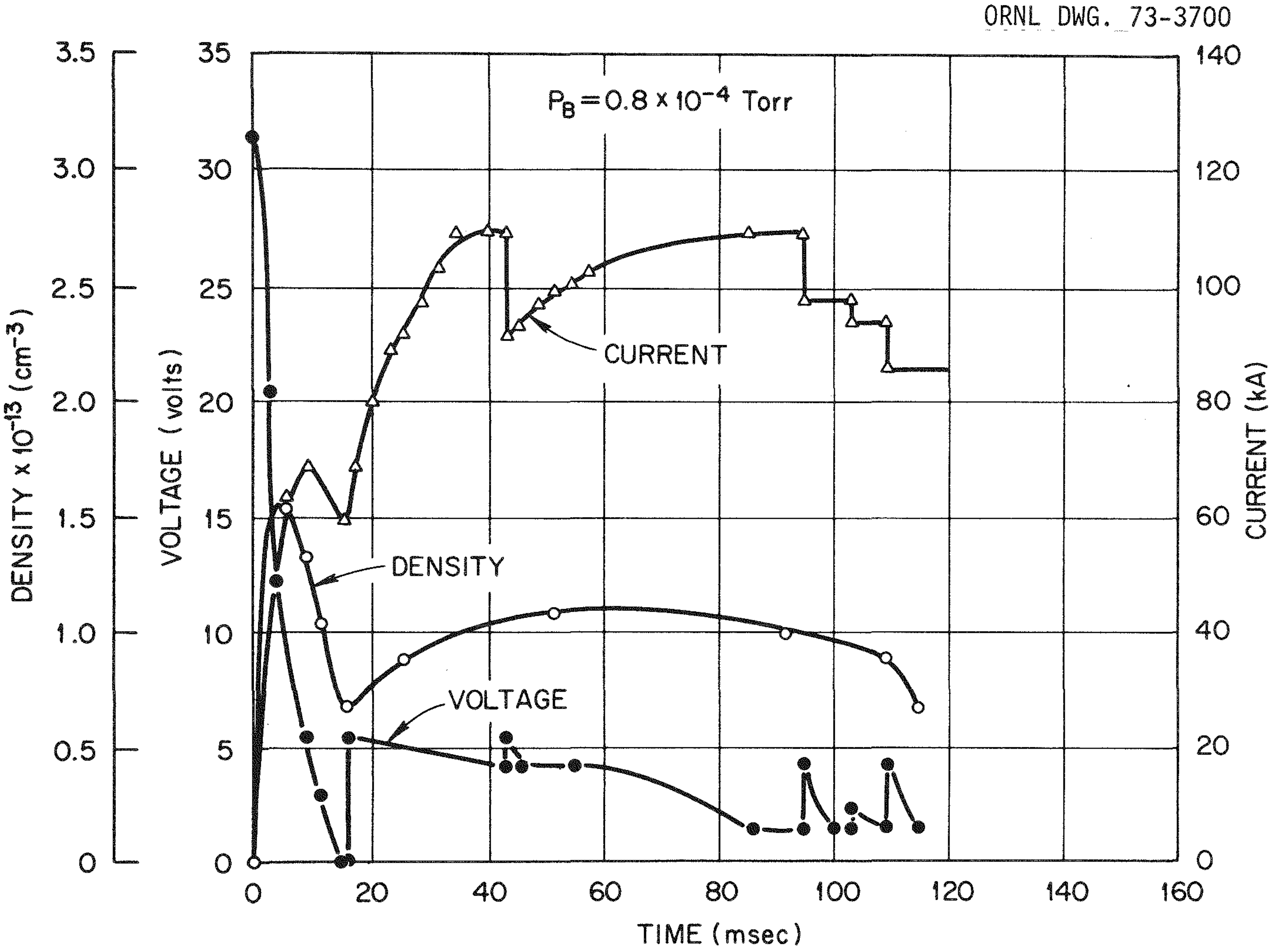

FIGURE II-7

Density, Current, and Voltage vs. Time for a Typical Battery-Driven Runaway Discharge.

assumption that Fig. II-1 represents runaway current plus plasma current while Fig. II-2 represents the small amount of plasma current present in the discharge of Fig. II-1. Subtracting the current of Fig. II-2 from that of Fig. II-1 was thus assumed to give the runaway segment of the current. It was this current against which the above theory was compared.

Figure II-8 shows results for the capacitor-driven case. It may be noted that various values of beam radius and runaway density can be chosen to give reasonable agreement with the experimental data. Lower densities with larger radii were found to result in a leveling-off in the current similar to that which is apparent in Figs. II-8a and II-8d. This occurs when all electrons across the beam reach relativistic energies so that further acceleration does not significantly increase the total current. At low densities, this occurs more rapidly because of the earlier penetration of the electric field into the beam. In Fig. II-9, the time evolution of the relativistic factor γ is plotted as a function of the radial position in the beam. As pointed out earlier, the most energetic electrons are at the outer edges of the beam with the central electrons being least energetic since they receive less acceleration. Figs. II-10 and II-11 show results for the first 44 msec of the battery-driven case. It is found that only a relatively narrow range of radii and runaway densities would provide agreement with the experiment in this case (densities of $2\text{-}3\text{x}10^{11}\text{cm}^{-3}$ and radii of 5-6 cm). Lower densities result in a leveling-off in current at too early a time in the discharge whereas with higher densities the leveling-off which occurs in the experimental data at about 34 msec could not be obtained.

ORNL DWG. 75-12798

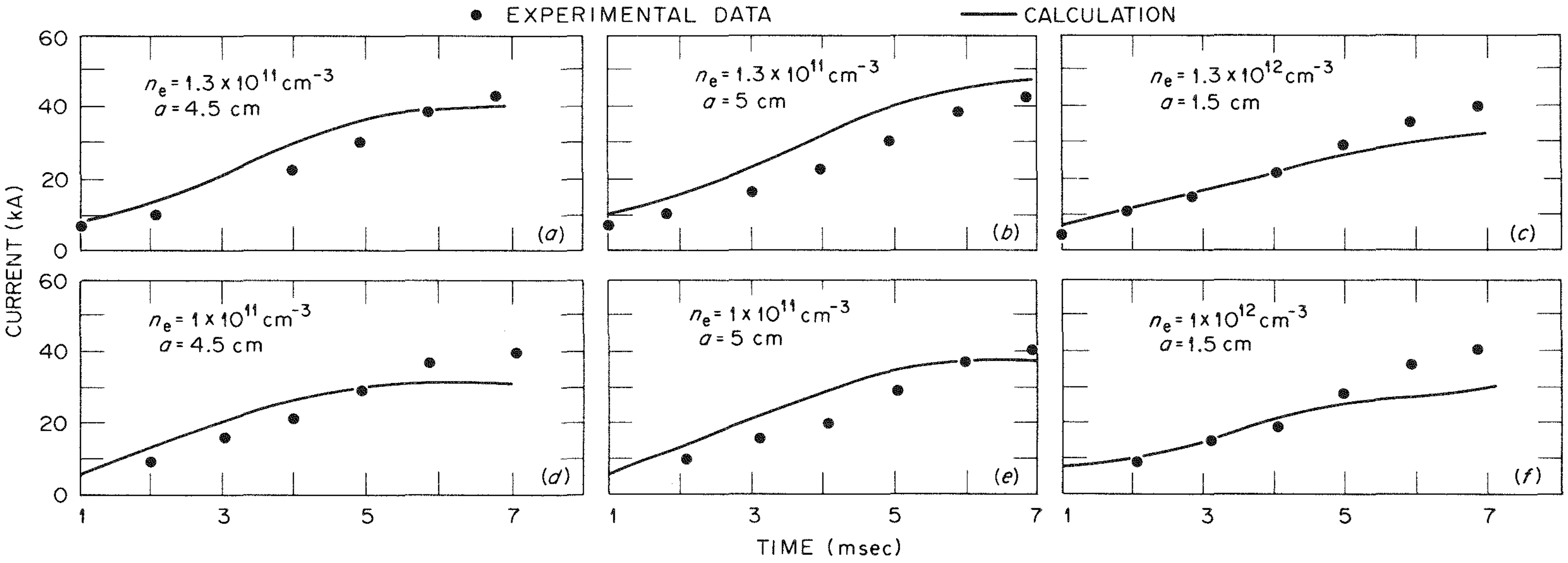

FIGURE II-8

Calculated and Experimental Runaway Currents for the Capacitor-Driven Case.

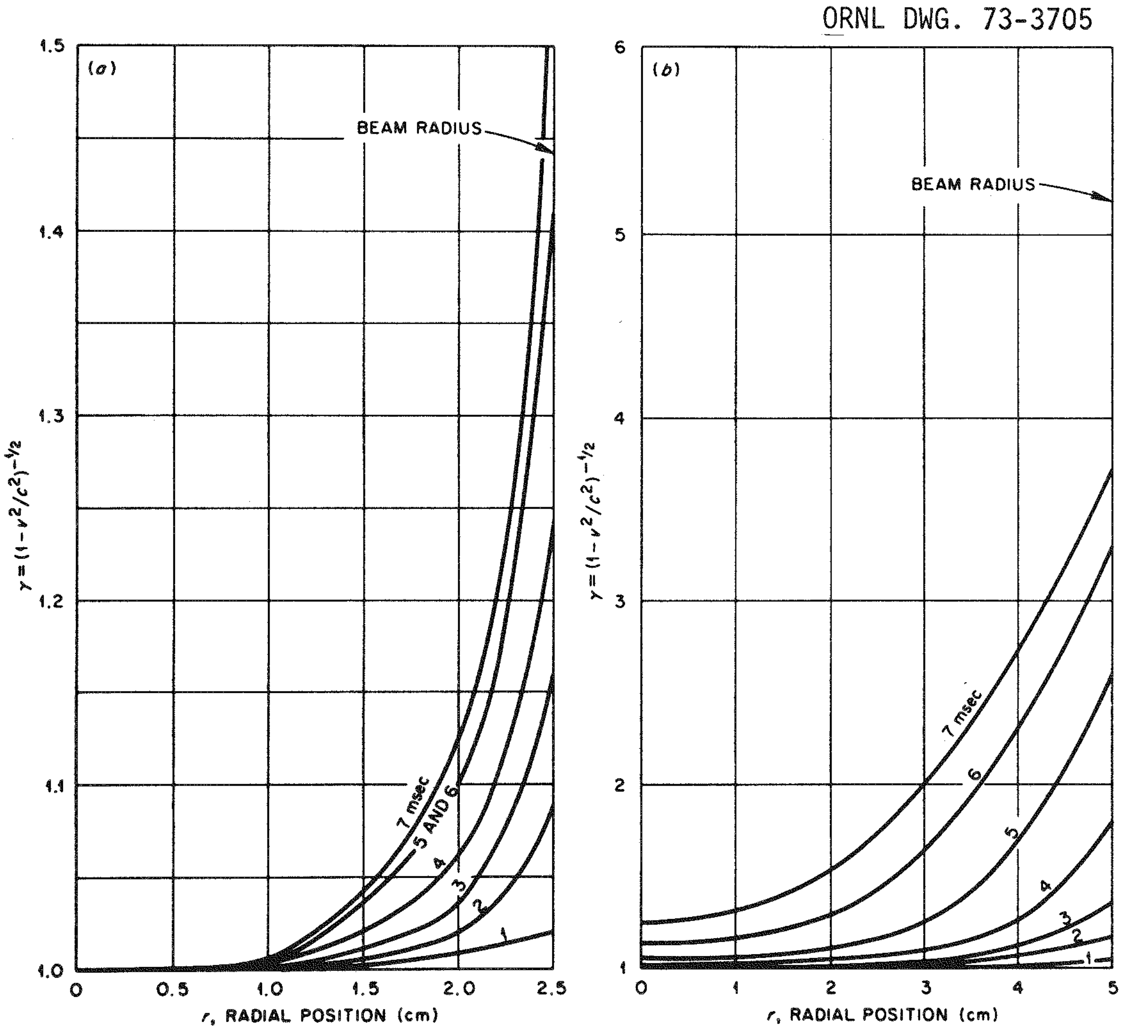

FIGURE II-9

γ as a Function of Radius and Time for the Capacitor-Driven Case for (a) $n_e = 10^{12}$ cm^{-3}, a = 2.5 cm, (b) $n_e = 1.3 \times 10^{11}$ cm^{-3}, a = 5 cm.

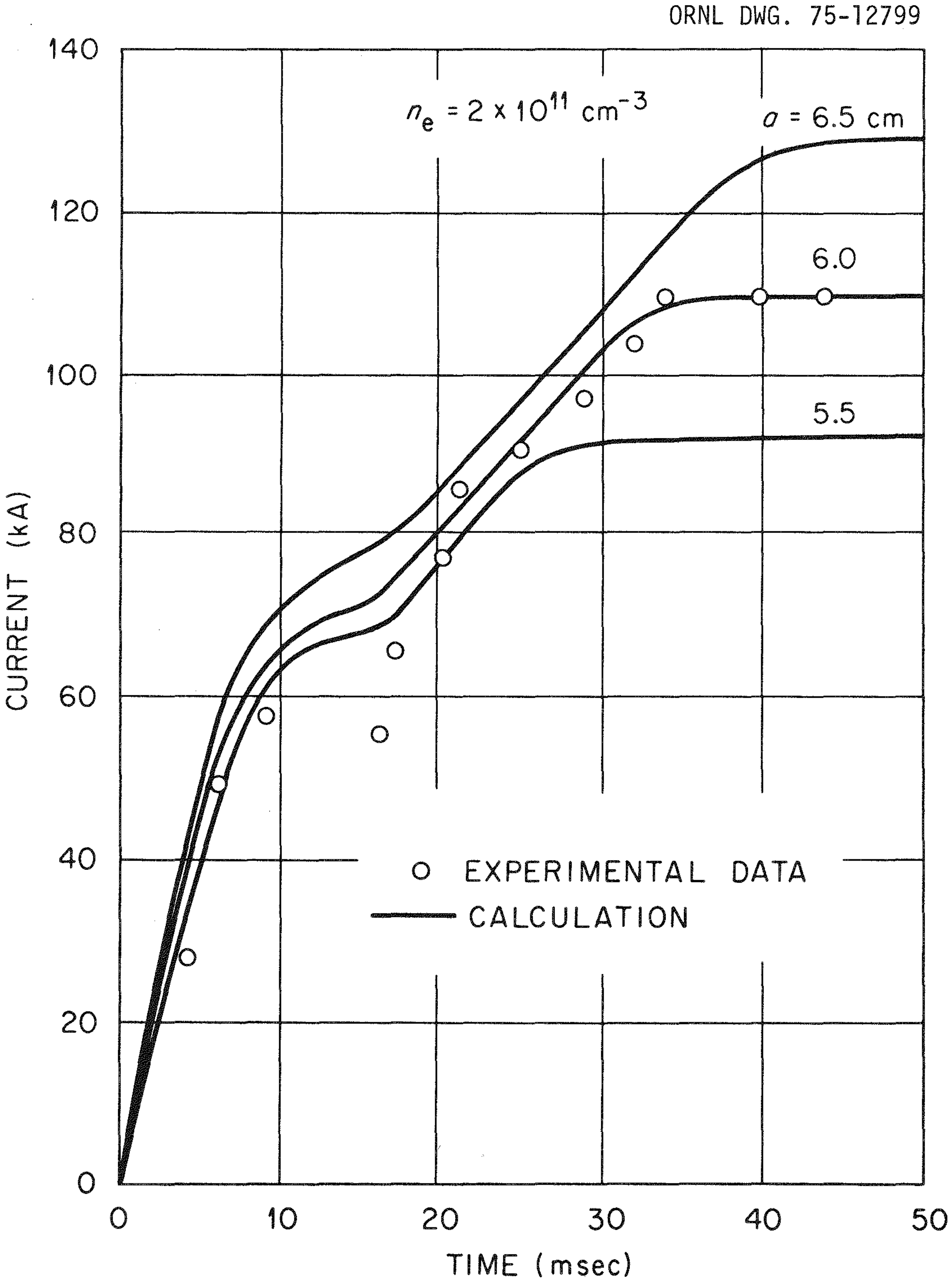

FIGURE II-10

Calculated and Experimental Runaway Currents for the Battery-Driven Case with $n_e = 2 \times 10^{11}$ cm^{-3}.

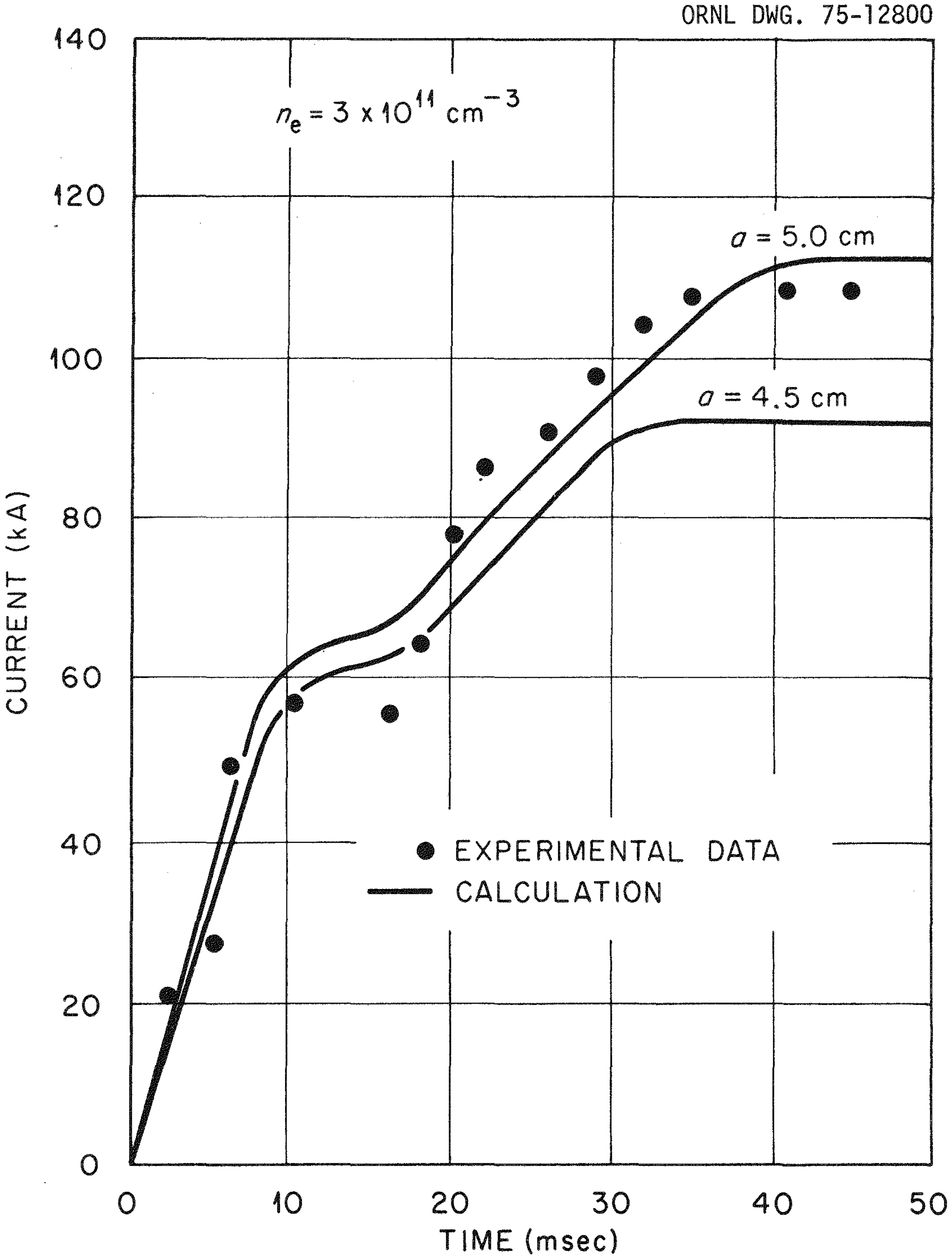

FIGURE II-11

Calculated and Experimental Runaway Currents for the Battery-Driven Case with $n_e = 3 \times 10^{11}$ cm^{-3}.

The dip in the experimental data at ~ 15 msec is due to the fact that the voltage is driven negative when the capacitor banks are turned off and the batteries are connected; this was not included in the theoretical calculation. The time evolution of the relativistic factor γ is presented in Fig. II-12 and shows a behavior similar to that of the capacitor-driven case.

In addition to the above parameter study, another source of information about the runaway beam radius is the horizontal plasma column displacement. In ORMAK runaway-dominated discharges, large outward shifts were inferred from the magnetic loop measurements (~6 to 9 cm). As was mentioned in Section I.2, similar observations were made on the Russian Tokamak-6 runaway experiments [15]. Vlasenkov, et al. [15] offered two possible explanations of this phenomenon -- one being that the major portion of the current is flowing within a 5-6 cm radius beam and the other that the electron plasma pressure is highly anisotropic ($p_{\parallel} >> p_{\perp}$). They found that if the runaway electrons are assumed to possess a longitudinal energy of 500-700 keV, then the large displacement can be explained without having to resort to the assumption of a small current channel (i.e. the internal inductance, ℓ_i, is the same as for the normal plasma regime). However, for ORMAK parameters, calculations based on the equilibrium theories of Mukhovatov and Shafranov [58], Ott and Sudan [59], and Mondelli and Ott [60] show that even with a highly anisotropic pressure ($E_{\parallel} \sim 1$ MeV), it is necessary to choose a runaway beam radius of the same magnitude as that obtained in the above parameter study (~6 cm) in order to give agreement with the experimentally-observed shift. A further compelling reason for choosing a beam radius

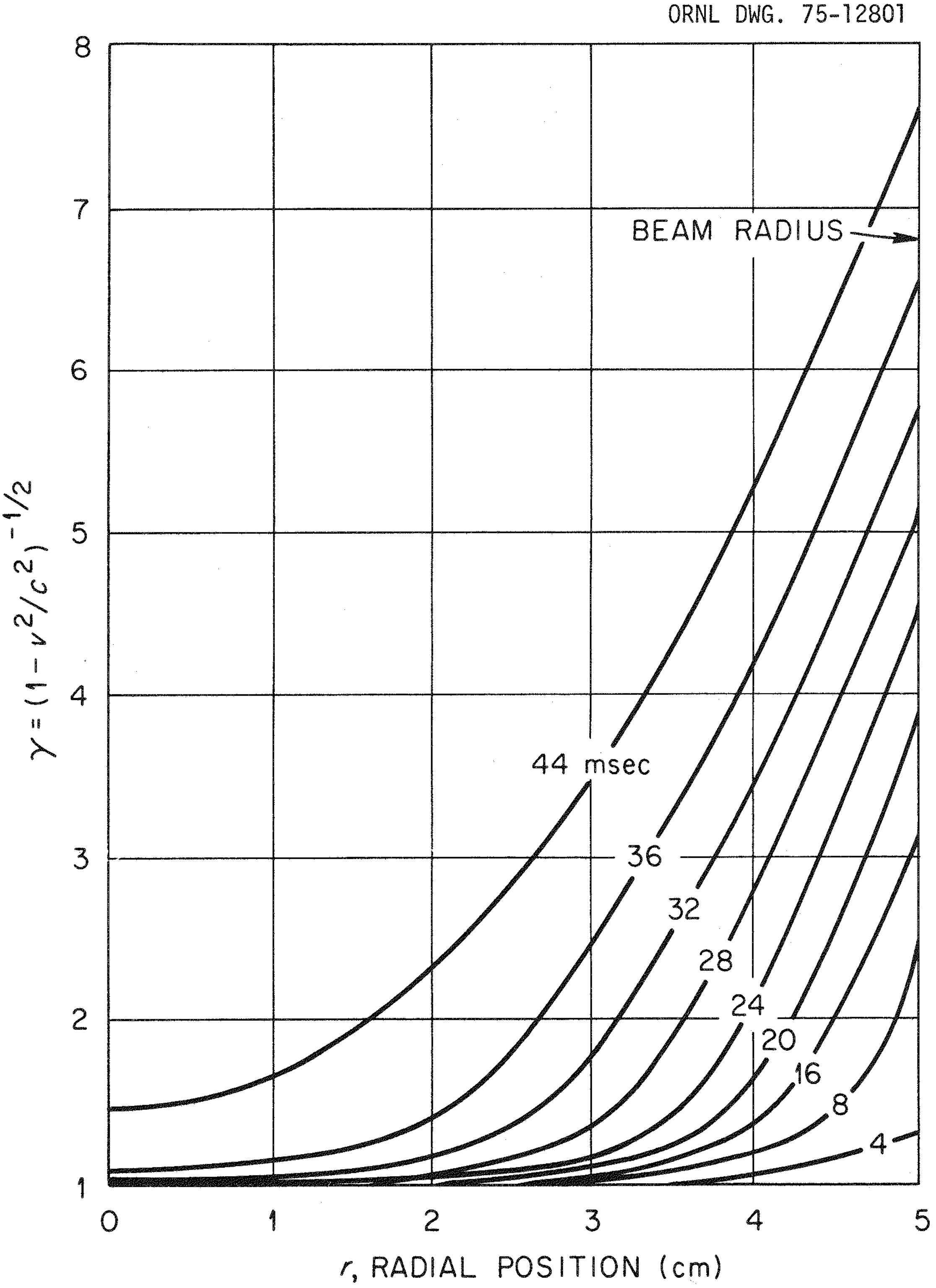

FIGURE II-12

γ as a Function of Radius and Time for the Battery-Driven Case with $n_e = 3 \times 10^{11}$ cm^{-3} and a = 5 cm.

significantly less than the plasma limiter radius is that a large beam subjected to an outward displacement (which is a large fraction of the limiter radius) would necessarily have to form a highly-distorted equilibrium and would probably hit the limiter early in the discharge. It may well be that the current dumps observed after ~44 msec in the battery-driven case (Fig. II-7) are due to a part of the runaway beam colliding with the limiter; however, if the beam radius were of the same order of magnitude as the limiter radius, these dumps would be expected to occur much earlier in the discharge.

One further rough indication of the beam size comes from the damage pattern on the first ORMAK limiter. This also indicates that most of the energy was localized within a region of the same order as the beam sizes given above.

In summary, the above considerations and parameter study lead to the conclusion that most of the runaway current is carried within a 5-6 cm region. If the runaways actually did carry most of the observed current and if the observed current dumps can be explained on the basis of the beam hitting the limiter (i.e. a loss of equilibrium rather than a loss of stability), then this would imply that low values of q (Kruskal-Shafranov safety factor) near 1/4 are being attained in the runaway regime without macroscopic instabilities. This point will be returned to in Chapter V where a theoretical stability analysis will be presented in relation to the discharges considered in this Chapter.

CHAPTER III

Single Particle Drift Orbits of Runaways in Tokamaks

An analysis of single particle orbits is the first step in considering a number of questions which regularly arise in plasma physics. Not only are orbit characteristics essential in relation to basic confinement, but they also are of importance in the areas of kinetic theory and stability analysis.

The treatment given in the present chapter relies on the guiding center or drift approximation. This is obtained by averaging over the fast gyromotion and has been derived by various authors including Northrup [61], Bogolyubov and Mitropol'skii [62], and Bernstein [63]. Such a description of the single particle orbits is expected to be adequate for locating the spatial position of runaways in ORMAK due to the fact that the gyroradii are quite small. For example, in the extreme case of a relativistic electron which has a 90° pitch angle (the pitch angle is the angle between the direction of the particle velocity and the magnetic field), the gyroradius for a typical ORMAK toroidal field is $\tilde{\sim} \gamma$ millimeters (where $\gamma = (1-v^2/c^2)^{-1/2}$). Thus, even at 10 MeV ($\gamma = 20.6$), gyroradii are an order of magnitude smaller than the machine minor radius.

In checking the validity of the drift approximation, one must also examine the conservation of the magnetic moment, μ. Since only static magnetic fields are assumed present, the conservation criterion is that the relative change in magnetic field strength seen by the particle over one gyroperiod is small; in a tokamak this change largely is due to the $^1/_R$ falloff of the toroidal field. In the case of a runaway with a pitch angle near 90°, this criterion is readily satisfied because of the small size of the gyro-orbit relative to the scale length of the field gradient. In the other limit where $v_\parallel >> v_\perp$, the change in field strength over a gyro-orbit is given by the following.

$$\frac{\Delta B}{B} \simeq \frac{\Delta R}{R_0} \qquad \text{III-1}$$

ΔR is the distance the particle moves along the major radius direction (over one gyroperiod); this depends on the pitch of the field lines. If it is assumed that q=1, then ΔR over one gyroperiod is given below:

$$\Delta R = \frac{2\pi v_\parallel}{\Omega_e} \frac{r}{R} \qquad \text{III-2}$$

where r = minor radius position of particle
Ω_e = cyclotron frequency

For $v_\parallel \simeq c$ and ORMAK parameters, one finds that $\Delta B/B \simeq .2\%$. Thus, the conservation of μ should be a reasonable assumption.

In the following Chapter, an analysis is first made of the effect of $\vec{E} \times \vec{B}$ drifts in strong runaway discharges. It would be expected that this drift would lead to an inward pinching of the runaway beam with time. This is shown to be relatively slow and thus the approximation made in Chapter II of a constant density, constant radius beam is valid.

Next, effects of curvature and gradient drifts are considered in relation to the weak runaway regime. As was mentioned in Chapter I, this regime is characterized by a small population ($\sim 10^7$ cm^{-3}) of high energy (5-12 MeV) runaways. These occur both in the type A (high density, narrow current profile, high MHD activity) and type B (lower density, broad current profile, lower MHD activity) discharges. In type A discharges runaways leave the plasma region at early times whereas in type B discharges, these particles come out near the end. In both cases the loss occurs when the energy becomes too high for the orbits to be contained in the machine. This loss is in particular expected to be a smooth gradual process in the type B discharges where runaways begin intersecting the limiter during the flatop section of the current pulse when most of the discharge parameters are not changing rapidly with time. The situation in type A discharges is somewhat more complicated since runaways leave the plasma at early times when plasma parameters are changing rapidly. The analysis in Sections III.2-III.4 will be in relation to type B discharges.

III.1 $\vec{E} \times \vec{B}$ Shrinkage Effects on Beam Radius and Density in the Runaway-Dominated Regime

The parameter study presented in Chapter II of the strong runaway regime made the simplifying assumption that the beam had a constant radius and constant density throughout its acceleration to relativistic energies. In the following, an analysis is undertaken of the approximate evolution of runaway electron drift surfaces in order to determine if the above assumption is a reasonable one.

The model assumed is that of a toroidally-confined electron beam which is being accelerated by a longitudinal electric field. Since the electrons are sufficiently energetic that they suffer very infrequent collisions, it is assumed that no collisional particle transport out of the beam occurs, i.e. the electrons are perfectly contained. It is also assumed that the beam has been sufficiently accelerated so that the relativistic factor $\gamma = (1-v^2/c^2)^{-1/2}$ is large over the whole cross-section.

The basic equations involved in the analysis are the relativistic drift equation [61], the continuity equation, the conservation of canonical angular momentum, and Ampere's law (written in terms of the poloidal flux function ψ):

$$\vec{v} = v_{\parallel}\hat{e}_1 + \frac{\hat{e}_1}{B} \times \left[-\vec{E} + \frac{\mu}{\gamma e}\vec{\nabla}B - \frac{P_{\parallel}^2}{\gamma e m_0}\frac{\partial \hat{e}_1}{\partial s} \right] \tag{III-3}$$

$$\frac{\partial n_R}{\partial t} + \vec{\nabla}\cdot(n_R\vec{v}) = 0 \tag{III-4}$$

$$P_\phi = m_0 c R\gamma\beta - e\psi = \text{constant} \tag{III-5}$$

$$\Delta^*\psi = \mu_0 R J_\phi \tag{III-6}$$

where $J_\phi = -e n_R v_\phi$

$\Delta^*\psi = R^2\vec{\nabla}\cdot(R^{-2}\vec{\nabla}\psi)$

$\psi = RA_\phi$

A_ϕ = ϕ component of the vector potential

Here $\hat{e}_1$ is a unit vector tangent to a field line ($\hat{e}_1=\vec{B}/B$), $\mu = P_\perp^2/2m_0B$ is the magnetic moment, m_0 = electron rest mass, and $\gamma = (1-v^2/c^2)^{-1/2}$. Both cylindrical and quasi-toroidal coordinates (r,θ,ϕ) will be employed; these are illustrated in Fig. II-6. $\hat{e}_1$ may be written in terms of the poloidal flux function as:

$$\hat{e}_1 = \frac{B_\phi}{B}\,\hat{\iota}_\phi - \frac{\hat{\iota}_\phi \times \vec{\nabla}\psi}{RB} \qquad \text{III-7}$$

In the following analysis, the drift velocity given by expression III-3 will first be written in terms of the surface quantity γ (ψ and γ surfaces are related by equation III-5). This velocity is then substituted into the continuity equation III-4 which results in a form for the runaway density as a function of γ. The field equation III-6 is then self-consistently solved to zeroth order in the inverse aspect ratio (cylindrical approximation). The requirement that the total number of runaways remain constant in time then gives an equation for shrinkage of the beam radius.

In equation III-3 it is assumed that beam electrons have negligible perpendicular thermal velocity so that the magnetic moment is zero. This leaves only $\vec{E} \times \vec{B}$ and curvature drift terms. The $\vec{E} \times \vec{B}$ drift is shown in the following analysis to result in a radial shrinkage of the electron density profile. The curvature drift term is in the Z-direction and produces a circulation of runaways around the minor cross-section of the torus; this is shown to distribute the runaways such that their density becomes a function only of the surface quantity γ. Both of these drifts will be retained in the analysis and the above-mentioned effects will be treated by an ordering procedure.

Substituting expression III-7 into equation III-3 and neglecting curvature in the poloidal magnetic field results in:

$$\vec{v} = \beta c\,\frac{\vec{B}}{B} + \frac{E_\phi \vec{\nabla}\psi}{RB_\phi^2} + \frac{m_0 c^2 \beta^2 \gamma}{eR}\left[-\frac{\hat{\iota}_Z}{B_\phi} + \frac{(\hat{\iota}_R \cdot \vec{\nabla}\psi)}{RB_\phi^2}\,\hat{\iota}_\phi\right] \qquad \text{III-8}$$

where $\beta = v/c$

Using equation III-5 to relate $\vec{\nabla}\psi$ and $\vec{\nabla}\gamma$, the above equation may be written in the following form.

$$\vec{v} = \beta c \left\{ \hat{\iota}_\phi \left[1 + \frac{c^2(\gamma^2-1)}{R_0^2\omega_{ce}^2} + \frac{c^2\gamma h}{R_0\omega_{ce}^2} (\hat{\iota}_R\cdot\vec{\nabla}\gamma) \right] \right.$$

$$\left. + \hat{\iota}_R \left(\frac{E_\phi}{B_\phi^0}\right)\frac{h\gamma}{R_0\omega_{ce}} + \vec{\nabla}\gamma \left(\frac{E_\phi}{B_\phi^0}\right)\frac{h^2}{\omega_{ce}\beta^2} - \hat{\iota}_\phi \times \vec{\nabla}\gamma \frac{ch}{\beta\omega_{ce}} \right\} \qquad \text{III-9}$$

where $\omega_{ce} = \frac{eB_\phi^0}{m_0}$, $B_\phi^0 = hB_\phi$, $h = 1 + \frac{r}{R_0} \cos\theta$

The second drift term in the $\hat{\iota}_\phi$ direction is of $O\ (\rho/R_0)^2$ and the third $\hat{\iota}_\phi$ term is of $O\ (\rho^2/aR_0)$ where $\rho = c/\omega_{ce}$ and a is the beam radius. For typical ORMAK runaway regime parameters [7] $\rho/a \sim 3\text{x}10^{-2}$ and $\rho/R_0 \sim 10^{-3}$. Thus, the second and third $\hat{\iota}_\phi$ terms may be neglected in comparison with unity. Writing the remaining terms in equation III-9 in terms of an $\hat{\iota}_\phi$, $\vec{\nabla}\gamma$, $\hat{\iota}_\phi \times \vec{\nabla}\gamma$ orthogonal coordinate system, the following equation is obtained.

$$\vec{v} = \beta c \left\{ \hat{\iota}_\phi + \vec{\nabla}\gamma \left(\frac{E_\phi}{B_\phi^0}\right)\left[\frac{h^2}{\omega_{ce}\beta^2} + \frac{\hat{\iota}_R\cdot\vec{\nabla}\gamma}{|\vec{\nabla}\psi|^2}\,\frac{h\gamma}{R_0\omega_{ce}}\right] \right.$$

$$\left. + \hat{\iota}_\phi \times \vec{\nabla}\gamma \left[-\frac{ch}{\beta\omega_{ce}} + \frac{\hat{\iota}_Z\cdot\vec{\nabla}\gamma}{|\hat{\iota}_\phi \times \vec{\nabla}\gamma|^2}\left(\frac{E_\phi}{B_\phi^0}\right)\frac{h\gamma}{R_0\omega_{ce}}\right] \right\} \qquad \text{III-10}$$

The $\vec{\nabla}\gamma$ terms are, respectively, of $O(v_E\rho/ca)$ and $O(v_E\rho/cR_0)$ whereas the $\hat{\iota}_\phi \times \vec{\nabla}\gamma$ terms are of $O(\rho/a)$ and $O(v_E\rho/cR_0)$. Here $v_E = E_\phi/B_\phi^0$ and $v_E/c \sim 4\text{x}10^{-7}$.

Neglecting small-order terms results in:

$$\vec{v} = \beta c \left[\hat{\imath}_\phi + \vec{\nabla}\gamma \left(\frac{E_\phi}{B^0_\phi}\right) \frac{h^2}{\omega_{ce}\beta^2} - \hat{\imath}_\phi \times \vec{\nabla}\gamma \frac{ch}{\beta\omega_{ce}} \right] \qquad \text{III-11}$$

We now substitute this velocity into the continuity equation III-4, using $E_\phi = (-1/R)\ (\partial\psi/\partial t)$ and assuming axisymmetry (which implies that $\vec{\nabla} \cdot\ (nv_\phi \hat{\imath}_\phi) = 0$) to obtain the following equation:

$$\frac{1}{h^2} \frac{\partial n^*}{\partial t} - \frac{c^2}{\omega_{ce}} \left[\frac{(\hat{\imath}_\phi \times \vec{\nabla}\gamma) \cdot \vec{\nabla} n^*}{h} \right] - \frac{c^2}{\omega_{ce}^2}\ \vec{\nabla} \left[\frac{n^*\gamma}{\gamma^2 - 1} \vec{\nabla}\gamma \frac{\partial\gamma}{\partial t} \right] = 0 \qquad \text{III-12}$$

where n^* is the normalized density $(=nh^2/N)$ and N is the initial runaway density.

The terms in III-12 are ordered by noting the existence of three time scales. These are defined as follows:

τ_d = characteristic time for a change in runaway density to occur.

τ_t = time for an electron with velocity near the speed of light to make one transit around the torus.

τ_E = characteristic time for a change to occur in particle energy as the electron accelerates in the applied electric field.

The first term in equation III-12 is of $O(\tau_d^{-1})$, the second of $O(2\pi R_0 \rho \tau_t^{-1}/a^2)$ and the third of $O(\rho^2 \tau_E^{-1}/a^2)$. Equation III-12 may be simplified by observing that τ_E, $\tau_d >> \tau_t$, i.e. electrons moving near the speed of light will make a large number of transits around the torus before significant changes occur in particle density or energy. Thus, the second term in equation III-12 is much larger than the first or third terms. It may be noted that the second term came from the curvature drift and represents a flux of runaways in the $\hat{\imath}_\phi \times \vec{\nabla}\gamma$ (poloidal) direction whereas the third term came from the $\vec{E} \times \vec{B}$ drift and represents a flux of runaways in the $\vec{\nabla}\gamma$ (radial) direction. Keeping only the dominant term in equation III-12 requires that $\vec{\nabla}n^*\cdot(\hat{\imath}_\phi \times \vec{\nabla}\gamma)=0$; this implies n^* is a function only of γ, $n^*=n^*(\gamma)$. Substituting this result into equation III-12 and assuming that γ is large enough so that all terms of $O(\gamma^{-2})$ and higher may be discarded, the equation given below is obtained.

$$\frac{dn^*}{d\gamma}\frac{\partial\gamma}{\partial t}\left[h^{-2} - \frac{c^2}{\omega_{ce}^2}|\vec{\nabla}\gamma|^2\right] - n^*\frac{c^2}{\omega_{ce}^2} \times\left[\frac{\partial\gamma}{\partial t}\nabla^2\gamma + \vec{\nabla}\gamma\cdot\vec{\nabla}\left(\frac{\partial\gamma}{\partial t}\right)\right] = 0 \qquad \text{III-13}$$

Using equations III-5 and III-6 to relate $\nabla^2\gamma$ to n^* and keeping terms only to zero order in the inverse aspect ratio results in $\nabla^2\gamma \simeq \omega_{pe}^2 n^*/c^2$. The terms in equation III-13 may then be ordered as:

$$\frac{c^2}{\omega_{ce}^2}|\vec{\nabla}\gamma|^2 \sim O\left(\frac{\rho}{a}\right)^2$$

$$\left(\frac{\omega_{pe}}{\omega_{ce}}\right)^2 n^*\frac{\partial\gamma}{\partial t} \sim O\,(\rho k)^2\,\tau_E^{-1} \qquad k = \omega_{pe}/c$$

$$\frac{c^2}{\omega_{ce}^2}\vec{\nabla}\gamma\cdot\vec{\nabla}\left(\frac{\partial\gamma}{\partial t}\right) \sim O\left(\frac{\rho}{a}\right)^2\tau_E^{-1}$$

For parameters typical of the ORMAK runaway regime [7] $\rho/a \sim 3 \times 10^{-2}$ and $\rho k \sim 10^{-1}$.

Neglecting all terms in equation III-13 which are down by an order of magnitude or more results in the following non-linear Ricatti equation:

$$\frac{dn^*}{d\gamma} - \alpha n^{*2} = 0 \qquad \text{where } \alpha = (\omega_{pe}/\omega_{ce})^2 \qquad \text{III-14}$$

which has the solution: $n^* = (1 - \alpha\gamma)^{-1}$ III-15

The singularity in n^* which occurs at $\gamma = \alpha^{-1}$ represents an approximate limitation on γ for a fixed ω_{pe} and ω_{ce}. This may also be viewed as a limitation of the particle energy density obtainable in a runaway discharge; the inequality $\gamma \lesssim \alpha^{-1}$ may be written equivalently as $N\gamma m_0 c^2 \lesssim (B_\phi^0)^2/\mu_0$, i.e., the runaway electron energy density must be kept less than twice the toroidal magnetic field energy density. Such a limitation comes about from an inward collapse of the runaway beam on itself due to the $\vec{E} \times \vec{B}$ drifts. The accumulated effects of these drifts are dependent on $\int E_\phi dt$ (see equations III-19 and III-20 below), the total volt-seconds applied to the beam. The shrinkage also depends on the B_ϕ^0 field strength since electrons must move perpendicularly to the field in their radial $\vec{E} \times \vec{B}$ drifts. A larger toroidal field energy density would be expected to require a larger $\int E_\phi dt$ (runaway energy density) for beam collapse to occur. It is interesting to note that the above limitation is identical to the firehose stability criterion which will be derived in Chapter IV; since the firehose limit does not directly depend on the presence of an applied electric field, this is apparently only coincidental.

Using equation III-15 for the runaway density, it is possible to make an estimate of the radial shrinkage of the runaway beam.

Since $\alpha^{-1} \sim 10^2$ and $\gamma \sim 6$ to 8 for typical ORMAK runaway discharges, $\alpha\gamma$ is a small quantity and n^* may be adequately approximated by expanding to first order in powers of $\alpha\gamma$:

$$n^* \simeq 1 + \alpha\gamma \qquad \text{III-16}$$

The beam shrinkage as a function of time is then determined by requiring the total number of beam electrons to remain constant in time:

$$\int_0^{2\pi} d\phi \int_0^{2\pi} d\theta \int_0^{a} drRrn^*(\gamma) = 2\pi^2 a_0^2 R_0 \qquad \text{III-17}$$

where a_0 is the initial beam radius.

To perform this integral, it is necessary to determine γ as a function of r and t. This is found by substituting expression III-16 into the field equation III-6 and using III-5 to relate γ and ψ. The boundary condition on ψ is given (as in ref. 7) by the measured voltage minus the inductive component of the beam. It shall be assumed, since the large γ limit has been taken, that all runaways are moving near the speed of light and that the total beam current is constant in time. Performing these manipulations, the following transcendental equation for the beam radius, a, as a function of time is obtained:

$$k\sqrt{\alpha}\, a \, \frac{I_1(k\sqrt{\alpha}\, a)}{I_0(k\sqrt{\alpha}\, a)} \left[\frac{1}{\alpha} + \frac{e}{2\pi m_0 c R_0} \int_0^t \varepsilon \, d t' \right] = \frac{k^2 a_0^2}{2} \qquad \text{III-18}$$

Since equation III-18 cannot be directly solved for a, two limits will be examined: $k\sqrt{\alpha}\, a \gg 1$ and $k\sqrt{\alpha}\, a \ll 1$. The large $k\sqrt{\alpha}\, a$ limit gives the expression below.

$$a = \frac{k a_0^2}{2\sqrt{\alpha}} \left[\frac{1}{\alpha} + \frac{e}{2\pi m_0 c R_0} \int_0^t \varepsilon \, d t' \right]^{-1} \qquad \text{III-19}$$

while small $k\sqrt{\alpha}\,a$ limit gives the following.

$$a = \frac{a_0}{\sqrt{\alpha}} \left[\frac{1}{\alpha} + \frac{e}{2\pi m_0 c R_0} \int_0^t \varepsilon \, d\, t' \right]^{-1/2} \qquad \text{III-20}$$

It should be clear from both of these equations that the beam radius decreases with increasing volt-seconds in both limits.

A rough estimate of the above shrinkage effect for the ORMAK runaway regime, e.g. $n_b = 10^{11}$ cm^{-3}, a = 6 cm, $\int \varepsilon \, d\, t' = 0.3$ volt - second, $B_\phi = 1.2$ wb•m^{-2}, indicates that the beam radius should shrink no more than 10% and that $\gamma_{max} \sim 140$. Here γ_{max} denotes the value of γ where the beam collapse would be expected to occur. Thus, drift orbit effects are relatively minor and since $\alpha = 7\text{x}10^{-3}$, equation III-15 shows that the density is nearly constant over the beam cross-section. However, for higher energy density beams, more significant effects might be observed, e.g. if $n_b = 2\text{x}10^{12}$ cm^{-3}, a = 10 cm, $\int \varepsilon \, d\, t'$ 0.6 volt - seconds, B_ϕ = 5 wb•m^{-2}, then the beam radius should shrink by roughly 25%. In this case, $\gamma_{max} \sim 120$.

III.2 Curvature Drift Effects

Throughout the drift orbit analysis in the present section, the $\vec{E}\text{x}\vec{B}$ term will be neglected since, as shown in the preceding section for runaway-dominated discharges, it has a relatively minor effect; this is also expected to be the case for high energy runaways in normal discharges. This drift is then implicitly included again in Section III.3 where the change in minor radius of a relativistic electron undergoing acceleration is examined; however, the effect found there is an expansion of the orbit's minor radius which predominates over any gradual shrinkage due to $\vec{E}\times\vec{B}$ drifts.

The remaining terms in the drift equation are then the gradient and curvature drifts.

$$\vec{v}_d = \frac{\hat{e}_1}{B} \times \left[\frac{\mu}{\gamma e} \vec{\nabla} B - \frac{P_{\parallel}^2}{\gamma e m_0} \frac{\partial \hat{e}_1}{\partial S} \right]$$

$$= \frac{1}{R\Omega_T} \left(v_{\parallel}^2 + \frac{v_{\perp}^2}{2} \right) \qquad \text{III-21}$$

These two drifts are both approximately in the vertical direction (along the Z-axis in Fig. II-6). When added onto the basic motion along field lines, they affect the orbits in various ways depending on which one predominates. Toroidal orbits have been discussed in some detail in references [4], [64], and [65]. In the case where the curvature drift is predominant, the orbits are displaced off-center from the centroid of the current distribution either inward or outward, depending on whether the particles are moving antiparallel or parallel with the toroidal current. Runaways, of course, are always antiparallel to the current and in ORMAK type B discharges are displaced outward. When the gradient drift is of importance, mirroring of particles can occur as they move into the toroidal field gradient leading to the well-known banana orbits.

For runaways which are undergoing acceleration, the predominant drift is expected to be the curvature term (i.e. $v_{\parallel}^2/R\Omega_T$) since $v_{\parallel} >> v_{\perp}$. The gradient drift is only expected to possibly be of importance when the voltage is off and runaways begin slowing down; as long as they are under acceleration, energy is primarily going into $v_{\parallel}$. Since the area of major interest relative to the ORMAK type B discharges is the gradual loss of runaways during the steady-state portion of the discharge, the gradient drift will be neglected in the following section. It will be included, however, in Section III.4 where trapping boundaries will be examined for runaways which are just intersecting the limiter. It might be also noted that synchrotron radiation should strongly limit the amount of pitch angle scattering which could accumulate for high energy electrons.

III.2.A. Runaway Orbits for Flat Current Profiles

Orbits are first examined here for the case where the toroidal current distribution is flat. The reason for considering this case is because an exact analytic treatment is possible.

One method of determining particle trajectories is by using the canonical invariants of the motion. For the tokamak, a convenient invariant is the canonical angular momentum, P_ϕ. The invariance of P_ϕ depends on the axisymmetry of the device (i.e. the fact that $d/d\phi$ of all quantities equals zero) and is given below.

$$P_\phi = \gamma m_0 R v_\phi - \frac{e}{c}\psi \qquad \text{III-22}$$

For a flat current profile B_θ and ψ may be written as follows [66].

$$B_\theta = \beta(r)\frac{R_0}{R} \simeq \frac{2Ir}{cr_L^2}\frac{R_0}{R} \qquad (r \leq r_L)$$

$$\psi = \int_0^r B_\theta R\,dr = \frac{R_0 I r^2}{cr_L^2} \qquad (r \leq r_L) \qquad \text{III-23}$$

where r_L = radius of current carrying region

R_0 = major radius of torus

I = total toroidal current

Using the poloidal flux as given above in equation III-22 results in the following:

$$P_\phi = \gamma m_0 R v_\phi - \frac{eR_0 I r^2}{c^2 r_L^2} \qquad \text{III-24}$$

Since $r^2 = (R-R_0)^2 + Z^2$ (see Fig. II-6 for coordinate system) and P_ϕ is known to be a constant over the orbit, equation III-24 is simply the equation for a shifted circle, as may be seen by completing the square.

$$P_\phi + \text{constant terms} = -\frac{R_0 eI}{c^2 r_L^2}\left\{(R-R_0-\Delta)^2 + Z^2\right\} \qquad \text{III-25}$$

where Δ = outward orbit shift = $\frac{\rho_{pol}(r_L)}{A}$

$\rho_{pol}(r_L)$ = poloidal gyroradius evaluated at $r = r_L$

= v_ϕ/Ω_p

A = aspect ratio = $\frac{R_0}{r_L}$

$\Omega_p = \frac{eB_\theta(r_L)}{\gamma m_0 c}$

The orbits then are circles which are shifted outward from the center of the current distribution by an amount $\rho_{pol}(r_L)/A$. By examining the drift velocity (equation II-21) and the motion along field lines, one may also show that the center of these orbits is the stagnation point. This is defined as the point at which the vertical drift cancels the vertical component of the motion along field lines, i.e.

$$\frac{v_\parallel^2}{R\Omega_T} = v_\parallel \frac{B_\theta}{B_T} \qquad \text{III-26}$$

or $$X_s = \frac{r_L v_\parallel}{R_0 \Omega_p (r_L)} \qquad \text{III-27}$$

For the current profile to be examined in Subsection III.2.B, the orbits are not exactly circles (although they are close) and the orbit center does not exactly coincide with the stagnation point.

III.2.B. Runaway Orbits for ORMAK Type B Current Profiles

The current profile for ORMAK type B discharges has been inferred from laser Thomson scattering measurements of the electron temperature [67] and assuming that current is proportional to $T_e^{3/2}$. This class of discharges is characterized by having much broader current profiles than those of the type A discharges. Various analytic fits have been made to the type B profiles, but the one used here will be the following:

$$j(r) = j_0 \left[1 - \left(\frac{r}{r_L}\right)^3\right] \qquad \text{III-28}$$

r_L = radius of current region (or limiter radius)

A plot of the above current profile along with $B_\theta(r)$ and $q(r)$ is shown in Fig. III-1. As may be seen, $B_\theta(r)$ is larger over the entire radius in this case than for a flat current profile. This will allow higher energy orbits to be contained for the type B profile than would be the case in a flat current profile.

First, an approximate analytic calculation will be made of the orbit shift using the same methods as in Subsection III.2.B (i.e. conservation of P_ϕ). Next, orbits will be presented which are obtained by a numerical integration along the trajectories for those orbits which are just intersecting the outside of the limiter. It is of particular interest, with regard to interpreting the experimental results,

ORNL DWG. 75-12802

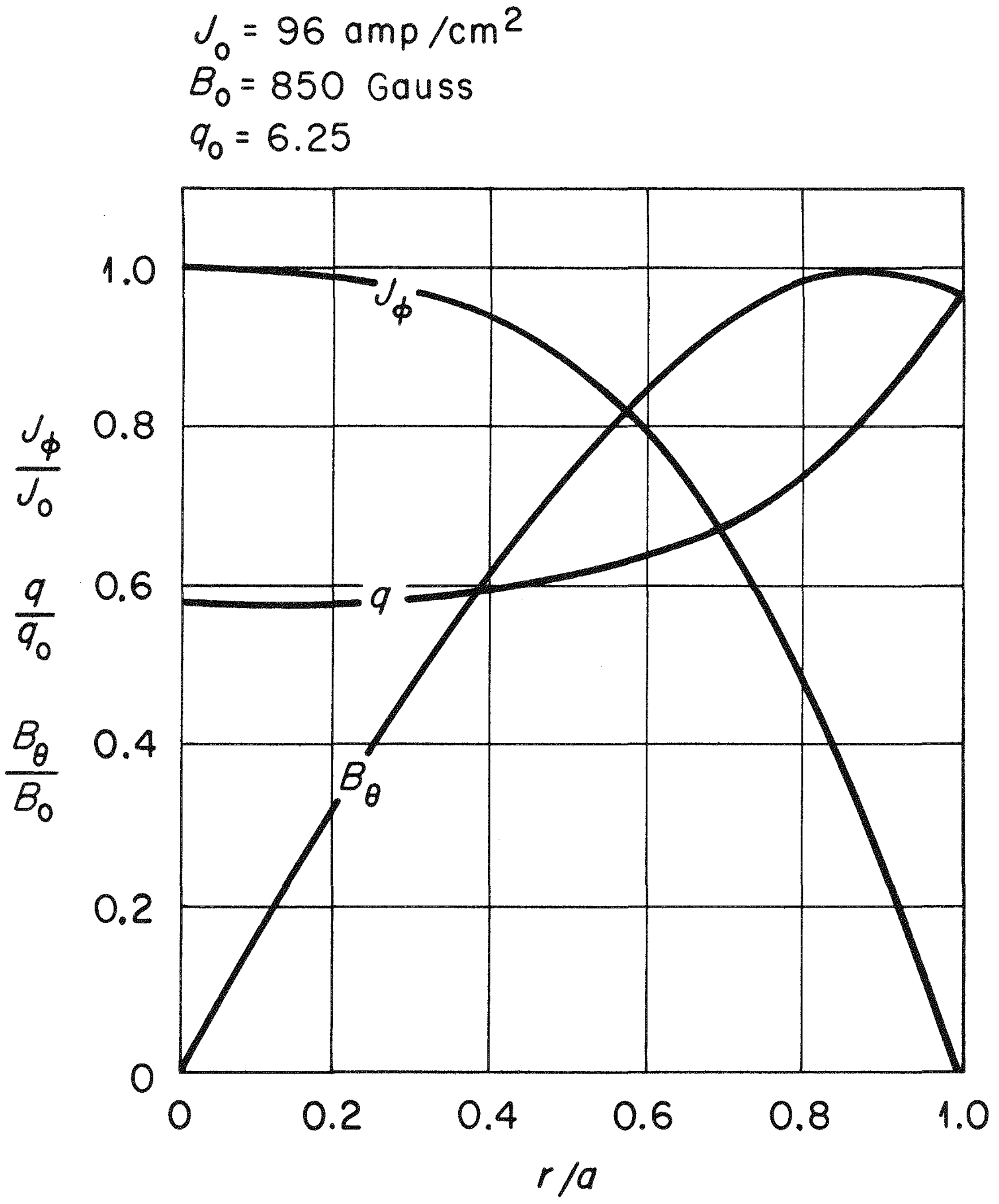

FIGURE III-1

B_θ, J_ϕ, and q as a Function of Radius for an ORMAK Type B Current Profile.

to determine under what conditions of energy, current and orbit radius this intersection occurs. These numerical results will then be compared with the analytic estimate.

For the current distribution of equation III-26, B_θ and the poloidal flux function are given as follows:

$$B_\theta(r) = \frac{20IrR_0}{3r_L^2 cR}\left[\frac{1}{2} - \frac{1}{5}\left(\frac{r}{r_L}\right)^3\right] \qquad \text{III-29}$$

$$\psi(r) = \frac{20Ir^2R_0}{3r_L^2 c}\left[\frac{1}{4} - \frac{1}{25}\left(\frac{r}{r_L}\right)^3\right]$$

Here I is the total toroidal current.

$$I = 2\pi \int_0^{r_L} rdrj(r) = \frac{3\pi}{5} j_0 r_L^2 \qquad \text{III-30}$$

Substituting the above results into equation III-22 for P_ϕ gives the following:

$$P_\phi = \gamma m_0 R v_\phi - \frac{20R_0 I e}{3r_L^2 c^2}\left[(R-R_0)^2 + Z^2\right]\left[\frac{1}{4} - \frac{1}{25}\left(\frac{r}{r_L}\right)^3\right] \qquad \text{III-31}$$

At this point, it is necessary to make an approximation in order to analytically obtain the orbit shift. The approach taken will be to neglect the (1/25) $(r/r_L)^3$ term in comparison with 1/4. The neglected term is an order of magnitude less than the one retained for $r/r_L < 0.85$. This approximation should not be unreasonable except for orbits with large minor radii $\simeq r_L$ or which are shifted far out near the limiter so that they spend most of their trajectory near $r \simeq r_L$. The resulting equation for P_ϕ may then be written as follows:

$$P_\phi = \frac{5R_0 I}{3r_L^2 c}\left[\left(R-R_0 - \frac{3r_L^2 c^2}{10R_0 I\, e}\gamma m_0 v_\phi\right)^2 + Z^2 + \text{constant terms}\right] \qquad \text{III-32}$$

III-32 is the equation of a shifted circle with the shift, Δ, given as:

$$\Delta = \frac{3r_L^2 c^2}{10R_0 I\, e}\gamma m_0 v_\phi = \frac{3}{5}\frac{r_L}{R_0}\rho_{pol}\;(r_L) \qquad \text{III-33}$$

In order to more adequately examine drift orbits for the above current profile, a numerical drift orbit code developed by J. A. Rome and J. C. Twichell at Oak Ridge has been employed; this code integrates the drift equation (III-21) from a specified set of initial conditions using a Cauchy-Euler scheme. It assumes circular, centered flux surfaces. The step size for the integration method is automatically adjusted in order to maintain a certain prespecified accuracy; for the orbits calculated here the relative accuracy is set at 10^{-4}. In Figs. III-2 and III-3 a series of cases are presented for a range of energies and toroidal currents. The orbits are projected back onto a minor cross section and the first orbit on the left is at 1/2 MeV while the remaining ones go up in 1/2 MeV steps to 15 MeV. All of these orbits are started out near the outside of the torus ($r/r_L = .99$) on the equatorial plane and thus represent the marginal condition for orbits to be just contained. It is assumed that the magnetic moment is zero (pitch angle = 0°) for all of these cases.

The marginal condition for orbits to be just confined may be written as follows:

$$\Delta + r_{ci} = r_L \qquad \text{III-34}$$

where Δ = shift of the orbit center away from center of torus

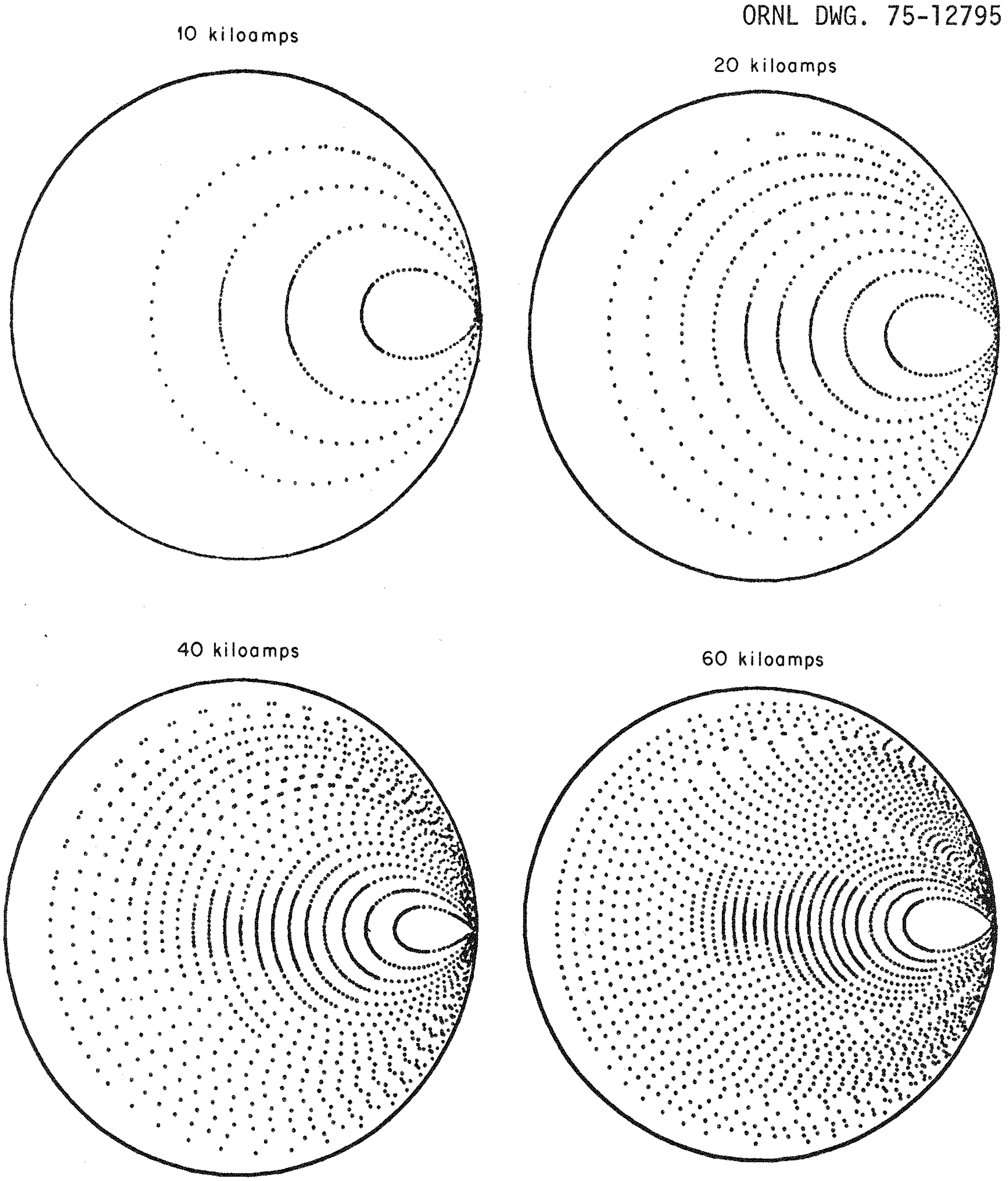

FIGURE III-2

Orbit Trajectories Projected onto a Minor Cross-Section for Relativistic Electrons of Energies Starting at 1/2 MeV and going up in 1/2 MeV Increments for 10, 20, 40, 60 kiloamps Toroidal Current.

ORNL DWG. 75-12796

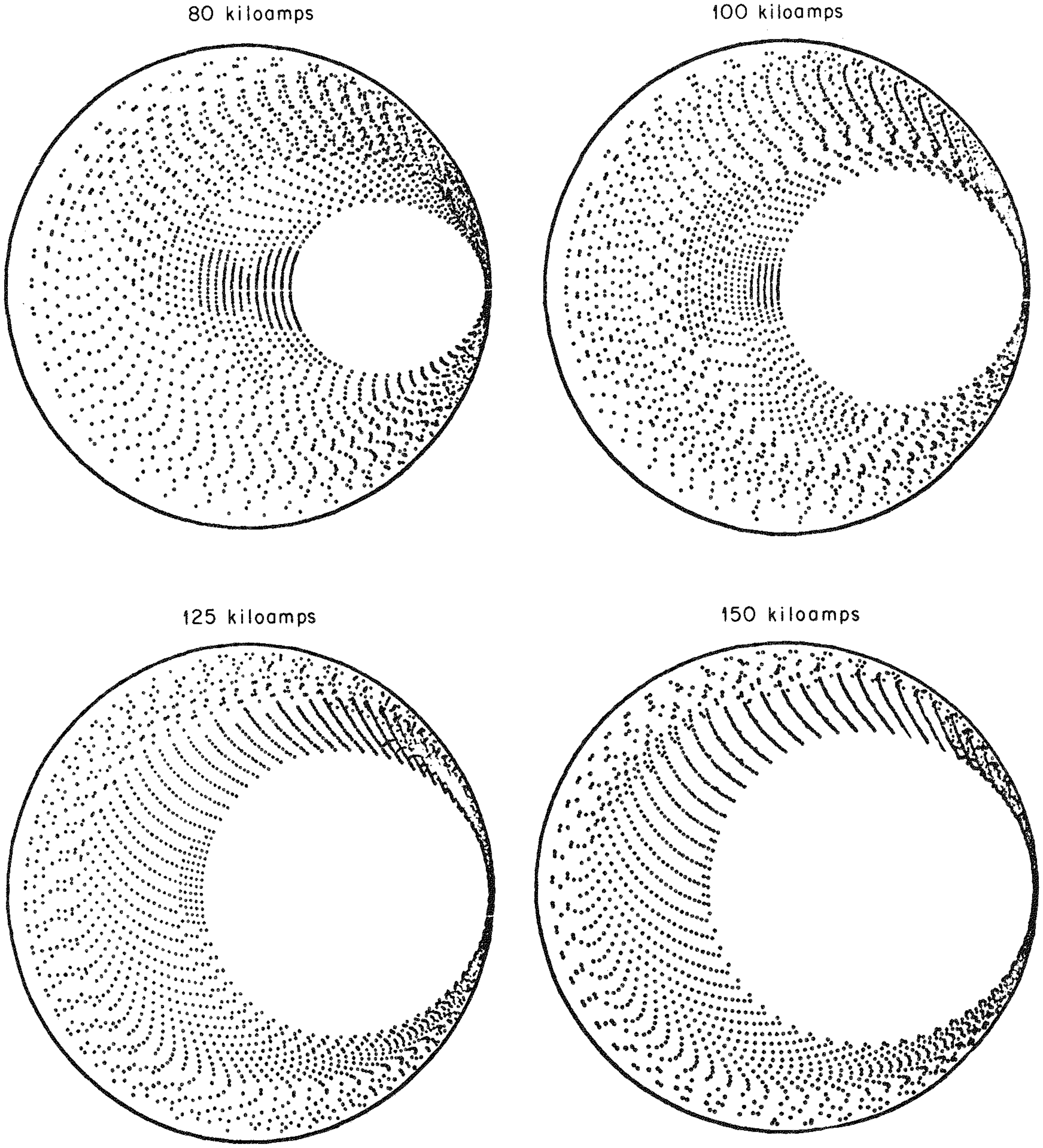

FIGURE III-3

Orbit Trajectories Projected onto a Minor Cross-Section for Relativistic Electrons of Energies Starting at 1/2 MeV and going up in 1/2 MeV Increments for 80, 100, 125, 150 kiloamps Toroidal Current.

r_{ci} = critical orbit radius where orbit just intersects the limiter

r_L = limiter radius

Using equation III-31 for Δ results in the equation given below:

$$\frac{3}{5}\,\frac{r_L}{R_0}\,\rho_{pol}(r_L) + r_{ci} = r_L \qquad \text{III-35}$$

This can also be written in the following manner:

$$\frac{3r_L^2}{10R_0}\,\frac{I_A}{I} + r_{ci} = r_L \qquad \text{III-36}$$

where $I_A = \beta\gamma\,\frac{m_0c^3}{e} = 17.1\ \beta\gamma$ (k Amps)

is the Alf'ven current

III-36 then defines a relation between the energy of the electron (or γ), the toroidal current and the radius of the orbit which is just beginning to lose confinement. A similar relation may be found for the flat current profile. The two cases are given below.

$$\frac{\sqrt{\gamma^2-1}}{I} = \frac{A}{5.13}\left(1-\frac{r_{ci}}{r_L}\right) \qquad \text{III-37}$$

(Type B current distribution)

$$\frac{\sqrt{\gamma^2-1}}{I} = \frac{A}{17.1}\left(1-\frac{r_{ci}}{r_L}\right) \qquad \text{III-38}$$

(Flat current distribution)

where A = aspect ratio = $\frac{R_0}{r_L}$

In Fig. III-4 both of these are displayed along with a plot of

$\sqrt{\gamma^2-1}/I$ vs. r_{ci}/r_L which is obtained from the numerical calculations. The latter curve has been deduced from the orbits plotted in Figs. III-2 and III-3 as well as runs which are not shown in Figs. III-2 and III-3 at 2kA, 4kA, 30kA, 50kA, ..., 90 kA (the curve labeled orbit expansion will be discussed in the next section). The lines in Fig. III-4 define the transition region between confined and unconfined orbits; orbits corresponding to parameters above these lines are unconfined whereas orbits corresponding to points below the lines are confined.

As may be seen, the line obtained from the numerical orbit integrations deviates from the analytic approximations for the type B profile at low values of r_{ci}/r_L ($< .3$) and also in the range $.5 < r_{ci}/r_L < 1$; the two calculations are always within .5 I_A/I of each other. The deviation at the high values of r_{ci}/r_L might be expected since the analytic calculation assumes $(r/r_L)^3 << 1$. The deviation at the lower end of the curve has to do with the fact that the shape of these orbits deviates substantially from circular as may be seen from Figs. III-2 and III-3. The elongation along the major radius which is present for the inner orbits in Fig. III-2 is caused when an orbit comes close to the maximum in B_θ (see Fig. III-1) such that one side of the orbit is just to the inside of $B_{\theta max}$ and the other side is just to the outside of $B_{\theta max}$. This results in a relatively larger rotational transform over the top and bottom of the orbit than on the sides. Thus, the vertical drift term is more important on the sides and relatively less important on top and bottom. This, then leads to the observed elongation.

ORNL DWG. 75-13763

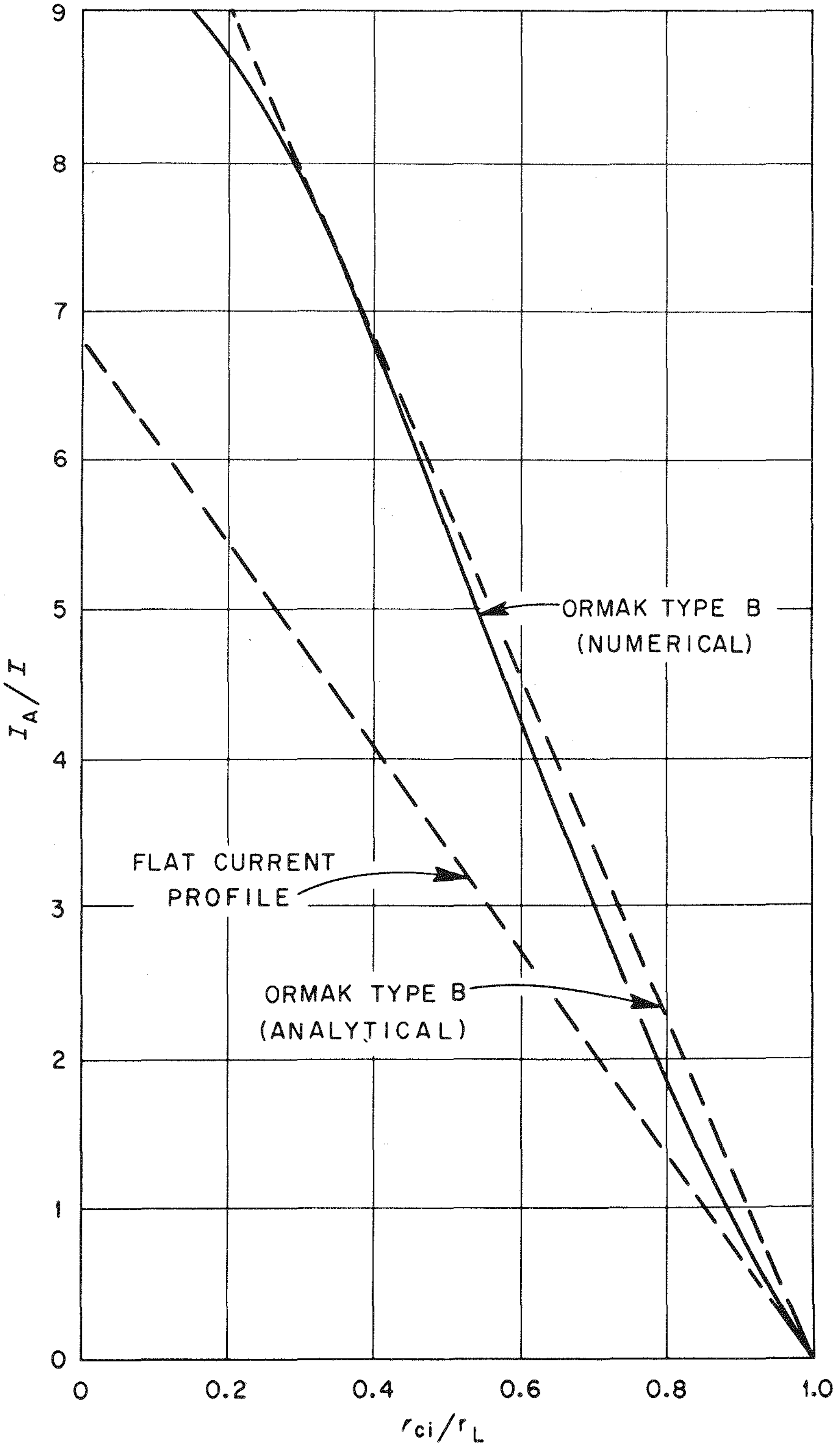

FIGURE III-4

I_A/I vs. r_{ci}/r_L for a Flat Current Profile, and ORMAK Type B Profile (using both the Analytic and Numerical Results).

As may be seen from Fig. III-1, $B_{\theta max}$ occurs at $r/r_L \simeq 0.86$ for ORMAK type B profiles.

Fig. III-4 demonstrates, as was mentioned earlier, that the flat current profile results in substantially poorer confinement properties for high energy runaways than the type B profile. This may be explained from Fig. III-1 where it is clear that the poloidal field B_θ, and thus the rotational transform, is larger over the discharge area for the type B profile than for the flat profile.

III.3 Expansion of the Orbit Minor Radius with Applied Electric Field

The orbits which were investigated in Section III.2 represent the final position of runaways just before they impact the limiter and produce bremsstrahlung which can be experimentally measured. It is also of interest to know how the orbits evolved to this position as they were accelerating. It would be expected that the center of the orbit will gradually displace further out from the center of the current distribution as the electron accelerates to relativistic energies; however, the question of whether the minor radius of the orbit, r_{ci}, as it is just intersecting the limiter is the same as at earlier times needs further examination. This is treated in the present section.

The calculations to follow will demonstrate that as a runaway accelerates, the minor radius increases with time. On the surface, this may appear to be inconsistent with the results of Section III.1; there a slight shrinkage was found in the beam radius for the strong runaway regime. The reasons for the contrasting results of these two sections arise from the differing physical models used. In the present section, single particle runaway orbits are analyzed assuming that the runaways carry a very negligible fraction of the total toroidal current (as is appropriate to the weak runaway regime); this allows one to decouple the single particle orbit problem from the self-consistent poloidal magnetic field problem. In Section III.1 this simplification was not possible since runaways were assumed to carry all of the toroidal current. Thus, evolution of the orbits of Section III.1 was self-consistently coupled with the poloidal magnetic field description. As a result, large changes in the minor radius of the orbits did not occur, as they were accelerated, since this would also have caused substantial changes in the toroidal current distribution. However, for the weak runaway regime, sizeable changes in the minor radius of the accelerating orbits are possible since the runaway component accounts for only a negligible fraction of the toroidal current ($\lesssim .1\%$).

III.3.A. Flat Current Profile

The flat current distribution will be treated first using the geometry illustrated in Fig. II-6. The toroidal current, I, and electric field, E_ϕ, are in the $-\phi$ direction; the runaway velocity, v_ϕ, is in the $+\phi$ direction. Centered circular flux surfaces are assumed so that the flux function is given as in equation III-23.

$$\psi(R,Z) = \frac{R_0 I}{c r_L^2} \left[(R-R_o)^2 + Z^2\right] \qquad \text{III-39}$$

This problem will be treated using the Lagrangian equations of motion. The Lagrangian for a relativistic electron in space-time form is given by the following:

$$L = -m_0c^2 \sqrt{1- v^2/c^2} - \frac{e}{c} \vec{v}\cdot\vec{A} + e\phi \qquad \text{III-40}$$

In the subsequent calculations, electric fields due to a potential (e.g., radial electric fields), will be neglected so that $\phi = 0$. The equations of motion are then as indicated below.

$$\frac{d}{dt}\left(\frac{\partial L}{\partial \dot{q}_i}\right) - \frac{\partial L}{\partial q_i} = Q_i = \text{force in ith coordinate direction} \qquad \text{III-41}$$

Since the only force present is that due to the electric field E_ϕ, only the ϕ component of III-41 will be considered. Axisymmetry is assumed so that $\partial L/\partial \phi = 0$, resulting in the following.

$$\frac{d}{dt}\left(\frac{\partial L}{\partial \dot{\phi}}\right) = \frac{d}{dt} \left[R\gamma m_0 v_\phi - \frac{e}{c} A_\phi\right] = (-e)\ (-E_\phi)\frac{\partial r_\phi}{\partial \phi} = eRE_\phi = e\varepsilon_\phi/2\pi \qquad \text{III-42}$$

where ε_ϕ = toroidal voltage

Integrating III-42 with respect to time and substituting the flux function as given in III-39 one obtains the equation given below.

$$\frac{e}{2\pi} \int \varepsilon_\phi(t')dt' + P_\phi^0 = \gamma m_0 R v_\phi - \frac{eR_0 I}{c^2 r_L^2} \left[(R-R_o)^2 + Z^2\right] \qquad \text{III-43}$$

Here P_ϕ^0 is a constant of integration. Its significance is determined by setting $t = 0$, $v_\phi = 0$, and $r = r_0$, the initial radius before acceleration. One then obtains the following.

$$P_\phi^0 = - \frac{eR_0 I}{c^2 r_L^2}\, r_0^2 \qquad \text{III-44}$$

Equation III- 43 may then be written in the form given below.

$$-\frac{c^2 r_L^2}{2\Pi R_0 I} \int \epsilon_\phi(t')dt' + r_0^2 = -2\frac{r_L}{R_0}\rho_{pol}(r_L)R + (R-R_0)^2 + Z^2 \qquad \text{III-45}$$

Completing the square on the right-hand side of equation III-45 results in an equation for shifted circular orbits with a minor radius which depends on time.

$$(R - R_0 - \frac{r_L}{R_0}\rho_{pol})^2 + Z^2 = r^2(t)$$

$$\text{where } r^2(t) = r_0^2 - \frac{c^2 r_L^2}{2\pi R_0 I}\int\epsilon_\phi(t')dt' + 2r_L\rho_{pol} + \frac{r_L^2}{R_0^2}\rho_{pol}^2 \qquad \text{III-46}$$

In order to complete this description of orbits, it is necessary to determine the time dependence of ρ_{pol} in a constant applied electric field. This may be obtained by again using the Lagrangian given in III- 40. The total time derivative of L is given by the following:

$$\frac{dL}{dt} = \sum_i \frac{\partial L}{\partial q_i}\frac{dq_i}{dt} + \sum_i \frac{\partial L}{\partial \dot{q}_i}\frac{d\dot{q}_i}{dt} \qquad \text{III-47}$$

It has been assumed here, for the sake of simplicity, that L is not explicitly time-dependent - as it would be, for example, in the current build-up and decay phases of the discharge. These effects could be incorporated by adding a $\partial L/\partial t$ term to III-47 Using equation III-41 in the above, one obtains the result given below.

$$\frac{dL}{dt} = \sum_i \frac{d}{dt}\left(\dot{q}_i\frac{\partial L}{\partial \dot{q}_i}\right) - \dot{\phi}\, Q_\phi \qquad \text{III-48}$$

Here $\dot{\phi}$ is the angular frequency about the torus axis. Integrating III-48 then gives the following.

$$L + \text{constant} = \sum_i \dot{q}_i\frac{\partial L}{\partial \dot{q}_i} - \frac{e}{2\pi}\int dt'\,\dot{\phi}(t')\epsilon_\phi(t') \qquad \text{III-49}$$

By setting $t = 0$ and $\gamma = 1$ the left-hand side of this equation may be identified as m_0c^2, the rest mass energy. For a constant electric field III-49 results in the equation given below.

$$\gamma m_0 c^2 = m_0 c^2 + \frac{e}{2\pi} \phi \, \varepsilon_\phi \qquad \text{III-50}$$

where ϕ = total angular distance traveled (radians) during acceleration

$$= \int_0^t \frac{v_\phi}{R} \, dt'$$

In calculating ρ_{pol}, the approximation is made that $v_\phi \simeq \beta c$.

$$\rho_{pol} = \frac{m_0 c^3 r_L}{2eI} \left\{ \left[1 + \frac{e\phi\varepsilon_\phi}{2\pi m_0 c^2} \right]^2 - 1 \right\}^{1/2} \qquad \text{III-51}$$

A reasonable approximation for runaways in ORMAK is that the total angular distance ϕ traveled around the torus by the end of the discharge should be adequately given by $\phi = c\tau/R_0$ where τ is the time over which acceleration occurs. This may be justified by the fact that the runaways reach relativistic velocities early in the discharge. ρ_{pol} under this approximation becomes the following.

$$\rho_{pol} = \frac{m_0 c^3 r_L}{2eI} \left\{ \left[1 + \frac{e\tau\varepsilon_\phi}{2\pi m_0 R_0 c} \right]^2 - 1 \right\}^{1/2} \qquad \text{III-52}$$

Substituting this into equation III-46 results in the orbit locus given below.

$$\left(R - R_o - \frac{r_L}{R_0} \rho_{pol}\right)^2 + Z^2 = r_0^2 - r_L^2 \frac{m_0 c^3}{eI} \left[(\gamma^2 - 1)^{1/2} - (\gamma - 1) \right]$$

$$+ \frac{r_L^2}{4} \left(\frac{r_L}{R_0} \right)^2 \left(\frac{m_0 c^3}{eI} \right)^2 (\gamma^2 - 1) = r^2(t) \qquad \text{III-53}$$

Plots of r/r_0 and Δ for several different initial orbit radii, energies, and toroidal currents are given in Figs. III-5 and III-6.

III.3.B. ORMAK Type B Profile

The preceding calculations may be readily modified for the case of an ORMAK type B current profile by making similar approximations as those used in Section III.2.B. At present, the numerical orbit integration code used in III.2.B. is not capable of treating the orbit expansion effect which occurs in an accelerating runaway; thus, only an analytic calculation is presented.

The flux function in this case was given by equation III-27 as the following:

$$\psi\ (r) = \frac{20IR_0r^2}{3r_L^2c}\ [\frac{1}{4} - \frac{1}{25}\ (\frac{r}{r_L})^3] \qquad \text{III-54}$$

Again, as in Subsection III.2.B., the second term in brackets will be neglected since it is an order of magnitude less than the first for $r/r_L < .85$. The remaining derivation then proceeds in an analogous fashion as that of Subsection III.3.A. and the equation given below is obtained for the orbit locus as a function of energy and current.

$$(R-R_0 - \frac{3}{5}\frac{r_L}{R_0}\rho_{pol})^2 + Z^2 = r^2 \qquad \text{III-55}$$

$$\text{where } r^2 = r_0^2 - r_L^2\ \frac{c^3m_0}{eI}\left\{\frac{3}{5}\ [\gamma - 1 - \sqrt{\gamma^2 - 1}] - .09\ \frac{m_0c^3}{eI}\ \left(\frac{r_L}{R_0}\right)^2 (\gamma^2 - 1)\right\}$$

Comparing III-55 and III-53 it may be seen that the minor radius of an orbit being accelerated in a type B current profile expands more

ORNL DWG. 75-13765

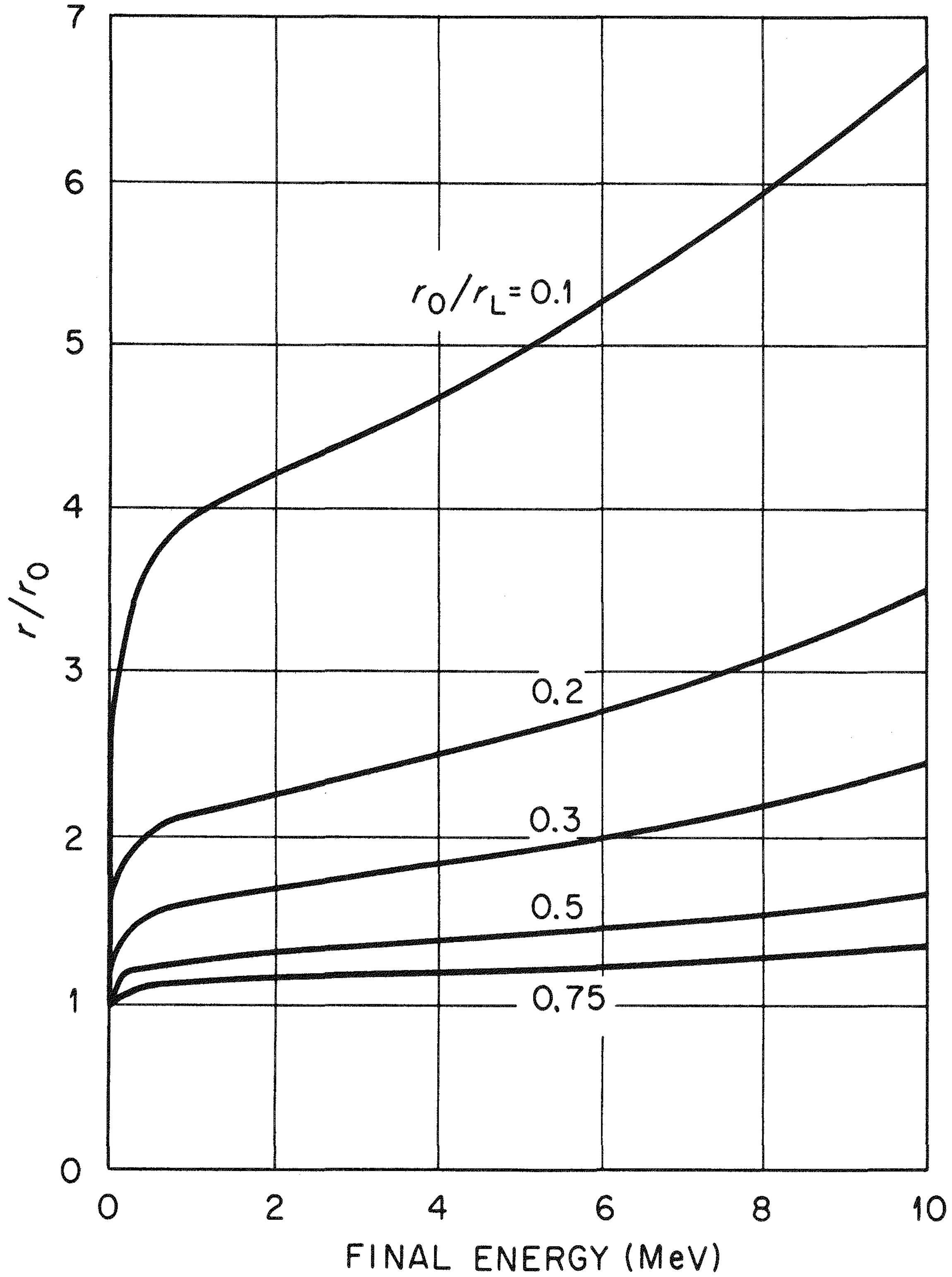

FIGURE III-5

r/r_0 vs. Final Energy for Relativistic Electrons Accelerated in Flat Current Profiles.

ORNL DWG. 75-13766

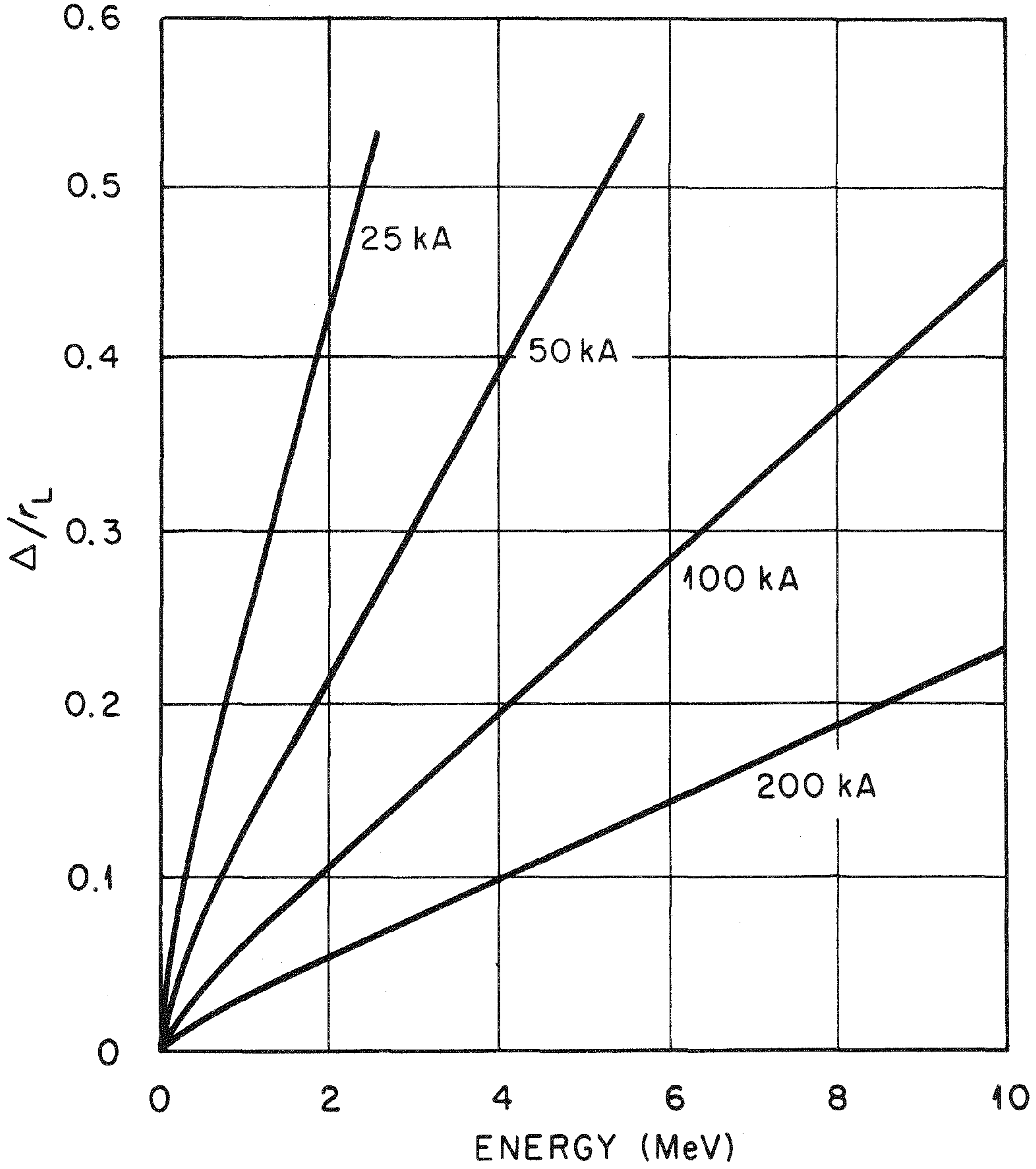

FIGURE III-6

Δ/r_L vs. Energy for Relativistic Electrons in Flat Current Profiles.

slowly and shifts outward a smaller amount than for the flat current profile. For the case where $\gamma >> 1$, the dependence of the radius is given as follows in terms of r_0, the initial orbit radius before acceleration.

$$\frac{r}{r_0} = \left[1 + \frac{\rho_{pol}^2}{R_0^2} \frac{r_L^2}{r_0^2}\right]^{1/2} \qquad \text{III-56}$$

(flat current profile)

$$\frac{r}{r_0} = \left[1 + \frac{9}{25} \frac{\rho_{pol}^2}{R_0^2} \frac{r_L^2}{r_0^2}\right]^{1/2} \qquad \text{III-57}$$

(ORMAK type B profile)

In Fig. III-7 a plot of I_A/I vs. r_0/r_L is indicated for several energies using equation III-55. Here the radius plotted on the horizontal scale is the initial radius r_0 of the orbit before acceleration was applied. This line then represents the orbits with initial radius r_0 which will just intersect the limiter by the time they reach an energy $(\gamma - 1)m_0c^2$ in a toroidal current I. The minor radius which they have as they intersect the limiter then may be obtained from the ORMAK type B curves plotted in Fig. 4.

III.4 Effects of Finite Pitch Angle (Gradient Drifts) on Runaway Orbits

The preceding analysis of Sections III.2 and III.3 has treated the case where the pitch angle is equal to zero. In the present section, this constraint will be relaxed and trapping boundaries are investigated for runaways which are just intersecting the limiter. The rationale for considering this problem is to determine the amount of pitch angle

ORNL DWG. 75-13764

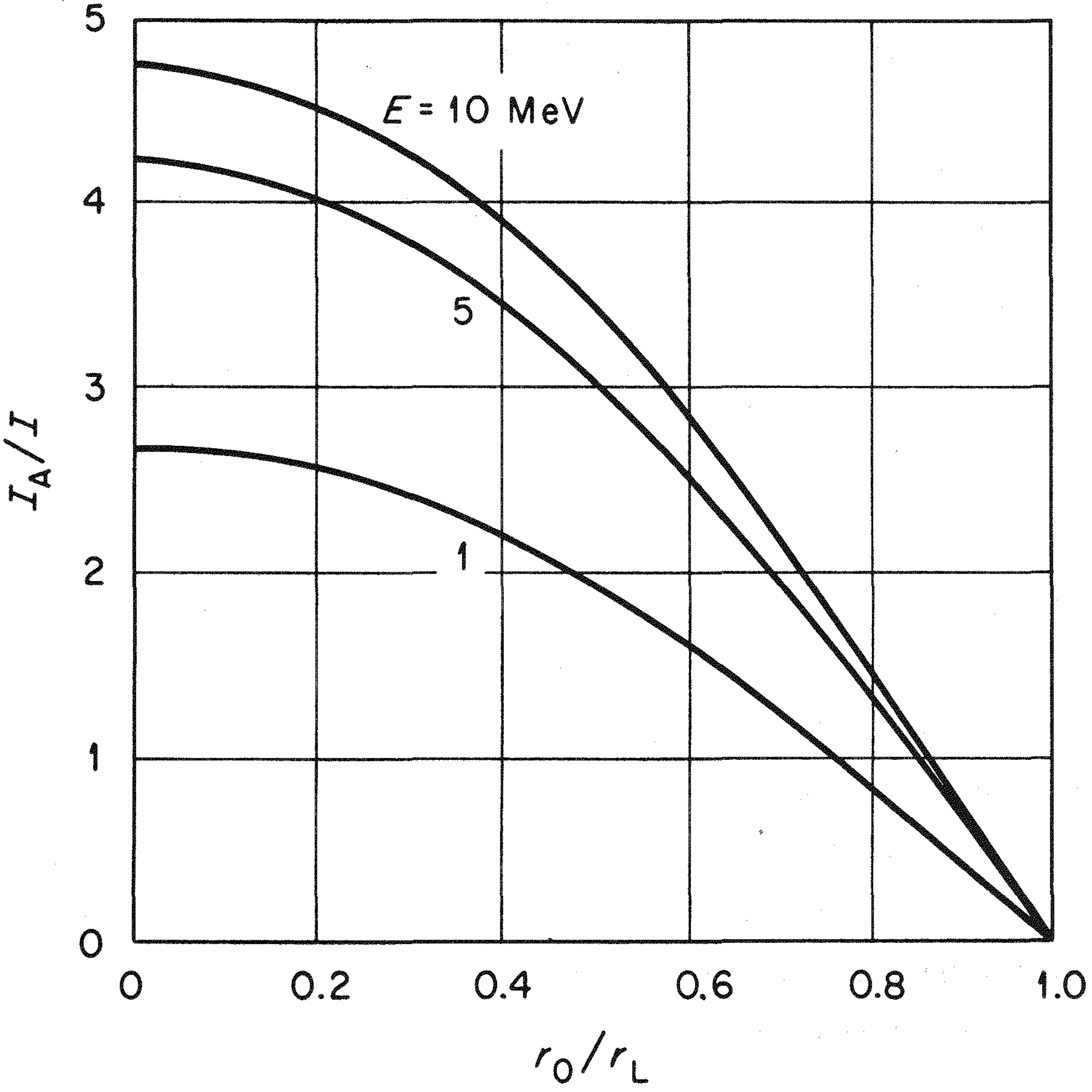

FIGURE III-7

I_A/I vs. r_0/r_L with the Inclusion of the Orbit Expansion Effect for Energies of 1,5 and 10 MeV.

scattering which must take place before significant changes occur in the orbits away from the untrapped cases considered in Section III-2. This is of importance in interpreting the dumps of hard X-rays seen in ORMAK type B discharges since one would like to infer from these measurements the radial location from which the runaways came. As was pointed out earlier, it is expected that $v_{\parallel} >> v_{\perp}$ for runaways; however, they will always have a certain finite pitch angle. Measurements of enhanced microwave emission from runaways may eventually reveal information on the amount of transverse energy in this component.

In a tokamak, mirroring of particles can occur as a result of moving into the region of higher toroidal field on the inside of the torus. If one gradually increases the pitch angle on a given orbit, then the point where $v_{\parallel} = 0$ will first appear on the equatorial plane. This first, barely-trapped orbit will be D-shaped; as the pitch angle is further increased, two $v_{\parallel} = 0$ points will be present and the orbit becomes banana-shaped. The transition point from an untrapped to a trapped orbit then occurs with the presence of the D-shaped orbit where $v_{\parallel} = 0$ on the equatorial plane. The onset of this particular orbit will be investigated in the present section for high energy runaways.

For a relativistic particle, $v_{\parallel}$ may be written in the following form.

$$v_{\parallel} = \pm \sqrt{1 - \frac{m_0^2 c^4}{(\varepsilon + m_0 c^2)^2} - \frac{2\mu B}{\gamma^2 m_0 c^2}} \qquad \text{III-58}$$

where ε = energy = $(\gamma - 1)\, m_0 c^2$

μ = magnetic moment

$$= \frac{p_\perp^{\;2}}{2m_0B} = \frac{\gamma^2 m_0 v_\perp^{\;2}}{2B}$$

Thus, the trapping boundary for the relativistic orbits is defined by:

$$1 - \frac{m_0^{\;2}c^4}{(\varepsilon+m_0c^2)^2} - \frac{2\mu B}{\gamma^2 m_0 c^2} = 0 \qquad \text{III-59}$$

At this point, it is convenient to define a pitch angle, χ, with reference to the particle's velocity at the outermost edge of the torus (at $R = R_0 + r_L$ where it is just beginning to intersect the limiter) by $\chi = \tan^{-1}(v_\perp/v_\parallel)$. The magnetic moment, μ, may then be written as:

$$\mu = \frac{\gamma^2 m_0 (R_0 + r_L)\, v^2 \sin^2\chi}{2B_0R_0} \qquad \text{III-60}$$

Here it has been assumed that the magnetic field is equal to the toroidal field, $B = B_0R_0/R$. The trapping condition may now be written in the following form.

$$1 - \frac{1}{\gamma^2} - \frac{R_0 + r_L}{R_0 - r_c}\,\beta^2 \sin^2\chi = 0$$

$$\text{or } \sin\chi = \sqrt{\frac{R_0 - r_c}{R_0 + r_L}} \qquad \text{III-61}$$

where r_c = the minor radius to the position on the equatorial plane where $v_\parallel = 0$

The position r_c must now be determined from the conservation of P_ϕ. It will be assumed that $v_\parallel \simeq v_\phi$; P_ϕ is then given as below.

$$P_\phi = \gamma m_0 R\, c\, \beta \cos\chi - \frac{e}{c}\psi(r) \qquad \text{III-62}$$

For the orbit which is just intersecting the limiter, the position, r_c, where trapping just begins, is found by setting P_ϕ at $r = r_L$ equal to P_ϕ at $r = r_c$ (where $v_\parallel = 0$).

$$\gamma m_0 (R_0 + r_L)\ c\ \beta \cos\chi - \frac{e}{c}\psi(r_L) = -\frac{e}{c}\psi(r_c) \qquad \text{III-63}$$

Obtaining r_c for general current profiles is difficult due to the complicated dependence of ψ on r. However, for a flat current profile, or for the approximate ORMAK type B profile used in Section III-2, r_c may be readily obtained and is given below.

$$r_c^2 = r_L^2 \left[1 - \frac{I_A}{I}\ \frac{R_0 + r_L}{R_0}\ \cos\chi\right]$$

(flat profile) III-64

$$r_c^2 = r_L^2 \left[1 - \frac{3}{5}\ \frac{I_A}{I}\ \frac{R_0 + r_L}{R_0}\ \cos\chi\right]$$

(ORMAK type B profile)

where I_A = Alfvén current = 17.1 $\beta\gamma$ KAMPS

Now that solutions are obtained for r_c in terms of the pitch angle, the trapping boundary is found by combining equations III-64 and III-61.

$$(A + 1)\ (\cos\chi)^3 - 2\cos\chi + \frac{I_A}{AI} = 0$$

(flat profile) III-65

$$(A + 1)\ (\cos\chi)^3 - 2\cos\chi + \frac{3}{5}\ \frac{I_A}{AI} = 0$$

(ORMAK type B profile)

here A = aspect ratio = R_0/r_L

These two equations determine the pitch angle χ where trapping begins for the runaway just intersecting the limiter. They have been solved for a range of the parameter I_A/AI and the results are plotted in Fig. III-8.

ORNL DWG. 75-13724

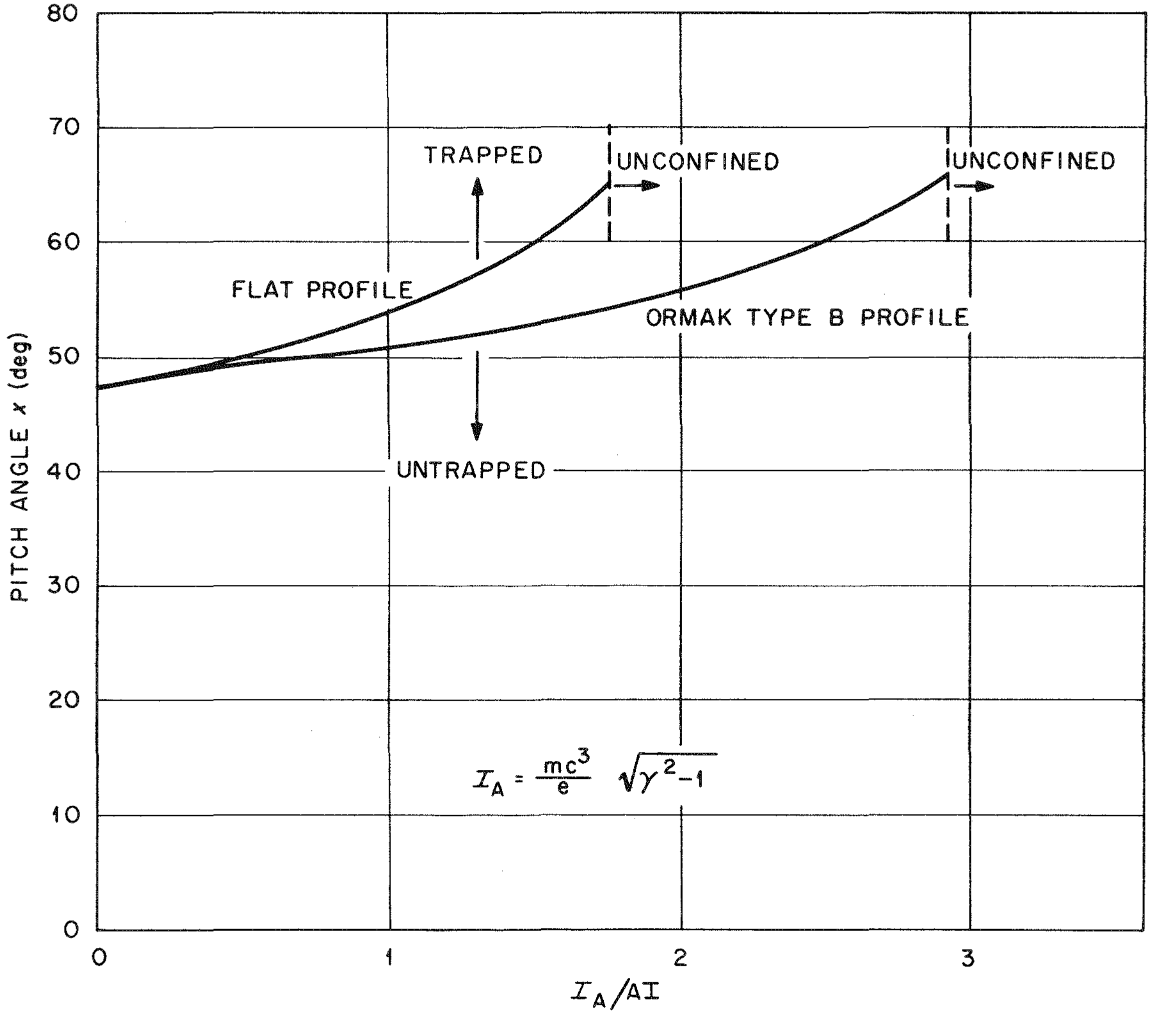

FIGURE III-8

Trapping Boundaries for Relativistic Electrons in Flat and ORMAK Type B Current Profiles.

For each of the two curves shown, electrons corresponding to points above the line are trapped while those below it are untrapped. As may be observed from the plot, higher energies and lower currents (i.e. higher values of I_A/AI) require larger pitch angles for trapping than at lower energies or higher currents. This may be explained by the fact that as I_A/AI becomes large, the inside edge of the orbit is displaced farther out (i.e. r_c is smaller); thus the trajectory does not move as far into the toroidal field gradient and a relatively larger pitch angle is required for trapping. A similar explanation applies to the difference between the flat profile and type B profile curves. The type B orbits are better confined (more nearly centered) than those for the flat current profile. They therefore, in general, move farther into the toroidal field gradient and will become trapped at relatively lower pitch angles.

All points to the right of the dashed lines in Fig. III-8 correspond to unconfined orbits.

In addition to the above calculations, a number of cases have been run using the drift orbit code of Twichell and Rome for ORMAK type B current profiles; these are displayed in Fig. III-9. Energies of 1 MeV, 2 MeV, 3 MeV, 5 MeV, 10 MeV are included with pitch angles ($\chi = \tan^{-1} v_\perp/v_\parallel$) of 0°, 20°, 40°, 60°, and 80° at each energy (for 100 kiloamps toroidal current). As may be seen, a significant deviation from an untrapped orbit ($\chi = 0^\circ$) does not occur until the 60° pitch angle case. The 60° and 80° orbits are trapped banana orbits which become fatter as the energy is increased; at 10 MeV the 60° orbit is no longer trapped, but has become barely untrapped. These trapping

ORNL DWG. 75-12844

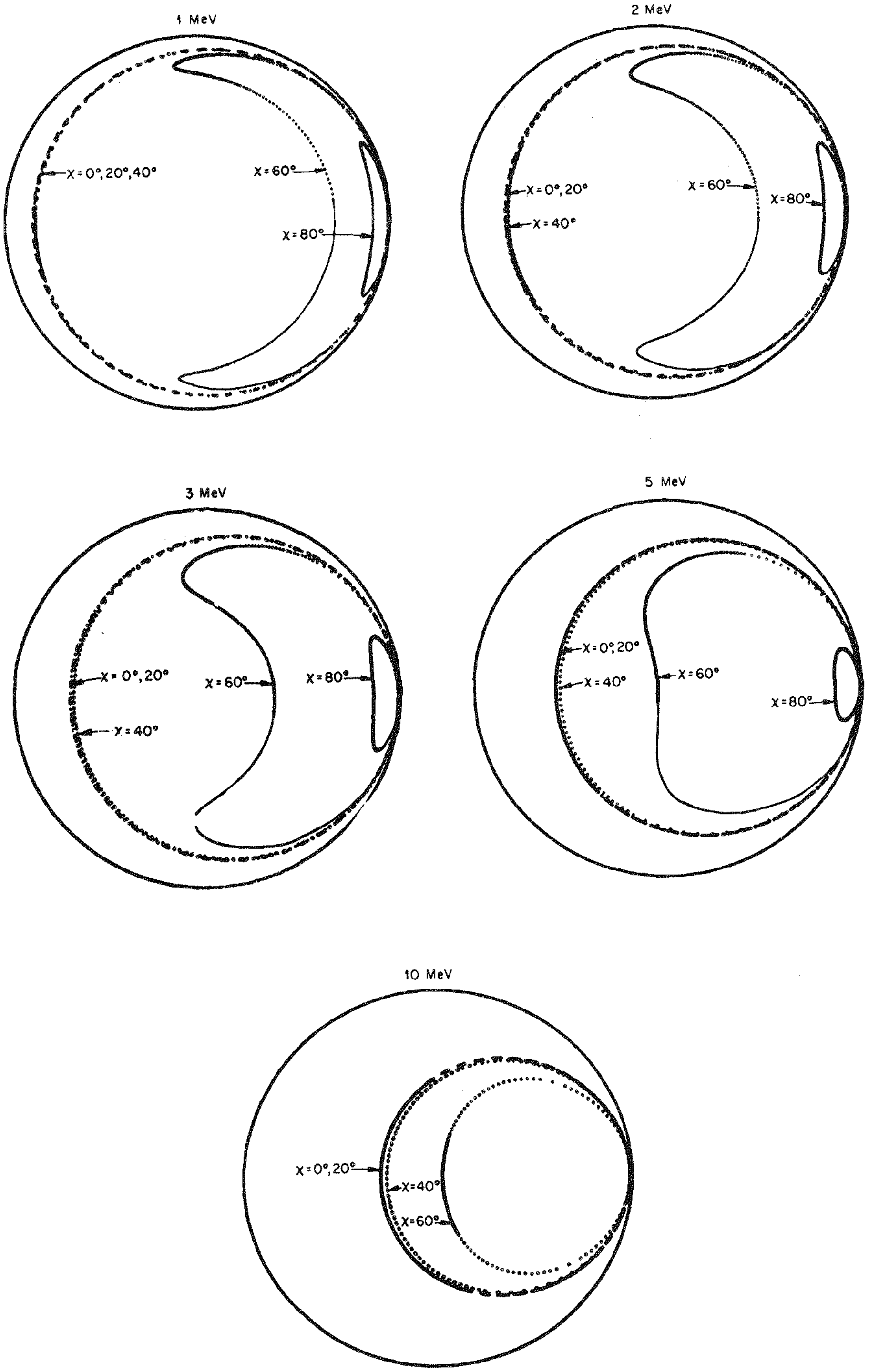

FIGURE III-9

Orbit Trajectories Projected onto a Minor Cross-Section for Relativistic Electrons at 1,2,3,5, and 10 MeV and with Pitch Angles of 0°,20°,40°,60° and 80° (Toroidal Current = 100 kiloamps).

boundaries are in agreement with the type B profile curve of Fig. III-8. The conclusion then is that for pitch angles of 40° or less, the predominant effect on the orbit is caused by the curvature drift (i.e. the orbits are reasonably well approximated by $\chi = 0^{\circ}$).

III.5 Relevance of Orbit Theory to Hard X-ray Dumps in ORMAK Type B Discharges

The experimental results for weak amounts of runaway in ORMAK type B discharges were mentioned earlier in Section I.2. The typical signature left by runaways in these discharges is a gradual dump, beginning at around 35 msec. The energy and intensity then monotonically increase up until the beginning of the current decay (at about 60 msec) where the peak intensity and energy occur. The maximum energies are in the 10 - 12 MeV range and the intensities indicate that roughly 10^{13} runaways were present in the discharge (corresponding to a density of around 10^{7} cm^{-3}).

The single particle orbit theory presented in this chapter is thought to provide a valid explanation of the observed loss of runaways. The curves of Fig. III-4 indicate that there are a class of orbits which will become unconfined for runaway energies and toroidal currents characteristic of type B discharges. Certainly the final loss of these of the particles may be affected by such factors as interaction with image currents in the wall, toroidal field ripples, etc. However, the basic gradual outward displacement of the orbits with increasing energy should be adequately described by the drift orbit model developed here.

There is no direct experimental means of measuring the minor radius of the orbit; this quantity must be deduced from the theoretical model using the measured energy and toroidal current. The intensity at a given energy and current level then provides information on the density of runaways at that energy and radial position. The number of runaways ΔS_R driven into the limiter per unit time by the orbit shift is given by the following equation [8].

$$\frac{\Delta S_R}{\Delta t} = 4\pi^2 R r_{ci} n_R \frac{\Delta r_c}{\Delta t} \qquad \text{III-66}$$

where n_R = density profile of the runaways

R = major radius

r_{ci} = radius of runaway orbit as it is intersecting the limiter

$\frac{\Delta r_c}{\Delta t}$ = rate at which the runaway orbit is being driven into the limiter.

Since $r_{ci}(t)$ can be obtained from the curves of Fig. III-4 as a function of measurable quantities (γ, I), the runaway density as a function of radius in the discharge may be unfolded. This can either be obtained at the moment when the dump occurs or at an earlier time in the discharge by use of the orbit expansion model. Such an analysis has been reported in ref. 8 for a typical ORMAK type B, low density, stable discharge.

In Fig. 3 of ref. 8 the energy, intensity, and deduced runaway density profile is presented, indicating a maximum in density at $r \simeq 17$ cm. The location of this maximum in runaway density may possibly be related to the pronounced skin effect which is thought to occur early in a tokamak discharge when most of the runaways are formed.

The above technique for obtaining $n_R(r)$ has interesting potential applications for accurately diagnosing the early breakdown and current penetration phase of a tokamak discharge -- an area which at present remains largely unexplored. Runaway production, as indicated in Chapter II, is a highly sensitive function of parameters such as electric field, plasma density, neutral density, temperature, and impurity content. Thus, as the rate of runaway formation becomes better understood, an unfolding of the $n_R(r)$ profile which reveals information on these parameters can be considered.

A further, more direct experimental application which is possible is the use of the inferred $\gamma(r)$ profile to diagnose the radial dependence of the Ohmic heating field. Since the final energy of the runaways is sensitive to the total volt-seconds they have been subjected to, the $\gamma(r)$ profile should accurately reflect the $\varepsilon_\phi(r)$ profile. Modifications to the shape of the Ohmic heating profile may be produced, for example, by neutral injection [68] and impurity transport.

CHAPTER IV

Macroscopic Relativistic Beam-Plasma Equilibria and β_p Limits

Macroscopic beam-plasma equilibria and stability are primarily of relevance to the runaway-dominated regime in tokamaks and also may be of importance in considerations of application of relativistic beams to toroidal plasma heating and confinement. The large toroidal momentum carried by high energy electrons can significantly modify tokamak equilibrium properties. A similar problem may arise from momentum flows induced by neutral injection; this process is presently under intense examination as a heating technique for tokamak plasmas. However, in the latter case, toroidal field ripples may be effective in preventing the build-up of large flows [69]. In the present chapter, a theory is developed in order to investigate the effects of the centrifugal force of a relativistic electron beam on the pressure balance in a toroidal plasma. Mathematically-imposed limitations on the solution of the resulting nonlinear partial differential equation are discussed and related to physical considerations. Several examples of numerical solutions to the equilibrium equation are given for a simple model of plasma pressure and beam flow velocity; these are then compared with the existing analytic equilibrium theories. Finally, an estimate is made of possible β_p limitations in toroidal relativistic beam-plasma configurations.

As was mentioned in Chapter I, large outward shifts in the equilibrium position have been observed in strong runaway discharges on the ORMAK and Russian T-6 devices. The cause of these anomalous shifts has been attributed either to the effect of the large toroidal momentum carried by the runaways or to the increased internal inductance of the beam-plasma channel (i.e. if the runaways were initially formed as a beam). It is difficult at present to experimentally distinguish between these two possibilities since the measured magnetic probe signals are only sensitive to the composite quantity $\beta_\perp + \beta_\parallel + \ell_i$. One possible means for separating the poloidal betas from the internal inductance is to investigate the dependence of the shift signal on toroidal current. If other discharge parameters can be held constant, then the poloidal betas for both beam and plasma should increase with decreasing current whereas ℓ_i will remain constant (since it only depends on the profile rather than on the magnitude of the toroidal current). Exploratory experiments have been performed on the ORMAK device [14] at lower current levels than the early runaway discharges [7] which are indicative of this effect. An example of this phenomenon is shown in Fig. IV-1 where the total current and inferred value of $\beta_{pol} + \ell_i/2$ are plotted. The values of $\beta_p + \ell_i/2$ have been calculated using the measured in-out magnetic probe signals, toroidal current, and applied vertical field. This data is used in the equilibrium shift code [70] developed by R. J. Colchin of Oak Ridge; this code takes into account the time-dependent soakage of the fields into the aluminum shell surrounding the plasma. As may be seen, $\beta_{pol} + \ell_i/2$ rises to extremely high values near the end of the discharge. For the reasons mentioned above, most of the observed increase in these particular discharges comes from the poloidal beta of the runaway beam.

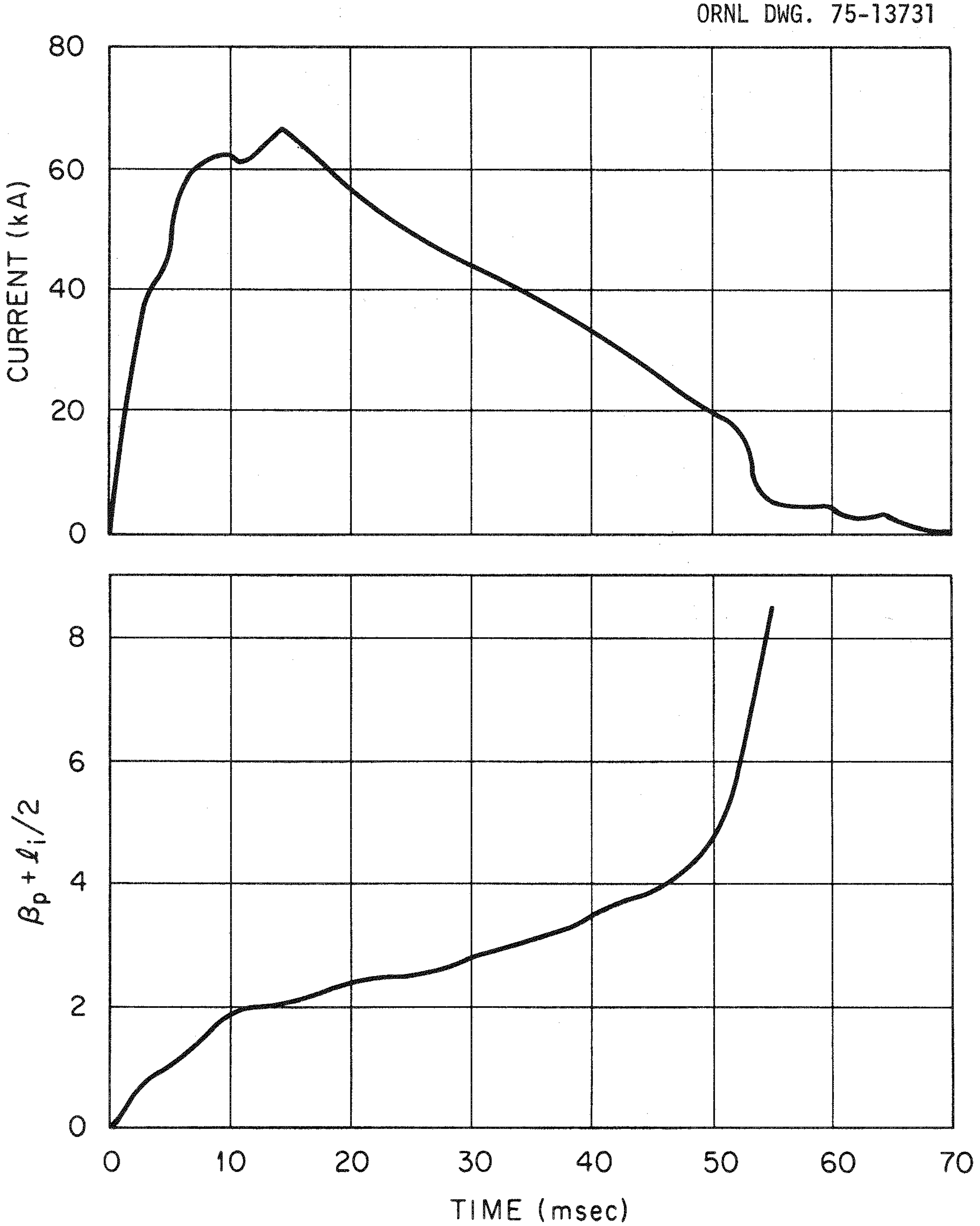

FIGURE IV-1

Toroidal Current and $\beta_p + \ell_i/2$ for a Typical Low-Current Runaway Dominated Discharge.

The presence of large values of the quantity $\beta_{pol} + \ell_i/2$ in runaway discharges, however, leads to significant problems of interpretation since most of the existing analytic theories of toroidal equilibrium implicitly assume a low beta poloidal ordering [71,72,73]. In the following, a theory is developed which does not necessarily assume such an ordering for the beam or plasma.

The equilibrium properties of a charge-neutralized toroidal relativistic beam have been examined by Ott and Sudan [59] and Mondelli and Ott [60]. In these papers, the beam was modeled by choosing a beam distribution function dependent on the constants of the motion: H, the energy, and P_ϕ, the canonical angular momentum. Specifically, the distribution used was $\delta(H-H_0)\ \delta(P_\phi - P_0)$. In ref. [59], the plasma was included only to provide charge neutralization and did not carry any current or have pressure. However, in Ref. [60], the background plasma had finite pressure and carried current; this was included by means of the ideal MHD equations. The relativistic beam was introduced through adding its current to the toroidal plasma current and by including its centripetal force in the virial theorem. The effect of the beam on the equilibrium was to augment the outward displacement of the plasma column. It was also noted that for the particular beam distribution chosen, the beam current profile was quite nonuniform for large values of the ratio I/I_A, the total current (beam plus plasma) to the Alf'ven current ($I_A = 17.1\ \beta\gamma$ KAMPS). This nonuniformity decreased the internal inductance of the beam-plasma column and tended to decrease the outward shift. In both the treatments of Ott and Sudan and Mondelli and Ott, a low beta poloidal ordering is inherently assumed due to the approximation of treating the asymmetry in the poloidal field only to first order in the inverse aspect ratio.

Green and Zehrfeld [74-76] have investigated a related problem -- finite resistivity stationary states with poloidal and toroidal flows. They employ the MHD pressure balance equations with inertial flow, Ohm's law, Maxwell's equations, the mass continuity equation, and an equation of state. Three coupled equations are derived which describe the equilibrium; various limitations on the solvability of these equations are examined. A large aspect ratio limit is taken in order to obtain an analytic solution. Again, the asymmetry in the poloidal field is only treated to first order in the inverse aspect ratio; thus, the results obtained are limited to relatively small energy densities for the flows and plasma pressure relative to the poloidal field energy density.

IV.1 Basic Equations for Anisotropic Beam-Plasma Equilibria

The following analysis is based on the static scalar pressure force balance relation for the plasma, a zero pressure equation of motion for the beam, Maxwell's equations, and a mass continuity equation for the beam component.

$$n_b m_0 \left[\frac{\partial}{\partial t} + \vec{v} \cdot \vec{\nabla} \right] (\gamma \vec{v}) = \frac{1}{c} \vec{J}_b \times \vec{B} \qquad \text{IV-1}$$

$$\vec{\nabla} p = \frac{1}{c} \vec{J}_p \times \vec{B} \qquad \text{IV-2}$$

$$\vec{\nabla} \times \vec{B} = \frac{4\pi}{c} \vec{J} + \frac{1}{c} \frac{\partial \vec{E}}{\partial t} \qquad \text{IV-3}$$

$$\vec{\nabla} \cdot \vec{B} = 0 \qquad \text{IV-4}$$

$$\frac{\partial n_b}{\partial t} + \vec{\nabla} \cdot (n_b \vec{v}) = 0 \qquad \text{IV-5}$$

where $\vec{J}_p$ = plasma current

$\vec{J}_b$ = beam current $\quad \vec{J}=\vec{J}_p + \vec{J}_b$

n_b = beam density

γ = $(1-v^2/c^2)^{-1/2}$

$\vec{v}$ = beam velocity

To obtain a stationary toroidal equilibrium, all explicit time derivatives are neglected. Combining equations IV-1 and IV-2 then results in the following force balance relation.

$$n_b m_0 \vec{v}\cdot\vec{\nabla}(\gamma\vec{v}) + \vec{\nabla}p = \frac{1}{c}\vec{J}\times\vec{B} \qquad \text{IV-6}$$

A vector identity is now used to combine the two terms on the left-hand side of IV-6.

$$\vec{\nabla}\cdot(n_b\vec{v}\gamma\vec{v}) = \gamma\vec{v}\vec{\nabla}\cdot(n_b\vec{v}) + n_b(\vec{v}\cdot\vec{\nabla})(\gamma\vec{v}) \qquad \text{IV-7}$$

The first term on the right-hand side is identically equal to zero by virtue of the time independent continuity equation. Equation IV-6 may then be written as follows.

$$\vec{\nabla}\cdot\,[p\overleftrightarrow{I} + \gamma n_b m_o\vec{v}\,\vec{v}] = \frac{1}{c}\vec{J}\times\vec{B} \qquad \text{IV-8}$$

where $\overleftrightarrow{I}$ = diagonal identity tensor

It will be assumed that the predominant beam velocity is along field lines, i.e. $\vec{v} \simeq v_{\parallel}\hat{b}$ where $\hat{b} = \vec{B}/|B|$ (the beam is nearly force-free). This assumption results in a diagonal tensor on the left-hand side of IV-7.

$$p\overleftrightarrow{I} + \gamma\, n_b m_0\vec{v}\,\vec{v} = \begin{bmatrix} p & 0 & 0 \\ 0 & p & 0 \\ 0 & 0 & p+\gamma n_b m_o v_{\parallel}^2 \end{bmatrix} \qquad \text{IV-9}$$

In writing the tensor in equation IV-9, an orthogonal coordinate system has been chosen which has $\hat{b} = \vec{B}/|B|$ as one of its directions; the other two are perpendicular to $\vec{B}$.

The form of the force balance relation in equation IV-8 is now the same as that for an anisotropic tensor pressure plasma model. Techniques for treating this problem have been discussed in references [77-79]; similar procedures will be employed for reducing equations IV-3, IV-4, and IV-8 and will be discussed in the following.

Substituting IV-9 into the force balance relation IV-8 gives the following equation.

$$\frac{1}{c}\vec{J}\times\vec{B} = \vec{\nabla}p + \gamma n_b m_o v_{\parallel}^2\,[(\vec{\nabla}\cdot\hat{b})\hat{b} + (\hat{b}\cdot\vec{\nabla})\hat{b}] + \hat{b}(\hat{b}\cdot\vec{\nabla})\,(\gamma n_b m_0 v_{\parallel}^2) \qquad \text{IV-10}$$

This may be written in a slightly different form by noting that $(\hat{b}\cdot\vec{\nabla})\hat{b} = \vec{\kappa}$, where $\vec{\kappa}$ is the magnetic field line curvature. Also, the identity given below will be employed.

$$\vec{\nabla}\cdot\hat{b} = \frac{1}{B}\,(\vec{\nabla}\cdot\vec{B}) + \vec{B}\cdot\vec{\nabla}\,(\frac{1}{B}) = -\frac{1}{B}\frac{\partial B}{\partial \ell} \qquad \text{IV-11}$$

Equation IV-10 may then be written in the following manner.

$$\frac{1}{c}\vec{J}\times\vec{B} = \vec{\nabla}p + \gamma n_b m_0 v_{\parallel}^2 \left[-\frac{1}{B}\frac{\partial B}{\partial \ell}\hat{b} + \vec{\kappa}\right] + \hat{b}\frac{\partial}{\partial \ell}\,(\gamma n_b m_0 v_{\parallel}^2) \qquad \text{IV-12}$$

An equilibrium relation is obtained by examining the component of IV-12 perpendicular to the field lines. However, first an identity will be derived by taking the component of IV-12 parallel to field lines; this identity will determine the functional dependence of p and $\gamma m_0 n_b v_{\parallel}^2$ which can be allowed. The parallel component is given below.

$$0 = \frac{\partial p}{\partial \ell} + \gamma n_b m_0 v_{\parallel}^2 \left[-\frac{1}{B}\frac{\partial B}{\partial \ell} + \vec{\kappa}\cdot\hat{b}\right] + \frac{\partial}{\partial \ell}\,(\gamma m_0 n_b v_{\parallel}^2) \qquad \text{IV-13}$$

The field line curvature is always perpendicular to $\vec{B}$ so that $\vec{\kappa}\cdot\hat{b}\equiv 0$. Equation IV-13 thus reduces to the following identify.

$$\frac{\partial}{\partial B}\left(p + \gamma n_b m_0 v_{\parallel}^2\right) - \frac{\gamma m_0 n_b v_{\parallel}^2}{B} = 0 \qquad \text{IV-14}$$

For the case of an axisymmetric tokamak equilibrium, equation IV-14 may be satisfied by the following choices.

$$\begin{aligned} p &= p(\psi) \\ \gamma n_b m_0 v_{\parallel}^2 &= \frac{B}{B_0}\,\rho(\psi) \end{aligned} \qquad \text{IV-15}$$

where p (ψ) and ρ (ψ) are functions which depend only on ψ, the poloidal flux function. B_0 is the magnetic field at the center line of the torus and $B = |\vec{B}|$.

The component of IV-12 perpendicular to field lines will now be examined; this is given below.

$$\vec{\nabla}_{\perp} p + \gamma m_0 n_b v_{\parallel}^2 \vec{\kappa} = \frac{1}{c}\,\vec{J}\times\vec{B} \qquad \text{IV-16}$$

In the manipulations to follow, it is convenient to write the field line curvature in the following form (for a derivation of this, see ref. [77]).

$$\vec{\kappa} = \frac{1}{B}\vec{\nabla}_{\perp} B + \frac{1}{B^2}\left(\vec{\nabla}\times\vec{B}\right)\times\vec{B} \qquad \text{IV-17}$$

Employing Ampere's law and equation IV-17, IV-16 may be written in the form given below.

$$\sigma(\vec{\nabla}\times\vec{B})\times\vec{B} = \vec{\nabla}_{\perp} p + \frac{\gamma m_0 n_b v_{\parallel}^2}{B}\,\vec{\nabla}_{\perp} B \qquad \text{IV-18}$$

$$\text{where } \sigma \equiv \frac{1}{4\pi} - \gamma m_0 n_b v_{\parallel}^2/B^2$$

The following identity is now used to convert IV-18 into the form in which the general tensor pressure equilibrium equation is usually written.

$$\vec{B} \times [\vec{\nabla}\times(\sigma\vec{B})] = \sigma\vec{B} \times (\vec{\nabla}\times\vec{B}) + \vec{B} \times (\vec{\nabla}\sigma\times\vec{B})$$

$$= \sigma\vec{B} \times (\vec{\nabla}\times\vec{B}) + B^2\vec{\nabla}\sigma - (\vec{B}\cdot\vec{\nabla}\sigma)\,\vec{B}$$

$$= \sigma\vec{B} \times (\vec{\nabla}\times\vec{B}) - B^2\vec{\nabla}_\perp\left(\frac{\gamma m_0 n_b v_\parallel^2}{B^2}\right) \qquad \text{IV-19}$$

$$= \sigma\vec{B} \times (\vec{\nabla}\times\vec{B}) - \vec{\nabla}_\perp(\gamma m_0 n_b v_\parallel^2) - \frac{2\gamma m_0 n_b v_\parallel^2}{B}\vec{\nabla}_\perp B$$

Using the above relation in IV-18 results in the following equation.

$$[\vec{\nabla}\times(\sigma\vec{B})] \times \vec{B} = \vec{\nabla}_\perp(p+\gamma m_0 n_b v_\parallel^2) - \frac{\gamma m_0 n_b v_\parallel^2}{B}\vec{\nabla}_\perp B \qquad \text{IV-20}$$

Further use of IV-20 now requires specification of a coordinate system and a means of labeling magnetic field lines. For the case of an axisymmetric tokamak, the magnetic field is given below.

$$\vec{B} = \frac{F}{R}\hat{\iota}_\phi + \frac{\vec{\nabla}\psi\times\hat{\iota}_\phi}{R} \qquad \text{IV-21}$$

where $F = RB_T$

B_T = toroidal magnetic field

Here a cylindrical (R,ϕ,Z) coordinate system is employed as is shown in Fig. II-6. Since p and $\gamma m_0 n_b v_\parallel^2$ must have the B and ψ dependences as indicated in equation IV-15, the right-hand side of IV-20 becomes the following.

$$\text{R.H.S.} = \frac{\partial p}{\partial\psi}\vec{\nabla}\psi + \frac{\partial}{\partial\psi}(\gamma n_b m_0 v_\parallel^2)\,\vec{\nabla}\psi$$

$$+ \frac{\partial}{\partial B}(\gamma n_b m_0 v_\parallel^2)\,\vec{\nabla}_\perp B - \frac{\gamma m_0 n_b v_\parallel^2}{B}\vec{\nabla}_\perp B \qquad \text{IV-22}$$

$$= \frac{\partial}{\partial\psi}(p + \gamma m_0 n_b v_\parallel^2)\,\vec{\nabla}\psi$$

Substitution of the field given in IV-21 into the left-hand side of IV-20 results in the expression given below.

$$-\frac{R^2}{\sigma}[\vec{\nabla}x(\sigma\vec{B})] \; x \; \vec{B} = (\Delta^*\psi)\,\vec{\nabla}\psi + \frac{1}{\sigma}\left(\vec{\nabla}\sigma\cdot\vec{\nabla}\psi\right)\vec{\nabla}\psi$$

$$+ \frac{F}{\sigma}\vec{\nabla}\,(\sigma F) + \frac{R^2}{\sigma}\vec{\nabla}\psi x\vec{\nabla}\,(\sigma F) \qquad \text{IV-23}$$

$$\text{where } \Delta^*\psi \equiv R^2\vec{\nabla}\cdot\,(R^{-2}\vec{\nabla}\psi)$$

Thus, the vector equilibrium force balance equation is as follows.

$$(\Delta^*\psi)\vec{\nabla}\psi + \frac{1}{\sigma}(\vec{\nabla}\sigma\cdot\vec{\nabla}\psi)\,\vec{\nabla}\psi + \frac{F}{\sigma}\vec{\nabla}(\sigma F) + \frac{R^2}{\sigma}\vec{\nabla}\psi x\vec{\nabla}\,(\sigma F)$$

$$= -\frac{R^2}{\sigma}\frac{\partial}{\partial\psi}(p + \gamma m_0 n_b v_{\parallel}{}^2)\,\vec{\nabla}\psi \qquad \text{IV-24}$$

Dotting equation IV-24 with $\hat{\imath}_\phi$, the unit vector in the ϕ-direction, and assuming axisymmetry, results in the equation given below.

$$\hat{\imath}_\phi\cdot\,[\vec{\nabla}\psi x\vec{\nabla}(\sigma F)] = 0 \qquad \text{IV-25}$$

The meaning of this identity is as follows. Since axisymmetry is present, neither $\vec{\nabla}\psi$ nor $\vec{\nabla}(\sigma F)$ can have a component in the ϕ direction; thus, $\vec{\nabla}\psi x\vec{\nabla}(\sigma F)$ cannot be perpendicular to $\hat{\imath}_\phi$. Equation IV-25 then implies that $\vec{\nabla}\psi x\vec{\nabla}(\sigma F) = 0$. Therefore, $\vec{\nabla}\psi$ must be in the same direction as $\vec{\nabla}(\sigma F)$ and constant ψ contours coincide with constant σF contours, i.e., σF is only a function of ψ. It may be noted that this result is slightly modified from that of ideal MHD scalar pressure toroidal equilibrium theory where F is only a function of ψ. This result would, of course, be obtained in the above analysis in the limit that $\gamma m_0 n_b v_{\parallel}{}^2 \rightarrow 0$ (i.e. the beam disappears). However, since the toroidal beta associated with the beam (ratio of the beam's kinetic energy density to the toroidal field energy density) will usually not be more than a few per cent, σ is nearly a constant. Thus, the function F comes close to being a function only of ψ in most cases of interest.

Using the above fact, the third term of the left-hand side of equation IV-24 may be written as follows.

$$\frac{F}{\sigma}\vec{\nabla}(\sigma F) = \frac{F}{\sigma}\frac{\partial}{\partial\psi}(\sigma F)\vec{\nabla}\psi \tag{IV-26}$$

Now all the terms of equation IV-24 are in the $\vec{\nabla}\psi$ direction and the equilibrium is determined by the equation given below.

$$\Delta^*\psi + \frac{1}{\sigma}(\vec{\nabla}\sigma\cdot\vec{\nabla}\psi) + \frac{F}{\sigma}\frac{\partial}{\partial\psi}(\sigma F) = -\frac{R^2}{\sigma}\frac{\partial}{\partial\psi}(p + \gamma m_0 n_b v_{\parallel}{}^2) \tag{IV-27}$$

This is of a similar form as the anisotropic tensor pressure equilibrium equation given, for example, by Grad [78] for an axisymmetric system. It is, for general choices of p and $\gamma m_0 n_b v_{\parallel}{}^2$, a nonlinear, two-dimensional partial differential equation. For the choices of $p(\psi)$ and $\gamma m_0 n_b v_{\parallel}{}^2$ given in equation IV-15, it is always elliptic, as will be shown in Section IV.2.

As was mentioned above, in the case where the directed beam kinetic energy is much less than the toroidal magnetic field energy, $\sigma \simeq (4\pi)^{-1}$ and IV-27 reduces to the following.

$$\Delta^*\psi = -4\pi R^2\frac{\partial}{\partial\psi}(p + \gamma n_b m_0 v_{\parallel}{}^2) - F\frac{\partial F}{\partial\psi} \tag{IV-28}$$

This is similar to the tokamak scalar pressure equilibrium equation [80] except for the additional term $-4\pi R^2 \frac{\partial}{\partial\psi}(\gamma m_0 n_b v_{\parallel}{}^2)$ caused by the presence of a runaway beam.

In conclusion, equation IV-27 represents the equilibrium condition for a zero pressure, streaming runaway beam with the predominant flow velocity along the field lines, $\vec{v} \simeq v_{\parallel}\hat{b}$. Conditions for the existence of solutions to this equation will be discussed in the following section and numerically computed solutions will be examined in Section IV.3.

IV.2 Conditions on the Existence of Solutions

Two conditions must be satisfied by equation IV-27 in order for a solution to exist; these will be examined in the present section. They are known as the firehose and mirror instability conditions.

A. Firehose Instability

The firehose instability, as its name suggests, occurs in anisotropic plasmas where the pressure parallel to the field lines is much greater than that transverse to field lines. The exact condition for the firehose instability is that $\sigma=0$ at some point in the plasma. As may be seen from equations IV-20 and IV-22, this would lead to the following.

$$\frac{\partial}{\partial \psi} (p + \gamma m_0 n_b v_{\parallel}^2) \vec{\nabla}\psi = 0 \qquad \text{IV-29}$$

This then implies that either ψ=constant or $p + \gamma m_0 n_b v_{\parallel}^2$=constant. In order to avoid such a situation, σ must be greater than zero over the plasma cross-section or,

$$\gamma m_0 n_b v_{\parallel}^2 < \frac{B^2}{4\pi} \qquad \text{IV-30}$$

As may be recalled from Chapter II, this was also the condition which had to be satisfied in order to prevent collapse of the beam due to $\vec{E}\times\vec{B}$ drifts. For runaway regimes in present tokamaks, the above condition is well satisfied. Significantly higher energies and runaway densities would be required before this limit would be approached.

B. Mirror Instability

The mirror instability is normally associated with equation IV-27 not being elliptic. Since the boundary conditions on ψ are usually of the Dirichlet type on a closed surface (e.g., a conducting shell), equation IV-27 is a well-posed, unique problem only when it is elliptic. If it becomes parabolic or hyperbolic, then unique solutions no longer exist. For the case of a toroidal relativistic beam immersed in an isotropic plasma, equation IV-27 is always elliptic; this will be proven in the following.

Using equation IV-15 in IV-27 results in the equation given below.

$$\Delta^*\psi + \frac{1}{\sigma}(\vec{\nabla}\sigma\cdot\vec{\nabla}\psi) + \frac{F}{\sigma}\frac{\partial}{\partial\psi}(\sigma F) = -\frac{R^2}{\sigma}\left(p' + \frac{B}{B_0}\rho'\right)$$

$$\text{where } \sigma = \frac{1}{4\pi} - \frac{\rho}{B\,B_0} \qquad \text{IV-31}$$

and primes denote derivatives with respect to ψ

Ellipticity is defined as follows for a second order partial differential equation.

$$a\frac{\partial^2 u}{\partial x_1^2} + 2b\frac{\partial^2 u}{\partial x_1\,\partial x_2} + c\frac{\partial^2 u}{\partial x_2^2} + d = 0 \qquad \text{IV-32}$$

IV-32 is elliptic provided $ac-b^2 > 0$; for $ac-b^2 < 0$ it is hyperbolic. In order to check this condition on equation IV-31, it is first necessary to work out what the second term on the left-hand side of IV-31 is.

$$\vec{\nabla}\sigma = \frac{1}{B\,B_0}\left(\rho'\vec{\nabla}\psi + \frac{\rho}{B}\vec{\nabla}B\right) \qquad \text{IV-33}$$

Using $B=R^{-1}(F^2 + |\vec{\nabla}\psi|^2)^{1/2}$, $\vec{\nabla}B$ is given by the following.

$$\vec{\nabla} B = \left(1 - \frac{F}{R^2 B} \frac{\partial F}{\partial B}\right)^{-1} \left\{ - \frac{B}{R} \hat{\iota}_R + \frac{1}{R^2 B} \left[F \frac{\partial F}{\partial \psi} \vec{\nabla}\psi + (\vec{\nabla}\psi \cdot \vec{\nabla}) \vec{\nabla}\psi\right] \right\} \qquad \text{IV-34}$$

$\vec{\nabla}\sigma \cdot \vec{\nabla}\psi$ is then given as below.

$$\vec{\nabla}\sigma \cdot \vec{\nabla}\psi = - \frac{\rho'}{B\, B_0} |\vec{\nabla}\psi|^2 + \frac{\rho}{B^2 B_0} \left(B - \frac{F}{R^2} \frac{\partial F}{\partial B}\right)^{-1} \left\{ - \frac{1}{R} \frac{\partial \psi}{\partial R} \right.$$

$$\left. + \frac{1}{R^2 B^2} \left[F \frac{\partial F}{\partial \psi} |\vec{\nabla}\psi|^2 + \left((\vec{\nabla}\psi \cdot \vec{\nabla}) \vec{\nabla}\psi\right) \cdot \vec{\nabla}\psi\right] \right\} \qquad \text{IV-35}$$

Substituting IV-35 into equation IV-31, writing out the $\Delta^*\psi$ $\left((\vec{\nabla}\psi \cdot \vec{\nabla}) \vec{\nabla}\psi\right) \cdot \vec{\nabla}\psi$ terms in (R,ϕ,z) coordinates, collecting second derivatives in R and Z, and substituting into the ellipticity condition gives the following.

$$\left[1 + A \left(\frac{\partial \psi}{\partial R}\right)^2\right] \left[1 + A \left(\frac{\partial \psi}{\partial Z}\right)^2\right] - A^2 \left(\frac{\partial \psi}{\partial R}\right)^2 \left(\frac{\partial \psi}{\partial Z}\right)^2 > 0 \qquad \text{IV-36}$$

$$\text{or } 1 + A |\vec{\nabla}\psi|^2 > 0$$

$$\text{where } A = \frac{\rho}{\sigma R^2 B_0 B^2} \left(B - \frac{F}{R^2} \frac{\partial F}{\partial B}\right)^{-1}$$

The derivative, $\partial F/\partial B$, may be calculated using the fact that σF depends only on ψ. This results in the equation given below.

$$\frac{\partial F}{\partial B} = - \frac{F}{\sigma} \frac{\rho}{B^2 B_0} \qquad \text{IV-37}$$

Using $|\vec{\nabla}\psi|^2 = B^2 R^2 - F^2$ and IV-37 in IV-36 gives the following condition.

$$\sigma B_0 B^2 \left(BR^2 + \frac{F^2}{\sigma} \frac{\rho}{B_0 B^2}\right) + \rho(BR^2 - F^2) > 0 \qquad \text{IV-38}$$

Substituting in $\sigma = 1/4\pi - \rho/B\, B_0$, equation IV-38 reduces to $B\, B_0/4\pi > 0$ which is always satisfied. Thus, equation IV-27 is elliptic.

IV.3 Numerical Results and Comparison with Analytic Equilibrium Theories

The numerical solution of equation IV-27 has been investigated using a modification of the scalar pressure equilibrium code developed by Callen, Dory, and Fowler [80] at Oak Ridge. This uses the successive overrelaxation technique; ghost points are employed to satisfy flux conserving (conducting shell) boundary conditions.

Both the plasma pressure and beam momentum functions, $p(\psi),\rho(\psi)$, given in equation IV-15, are modeled as quadratic in ψ plus a small higher order term in ψ to insure that both $p'(\psi)$ and $\rho'(\psi)$ go to zero at the plasma boundary. The function σF, which depends only on ψ is chosen as indicated below.

$$g^2(\psi) = (\sigma F)^2 = g_w^2 + 8\pi R_0^2 (p+\rho)\left(\frac{1}{\beta_T} - 1\right) \qquad \text{IV-39}$$

where g_w = a constant

$\beta_T = \beta_p + \beta_{pb}$

β_p = poloidal plasma beta

β_{pb} = poloidal beam beta

The procedure used for solving IV-27 then is the following. σ is initially set equal to $1/4\pi$. Using the specified functions $p(\psi)$, $\rho(\psi)$, and $g(\psi)$, equation IV-27 is solved by successive overrelaxation to a desired degree of accuracy. A new value for σ is then calculated according to the following.

$$\sigma_{new} = \frac{1}{4\pi} - \frac{\rho(\psi)}{B_0 B} \qquad \text{IV-40}$$

where $B = \frac{1}{R}\left[|\vec{\nabla}\psi|^2 + \frac{g^2(\psi)}{\sigma_{old}^2}\right]^{1/2}$

These values of σ and B are next used in equation IV-27, and it is solved a second time. New values of σ and B are then calculated, equation IV-27 is solved, etc. This iteration is continued until a desired degree of accuracy is obtained in σ and B.

Some typical equilibria are shown in Fig. IV-2; these are plots of constant ψ contours. In Fig. IV-3 the current distribution on the equatorial plane is shown as a function of R for several values of β_p and β_{pb}.

A comparison has been made between the above numerically-computed equilibria and analytic calculation given in refs. [60,73,76]. The analytic approaches come to essentially the same conclusion regarding the shift of the outermost plasma flux surface.

$$\Delta_0 = \frac{b^2}{2R_0} \left[\ln \frac{b}{a} + \left(\Lambda * + \frac{1}{2}\right)\left(1 - \frac{a^2}{b^2}\right)\right] + \frac{cb^2}{2I} B_\perp \qquad \text{IV-41}$$

where $\Lambda * = \beta_p + \frac{\beta_{pb}}{2} + \frac{\ell i}{2} - 1$

β_p = poloidal beta of plasma

β_{pb} = poloidal beta of beam $= \dfrac{8\pi\langle n_b \gamma m_0 v_{\parallel}{}^2\rangle}{B_\theta{}^2(a)}$

β = externally applied vertical field

I = total toroidal current

a = radius of beam-plasma column

b = radius of conducting shell

R_0 = major torus radius

ℓ_i = internal inductance

For the numerical calculations, no vertical field is present and the

ORNL DWG. 75-13737

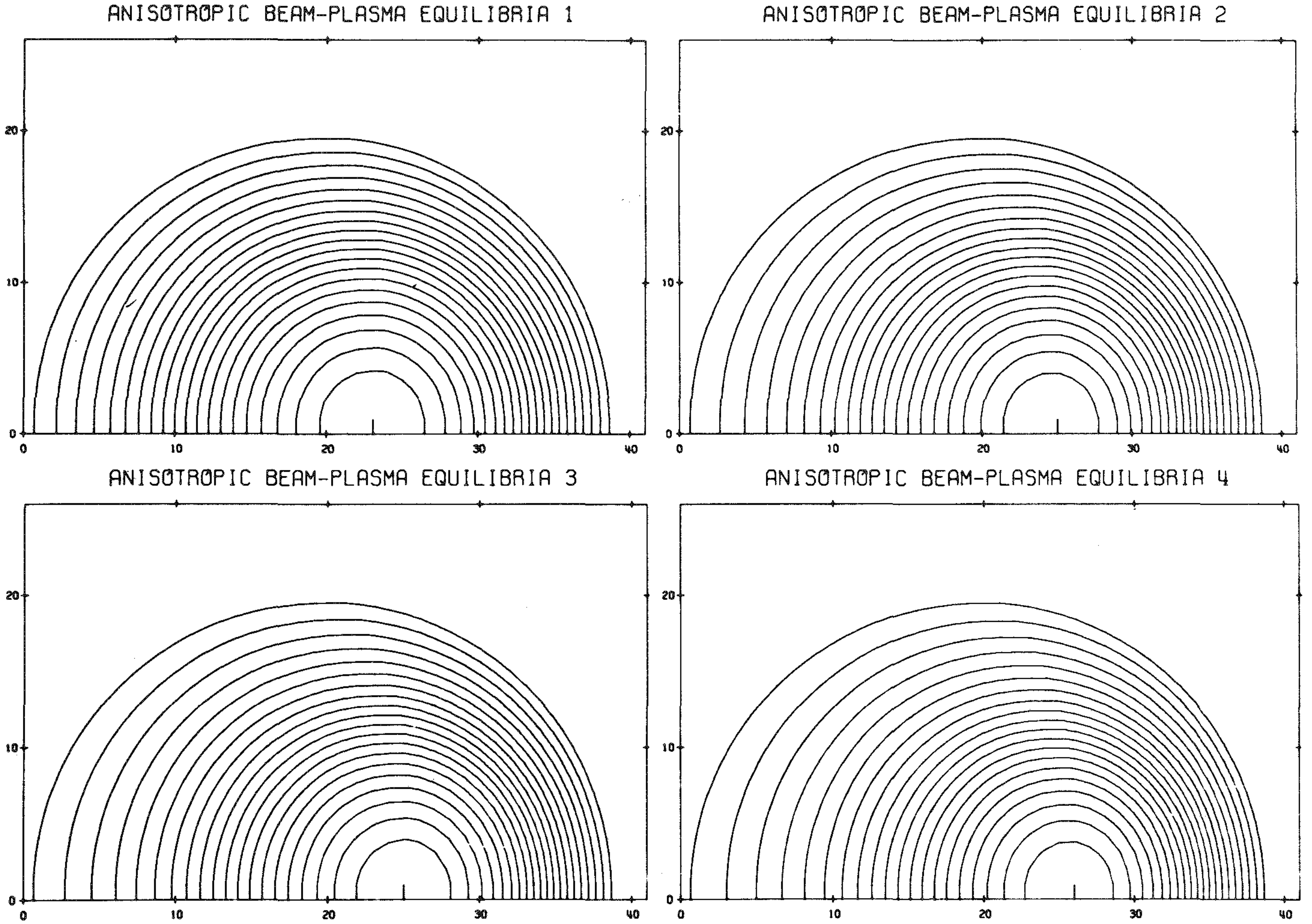
ANISOTROPIC BEAM-PLASMA EQUILIBRIA 1

ANISOTROPIC BEAM-PLASMA EQUILIBRIA 2

ANISOTROPIC BEAM-PLASMA EQUILIBRIA 3

ANISOTROPIC BEAM-PLASMA EQUILIBRIA 4

FIGURE IV-2

Anisotropic Toroidal Beam Plasma Equilibria: (1) $\beta_p = .64$, $\beta_{pb} = 1.2$; (2) $\beta_p = 1.2$, $\beta_{pb} = 2.3$; (3) $\beta_p = .38$, $\beta_{pb} = 4.6$; (4) $\beta_p = .35$, $\beta_{pb} = 5.7$

ORNL DWG. 75-13730

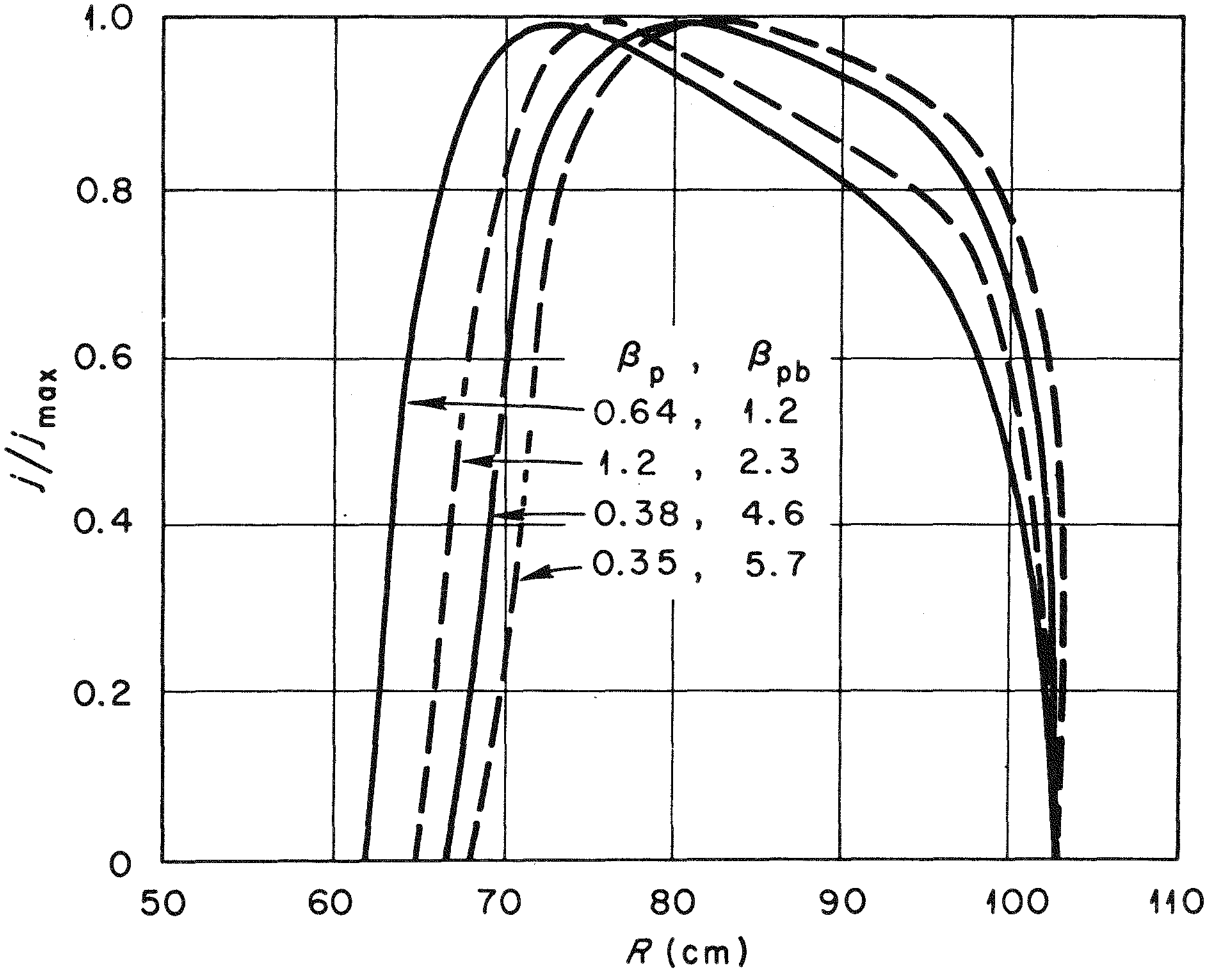

FIGURE IV-3

Toroidal Current Distribution as a Function of Major Radius for Equilibria of Fig. IV-2.

poloidal betas are calculated after the iterations have converged using the equation given below.

$$\beta_p \text{ or } \beta_{pb} = \frac{2c^2 \int (p \text{ or } \frac{B}{B_0} \rho)\, dRdz}{[\int j_\phi dRdz]^2} \qquad \text{IV-42}$$

Δ_0 is obtained by measuring the shift of the center of the outermost plasma flux surface away from the center of the minor cross-section. Results are plotted in Fig. IV-4. As may be seen, when β_{pb} becomes large relative to β_p, there seems to be a substantial discrepancy between the results of the code and the analytic theory. The shift predicted by the numerical calculation is generally less than that of equation IV-41. Part of this is perhaps due to the fact that the analytic theory is based on an inverse aspect ratio expansion-to first order - and does not take into account the non-circularity of flux surfaces which occurs for large Δ_0. The aspect ratio used here is that of ORMAK, A = 3.4. The discrepancy also may be caused by the model used, i.e. the functional dependences chosen in IV-15 for p and $\gamma m_0 n_b v_\parallel^2$. Apparently the 1/R dependence introduced into $\gamma m_0 n_b v_\parallel^2$ by its linear dependence on B (as required by equation IV-14) results in the beam term of equation IV-27 having relatively less of an effect on the equilibrium than the plasma pressure term. This is related to the fact that the plasma term goes as R^2 times a function of ψ while the beam term goes as R times a function of ψ. The former thus has a stronger variation around a flux surface than the latter, and thus has a more marked effect on the poloidal asymmetry (i.e. the outward shift) in the flux function contours.

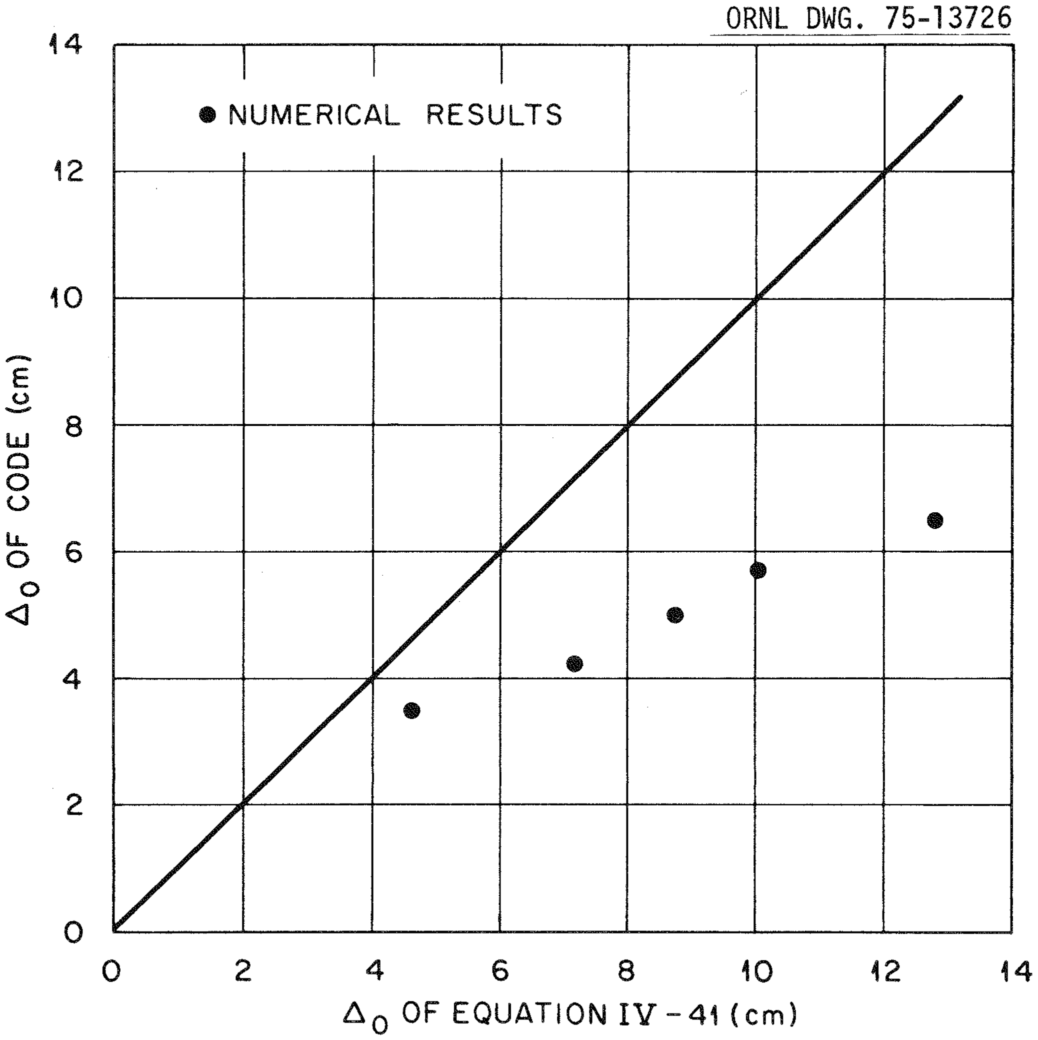

FIGURE IV-4

Comparison Between the Results of Numerically-Obtained Equilibrium Shift and that of Equation IV-41.

IV.4 Estimates of β_p Limitations on Toroidal Beam-Plasma Equilibria

Beta poloidal limits are an important consideration in the feasibility of a tokamak fusion reactor since the total β is related to β_p by $\beta = \beta_p/A^2q^2$ where A is the aspect ratio, and q is the Kruskal-Shafranov factor. For example, typically $A \simeq 3$, $q(a) > 2$ and $\beta_p \leq A$ so that β is limited to less than about 10%. The limit on β_p comes about when the externally-applied vertical field (used to counteract the outward plasma expansion force) becomes equal to the poloidal field on the inside of the torus. At this point, a second magnetic axis can form on the inside edge of the plasma and deterioration of the confinement properties would be expected to occur, i.e. particles can escape from the plasma region at the thermal velocity near the separatrix. Estimates of how large β_p can become before this phenomenon occurs have been made by various researchers and are reviewed in ref. [80]. However, in most of this literature, the equilibrium is treated by making an expansion in ε, the inverse aspect ratio, and assuming the orderings $\beta_p \simeq 1$, $\Delta/a \ll 1$ (Δ=shift of the center of the plasma column, a=plasma minor radius). Thus, the limitation obtained, i.e. that $\beta_p \lesssim A$, is beyond the assumed orderings. In ref.[80] toroidal plasma equilibrium is examined for devices of arbitrary aspect ratio and without any ordering in Δ/a or β_p. This is accomplished by a numerical solution of the problem similar to that used in Section IV.3 . It was found there that β_p can be as high as desired, but the requirement that q_{min} (the minimum value of the Kruskal-Shafranov factor) be greater than unity prevented any significant improvement in the total β. The reason for this was that as β_p

is increased, the plasma becomes increasingly diamagnetic - thus reducing the allowable toroidal current if q_{min} is to be maintained > 1. As a result, $(B_{pol})_{max}$ is decreased along with β for a fixed β_p.

The presence of a relativistic electron beam would be expected to augment the outward force of the beam-plasma column (due to the centripetal force) and thus aggravate the β limitation. In the following analysis, this effect is examined and conditions on the ν/γ of the beam are noted for which a second magnetic axis would be expected to occur. (ν=N r_0, N = density of beam electrons per unit length, r_0 = classical electron radius = e^2/m_0c^2, $\gamma = (1-v^2/c^2)^{-1/2}$). It should be pointed out, however, that this treatment is based on a simple force balance which inherently assumes a low beta ordering. The ultimate answer to the question of beta poloidal limits with relativistic beams will perhaps have to come from a numerical solution of the equilibrium problem such as that discussed in Sections IV.1 and IV.2.

The outline of this section is as follows. First, to put the method used in perspective, a β_p limit is obtained for a toroidal plasma without a beam. Next, the analagous equilibrium limit is found for a cold beam in a cold pressureless plasma. Finally, the same limit for a cold beam in a warm plasma is calculated. Since toroidal relativistic beams may be able to attain low q values, the latter limit is examined with respect to the question of what beam parameters would not result in a degradation of the equilibrium limit for the plsma species alone if there were no limits on the beam current density. Possible limits on the beam current density will be investigated in Chapter V.

IV.4.A. Equilibrium Force Balance for a Toroidal Plasma

In the following, the force balance in the direction of the major radius is considered for a toroidal plasma. This has been given by Shafranov [72]; it was obtained there by using a variational principle on the functional $Q = \int (B^2/8\pi + p)dv$, the total energy of the plasma and magnetic fields. The resulting major radius force balance may be written as follows.

$$\frac{\pi a^2}{R_0}\left\{\frac{B_\theta^2(a)}{4\pi}\left(\ln\frac{8R_0}{a} - 1 + \frac{\ell_i}{2}\right) + \bar{p} + \frac{B_e^2 - \bar{B}_i^2}{8\pi}\right\} = \frac{B_\perp I}{c} \qquad \text{IV-43}$$

where R_0 = major torus radius

a = minor torus radius

$\bar{p}$ = plasma pressure averaged over the minor cross-section

B_e = toroidal field external to plasma

$\bar{B}_i$ = toroidal field internal to plasma
- averaged over the minor cross-section

ℓ_i = internal inductance

$B_\perp$ = external vertical field

I = total plasma current

c = speed of light

A β_p limit may be obtained from IV-43 by requiring that $B_\perp < B_\theta(a)$. However, first the physical significance of the terms in IV-43 will be pointed out.

The first term is related to the fact that in a current-carrying plasma ring there is an outward force caused by unbalanced $\vec{J} \times \vec{B}$ forces. The poloidal field crossed with the ring current results in a net force along the major radius due to the asymmetry of the poloidal field about the ring axis. A simple means of calculating this force is by the method of virtual displacements. A slight outward displacement is made in the major radius of the plasma and the change in inductive energy is calculated. From this a force may be obtained.

$$F_R = \frac{1}{2\pi R_0} \frac{\delta w}{\delta R_0} \qquad \text{IV-44}$$

here w = poloidal field energy = $\frac{1}{2} \frac{I^2}{c^2} L$

and L = total inductance = $L_{ext} + L_{int}$

For a toroidal plasma without a conducting shell boundary, the inductance is given by the following.

$$L_{ext} = 4\pi R_0 \left(\ln \frac{8R_0}{a} - 2\right)$$

$$L_{int} = 2\pi R_0 \ell_i = 2\pi R_0 \overline{B_\theta^2}/B_\theta^2(a) \qquad \text{IV-45}$$

Therefore, the outward force along the major radius is given as below.

$$F_R = \frac{\pi a^2}{R_0} \frac{B_\theta^2(a)}{4\pi} \left(\ln \frac{8R_0}{a} - 1 + \frac{\ell_i}{2}\right) \qquad \text{IV-46}$$

In the case where the plasma is located inside a perfectly conducting shell, the external inductance is given as follows:

$$L_{ext} = 4\pi \left\{R_0 \ln \frac{b}{a} - \frac{\Delta}{2} \left[\left(1 + \frac{a^2}{b^2}\right) \left(\Lambda + \frac{1}{2}\right) + \ln \frac{b}{a}\right]\right\} \qquad \text{IV-47}$$

where Δ = displacement of plasma column in shell

In this case the radial force is given by:

$$F_R = \frac{\pi a^2}{R_0} \frac{B_\theta^2(a)}{4\pi} \left(\ln \frac{b}{a} + \frac{\ell_i}{2}\right) \qquad \text{IV-48}$$

The situation with no conducting shell present, equation IV-46, would correspond to late times in a tokamak discharge when the fields have diffused through the metallic shell. The case with a perfectly conducting shell, equation IV-48, corresponds to times early in the discharge when the metallic shell is still effectively perfectly conducting. For most present-day tokamaks, the latter approximation is of relevance.

The second term in the force balance equation, $\pi a^2 \bar{p}/R_0$, originates from the outward expansion force per unit length due to finite plasma pressure. This may be seen by examining Fig. IV-5 where a segment of a toroidal plasma is shown. Adding up the components of force in the direction of the major radius results in the following.

$$\text{Net outward force per unit length} = \frac{2\pi a^2 \bar{p}(d\phi/2)}{R_0 d\phi} = \frac{\pi a^2 \bar{p}}{R_0} \qquad \text{IV-49}$$

The third term in the force balance is caused by the curvature of the toroidal magnetic field and may be verified by integrating the magnetic stress-energy tensor over the minor cross-section. Combining IV-43 with the minor radius force balance given below

$$\bar{p} + \frac{\overline{B_i^2} - B_e^2}{8\pi} = \frac{B_\theta^2(a)}{8\pi} \qquad \text{IV-50}$$

and requiring that $B_\perp < B_\theta(a)$ (which insures that a separatrix will not form on the inner edge of the torus) results in the following.

$$\frac{\pi a^2}{R_0} \left\{ \frac{B_\theta^2(a)}{4\pi} \left(\ln \frac{8R_0}{a} - \frac{3}{2} + \frac{\ell_i}{2}\right) + 2\bar{p} \right\} < \frac{B_\theta(a)\, I}{c} \qquad \text{IV-51}$$

(no conducting shell)

ORNL DWG. 75-13725

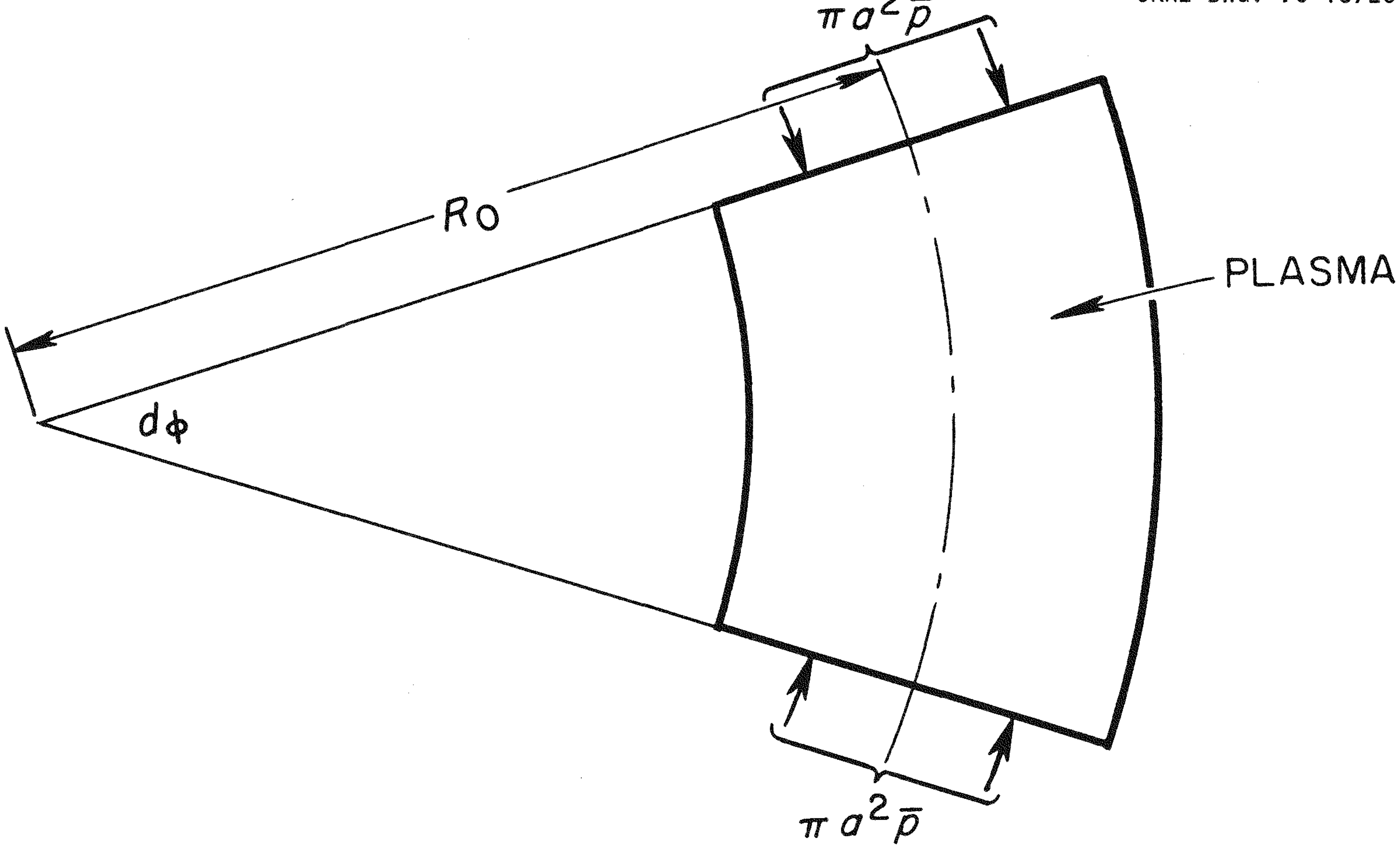

FIGURE IV-5

Plasma Expansion Forces Acting upon a Segment of Toroidal Plasma.

$$\frac{\pi a^2}{R_0}\left\{\frac{B_\theta^2(a)}{4\pi}\left(\ln\frac{b}{a}-\frac{1}{2}+\frac{\ell_i}{2}\right)+2\bar{p}\right\}<\frac{B_\theta(a)I}{c} \qquad \text{IV-52}$$

(conducting shell at r=b)

Using $B_\theta(a) = 2I/ca$ and dividing IV-51, IV-52 by $(\pi a^2/R_0)$ $(B_\theta^2(a)/4\pi)$ one obtains the equations given below.

$$\beta_p + \frac{\ell_i}{2} < 2A - \ln 8A + \frac{3}{2} \qquad \text{IV-53}$$

(no conducting shell)

$$\beta_p + \frac{\ell_i}{2} < 2A - \ln\frac{b}{a} + \frac{1}{2} \qquad \text{IV-54}$$

(conducting shell)

In Fig. IV-6 a plot is made of the two above relations for a range of aspect ratios and for several wall to plasma ratios, b/a. As may be seen, the above limits on $\beta_p + {}^{\ell_i}/_2$ come out somewhat higher than what is conventionally assumed to be the limit, i.e. $\beta_p + {}^{\ell_i}/_2 \lesssim A$. The reasons for this discrepancy are not entirely clear; however, it perhaps is related to the fact that the usual limit was obtained from a partial differential equation describing plasma equilibrium whereas the above limit is obtained from an integral form of the equilibrium equation. Both approaches inherently assume circular flux surfaces, small horizontal column shifts, and large aspect ratio.

IV.4.B. Cold Beam-Cold Plasma Equilibrium Limit

A force balance is now examined for the case of a toroidal relativistic electron beam with a cold, pressureless background plasma which serves only to provide charge neutralization and carries no net current. The electron beam is assumed to have no transverse pressure, but does

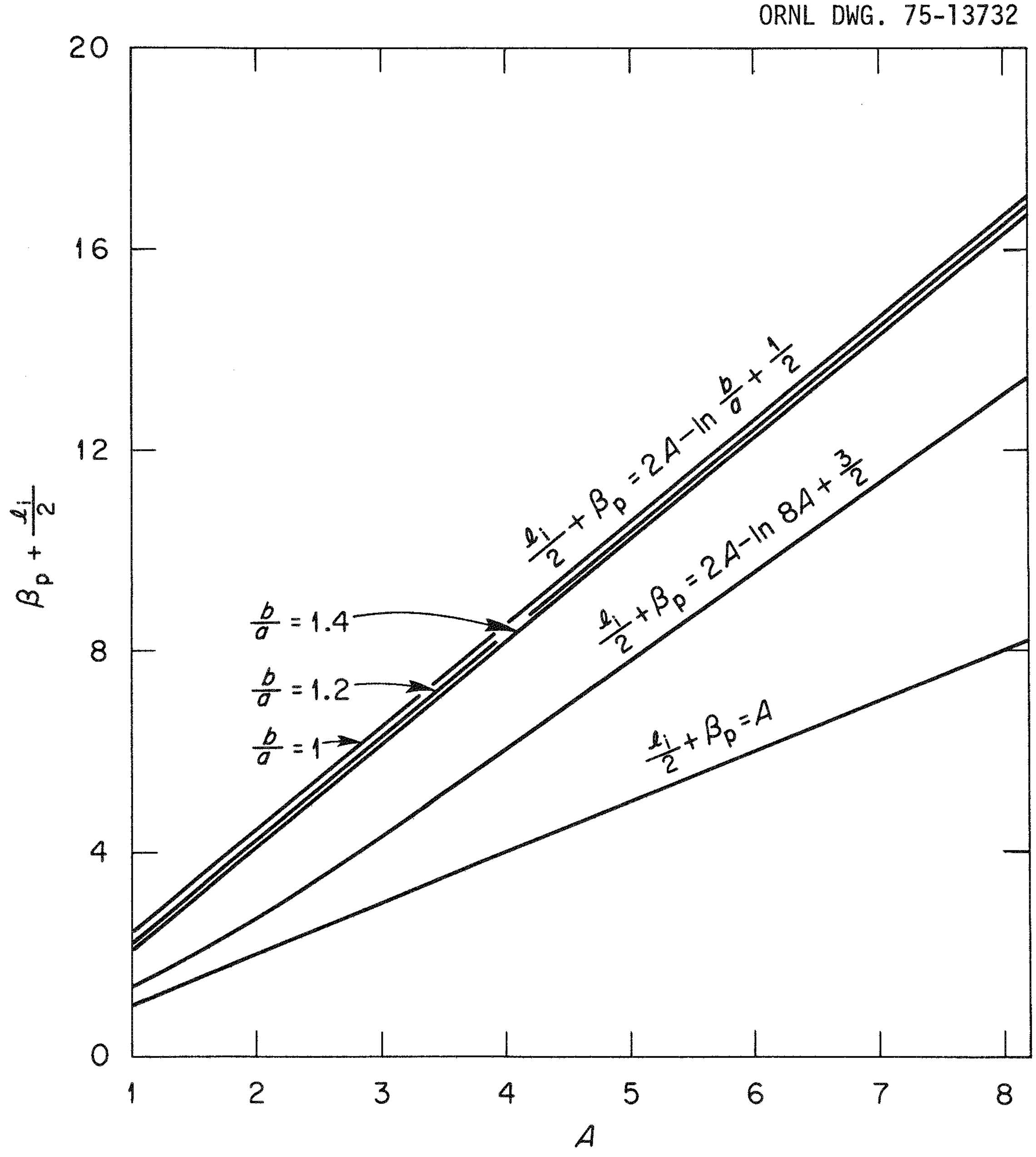

FIGURE IV-6

Limitations on $\beta_p + \ell_i/2$ vs. Aspect Ratio as Obtained from the Major Radius Force Balance.

have parallel momentum and produces a net self-field. It is assumed that the presence of the beam does not significantly modify the toroidal field, i.e. the beam is neither paramagnetic nor diamagnetic. There are then two forces which must be balanced by the external vertical field -- the centrifugal force and the ring current expansion force. The force due to the curvature in the toroidal field goes as $B_e^2 - \overline{B}_i^2$ and thus is zero under the above assumptions. These considerations result in the following equation.

$$\frac{\pi a_1^2 \, \overline{n}_b \gamma m_0 c^2}{R_0} + \frac{1}{2\pi R_o} \frac{\partial w}{\partial R_o} \leq \frac{B_\theta(a_2) I_b}{c} \qquad \text{IV-55}$$

where $w = 2\pi R_0 \frac{I^2}{c^2} \left(\ln \frac{8R_0}{a_1} - 2 + \frac{\ell_i}{2}\right)$

(no conducting shell)

$$= 2\pi \frac{I^2}{c^2} \left\{ R_0 \ln \frac{b}{a_1} - \frac{\Delta}{2} \left[\left(1 + \frac{a_1^2}{b^2}\right) \left(\Lambda + \frac{1}{2}\right) - \ln \frac{b}{a_1} \right] + R_0 \frac{\ell_i}{2} \right\}$$

(conducting shell)

a_1 = beam radius

a_2 = shell radius

I_b = beam current

$\overline{n}_b$ = average of beam density over the minor cross-section

Rearranging IV-55 gives the equations listed below

$$\frac{1}{2} (\beta_b + \ell_i) < 2 \frac{a_2}{a_1} A_b - \ln 8A_b + 1 \qquad \text{IV-56}$$

(no conducting shell)

$$\frac{1}{2} (\beta_b + \ell_i) < 2 \frac{a_2}{a_1} A_b - \ln \frac{b}{a_1} \qquad \text{IV-57}$$

(conducting shell)

A_b = aspect ratio of beam = $\frac{R_0}{a_1}$

β_b = $8\pi \bar{n}_b \gamma m_0 v_{\parallel}^2 / B_\theta^2(a_1)$

In the limit that $v_{\parallel} \simeq c$, the beta poloidal of the beam is equal to $2\gamma/\pi\nu$ where ν is the Budker's parameter ($\nu = Nr_0$, N = number of electrons per unit length, r_0 = classical electron radius = e^2/m_0c^2). Equations IV-56 and IV-57 may also be written as lower limits on ν/γ:

$$\nu/\gamma > \frac{1}{\pi}\left[2\,\frac{a_2}{a_1}A_b - \ln 8A_b + 1 - \frac{\ell_i}{2}\right]^{-1} \qquad \text{IV-58}$$

$$\nu/\gamma > \frac{1}{\pi}\left[2\,\frac{a_2}{a_1}A_b - \ln\frac{b}{a_1} - \frac{\ell_i}{2}\right]^{-1} \qquad \text{IV-59}$$

IV.4.C. Cold Beam - Warm Plasma Equilibrium Limit

The models of Subsections IV.4.A and IV.4.B will now be combined in order to consider the equilibrium limitation on a toroidal relativistic beam immersed in a warm plasma which carries current. The forces acting on the plasma are then the net $\vec{J} \times \vec{B}$ ring expansion force, the outward component of the pressure force, and the curvature in the toroidal field whereas the beam forces consist of the current ring expansion and centripetal forces. It is again assumed that the beam does not modify the toroidal field; however, the plasma is diamagnetic. The force balance equation is then given as follows.

$$\frac{\pi a_1^2 n_b \gamma m_0 c^2}{R_0} + \frac{1}{2\pi R_0}\,\frac{\partial w}{\partial R_0} + \frac{\pi a_2^2}{R_0}\left[\bar{p} + \frac{B_e^2 - \bar{B}_i^2}{8\pi}\right] \leq \frac{I_t B_\theta(a_2)}{c} \qquad \text{IV-60}$$

$$\text{where } w = \frac{2\pi I_t^{\,2}}{c^2} \begin{cases} R_0 \left(\ln \frac{8R_0}{a_2} - 2 + \frac{\ell_i}{2}\right) & \text{(no conducting shell)} \\ R_0 \ln \frac{b}{a_2} - \frac{\Delta}{2} \left[\left(1 + \frac{a_2^2}{b^2}\right) \left(\Lambda + \frac{1}{2}\right) - \ln \frac{b}{a_2}\right] + R_0 \frac{\ell_i}{2} & \text{(conducting shell)} \end{cases}$$

$I_t = I_b + I_p$ = beam plus plasma current

$\ell_i = \overline{B_\theta^2}/B_\theta^2\,(a_2)$

a_2 = plasma radius $\qquad$ a_1 = beam radius

IV-60 then results in the two β_p limits given below.

$$\frac{1}{2}(\beta'_b + \ell_i) + \beta_p < 2A - \ln 8A + \frac{3}{2} \quad \text{(no conducting shell)} \qquad \text{IV-61}$$

$$\frac{1}{2}(\beta'_b + \ell_i) + \beta_p < 2A - \ln \frac{b}{a_2} + \frac{1}{2} \quad \text{(conducting shell)} \qquad \text{IV-62}$$

where $\beta'_b = 8\pi \bar{n}_b\, m_0 c^2/B_\theta^2\,(a_2)$

$\beta'_p = 8\pi \bar{p}/B_\theta^2\,(a_2)$

The poloidal betas above are defined with respect to the total poloidal magnetic field (from both the beam and plasma currents) evaluated at the boundary of the plasma. In order to determine the extent to which the presence of a beam aggravates the plasma equilibrium limit derived in Subsection IV.4.B, the above two inequalities will be rewritten in terms of β's which are defined with respect to the poloidal fields of each component separately. For simplicity, it is assumed that $a_1 = a_2 = a$. The situation where $a_1 \neq a_2$ will be considered subsequently. The limits

IV-61 and IV-62 then become the following.

$$\frac{\hat{\beta}_b}{2} \frac{I_b^2}{I_t^2} + \hat{\beta}_p \frac{I_p^2}{I_t^2} < Z \qquad \text{IV-63}$$

where $\hat{\beta}_b = \beta_b' \dfrac{I_t^2}{I_b^2}$ = poloidal beta of the beam referenced to the beam's self field

$\hat{\beta}_p = \beta_p' \dfrac{I_t^2}{I_p^2}$ = poloidal beta of the plasma referenced to the poloidal field produced by the plasma current

$$\text{and } Z = \begin{cases} 2A - \ln 8A + \frac{3}{2} - \frac{\ell_i}{2} & \text{(no conducting shell)} \\ 2A - \ln \frac{b}{a} + \frac{1}{2} - \frac{\ell_i}{2} & \text{(conducting shell)} \end{cases}$$

Equation IV-63 may then be rearranged to obtain the limitation on the plasma beta poloidal, $\hat{\beta}_p$:

$$\hat{\beta}_p < \frac{I_t^2}{I_p^2} \left(Z - \frac{1}{2} \hat{\beta}_b \frac{I_b^2}{I_t^2}\right) \qquad \text{IV-64}$$

It may be recalled from Subsection IV.4.B. that $\hat{\beta}_p$ was limited to less than Z for a warm plasma without a beam. Equation IV-64 indicates that if there is no limit on the beam current, then it may be possible to make the right-hand side of IV-64 greater than Z. That is, the presence of the beam may actually allow an enhancement over the usual plasma beta poloidal limitation. This will occur when the following inequality is satisfied.

$$\frac{I_t^2}{I_p^2} \left(Z - \frac{1}{2} \hat{\beta}_b \frac{I_b^2}{I_t^2}\right) > Z \qquad \text{IV-65}$$

Using the fact that $I_b = \frac{\nu}{\gamma} I_A$ and $\hat{\beta}_b = \frac{2}{\pi}\gamma/\nu$ for $v_{\parallel} \simeq c$ where $I_A = (m_0 c^3/e)\gamma\beta$ is the Alfvén current, it is possible to rearrange equation IV-65 into the form given below.

$$\frac{\nu}{\gamma} > \frac{1}{\pi Z} - 2\frac{I_p}{I_A} \qquad \text{IV-66}$$

Note that as $I_p \to 0$, the result of Subsection IV.4.B. (with $a_1 = a_2$) is recovered.

The case where $a_1 \neq a_2$ is now considered, i.e. the beam radius is less than the plasma radius. The internal inductance, ℓ_i, may become large as the current distribution is narrowed; in the following, a simple current distribution is assumed -- that of a flat beam current profile added onto a flat plasma current profile. In this case, the internal inductance is given as below.

$$\ell_i = \frac{1}{2} + f_b f_p (1 - \varepsilon^2) + 2 f_b^2 \ln\frac{1}{\varepsilon} \qquad \text{IV-67}$$

where $\varepsilon = a_1/a_2$ $\qquad f_b = I_b/I_t$

$f_p = I_p/I_t$

Using equation IV-67 in equation IV-64 then leads to the following limit.

$$\frac{1}{2}\hat{\beta}_b f_b^2 + \hat{\beta}_p f_p^2 < Z' - \frac{f_b}{2} + \frac{\varepsilon^4}{4}(f_p - f_b) - f_b^2 \ln\varepsilon \qquad \text{IV-68}$$

where $Z' = Z + \frac{\ell_i}{2}$

The resulting limitation on $\hat{\beta}_p$ is as given below.

$$\hat{\beta}_p < \frac{1}{f_p^2}\left[Z' - \frac{f_b}{2} + \frac{\varepsilon^4}{4}(f_p - f_b) - f_b^2 \ln\varepsilon - \frac{1}{2}\hat{\beta}_b f_b^2\right] \qquad \text{IV-69}$$

The conclusion, then, of the above treatment of β_p limits is that for certain values of ν/γ, the beam does not deteriorate the β poloidal limit of the plasma without a beam. However, for lower values of ν/γ, the presence of a beam can severely limit the allowable beta poloidal of the plasma.

As may be seen from Fig. IV-1 (discussed earlier), the above limits have already been approached in runaway-dominated discharges on ORMAK. Although these discharges have not yet been thoroughly diagnosed, it was observed that the plasma thermal energy was very low. One possible explanation for this might be the rapid plasma energy transport which would occur if a separatrix were actually formed near the inner surface of the plasma.

CHAPTER V

Helical Instability Modes in Tokamak Runaway Discharges

One of the fundamental limitations in tokamak devices is that posed by macroscopic MHD instabilities with spatial dependences of the form $f(r) \exp [i(m\theta + n\phi)]$ where $m = 0,1,2,\ldots$ and $n = 0,1,2$. These correspond to helical perturbations of the plasma column normally known as kink and flute modes; flutes are driven principally by plasma pressure whereas kinks are driven by magnetic field energy. The poloidal (m) and toroidal (n) mode numbers of the instability are roughly related to the safety factor q by $q = m/n$ where $q = 2\pi/i = rB_t/R\,B_p$ (r and R are the minor and major radii, i is the rotational transform). Thus, the perturbations conform closely with the pitch of the helical magnetic field lines. A good discussion of the linear theory of these modes for circular cross-section tokamaks is contained in a paper by Shafanov [81]. Experimentally, kink modes have been observed since the early days of tokamak work [82] and continue to be an area of active research due to their potential for deteriorating plasma energy confinement [83,84].

When the safety factor q goes below unity either inside or outside the plasma, the $m = 1$, $n = 1$ mode is unstable; this is usually thought to be the most serious of the kink instabilities and may be avoided by satisfying the well-known Kruskal-Shafranov condition: $q > 1$ or $I < r^2 B_t/2R$. Flute modes are also predicted to be unstable at $q < 1$; however, at larger values of q, flutes are prevented in the tokamak by the average minimum B stabilization which is present [86]. In order that q not fall below unity anywhere within the plasma or vacuum region, most tokamak designs assume that q must be maintained above 2.5-3 at the plasma edge; this criterion is predicted by resistive MHD theory. However, results on recent devices [83,85], such as TFR, indicate that in order to obtain maximum plasma energy confinement times, even higher values of q(a) (6 to 9) may be required. Extrapolation of these results to larger devices is not completely clear at present.

Since there is a maximum attainable toroidal magnetic field (imposed by technological constraints) and a limit on β_p (normally taken as $\beta_p \lesssim A$), the fusion power density in a tokamak reactor may be shown to scale in proportion to q to the inverse fourth power. Thus, the above q limitations impose a severe constraint on the power per unit volume and result in large minimum plasma sizes in order to obtain significant energy multiplication in a tokamak.

Macroscopic kink instabilities also are of relevance to runaway-dominated discharges and to considerations of toroidal relativistic beam injection. The basic reason for this is the high current densities which may be obtained when most of the current is carried by electrons moving near the speed of light, i.e., $j_b = \bar{n}_b ec \simeq 50\ (\bar{n}_b/10^{13})$ kAmps/cm^2 ($\bar{n}_b$ in cm^{-3}). Thus, for toroidal fields and major radii typical of present-day tokamaks, the q limitation may be exceeded within the discharge even when a relatively small fraction of the background plasma density is running away. This may be seen by expressing the q value at the edge of a relativistic beam in terms of $\bar{n}_b$, R, and B_T.

$$q(a) \simeq \frac{10^9}{\pi} \frac{B_T}{R\,\bar{n}_b} \qquad \text{V-1}$$

B_T = toroidal field (gauss)

R = major radius (cm)

For example, with R = 80 cm, B_T = 20 kG, q would reach unity if a density of 8×10^{10} cm^{-3} relativistic electrons were carrying all the current. For most tokamaks, this is less than 1% of the typical plasma electron density.

As was mentioned in Chapter I, the experimental evidence on runaway-dominated discharges in tokamaks has indicated certain signs of macroscopic instabilities; however, the characteristic features of instabilities in these discharges differ significantly from those of MHD modes in the normal tokamak regime. Typically, current dumps are observed which correlate with positive (and sometimes negative) voltage spikes. The size of these dumps varies from a few percent up to 20% of the total current, as in some of the early ORMAK discharges [7]. In the latter case, the large current steps were thought to have been related to the poor horizontal positioning of the plasma. However, a more recent series of strong runaway discharges on ORMAK [14] which were well-centered, still showed definite, but smaller jumps in current ($\lesssim 4\%$). The MHD magnetic probes, which are sensitive to rapid fluctuations in the poloidal field, generally exhibit a much quieter level of activity in the strong runaway regime than in the normal tokamak discharges. This feature has been observed on both the Russian T-6 and ORMAK devices. The only noticeable activity on these measurements are the occasional spikes which correspond to changes in poloidal field induced by the current dumps.

The instability analysis presented in this chapter has been motivated on the above observations along with the conclusions of the parameter study of Chapter II. On one hand, there appears to be evidence of macroscopic instabilities in runaway-dominated discharges which lead to fast current dumps, etc. However, on the other hand, the general level of magnetic field fluctuations and the parameter study of Chapter II indicate that the runaway regime might possibly have enhanced stability properties over what is normally the case in tokamaks. In order to better understand these features and to examine the implications with respect to fusion applications of toroidal relativistic beams, several mechanisms will be investigated here which are thought to be distinct to runaway-dominated discharges. These include: velocity shear in the runaway beam, effects of the longitudinal dynamics of the relativistic electrons, influence of the high transit frequency of the runaways around flux surfaces, and consideration of toroidal drifts.

Relatively little work has been done to-date on the macroscopic stability theory of toroidal relativistic beams in strong magnetic fields. The first treatment was made by Lee [43] in 1972 who considered a cylindrical model with a flat current profile. The beam was immersed in a cold, pressureless, ideal MHD plasma and periodic boundary conditions were imposed on the perturbed fields along the beam propagation direction in order to introduce toroidal effects. The beam was assumed to be cold and rigid such that a beam segment as a whole undergoes transverse displacement without internal distortion. Also, it was assumed that the only significant forces acting on the beam were due to perturbed magnetic fields -- effects of perturbed electric fields were neglected. The conclusion was that a small margin of stability could be attained over the usual Kruskal-Shafranov condition; specifically, the instability threshold for $\tilde{m} = \pm 1$, n=1 kink modes was found at $q = (1+\varepsilon)^{-1}$ where $\varepsilon = \gamma m_0 c^2 \beta / e R_0 B_Z$ and thus enhanced stability properties are only obtained at very high energy densities where sychrotron losses would be prohibitive. Growth rates for the instability were estimated at the Alfvén transit time around the torus.

Lovelace[44] has also examined kink and flute instabilities in toroidal relativistic beams. He attempted to derive an energy principle whereas Lee's analysis was based on a normal mode approach. His treatment also differed from Lee's in that he included effects due to the finite ratio of beam kinetic energy to magnetic field energy density. A sufficient condition for the stability of kink modes was obtained which indicated that $q>1$ was required for stability of beams with decreasing energy density as a function of radius. It is of interest to note that for hollow beams, such as those examined in Chapter II, Lovelace's stability criterion would allow stability at $q<1$. A necessary condition was found for the stability of flute modes which was similar to the standard Suydam condition for an isotropic plasma -- if the plasma pressure were replaced by the directed beam kinetic energy.

Theoretical work has also been done concerning kink and sausage modes in relativistic beams with no external magnetic field [87-90]. This will not be reviewed in any detail here since it is not of direct relevance to tokamak runaway regimes. These instabilities are usually known as "hose" modes and result from an interaction between the beam and induced eddy currents in the background plasma. The perturbations are of the same form as kinks, i.e. $\exp[i(m\theta + k_{\parallel} Z)]$ and growth rates are of the order of the skin diffusion time of the perturbed fields. This is physically related to the fact that it is difficult to produce the perturbed currents in the beam necessary for growth of a kink because of the longitudinal stiffness (effective parallel mass = $\gamma^3 m_0$, transverse mass = γm_0) characteristic of relativistic electrons. They must be induced in the background plasma and the time scale for this to occur is governed by the diffusion times of the perturbed magnetic fields.

The outline of the present chapter will be as follows. In Section V.1, the effects of velocity and energy shear will be considered by means of a two-region beam model. Similar techniques and approximations are used as employed by Lee, i.e. cold beam and plasma, ideal MHD, etc. A marginal stability condition is derived for the $n = 1$, $m = 1$ kink mode. In Section V.2, a number of the restrictions on the analysis of Section V.1 will be relaxed. The longitudinal beam dynamics are considered and perturbed electric field forces on the beam are taken into account as well as those due to perturbed magnetic fields. The model for the background plasma still assumes low temperature, but is not restricted to frequencies much less than ω_{ci}, as is the ideal MHD model. This is of importance since the basic drift frequency of the relativistic electrons around a flux surface can be of the order of ω_{ci} for the parameter range under consideration. As will be discussed in Section V.2, over certain ranges of q this can act to short out instabilities which normally grow on longer (MHD) time scales. Energy spread in the beam electrons is formally treated and the effect of toroidal curvature drifts is discussed. Dispersion relations are derived for both free boundary and fixed boundary models. Finally, the spectrum of growth rates and real frequency components is numerically calculated and plotted for a range of parameters.

V.1 Kink Mode ($m = 1$, $n = 1$) in a Two-Region Relativistic Beam with Velocity Shear

A possibly important difference between a beam generated in a strong runaway discharge and that considered by Lee [43] is related to the presence of steep velocity shear and density gradients. The reason for this has to do with the fact that the externally-induced electric field producing the runaways will soak into the outer regions of the plasma first; as runaways are produced there and begin their acceleration, inductive effects will cancel out a large portion of the field from the central portion of the beam. Fewer runaway electrons will be produced in the center of the beam, and they will not be accelerated as much as the outer electrons; thus, there will be a higher recombination rate of these inner electrons back into the bulk electron distribution.

The purpose of this section is to examine the stability of a toroidal relativistic beam with velocity shear against kink modes ($m = 1$, $n = 1$). The model chosen is that of a cylindrical beam consisting of two regions with different constant velocities over each region. Similar assumptions will be made as in Lee's analysis [43]. These are listed as follows:

(a) The plasma is a pressureless, uniform fluid obeying ideal MHD. No currents are flowing in equilibrium other than that of the beam.

(b) The electron beam is a cold, rigid body with a finite velocity and inertia in addition to current. When the beam is perturbed perpendicular to its direction of motion, the displacement is rigid -- a beam segment as a whole undergoes transverse displacement. The center of mass of both velocity regions displaces the same amount so that there is no internal distortion in the beam.

(c) Beam velocities in both regions are assumed to be large compared to the plasma Alfvén velocity; this allows one to neglect the electric forces acting on the beam in comparison with magnetic forces. For ORMAK $v_A \simeq 10^7$ m/sec in the runaway regime operation.

(d) The cylinder walls are perfectly conducting and the toroidal field (in z direction) is strong compared to the beam self field. The aspect ratio is assumed to be large so that the torus may be approximated by a cylinder with periodic boundary conditions.

In Fig. V-1 a side and cross-sectional view of the beam is presented. The beam moves in the z direction; in order to balance off the radial forces, an equilibrium is chosen which includes a rotation in the $-\hat{e}_\theta$ direction. The equilibrium quantities are given by the following.

$$n_B(r) = n_{B0}\, H(a_2 - r) \qquad H = \text{Heaviside function}$$

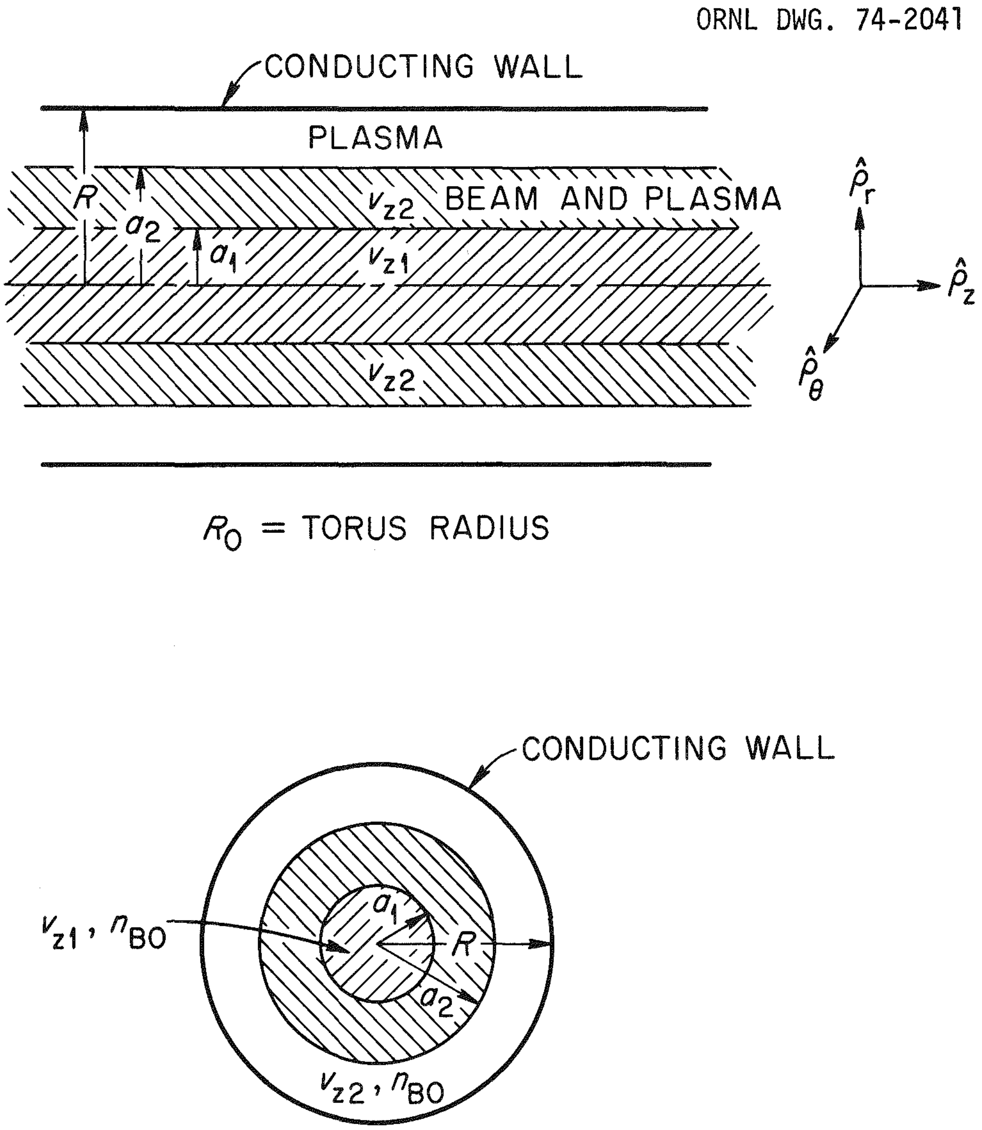

FIGURE V-1

Side and Cross-Sectional Views of Two-Region Relativistic Electron Beam.

$$v_Z(r) = (v_{Z_1} - v_{Z_2})\, H\, (a_1 - r) + v_{Z_2}\, H\, (a_2 - r)$$

$$v_\theta(r) = -r\, (\omega_1 - \omega_2)\, H(a_1 - r) - r\omega_2\, H(a_2 - r)$$

$$v_r = 0$$

$$\vec{J}_B = -en_B \vec{v} \qquad \text{V-2}$$

$$B_Z = \text{constant}$$

$$I_B = \text{total beam current}$$

$$= \pi e\, n_{B_0}\, [a_1^2\, v_{Z_1} + (a_2^2 - a_1^2)\, v_{Z_2}]$$

$$B_\theta(r) = \begin{cases} -\dfrac{2I_{B_1} r}{a_1^2 c} & 0 \leq r \leq a_1 \\[2ex] -\dfrac{2I_{B_1}}{rc} - \dfrac{2I_{B_2}(r^2 - a_1^2)}{rc(a_2^2 - a_1^2)} & a_1 \leq r \leq a_2 \\[2ex] -\dfrac{2I_{B_1}}{rc} - \dfrac{2I_{B_2}}{rc} & a_2 \leq r \leq R \end{cases} \qquad \text{V-3}$$

where $I_{B_1} = \pi a_1^2 e n_{B_0} v_{z_1}$ = current carried in region 1

$I_{B_2} = \pi (a_2^2 - a_1^2)\, e n_{B_0} v_{z_2}$ = current carried in region 2

The rotation frequencies ω_1 and ω_2 may be calculated by balancing the radial centrifugal force with the inward-directed Lorentz force for each region:

$$\frac{\gamma m v_\theta^2}{r} = \frac{e}{c} \quad (v_\theta B_Z - v_Z B_\theta) \qquad \text{V-4}$$

Letting $v_\theta = \omega r$ and solving for ω in each region results in the following.

$$\omega_1 = \omega \text{ for region 1}$$

$$= \frac{\omega_{c1}}{2}\left[1 + 4\frac{\omega_{\beta 1}^2}{\omega_{c1}^2}\right]^{1/2} - \frac{\omega_{c1}}{2} \qquad \text{V-5}$$

$$\omega_2 = \omega \text{ for region 2}$$

$$= \frac{\omega_{c2}}{2}\left\{1 + \frac{\omega_{\beta 2}^2}{r^2\omega_{c2}^2}\left[\frac{I_{B1}}{I_{B2}}(a_2^2 - a_1^2) + r^2 - a_1^2\right]\right\}^{1/2} - \frac{\omega_{c2}}{2} \qquad \text{V-6}$$

where ω_{c1}, ω_{c2}, $\omega_{\beta 1}$ and $\omega_{\beta 2}$ are defined by:

$$\omega_{c1} = \frac{eB_Z}{\gamma_1 mc} \qquad \omega_{c2} = \frac{eB_Z}{\gamma_2 mc}$$

$$\omega_{\beta 1}^2 = \frac{2ev_{Z1}I_{B1}}{\gamma_1 mc^2 a_1^2} \qquad \omega_{\beta 2}^2 = \frac{2ev_{Z2}I_{B2}}{\gamma_2 mc^2(a_2^2 - a_1^2)}$$

Equation V-4 has two possible solutions; those given in equations V-5 and V-6 represent the slower of the two frequencies, corresponding to motion along the helical field lines. The orbits are slightly separated from the field lines since $\vec{v} \times \vec{B}$ cannot be zero if the radial centrifugal force is to be balanced. The higher frequency solution which is obtained from equation V-4 is approximately equal to the gyrofrequency for the beam electrons.

The tangent of the pitch angle for the magnetic field lines in the two regions is given by the following.

$$\tan\psi = \frac{B_\theta(r)}{B_Z}$$

$$= \begin{cases} -\dfrac{\varepsilon_1 r}{a_1} & 0 \leq r \leq a_1 \\[2ex] -\dfrac{\varepsilon_1 a_1}{r} + \left(\dfrac{\varepsilon_2 a_2}{r} - \dfrac{\varepsilon_1 a_1}{r}\right)\left(\dfrac{a_1^2 - r^2}{a_2^2 - a_1^2}\right) & a_1 \leq r \leq a_2 \\[2ex] -\dfrac{\varepsilon_2 a_2}{r} & a_2 \leq r \leq R \end{cases} \qquad \text{V-7}$$

where $\varepsilon_1 = -\dfrac{B_\theta(a_1)}{B_Z} = \dfrac{2I_{B1}}{a_1 c B_Z}$

$$\varepsilon_2 = -\frac{B_\theta(a_2)}{B_Z} = \frac{2}{a_2 c B_Z} \quad (I_{B1} + I_{B2})$$

In the calculations to follow, ε_1 and ε_2 will be employed as ordering parameters for each region. If the larger of ε_1 and ε_2, i.e. $\varepsilon = \max(\varepsilon_1, \varepsilon_2)$ is assumed to be a small quantity, then a differential equation may be derived for the perturbed θ component of vector potential, δA_θ. The form assumed for the perturbations is $\delta A_\theta = \delta A_\theta(r) \exp[i(\tilde{m}\theta + kZ - \omega t)]$ where $\tilde{m} = \pm 1$, $k = n/R_0$, and $\mathrm{Im}(\omega) > 0$. The derivation of the following equation has been given by Lee[43] and will not be reproduced here.

$$\left(k^2 r - \frac{\omega^2 r}{v_A^2} + k\tilde{m} \tan\psi\right) \left[\frac{\delta A_\theta}{r} - \frac{1}{r}\frac{\partial}{\partial r} r \frac{\partial}{\partial r} r\, \delta A_\theta\right]$$

$$+ (\tilde{m}kr + \tan\psi)\left[\frac{\delta A_\theta \tan\psi}{r^2} - \frac{1}{r}\frac{\partial}{\partial r} r \frac{\partial}{\partial r} \tan\psi\, \delta A_\theta\right]$$

$$= \frac{4\pi}{c}\left(\delta J_{B\theta} - \delta J_{BZ} \tan\psi - i\tilde{m}\frac{\partial}{\partial r} r\, \delta J_{Br}\right) \equiv S \qquad \text{V-8}$$

Here v_A is the Alfvén velocity of the plasma. Since B_Z and ρ (plasma density) do not depend on r, neither does v_A.

As in Lee's model, the perpendicular displacement of the beam center of mass is described by a vector $\vec{Y}(z,t)$. The perturbed beam currents are then derived from $\vec{Y}$ by computing Eulerian derivatives of the beam velocity and density. The result is given below.

$$\vec{\delta J}_B = -en_B \frac{d\vec{Y}}{dt} + \vec{Y}\cdot\vec{\nabla}(en_B\vec{v}) \qquad \text{V-9}$$

The convective time derivative following the beam motion is employed for $\frac{d\vec{Y}}{dt}$, resulting in the following:

$$\frac{d\vec{Y}}{dt} = -i(\omega - kv_{Z1}) \simeq ikv_{Z1} \quad \text{(in region one)}$$

$$\text{V-10}$$

$$\frac{d\vec{Y}}{dt} = -i(\omega - kv_{Z2}) \simeq ikv_{Z2} \quad \text{(in region two)}$$

Here ω has been assumed low in comparison to kv_{Z1} and kv_{Z2}. Calculating perturbed beam currents for each region results in:

$$\vec{\delta J}_{B1} = -ien_{B_0}kv_{Z1}\, H(a_1-r)\vec{Y} - \vec{Y}\cdot\vec{\nabla}\,\vec{J}_{B1}$$

$$\text{V-11}$$

$$\vec{\delta J}_{B2} = -ien_{B_0}kv_{Z2}\, H\,(a_2-r)\vec{Y} - \vec{Y}\cdot\vec{\nabla}\,\vec{J}_{B2}$$

In order to satisfy the field equation V-8, the beam displacement (as was pointed out by Lee[43] must be of the form given below.

$$\vec{Y} = (\hat{e}_x + i\tilde{m}\,\hat{e}_y)Y \qquad Y=Y_0 \exp\,[i(kz-\omega t)] \qquad \text{V-12}$$

Combining equations V-8, V-9, and V-10 gives the following results for S_1, S_2, $\vec{\delta J}_{B1}$, $\vec{\delta J}_{B2}$.

$$\delta\vec{J}_{B1} = en_{B_0} Ye^{i\tilde{m}\theta} \Big\{ i(-kv_{Z1} + \tilde{m}\omega_1)\, H(a_1-r) + \hat{e}_\theta\, [H(a_1-r)\, (\tilde{m}kv_{Z1}-\omega_1) + \omega_1 a_1 \delta(r-a_1)] - v_{Z1}\, \hat{e}_Z\, \delta(r-a_1) \Big\} \qquad \text{V-13}$$

$$S_1 = -\frac{4\pi e n_{B_0}}{c}\, \delta(r-a_1) v_{Z_1}\, (\varepsilon_1 - \tilde{m}ka_1)\, Ye^{i\tilde{m}\theta} \qquad \text{V-14}$$

$$\delta\vec{J}_{B2} = en_{B_0}\, Ye^{i\tilde{m}\theta} \Big\{ i(\tilde{m}\omega_2 - kv_{Z2})\, [H(a_2-r) - H(a_1-r)] + \hat{e}_\theta \Big[\Big(\tilde{m}kv_{Z2} - \omega_2 - r\frac{d\omega_2}{dr}\Big) \Big(H(a_2-r) - H(a_1-r)\Big) + r\omega_2 \Big(\delta(r-a_2) - \delta(r-a_1)\Big)\Big] - v_{Z2}\, \hat{e}_Z\, [\delta(r-a_2) - \delta(r-a_1)] \Big\} \qquad \text{V-15}$$

$$S_2 = -\frac{4\pi e n_{B_0} v_{Z2}}{c} \Big[(k\tilde{m}a_1 - \varepsilon_1)\delta(r-a_1) - (k\tilde{m}a_2 - \varepsilon_2)\, \delta(r-a_2) \Big]\, Ye^{i\tilde{m}\theta} \qquad \text{V-16}$$

At this point it is necessary to evaluate Y in terms of δA_θ. For the two-region problem, it is convenient for later manipulations to evaluate Y in terms of either $\delta A_\theta(a_1)$ or $\delta A_\theta(a_2)$ alone. A relation of this form may be obtained by writing out equations of motion for each beam region separately. The equation of motion for region 1 is given below:

$$\pi a_1^2 n_{B_0} \gamma_1 m \frac{d^2\vec{Y}}{dt^2} = \frac{1}{c} \int_0^{a_1} r\,dr \int_0^{2\pi} d\theta\, [\delta\vec{J}_{B1} \times \vec{B} + \vec{J}_{B1} \times \delta\vec{B}]_\perp \qquad \text{V-17}$$

The equation of motion for region 2 is given by the following.

$$\pi(a_2^2 - a_1^2)\, n_{B_0} \gamma_2 m \frac{d^2\vec{Y}}{dt^2} = \frac{1}{c} \int_0^{R} r\,dr \int_0^{2\pi} d\theta\, [\delta\vec{J}_{B2} \times \vec{B} + \vec{J}_{B2} \times \delta\vec{B}]_\perp \qquad \text{V-18}$$

The portions of the force terms involving integrals over $\delta\vec{J}_{B1}$ and $\delta\vec{J}_{B2}$ may be evaluated in terms of Y using equations V-13 and V-15 and moved to the left-hand side. This leaves the $\delta\vec{B}$ term which may be written in terms of $\delta\vec{A}$. Performing the indicated integrations results in the equations given below.

$$Ye^{i\tilde{m}\theta} = \frac{ev_{Z1}}{\gamma_1 mca_1} \; \delta A_\theta(a_1) \; \frac{\tilde{m}ka_1-\varepsilon_1}{-k^2v^2_{Z1}-\omega_{c1}\tilde{m}kv_{Z1} + \omega^2_{\beta1}} \qquad \text{V-19}$$

and

$$Ye^{i\tilde{m}\theta} = \frac{ev_{Z2}}{\gamma_2 mc(a_2^2-a_1^2)} \quad (-k^2v_{Z2}^2 - \omega_{c2}\tilde{m}kv_{Z2} + \omega_{\beta2}^2)^{-1}$$

$$\times \; [a_2(\tilde{m}ka_2-\varepsilon_2) \; \delta A_\theta(a_2) - a_1(\tilde{m}ka_1-\varepsilon_1)\delta A_\theta(a_1)] \qquad \text{V-20}$$

Combining equations V-19 and V-20, an expression may be obtained for $Ye^{i\tilde{m}\theta}$ only in terms of $\delta A_\theta(a_2)$.

$$Ye^{i\tilde{m}\theta} = \frac{ev_{Z2}a_2}{\gamma_2 mc(a_2^2-a_1^2)} \quad \delta A_\theta(a_2) \quad \frac{(\tilde{m}ka_2 - \varepsilon_2)}{-k^2v_{Z2}^2(1+A_1)-\omega_{c2}\tilde{m}kv_{Z2}(1+A_2)+\omega_{\beta2}^2(1+A_3)} \qquad \text{V-21}$$

where $A_1 \equiv \dfrac{\gamma_1}{\gamma_2} \dfrac{I_{B1}}{I_{B2}}$

$A_2 \equiv \dfrac{a_1^2}{a_2^2 - a_1^2}$

$A_3 \equiv \dfrac{I_{B1}}{I_{B2}}$

Using equations V-18 and V-21, S_1 and S_2 may be written in the following form.

$$S_1 = \frac{2\omega_{\beta1}^2 \, (\varepsilon_1-\tilde{m}ka_1)^2\delta A_\theta(a_1)}{-k^2v_{Z1}^2-\omega_{C_1}\tilde{m}kv_{Z1}+\omega_{\beta_1}^2} \; \frac{\delta(r-a_1)}{a_1} \qquad \text{V-22}$$

$$S_2 = - \frac{2\omega_{\beta 1}^2 \frac{v_{Z2}}{v_{Z1}} (\varepsilon_1 - \tilde{m}ka_1)^2 \delta A_\theta(a_1)}{-k^2 v_{Z1}^2 - \omega_{C1}\tilde{m}kv_{Z1} + \omega_{\beta 1}^2} \; \frac{\delta(r-a_1)}{a_1}$$

$$+ \frac{2\omega_{\beta 2}^2 (\varepsilon_2 - \tilde{m}ka_2)^2 \delta A_\theta(a_2)}{-k^2 v_{Z2}^2(1+A_1) - \omega_{C2}\tilde{m}kv_{Z2}(1+A_2) + \omega_{\beta 2}^2(1+A_3)} \; \frac{a_2}{a_2^2 - a_1^2} \; \delta(r-a_2) \qquad \text{V-23}$$

Substituting S_1 and S_2 from equations V-22 and V-23 into the field equation V-8 then leads to the equation given below.

$$(k^2 r - \frac{\omega^2 r}{v_A^2} + k\tilde{m} \tan \psi) \left[\frac{\delta A_\theta}{r} - \frac{1}{r}\frac{\partial}{\partial r} r \frac{\partial}{\partial r} r\delta A_\theta\right]$$

$$+ \; (\tilde{m}kr + \tan \psi)\left[\frac{\delta A_\theta \tan\psi}{r^2} - \frac{1}{r}\frac{\partial}{\partial r} r \frac{\partial}{\partial r} \delta A_\theta \tan \psi\right] \qquad \text{V-24}$$

$$= \frac{2\omega_{\beta 1}^2 (1 - \frac{v_{Z2}}{v_{Z1}}) (\varepsilon_1 - \tilde{m}ka_1)^2 \delta A_\theta(a_1)}{-k^2 v_{Z1}^2 - k\omega_{C1}\tilde{m}v_{Z1} + \omega_{\beta 1}^2} \; \frac{\delta(r-a_1)}{a_1}$$

$$+ \frac{2\omega_{\beta 2}^2 (\varepsilon_2 - \tilde{m}ka_2)^2 \frac{a_2}{a_2^2 - a_1^2} \delta A_\theta(a_2)}{-k^2 v_{Z2}^2(1+A_1) - \omega_{C2}\tilde{m}kv_{Z2}(1+A_2) + \omega_{\beta 2}^2(1+A_3)} \; \delta(r-a_2)$$

Multiplying the above equation by $r\delta A_\theta^*$ and integrating over r from 0 to R results in the following real integral form for ω^2.

$$\frac{\omega^2}{v_A^2} \int_0^R rdr \left\{ |\delta A_\theta|^2 + |\frac{\partial}{\partial r} r \; \delta A_\theta|^2 \right\} = k^2 \int_0^R rdr |k\tilde{m}\delta A_\theta + \frac{\tan\psi}{r} \delta A_\theta|^2$$

$$+ \int_0^R r\,dr \left|k\tilde{m}\frac{\partial}{\partial r}(r\delta A_\theta) + \frac{\partial}{\partial r}\ (\delta A_\theta \tan\psi\right|^2$$

$$+ \frac{2\omega_{\beta 1}^2\ (1-v_{Z2}/v_{Z1})\ \ (\varepsilon_1-\tilde{m}ka_1)^2\ |\delta A_\theta(a_1)|^2}{k^2v_{Z1}^2 + \tilde{m}\omega_{C1}kv_{Z1} - \omega_{\beta 1}^2} \qquad \text{V-25}$$

$$+ \frac{2\omega_{\beta 2}^2\ \dfrac{a_2^2}{a_2^2-a_1^2}\ (\varepsilon_2-\tilde{m}ka_2)^2\ |\delta A_\theta(a_2)|^2}{k^2v_{Z2}^2(1+A_1)+\tilde{m}\omega_{C2}kv_{Z2}(1+A_2)-\omega_{\beta 2}^2(1+A_3)}$$

It may be noted that all terms in equation V-25 are positive-definite except for the last two. A sufficient condition for stability may then be obtained by requiring both of these to be greater than zero. For the first of the two terms, the condition given below results.

$$k^2v_{Z1}^2 + \tilde{m}\omega_{C1}kv_{Z1} - \omega_{\beta 1}^2 < 0 \qquad \text{V-26}$$

$$(\text{for } v_{Z2} > v_{Z1})$$

$$k^2v_{Z1}^2 + \tilde{m}\omega_{C1}kv_{Z1} - \omega_{\beta 1}^2 > 0 \qquad \text{V-27}$$

$$(\text{for } v_{Z1} > v_{Z2})$$

Requiring the last of the two terms to be positive gives the following condition.

$$k^2v_{Z2}^2(1 + A_1) + \tilde{m}\omega_{C2}kv_{Z2}(1 + A_2) - \omega_{\beta 2}^2(1 + A_3) > 0 \qquad \text{V-28}$$

In examining the implications of the above stability conditions, it is convenient to write them in terms of the value of the safety factor, q, at the positions $r = a_1$ and a_2.

$$q(a_1) = \frac{a_1 B_Z}{R_0 B_\theta(a_1)} = \frac{k\omega_{C1} v_{Z1}}{\omega_{\beta 1}^2} \qquad \text{V-29}$$

$$q(a_2) = \frac{a_2 B_Z}{R_0 B_\theta(a_2)} = \frac{k\omega_{C2} v_{Z2}}{\omega_{\beta 2}^2 (1+A_3)} \quad (A_2 + 1)$$

Here R_0 = torus major radius and it has been assumed that $k = {}^1/R_0$ for the $\tilde{m} = \pm 1$, $n = 1$ kink mode. Equations V-26 to V-28 thus become the following.

$$\alpha_1 + \tilde{m}\, q(a_1) - 1 < 0 \qquad \text{V-30}$$

$$(\text{for } v_{Z2} > v_{Z1})$$

$$\alpha_1 + \tilde{m}\, q(a_1) - 1 > 0 \qquad \text{V-31}$$

$$(\text{for } v_{Z1} > v_{Z2})$$

$$\alpha_2 (1 + A_1)\,(1 + A_3)^{-1} + \tilde{m}\, q(a_2) - 1 > 0 \qquad \text{V-32}$$

$$(\text{in both cases})$$

Here α_1 and α_2 are small quantities as given below.

$$\alpha_1 = \frac{\gamma_1 mc^2}{2\pi R_0^2 e^2 n_b} = \frac{I_{A1}}{2I_{B1}} \; \frac{a_1^2}{R_0^2}$$

$$\text{V-33}$$

$$\alpha_2 = \frac{\gamma_2 mc^2}{2\pi R_0^2 e^2 n_b} = \frac{I_{A2}}{2I_{B2}} \; \frac{(a_2^2 - a_1^2)}{R_0^2}$$

where

$$I_{A1} = \frac{m_0 c^3}{e} \; \gamma_1 \left(\frac{v_{Z1}}{c}\right) = \text{Alfvén current for region 1}$$

$$I_{A2} = \frac{m_0 c^3}{e} \; \gamma_2 \left(\frac{v_{Z2}}{c}\right) = \text{Alfvén current for region 2}$$

$q(a_1)$ may be related to $q(a_2)$, the q-value at the outside of the beam by the following.

$$\frac{q(a_1)}{q(a_2)} = \frac{a_1^2}{a_2^2} \frac{I_{B2}}{I_{B1}} \frac{A_2}{A_3(A_2 + 1)} \qquad \text{V-34}$$

Using the above relation and choosing $\tilde{m} = 1$, the sufficient stability conditions given in equations V-30 to V-32 may be written in terms of $q(a_2)$ as follows.

$$q(a_2) < \frac{(A_2+1)A_3}{A_2} (1 - \alpha_1) \qquad (\text{for } v_{Z2} > v_{Z1}) \qquad \text{V-35}$$

$$q(a_2) > \frac{(A_2+1)A_3}{A_2} (1 - \alpha_1) \qquad (\text{for } v_{Z1} > v_{Z2}) \qquad \text{V-36}$$

$$q(a_2) > 1 - \alpha_2 \frac{(1 + A_1)}{(1 + A_3)} \qquad (\text{in both cases}) \qquad \text{V-37}$$

The above equations indicate that for $v_{Z2} > v_{Z1}$ there will be a window of stability near $q = 1$ whereas for $v_{Z1} > v_{Z2}$ there is a lower limit on $q(a_2)$ for which stability is present. These sufficient stability conditions may be summarized in the following two inequalities.

$$1 - \alpha_2\left(1 + \frac{\gamma_1}{\gamma_2} \frac{v_{Z1}}{v_{Z2}} A_2\right) \left(1 + \frac{v_{Z1}}{v_{Z2}} A_2\right)^{-1} < q\,(a_2)$$

$$< (A_2 + 1)(1 - \alpha_1) \frac{v_{Z1}}{v_{Z2}} \qquad \text{V-38}$$

$$(\text{for } v_{Z2} > v_{Z1})$$

$$q(a_2) > \text{Max} \left\{ (A_2 + 1)(1 - \alpha_1) \frac{v_{Z1}}{v_{Z2}}, \; 1 - \alpha_2 \left(1 + \frac{\gamma_1}{\gamma_2} \frac{v_{Z1}}{v_{Z2}} A_2\right) \left(1 + \frac{v_{Z1}}{v_{Z2}} A_2\right)^{-1} \right\} \qquad \text{V-39}$$

$$(\text{for } v_{Z1} > v_{Z2})$$

For example, if $a_1 = 0.5\, a_2$, $\gamma_1 = 3$, $\gamma_2 = 9$, then a sufficient condition for stability is the following.

$$1 - 2.52\, \alpha_1 < q(a_2) < 1.27\, (1 - \alpha_1) \qquad \text{V-40}$$

whereas for $\gamma_1 = 9$, $\gamma_2 = 3$ the sufficient condition is $q(a_2) > 1.27$ $(1 - \alpha_1)$ which is equivalent to $q(a_1) > 1 - \alpha_1$ (using equation V-34). Since the parameter α_1 is small, except for high beam energies, the above example does not indicate any substantial region of stability for $q(a_2) < 1$.

A somewhat stronger sufficient condition for stability will now be derived from equation V-25. This is obtained by employing equations V-19 and V-20 to combine the last two terms of V-25. Equating V-19 and V-20 leads to the following relation.

$$\frac{\delta A_\theta(a_2)}{\delta A_\theta(a_1)} = \left(\frac{\tilde{m}ka_1-\varepsilon_1}{\tilde{m}ka_2-\varepsilon_2}\right) \left[\frac{\gamma_2(a_2^2 - a_1^2)}{a_2 v_{Z2}}\right] \left[\frac{v_{Z1}}{\gamma_1 a_1}\, \frac{k^2 v_{Z2}^2 + \tilde{m}\omega_{C2} k v_{Z2} - \omega_{\beta 2}^2}{k^2 v_{Z1}^2 + \tilde{m}\omega_{C1} k v_{Z1} - \omega_{\beta 1}^2} + \frac{a_1 v_{Z2}}{\gamma_2(a_2^2 - a_1^2)}\right] \qquad \text{V-41}$$

The last two terms of equation V-25 are given below.

$$2\, \left|\delta A_\theta(a_1)\right|^2 \left\{ \frac{\omega_{\beta 1}^2 \left(1 - \frac{v_{Z1}}{v_{Z2}}\right) (\varepsilon_1 - \tilde{m}ka_1)^2}{k^2 v_{Z1}^2 + \tilde{m}\omega_{C1} k v_{Z1} - \omega_{\beta 1}^2} \right.$$

$$\left. \frac{\frac{a_2^2}{a_2^2 - a_1^2}\, \omega_{\beta 2}^2\, (\varepsilon_2 - \tilde{m}ka_2)^2}{k^2 v_{Z2}^2\, (1+A_1) + \tilde{m}\omega_{C2} k v_{Z2} (1+A_2) - \omega_{\beta 2}^2 (1+A_3)} \left|\frac{\delta A_\theta(a_2)}{\delta A_\theta(a_1)}\right|^2 \right\} \qquad \text{V-42}$$

Substituting equation V-41 into V-42 and requiring the latter to be greater than zero as a sufficient condition for stability, leads to the following inequality.

$$\frac{\omega_{\beta 1}^2\left(1-\frac{v_{Z2}}{v_{Z1}}\right)}{k^2v_{Z1}^2+\tilde{m}\omega_{C1}kv_{Z1}-\omega_{\beta 1}^2}+\frac{\omega_{\beta 2}^2\left(\frac{a_2^2}{a_1^2}-1\right)}{k^2v_{Z2}^2(1+A_1)+\tilde{m}\omega_{C2}kv_{Z2}(1+A_2)-\omega_{\beta 2}^2(1+A_3)}$$

$$\times\left[\frac{\gamma_2}{\gamma_1}\;\frac{v_{Z1}}{v_{Z2}}\;\frac{k^2v_{Z2}^2+\tilde{m}\omega_{C2}kv_{Z2}-\omega_{\beta 2}^2}{k^2v_{Z1}^2+\tilde{m}\omega_{C1}kv_{Z1}-\omega_{\beta 1}^2}+\frac{a_1^2}{a_2^2-a_1^2}\right]^2>0 \qquad \text{V-43}$$

Writing V-43 in terms of $q(a_2)$, A_1, A_2, A_3 results in the stability criterion given below.

$$A_2\left(1-\frac{v_{Z2}}{v_{Z1}}\right)\left[\alpha_1+\tilde{m}\,q(a_2)-1\right]^2\left[\alpha_2(1+A_1)+\tilde{m}(1+A_3)q(a_2)-1-A_3\right]$$

$$+\left[\alpha_1+\tilde{m}\delta q(a_2)-1\right]\left\{A_2(\alpha_1-1)+\frac{v_{Z2}}{v_{Z1}}\left[(\alpha_2-1)+\tilde{m}q(a_2)\right]\right\}^2>0 \qquad \text{V-44}$$

where $\delta \equiv \dfrac{A_2}{A_3(A_2+1)}$

The above equation is cubic in $q(a_2)$ and for given values of v_{Z2}/v_{Z1}, γ_1/γ_2, a_1/a_2, α_1 and α_2, determines regions along the $q(a_2)$ axis where stability exists. Since other choices of these parameters may also cause the right-hand side of equation V-25 to be positive, this result is sufficient for stability, but not necessary.

It may also be noted that the above analysis results only in marginal conditions for stability and does not give information about growth rates near the instability thresholds. These will be treated in detail in Section V.2 .

A dispersion relation may be derived by solving the field equation V-25 in the regions $0 < r < a_1$, $a_1 < r < a_2$, and $a_2 < r < R$. Jump conditions on $\frac{\partial}{\partial r} \delta A_\theta$ are obtained by integrating equation V-25 from $a_1 - \varepsilon$ to $a_1 + \varepsilon$ and from $a_2 - \varepsilon$ to $a_2 + \varepsilon$; conducting shell boundary conditions are then assumed at $r=R$. Substituting the solutions of the field equation V-25 into the jump and boundary conditions and assuming the continuity of $\delta A_\theta(r)$ at a_1 and a_2 results in a dispersion relation. This is derived in Appendix A.

In conclusion, a stability analysis has been performed for kink modes in a two region, sheared velocity and energy relativistic beam. The method used is similar to that employed by Lee[43]. The result is several sufficient conditions for stability; when evaluated for parameters thought to be typical of the strong runaway regime in tokamaks, these indicate only a slight change from the usual $q > 1$ limitation.

V.2 Kinetic Beam-Plasma m=1,2,3,4, n=-1 Alfvén Wave Instabilities

A number of the assumptions made in the cold fluid plasma, mono-energetic beam analysis of Section V.1 will now be relaxed. An attempt is made here to further clarify the properties of the unstable kink modes and to explore the validity of the fluid plasma - rigid beam models by employing a more kinetic approach. A cylindrical beam-plasma configuration is assumed and radial velocity shear will not be treated in the present analysis; density profiles for beam and plasma will be taken as flat for simplicity.

Specifically, the new effects treated in this section include: influence of perturbed electric fields on the beam, longitudinal dynamics of the beam electrons, generalization of the background plasma model to include frequencies which are not small relative to the ion gyrofrequency, beam energy spread, and toroidal curvature drifts. Also, since the beam is treated kinetically, beam perturbations are taken into account by examining the perturbed particle orbits instead of using the macroscopic displacement vector which was utilized in the preceding section; thus, some degree of beam distortion is allowed.

Perturbed electric field forces are included in the analysis described in this section in order to examine the effect of the two mass approximation to relativistic particle dynamics.

$$\frac{d}{dt}(\gamma m_0\vec{v}) \simeq \gamma m_0 \frac{d\vec{v}_\perp}{dt} + \gamma^3 m_0 \frac{d\vec{v}_\parallel}{dt} \qquad \text{V-45}$$

Interest in this characteristic is based on an examination of the theoretical and experimental literature[87-90] on macroscopic modes in straight relativistic beams without external magnetic fields. As was mentioned earlier, the relative stiffness of beam electrons against acceleration along the propagation direction (due to the fact that their velocity cannot exceed the speed of light) may act to inhibit build-up of the axial perturbed currents necessary for a kinking of the beam to develop. If such an effect were of importance in strong runaway discharges, it could act to limit the growth rates of instabilities to magnetic skin diffusion times which are potentially much slower than the Alfvén transit time for high temperature plasmas. However, as will be discussed later, such an effect is found to be relatively unimportant, at least in the fixed boundary, high conductivity model (for which calculations have been done). This is due to the fact that the component of perturbed electric field along the beam propagation direction is much less than the transverse components. For a highly conductive plasma, the magnetic field is frozen in and ions are drawn into the kink motion; thus, the effect of the electron dynamics is negligible due to the small ratio of the electron to ion mass. It is only when resistivity is present that the freezing of the field is disrupted and the longitudinal beam electron dynamics are expected to become important.

The extension of the plasma model to include frequencies which are not small relative to the ion gyrofrequency is motivated by the following fact. The basic bounce or drift frequency of a relativistic electron ($\omega_{br} \simeq c/R_0 q$) around the poloidal direction is of the same order as the ion gyrofrequency for parameters characteristic of present-day tokamaks. Since MHD instability modes normally grow on much longer time scales than the ion gyroperiod, the presence of a high energy electron component which transits around flux surfaces on a much faster time scale can act to partially short out such instabilities. This is similar to the effect identified by Guest, et al.[91] for ballooning modes in high beta plasmas in the presence of hot electrons. Specifically, in terms of the following analysis, the above considerations require keeping terms in the plasma dielectric of at least order $(\omega^2-\omega_{ci}^2)^{-1}$ and retaining ω in comparison to $k_\parallel v_\parallel$ in the beam terms.

It will be recalled that in Lee's analysis[43] and in Section V.1,

ω was neglected relative to $k_{\parallel}v_{\parallel}$*. The calculations to follow indicate that over certain ranges of q this is not a necessarily valid assumption. Retaining this term in the beam perturbed currents results in complex eigenfrequencies, whereas without it only a pure real or pure imaginary spectrum is obtained. Physically, the reason for the complex eigenfrequency is due to the fact that the instability analysis is made from the lab frame; as the beam goes unstable to kinks, its relative motion results in an apparent oscillation superimposed on the exponential growth. Since the complex eigenvalues prevent use of an energy principle, a normal mode approach is taken.

As was pointed out by Lee[43], the instability criterion for toroidal relativistic beams against $\tilde{m} = \pm 1$, $n = 1$ modes is related to the closure of beam particle orbits as opposed to the more restrictive criterion of closure of field lines. Such a consideration has motivated the treatment of beam energy and toroidal curvature drifts. Finite thermal spread in the beam energy results in a broadening of the closed particle resonance condition and leads to an effect analogous to Landau damping. Toroidal curvature drifts were examined in some detail in Chapter III; they act to separate drift orbits away from flux surfaces and lead to a slightly longer transit time for beam electrons around the torus than would be the case if these drifts were not present. The condition of closed particle orbits thus would be expected to occur at slightly lower values of q than would be the case in a cylindrical model.

---

* ω was assumed to be of order v_A/R_0 while $k_{\parallel}v_{\parallel}$ is of order c/R_0.

V.2.A. Physical Model, Particle Orbits, and Field Equations

In the following analysis, the model assumed is that of a cylindrical relativistic electron beam immersed in a cold background plasma and surrounded by a conducting wall. A constant magnetic field is applied along the axis of the cylinder; the beam and plasma are assumed not to significantly modify this magnetic field, i.e. there is no net diamagnetism or paramagnetism. The effect of toroidicity is introduced by periodic boundary conditions on the perturbed fields. Helical perturbations of the form $\exp[i(m\theta + n\zeta - \omega t)]$, $\zeta = z/R_0$ (n,m are integers) are considered. The use of a cold plasma model is justified due to the long perpendicular wavelength of the kink instabilities. This is of the order of the plasma minor radius whereas electron and ion Larmor radii are, at most, a few millimeters. Thus, $k_\perp \rho_i$ and $k_\perp \rho_e << 1$ and finite Larmor radius corrections for the background plasma are negligible.

Since a uniform axial current density is assumed, B_θ and q are given by the following.

$$B_\theta(r) = \frac{4\pi}{cr} \int_0^r J(r)\, r dr = \begin{cases} 2Ir/ca^2 & 0 < r < a \\ 2I/cr & r > a \end{cases} \qquad \text{V-46}$$

$$q(r) = \frac{rB_Z}{R_0 B_\theta} = \begin{cases} q(a) & 0 < r < a \\ r^2 B_Z c/2R_0 I & r > a \end{cases} \qquad \text{V-47}$$

a = radius of current channel

In Cartesian coordinates B_θ may be expressed as given below.

$$B_x = -\frac{yB_Z}{qR_0} \qquad B_y = \frac{xB_Z}{qR_0} \qquad \text{V-48}$$

The unperturbed relativistic orbits are then given by the components of the force equation.

$$\frac{d}{dt}(\gamma v_x) = \Omega_e v_y - \frac{\Omega_e x}{qR_0} v_Z$$

$$\frac{d}{dt}(\gamma v_y) = -\Omega_e v_x - \frac{\Omega_e y}{qR_0} v_Z \qquad \text{V-49}$$

$$\frac{d}{dt}(\gamma v_Z) = \frac{\Omega_e}{qR_0}(x v_x + y v_y) \simeq 0$$

where $\Omega_e \equiv \frac{eB_Z}{m_0 c}$

Since no unperturbed electric field is present, γ = constant. Defining $v^{\pm} = v_x \pm iv_y$, $x^{\pm} = x \pm iy$ and assuming $x^{\pm} = x_{\perp} e^{\pm i\omega t}$ one obtains from V-49 the following equation for ω.

$$\gamma\omega^2 - \Omega_e\omega - \frac{\Omega_e v_Z}{qR_0} = 0 \qquad \text{V-50}$$

which has the two roots:

$$\omega_+ = \frac{\Omega_e}{2\gamma}\left[1 + \sqrt{1 + 4v_Z\gamma/qR_0\Omega_e}\,\right] \simeq \frac{\Omega_e}{\gamma}$$

$$\omega_- = \frac{\Omega_e}{2\gamma}\left[1 - \sqrt{1 + 4v_Z\gamma/qR_0\Omega_e}\,\right] \simeq -\omega_{br}\left(1 - \frac{2\gamma\omega_{br}}{\Omega_e}\right) \qquad \text{V-51}$$

where $\omega_{br} = \frac{v_Z}{qR_0}$ = transit or bounce frequency

ω_+ and ω_- are approximately the gyrofrequency of a relativistic electron and the frequency corresponding to motion along the field lines, respectively. The functional dependence of $v^{\pm}$ will now be explicitly calculated; this is necessary for the Vlasov beam model of

Subsection V.2.B. The guiding center motion is separated out as is indicated in Fig. V-2 and in the following equations.

$$\vec{\xi} = \vec{x} + \frac{\vec{v} \times \vec{\Omega}}{\Omega^2}\,\gamma = \vec{x} + (\vec{v} \times \hat{b})/\omega_+ \qquad \text{V-52}$$

here $\vec{\xi}$ = position of the orbit guiding center. The Cartesian components of $\vec{\xi}$ are given below.

$$\begin{aligned} \xi_x &= x + v_y/\omega_+ \\ \xi_y &= y - v_x/\omega_+ \end{aligned} \qquad \text{V-53}$$

Taking time derivatives of ξ_x and ξ_y results in the following equations.

$$\begin{aligned} \frac{d\xi_x}{dt} &= v_x + \frac{1}{\omega_+\gamma}\left[-\Omega_e v_x - \frac{\Omega_e y}{qR_0}\, v_Z\right] \\ \frac{d\xi_y}{dt} &= v_y - \frac{1}{\omega_+\gamma}\left[\Omega_e v_y - \frac{\Omega_e x}{qR_0}\, v_Z\right] \end{aligned} \qquad \text{V-54}$$

Substituting equation V-53 into V-54 one obtains:

$$\begin{aligned} \frac{d\xi_x}{dt} &= v_x\left(1 - \frac{\Omega_e}{\omega_+\gamma}\right) - \frac{\Omega_e v_Z}{\omega_+\gamma q R_0}\left(\xi_y + \frac{v_x}{\omega_+}\right) \\ \frac{d\xi_y}{dt} &= v_y\left(1 - \frac{\Omega_e}{\omega_+\gamma}\right) + \frac{\Omega_e v_Z}{\omega_+\gamma q R_0}\left(\xi_x - \frac{v_y}{\omega_+}\right) \end{aligned} \qquad \text{V-55}$$

Employing equation V-50 and combining the two above equations results in the following equation for $\xi^{\pm} = \xi_x \pm i\,\xi_y$

$$\frac{d\xi^{\pm}}{dt} = \pm\frac{i\Omega_e v_Z}{\omega_+\gamma q R_0}\,\xi^{\pm} \simeq \mp i\omega_-\xi^{\pm}$$

$$\therefore \xi^{\pm} = \xi_{\perp} e^{\pm i(\phi - \omega t)} \qquad \text{V-56}$$

ORNL DWG. 75-13727

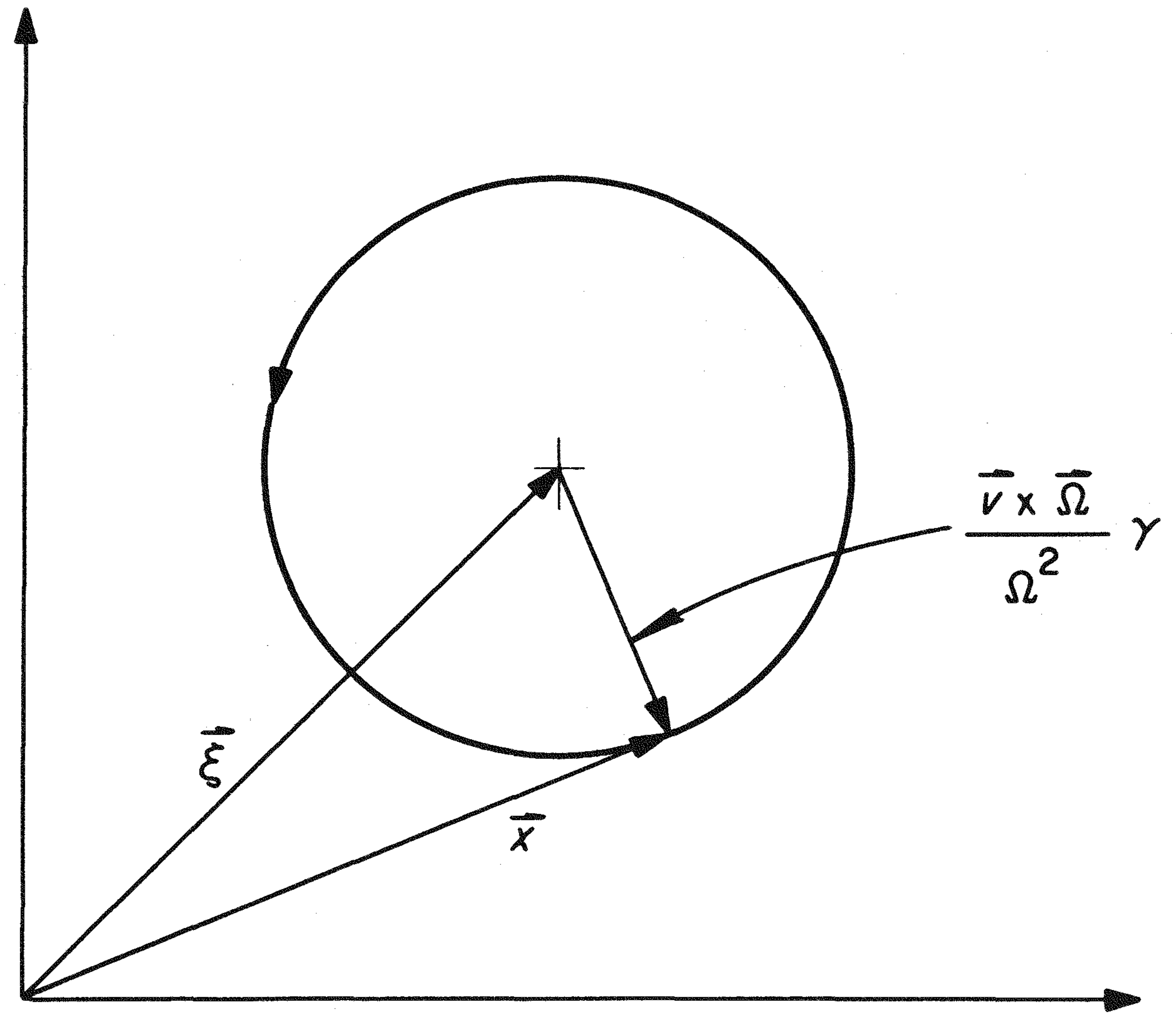

FIGURE V-2

Guiding Center and Gyromotion for a Relativistic Electron in a Magnetic Field.

where ϕ = an arbitrary phase factor

The transverse equations of motion (V-49) may now be written in the following manner.

$$\frac{d}{dt}(\gamma v_x) = \Omega_e v_y - \frac{\Omega_e v_Z}{qR_0}(\xi_x - v_y/\omega_+)$$

$$\frac{d}{dt}(\gamma v_y) = -\Omega_e v_x - \frac{\Omega_e v_Z}{qR_0}(\xi_y + v_x/\omega_+) \qquad \text{V-57}$$

From equations V-50 and V-51 two useful identities given below are obtained.

$$\Omega_e \omega_+ + \frac{\Omega_e v_Z}{qR_0} = \gamma \omega_+^{\,2}$$

$$\omega_+ \omega_- = -\Omega_e v_Z/\gamma q R_0 \qquad \text{V-58}$$

Using the above, equations V-57 may be combined.

$$\frac{dv^{\pm}}{dt} = \mp i\omega_+ v^{\pm} + \omega_- \omega_+ \xi^{\pm} \qquad \text{V-59}$$

Substituting equation V-56 for $\xi^{\pm}$ into V-59, the following solution is obtained for $v^{\pm}$.

$$v^{\pm} = v_{\perp} e^{\pm i(\psi - \omega_+ t)} \mp \frac{i\omega_- \omega_+ \xi_{\perp} e^{i\phi}}{\omega_+ - \omega_-}\left[e^{\mp i\omega_- t} - e^{\mp i\omega_+ t}\right] \qquad \text{V-60}$$

Equation V-60 has components corresponding both to the gyromotion (at ω_+) and the motion along field lines (at ω_-). The energy dependence of ω_- will be of importance in the Vlasov treatment; ω_- is dependent on γ since the finite mass of the electrons causes them to lag the field lines slightly. As was mentioned in Section V.1, this is necessary in order for the $\vec{v} \times \vec{B}$ force to exactly balance the centrifugal force associated with the helical motion of the electrons. A spreading out in the energy distribution of the relativistic electrons is related to a spreading out in the position of the particle orbits away from field lines.

For perturbed fields with the dependence $\exp[i(m\theta + n\zeta - \omega t)]$, the components of the curl $\vec{E}$ and curl $\vec{B}$ equations result in the following six equations:

$$\frac{1}{\rho}\frac{\partial}{\partial\rho}(\rho E_\theta) - \frac{im}{\rho}E_r = i\,B_z \qquad \text{V-61}$$

$$\frac{m}{\rho}E_z - n_\parallel E_\theta = B_r \qquad \text{V-62}$$

$$n_\parallel E_r + i\frac{\partial E_z}{\partial\rho} = B_\theta \qquad \text{V-63}$$

$$\frac{i}{\rho}\frac{\partial}{\partial\rho}(\rho B_\theta) + \frac{m}{\rho}B_r = E_z + \frac{4\pi i J_z}{\omega} \qquad \text{V-64}$$

$$-\frac{m}{\rho}B_z + n_\parallel B_\theta = E_r + \frac{4\pi i J_r}{\omega} \qquad \text{V-65}$$

$$-n_\parallel B_r - i\frac{\partial B_z}{\partial\rho} = E_\theta + \frac{4\pi i J_\theta}{\omega} \qquad \text{V-66}$$

here $\rho = \frac{r\omega}{c}$ and $n_\parallel = \frac{nc}{R_0\omega}$.

In the instability analysis to follow, these six equations will be combined in the following manner. B_r and B_θ from V-62 and V-63 will be substituted into V-65 and V-66 to obtain equations for E_r and E_θ in terms of E_z, B_z, J_r and J_θ. These are then substituted into equations V-61 and V-64 resulting in two differential equations for the perturbed longitudinal fields E_z and B_z:

$$\nabla_\perp^2 B_z + (1 - n_\parallel^2)B_z = \frac{4\pi}{\omega\rho}\left[i\omega J_r - \frac{\partial}{\partial\rho}(\rho J_\theta)\right] \qquad \text{V-67}$$

$$\nabla_\perp^2 E_z + (1 - n_\parallel^2)E_z = -\frac{4\pi i}{\omega}\left\{(1 - n_\parallel^2)J_z + \frac{n_\parallel}{\rho}\left[i\frac{\partial}{\partial\rho}(\rho J_r) - mJ_\theta\right]\right\} \qquad \text{V-68}$$

$$\text{where } \nabla_\perp^2(\ \ ) \equiv \frac{1}{\rho}\frac{\partial}{\partial\rho}\,\rho\,\frac{\partial(\ )}{\partial\rho} - \frac{m^2}{\rho^2}(\ \ )$$

The remaining task is to determine the perturbed currents $\delta\vec{J}$ in terms of the perturbed fields E_z and B_z; this will be worked out in Subsection V.2.B. Since $\delta\vec{J}$ will, in general, depend on both longitudinal and transverse components of $\vec{E}$ and $\vec{B}$, it is necessary to use equations V-62, V-63, V-65 and V-66 to express $\delta\vec{J}$ in terms of E_z and B_z. Once J_r and J_θ are specified, the transverse electric fields are obtained (in terms of E_z and B_z) by solving the equations given below.

$$\frac{4\pi i}{\omega}J_r + (1 - n_\parallel^2)E_r = -\frac{m}{\rho}B_z + in_\parallel\frac{\partial E_z}{\partial\rho} \qquad \text{V-69}$$

$$\frac{4\pi i}{\omega}J_\theta + (1 - n_\parallel^2)E_\theta = -\frac{mn_\parallel}{\rho}E_z - i\frac{\partial B_z}{\partial\rho} \qquad \text{V-70}$$

When $\vec{J} = 0$ (no plasma or beam), the above equations (V-67 to V-70) reduce to the usual waveguide TM and TE equations as are given, for example, in ref.93. Once two coupled eigenmode equations are obtained for E_z and B_z from equations V-67 and V-68, solution and application of appropriate boundary conditions results in a dispersion relation. This will be done in Subsection V.2.D for fixed boundary and free boundary models.

The kink instability treatments of Lee[43] and Lovelace[44] ignore the coupling between equations V-67 and V-68. Lovelace assumes $\delta\vec{E}\cdot\vec{B}=0$

whereas Lee neglects all perturbed electric fields. These approximations are based on the assumption of a highly conducting plasma and result in consideration only of equation V-67 (or its equivalent in terms of the vector potential δA_θ) with J_r and J_θ expressed in terms of δB_z (or δA_θ). In contrast, in the work which has been done on hose instabilities[87-90] (where the equilibrium B_z field is zero) only equation V-68 is typically considered and V-67 is neglected.

V.2.B. Perturbed Currents

1. Background Plasma

The dynamics of the electrons and ions in the background plasma described by the following force equations.

$$\frac{dv^{\pm}_{e,i}}{dt} = \mp i\Omega_{e,i} v^{\pm}_{e,i} - \frac{v_{ze,i}\Omega_{e,i}x^{\pm}_{e,i}}{qR_0} + \frac{e}{m_{e,i}} E^{\pm} \qquad \text{V-71}$$

$$\frac{dv_{ze,i}}{dt} = \frac{\Omega_{e,i}}{qR_0} \frac{d}{dt}\left(\frac{r^2}{2}\right) + \frac{e}{m_{e,i}} E_z \qquad \text{V-72}$$

In similarity with the analysis of Subsection V.2.A., the orbits are given below.

$$v^{\pm}_{e,i} = v_{\perp} e^{\pm i(\psi-\omega_+ t)} \mp \frac{i\omega_+\omega_-}{\omega_+ + \omega_-} \xi_{\perp} e^{\pm i\theta_0} \left[e^{\mp i\omega_- t} - e^{\mp i\omega_+ t}\right] \qquad \text{V-73}$$

$$v_{z_{e,i}} = \frac{\Omega_{e,i} r^2}{2qR_0} + v_{\parallel} \qquad \text{V-74}$$

where $v_{\parallel}$, $v_{\perp}$, θ_0, $\xi_{\perp}$ = initial conditions on orbits

ω_+ and ω_- are the nonrelativistic analogues of the frequencies defined in equation V-51. Since the analysis here is for a cylinder with a constant magnetic field, it will not include certain effects which occur in a toroidal geometry with time scales of order $(\omega_-)^{-1}$. These include trapping of electrons and ions in orbits which mirror on the high field side of the cross section. As a first approximation, all of these effects will be ignored as being important for kilocycle frequencies, but not for megacycle frequencies near the Alfvén transit frequency. The guiding center for the above orbits is defined by:

$$\xi_x = x + \frac{v_y}{\omega_+} \qquad \xi_y = y - \frac{v_x}{\omega_+} \qquad \text{V-75}$$

and has the time dependence $\xi^{\pm} = \xi_{\perp} e^{\pm i(\theta_0 - \omega_- t)}$.

Given the above unperturbed orbits, one may calculate perturbed velocities by retaining the perturbed electric field terms in equations V-71 and V-72. The following dependence has been assumed for the perturbed fields.

$$\vec{E} = \vec{\varepsilon}(r)\ \exp[i(m\theta + nz/R_0 - \omega t)] \qquad \text{V-76}$$

$$E^{\pm} = E_x \pm iE_y$$

$$= [\varepsilon_r(r) \pm i\varepsilon_\theta(r)]\exp i[(m \pm 1)\theta + nz/R_0 - \omega t]$$

Since only the long wavelength modes are of interest in this analysis, it is assumed that $\varepsilon_r(r)$ and $\varepsilon_\theta(r)$ are slowly varying functions of r,i.e.

$$\frac{1}{\varepsilon_\theta}\frac{d\varepsilon_\theta}{dr},\ \frac{1}{\varepsilon_r}\frac{d\varepsilon_r}{dr} \ll \frac{\Omega_{e,i}}{\sqrt{T_{e,i}/m_{e,i}}}\ .$$

For frequencies in the megacycle range, the above ordering implies that r and θ are essentially constant from the frame of reference of the nonrelativistic electrons and ions. Another way of viewing this is that if a snapshot is taken of the plasma particles over the time scale of the instability, only the gyromotion would be seen. Both electrons and ions would appear stationary with respect to their movement around the minor cross-section.

For these reasons, the perturbed plasma currents will be taken as simply those for a uniform infinite magnetic field.

$$4\pi J_{e,i}^{\pm} = \frac{i\omega_{pe,i}^{2} E^{\pm}}{\omega \mp \Omega_{e,i}}$$

$$4\pi J_{z_{e,i}} = -\frac{i\omega_{pe,i}^{2} E_{z}}{\omega} \qquad \text{V-77}$$

In the case of electrons ω will be neglected in comparison with Ω_e. For a resistive background plasma model the only change in the above is in the perturbed electron current along the longitudinal direction.

$$4\pi J_z\Big|_{\text{electron}} = \frac{i\omega_{pe}^{2} E_z}{\omega + i\nu_{ee}} \qquad \text{V-78}$$

$$\text{where } \nu_{ee} = \frac{4\pi e^4 n_e \ln\Lambda}{(2m_e)^{1/2}(k\,T_e)^{3/2}}$$

The transverse ion and electron currents are not affected here since the appropriate collision frequencies are much lower than $\Omega_{e,i}$. In fact, for temperatures typical of tokamaks, ν_{ee} will be generally a good deal less than ω unless a large fraction of impurities are present.

V.2.B.2 Relativistic Beam Perturbed Currents - Fluid Approach

The starting point for calculating the perturbed beam currents is the relativistic force equation; the Cartesian components of this equation are given as follows:

$$\frac{d}{dt}(\gamma v_x) = \Omega_e v_y - \frac{\Omega_e v_z x}{qR_0} - \frac{e}{m_0}(E_x + \frac{v_y B_z}{c} - \frac{v_z B_y}{c})$$

$$\frac{d}{dt}(\gamma v_y) = -\Omega_e v_x - \frac{\Omega_e v_z y}{qR_0} - \frac{e}{m_0}(E_y + \frac{v_z B_x}{c} - \frac{v_x B_z}{c}) \qquad \text{V-79}$$

$$\frac{d}{dt}(\gamma v_z) = -\frac{\Omega_e}{qR_0}(xv_x + yv_y) - \frac{e}{m_0}(E_z + \frac{v_x B_y}{c} - \frac{v_y B_x}{c})$$

Here the fields E_x, B_x, ... are perturbed fields; the equilibrium fields are contained in Ω_e and q. In the following analysis, the terms arising from transverse beam velocities crossed into longitudinal and transverse perturbed B fields will be neglected. These terms are expected to be of order $(qA)^{-1}$ as compared with the terms arising from the longitudinal velocities (near the speed of light) crossed into the transverse perturbed B fields. The validity of this assumption has been justified by examining the size of the perturbed fields at roots of the dispersion relation.

In treating the perturbed orbits, the approximation will be made that $\frac{d}{dt}(\gamma v_x) = 0$ and $\frac{d}{dt}(\gamma v_y) = 0$ to first order, i.e. the perturbed motion is adiabatic. This is also equivalent to a drift kinetic approximation since the fast gyromotion is neglected and the guiding center motion is retained. It will be recalled from Subsection V.2.A. that the unperturbed guiding center orbits are as follows.

$$v_x = -\omega_{br} y$$

$$v_y = \omega_{br} x \qquad \text{V-80}$$

$$\frac{d}{dt}(\gamma v_z) = -\frac{\Omega_e}{qR_0}(-\omega_{br}xy + \omega_{br}xy) = 0$$

The Cartesian coordinates of the unperturbed orbits are given as:

$$x = r\cos(\theta_0 + \omega_{br}t)$$

$$y = r\sin(\theta_0 + \omega_{br}t) \qquad \text{V-81}$$

$$z = z_0 + v_\parallel t.$$

The first order perturbed beam velocities are then given below.

$$v_x = -\omega_{br}y - \frac{e}{m_0\Omega_e}\left(E_y + \frac{v_z}{c}B_x\right)$$

$$v_y = \omega_{br}x + \frac{e}{m_0\Omega_e}\left(E_x - \frac{v_z}{c}B_y\right) \qquad \text{V-82}$$

$$\frac{d}{dt}(\gamma v_z) = -\frac{e}{m_0}E_z$$

Also, from the relativistic energy equation one has the following.

$$\frac{d\gamma}{dt} = -\frac{e}{m_0c^2}v_zE_z \qquad \text{V-83}$$

The perturbed velocities in the longitudinal and transverse directions are then obtained by integrating equations V-82 and V-83 with respect to time over the unperturbed orbits. First, for the perturbed velocity in the z direction, the results given below are obtained.

$$\delta(\gamma v_z) = \gamma\delta v_z + v_\parallel\delta\gamma = -\frac{e}{m_0}\int_{-\infty}^{t} dt'\,E_z(t') = -\frac{ie}{m_0}\frac{E_z}{\omega - (m+nq)\omega_{br}} \qquad \text{V-84}$$

Also, integrating the energy equation V-83 results in the following.

$$\delta\gamma = -\frac{ie}{m_0c^2}\frac{v_\parallel E_z}{\omega - (m+nq)\omega_{br}} \qquad \text{V-85}$$

Combining equations V-84 and V-85 gives the perturbed longitudinal velocity.

$$\delta v_z = \frac{-ie}{m_0\gamma^3}\,\frac{E_z}{\omega - (m+nq)\omega_{br}} \qquad \text{V-86}$$

In order to obtain the perturbed transverse beam velocities, it is necessary to first calculate the perturbed positions; these may be found by integrating the first two of equations V-82. In terms of $x^{\pm}$ and $v^{\pm}$ these are given by the following.

$$v^{\pm} = \frac{dx^{\pm}}{dt} = \pm i\omega_{br}x^{\pm} - \frac{e}{m_0\Omega_e}\left(\mp iE^{\pm} + \frac{v_z}{c}B^{\pm}\right) \qquad \text{V-87}$$

V-87 has the solution given below.

$$x^{\pm} = re^{\pm i(\theta_0 + \omega_{br}t)} + \delta x^{\pm} \qquad \text{V-88}$$

The perturbed position $\delta x^{\pm}$ is obtained by integrating over the unperturbed orbits and is given by:

$$\delta x^{\pm} = \pm\frac{e}{m_0\Omega_e}\,\frac{E^{\pm} \pm i\,\frac{v_z}{c}B^{\pm}}{\omega - (m+nq)\omega_{br}}\ . \qquad \text{V-89}$$

Substituting the above result back into V-87 leads to the desired transverse perturbed velocities.

$$v^{\pm} = v_{\perp}e^{\pm i(\theta_0 + \omega_{br}t)} + \delta v^{\pm}$$

$$\text{where } \delta v^{\pm} = \mp\frac{ie}{m_0\Omega_e}\left(E^{\pm} \pm i\,\frac{v_z}{c}B^{\pm}\right)\left[1 \mp \frac{\omega_{br}}{\omega - (m+nq)\omega_{br}}\right] \qquad \text{V-90}$$

Now that the perturbed velocities have been calculated, perturbed beam currents may be found. The perturbed distribution function is given by the following.

$$\delta f = F_0(v_{\perp},v_{\parallel},r) - \delta v_{\perp}\frac{\partial F_0}{\partial v_{\perp}} - \delta v_{\parallel}\frac{\partial F_0}{\partial v_{\parallel}} - \delta r\frac{\partial F_0}{\partial r} \qquad \text{V-91}$$

For the case of a beam of relativistic electrons with uniform velocity near the speed of light and no transverse thermal energy, an appropriate distribution function is $F_0 = \delta(v_z - v_0)\,\delta(v_\perp - r\omega_{br})$ where $v_0 \simeq c$. The perturbed currents in this case are given below.

$$4\pi J^{\pm} = \pm \frac{i\omega_{pb}^{2}}{\Omega_e} \left(E^{\pm} \pm i \frac{v_z}{c} B^{\pm}\right) \left[1 \mp \frac{\omega_-}{\omega - (m+nq)\omega_{br}}\right] \qquad \text{V-92}$$

$$4\pi J_z = \frac{i\omega_{pb}^{2}}{\gamma^3} \frac{E_z}{\omega - (m+nq)\omega_{br}}$$

$$+ \frac{iv_z}{\Omega_e} \frac{\partial}{\partial r} (\omega_{pb}^{2}) \frac{E_\theta + B_r}{\omega - (m+nq)\omega_{br}} \qquad \text{V-93}$$

$$\text{where } \omega_{pb}^{2} = \frac{4\pi n_b e^2}{m_0}$$

The final term in equation V-93 comes from $4\pi e \int d^3v\, \delta r\, v_z \frac{\partial F_0}{\partial r}$. A uniform density profile is assumed in the following analysis so that this last term of J_z will be absent. If it were desired to examine the case where the beam density was still uniform, but localized within the plasma at a radius r_b, then the final term of V-93 would contribute a δ function $\delta(r-r_b)$ to the perturbed J_z. This is physically due to the perturbed current caused by the gross motion of the beam boundary as it is undergoing displacement. In this situation, boundary conditions of the perturbed fields at $r=r_b$ must be derived by multiplying the two coupled equations V-67 and V-68 by rdr and integrating over the layer $r_b - \varepsilon$ to $r_b + \varepsilon$ with $\varepsilon \to 0$.

V.2.B.3. Relativistic Beam Perturbed Currents - Vlasov Beam Model

The starting point for a beam which has energy spread is the relativistically correct Vlasov equation.

$$\frac{\partial f}{\partial t} + \vec{v}\cdot\vec{\nabla}f + \frac{e}{m_0}[\vec{E} + \frac{1}{c}(\vec{v}\times\vec{B})]\cdot\frac{\partial f}{\partial \vec{p}} = 0 \qquad \text{V-94}$$

where $\vec{p} = \gamma m_0\vec{v}$ and $\gamma = (1-v^2/c^2)^{-1/2}$

The above equation is linearized by assuming $f = f_0 + \delta f$ where f_0 is an equilibrium distribution function.

$$\frac{\partial(\delta f)}{\partial t} + \vec{v}\cdot\vec{\nabla}(\delta f) + \frac{e}{m_0}[\vec{E}_0 + \frac{1}{c}(\vec{v}\times\vec{B}_0)]\cdot\frac{\partial(\delta f)}{\partial \vec{p}} = -\frac{e}{m_0}[\delta\vec{E} + \frac{\vec{v}\times\delta\vec{B}}{c}]\cdot\frac{\partial f_0}{\partial \vec{p}} \qquad \text{V-95}$$

δf is then obtained by integrating over the characteristics of the above equation (unperturbed orbits):

$$\delta f = \frac{e}{m_0}\int_{-\infty}^{t} dt' \,[\vec{E} + \frac{\vec{v}\times\vec{B}}{c}]\cdot\frac{\partial f_0}{\partial \vec{p}} \qquad \text{V-96}$$

The equilibrium distribution function f_0 depends only on the three constants of the motion which are given below.

$$\begin{aligned} H &= m_0 c^2\gamma \\ P_z &= \gamma m_0 v_z + \frac{e}{c}A_z \\ L_\theta &= \gamma m_0(xv_y - yv_x) + \frac{e}{c}rA_\theta \end{aligned} \qquad \text{V-97}$$

Therefore, $\partial f_0/\partial \vec{p}$ may be expanded, using the chain rule, to obtain the following.

$$\frac{\partial f_0}{\partial \vec{p}} = \frac{\partial f_0}{\partial H}\frac{\partial H}{\partial \vec{p}} + \frac{\partial f_0}{\partial P_z}\frac{\partial P_z}{\partial \vec{p}} + \frac{\partial f_0}{\partial L_\theta}\frac{\partial L_\theta}{\partial \vec{p}} \qquad \text{V-98}$$

The above derivatives of the constants of the motion are given below.

$$\frac{\partial H}{\partial \vec{p}} = \vec{v}$$

$$\frac{\partial P_z}{\partial \vec{p}} = \hat{\imath}_z$$

$$\frac{\partial L_\theta}{\partial \vec{p}} = x\hat{\imath}_y - y\hat{\imath}_x \qquad \text{V-99}$$

Equation V-96 may then be expressed in a somewhat simpler form:

$$\delta f = \frac{\partial f_0}{\partial H}\,\delta H + \frac{\partial f_0}{\partial P_z}\,\delta P_z + \frac{\partial f_0}{\partial L_\theta}\,\delta L_\theta \qquad \text{V-100}$$

$$\text{where} \quad \delta H = \int_{-\infty}^{t} dt'\,(\vec{v}\cdot\delta F)$$

$$\delta P_z = \int_{-\infty}^{t} dt'\,\delta F_z \qquad \text{V-101}$$

$$\delta L_\theta = \int_{-\infty}^{t} dt'(x\delta F_y - y\delta F_x)$$

In the above, $\frac{\partial f_0}{\partial H}, \frac{\partial f_0}{\partial P_z}, \frac{\partial f_0}{\partial L_\theta}$ have been removed from the time-history integrals since they depend only on the constants of the motion and thus are time-independent.

In what follows distribution functions which depend on only H and P_z will be considered, i.e. $f_0 = f_0(H,P_z)$. The next step in the analysis is to perform the time-history integrals indicated in equation V-101. From Subsection V.2.A., the unperturbed orbits, neglecting gyromotion, are given by the following.

$$r = \xi_\perp = \text{constant}$$

$$\theta = \theta_0 - \omega_- t \qquad \text{V-102}$$

$$z = z_0 + v_z t$$

Therefore, the wave-phase factor in the perturbed fields is as given below.

$$i(m\theta + nz/R_0 - \omega t) = i\left[m(\theta_0 + \omega_- t) + \frac{n}{R_0}(Z_0 + v_z t) - \omega t\right] \qquad \text{V-103}$$

Assuming that ω has a small positive imaginary part, the following expressions may then be obtained for δP_z and δH.

$$\delta P_z \simeq \frac{ie}{m_0} \frac{E_z}{\omega - \omega_{br} nq - m\omega_-} \qquad \text{V-104}$$

$$\begin{aligned} \delta H = {} & \frac{ie}{m_0(\omega - \omega_{br} nq - m\omega_-)} \Bigg\{ v_z E_z \\ & + \frac{r\omega_+\omega_-}{2}\left[\frac{e^{i\theta_0} E^-}{\omega - \omega_{br} nq - m\omega_-} + \frac{e^{-i\theta_0} E^+}{\omega - \omega_{br} nq - m\omega_- - \omega_+ + \omega_-}\right]\Bigg\} \\ & + \frac{ie}{2m_0}\left[\frac{v^+ E^-}{\omega - \omega_{br} nq - m\omega_- + \omega_+ - \omega_-} + \frac{v^- E^+}{\omega - \omega_{br} nq - m\omega_- - \omega_+ + \omega_-}\right] \end{aligned} \qquad \text{V-105}$$

Since $\omega_+ >> \omega_-$ and ω, the above equation for δH may be approximated as follows.

$$\delta H \simeq \frac{ie(v_z E_z - r\omega_2 E_\theta)}{m_0(\omega - \omega_{br} nq - m\omega_-)} - \frac{ie}{m_0\omega_+}(v_\theta E_r - v_r E_\theta) \qquad \text{V-106}$$

The perturbed beam current is then given by the equation below.

$$\delta\vec{J} = -e\int_0^\infty p_\perp dp_\perp \int_{-\infty}^\infty \vec{v} dp_\parallel \left[\delta P_z \frac{\partial f_0}{\partial P_z} + \delta H \frac{\partial f_0}{\partial H}\right] \qquad \text{V-107}$$

Substituting δP_z and δH as given in equations V-104 and V-106 into V-107 results in the following equation.

$$\vec{\delta J} = -i\omega_{pb}^{2}\int_{0}^{\infty} p_{\perp}dp_{\perp}\int_{-\infty}^{\infty} \vec{v}dp_{\|}\Big\{(\omega - \omega_{br}nq - m\omega_{-})^{-1} \times \Big[E_{z}\frac{\partial f_{0}}{\partial P_{z}} + (v_{z}E_{z} - r\omega_{br}E_{\theta})\frac{\partial f_{0}}{\partial H}\Big] - \frac{1}{\Omega_{e}c^{2}}(v_{\theta}E_{r} - v_{r}E_{\theta})\frac{\partial f_{0}}{\partial \gamma}\Big\} \tag{V-108}$$

The first term in the integrand may be integrated by parts to obtain the result given below.

$$\delta J = -i\omega_{pb}^{2}\int_{0}^{\infty} p_{\perp}dp_{\perp}\int_{-\infty}^{\infty} dp_{\|}\vec{v}\Big\{\frac{1}{m_{0}}(\omega - \omega_{br}nq - m\omega_{-})^{-1} \times \Big[\frac{f_{0}}{c\gamma^{3}}\;E_{z} + \frac{1}{c^{2}}(v_{z}E_{z} - r\omega_{br}E_{\theta})\frac{\partial f_{0}}{\partial \gamma}\Big] - \frac{1}{\Omega_{e}c^{2}}(v_{\theta}Er - v_{r}E_{\theta})\frac{\partial f_{0}}{\partial \gamma}\Big\} \tag{V-109}$$

From this point on it will be more convenient to convert the above integral to an integration over $v_{\|}$ and γ. The Jacobian of this transformation is given as the following.

$$p_{\perp}dp_{\perp} = p_{\perp}|J|dv_{\|}d\gamma$$

$$\text{where } J = \begin{vmatrix} \frac{\partial p_{\perp}}{\partial \gamma} & \frac{\partial p_{\perp}}{\partial v_{\|}} \\ \frac{\partial p_{\|}}{\partial \gamma} & \frac{\partial p_{\|}}{\partial v_{\|}} \end{vmatrix} = m_{0}^{2}v_{\perp}^{2}\gamma \tag{V-110}$$

In performing the above integrations, a highly-peaked distribution function in $v_{\|}$ will be considered with $v_{\|} \simeq c$. A spread, however, will be allowed in the energy dependence, i.e. $f_{0}(v_{\|},\gamma) = \delta(v_{\|}-v_{0})F(\gamma)$ where $v_{0} \simeq c$. If γ_{0} is defined as $\gamma_{0} = (1 - v_{0}^{2}/c^{2})^{-1/2}$, then $p_{\perp}|J|$

may be written as below.

$$p_\perp |J| = m_0^3 c^2 \left(\frac{\gamma^2}{\gamma_0^2} - 1\right) \qquad \text{V-111}$$

In the following analysis, a step function dependence will be considered for F (γ).

$$F(\gamma) = \begin{cases} 0 & \gamma < \gamma_0 \\ K & \gamma_0 < \gamma < \gamma_m \\ 0 & \gamma > \gamma_m \end{cases} \qquad \text{V-112}$$

The normalization constant K is obtained by requiring that $2\pi \int_0^\infty p_\perp dp_\perp \int_{-\infty}^{\infty} dp_\parallel f_0 = N_b$, where N_b = electron beam density. This results in the equation given below.

$$2\pi m_0^3 c^2 K \int_{\gamma_0}^{\gamma_m} d\gamma \left(\frac{\gamma^2}{\gamma_0^2} - 1\right) = N_b \qquad \text{V-113}$$

$$\therefore K = (N_b / m_0^3 c^2)\, \chi(\gamma_0, \gamma_m)$$

$\chi(\gamma_0, \gamma_m)$ is given by:

$$\chi(\gamma_0, \gamma_m) = \frac{3}{2\pi\gamma_0}\left[\frac{\gamma_m^3}{\gamma_0^3} - 3\frac{\gamma_m}{\gamma_0} + 2\right]^{-1}. \qquad \text{V-114}$$

Equation V-109 for $\vec{\delta J}$ may then be written in the following form.

$$\vec{\delta J} = -\frac{i\omega_{pb}^2}{m_0}\chi(\gamma_0, \gamma_m)\int_{\gamma_0}^{\gamma_m} d\gamma \left(\frac{\gamma^2}{\gamma_0^2} - 1\right)\int_{-\infty}^{\infty} \vec{v} dv_\parallel$$

$$\times \left\{(\omega - nq\omega_{br} - m\omega_-)^{-1}\left[\frac{f_0}{c\gamma^3}E_z + \frac{1}{c^2}(v_z E_z - r\omega_{br}E_\theta)\frac{\partial f_0}{\partial \gamma}\right]\right. \qquad \text{V-115}$$

$$\left. - \frac{1}{\Omega_e c^2}(v_\theta E_r - v_r E_\theta)\frac{\partial f_0}{\partial \gamma}\right\}$$

Performing the integrations indicated above and employing the fact that f_0 is even in v_r and v_θ, one obtains the perturbed currents given below.

$$\delta J_r = -\frac{2i\omega_{pb}^2}{m_0}\chi(\gamma_0,\gamma_m)\frac{\gamma_0-\gamma_m}{\omega_+\gamma_0^2c^2}E_\theta \qquad \text{V-116}$$

$$\delta J_\theta = \frac{2i\omega_{pb}^2}{m_0}\chi(\gamma_0,\gamma_m)\frac{\gamma_0-\gamma_m}{\omega_+\gamma_0^2c^2}E_r \qquad \text{V-117}$$

$$\delta J_z = -\frac{i\omega_{pb}^2}{m_0}\chi(\gamma_0,\gamma_m)\left[\frac{I_1}{\gamma_0^2}E_z - I_2E_z - \frac{2}{\gamma_0^2c^2}(cE_z - r\omega_{br}E_\theta)I_3\right] \qquad \text{V-118}$$

The integrals I_1, I_2, I_3 are given in Appendix B.

V.2.C. Inclusion of Toroidal Curvature Drifts

A possibly important effect which has not been included in the analysis of the present chapter (since a cylindrical model is used) is that of toroidal drifts. These were examined in some detail in Chapter III; there it was found that for low pitch angle electrons with energies in the 1 to 5 MeV range, the orbits are close to circular, but are significantly displaced from flux surfaces by an amount $\Delta = \rho_{pol}/A$ (ρ_{pol} = gyroradius in poloidal field, A = aspect ratio - this applies only to a flat current profile). Such an effect can alter the stability analysis in several ways. First of all, due to the deviation of orbits off of flux surfaces, the beam electrons will travel a slightly larger distance in going around the torus than if they were closely tied to field lines. Also, if substantial energy spread is present, then there will be a greater mixing or spread in transit frequency and spatial location of the orbits than in the cylindrical model. This feature may be seen in Fig.V-3 where orbits started out on the same flux surface at the left-hand side are plotted. Finally, the inclusion of the proper toroidal orbits will result in poloidal mode coupling.

It may be recalled from Section V.1 that the condition for kink instabilities in a relativistic beam derived by Lee[43] corresponded to the closure of particle orbits in one transit around the torus, i.e. $v_z/R_0 = \omega_-$ where $\omega_- = \frac{\omega_c}{2}\left[\sqrt{1 + 4\omega_\beta^2/\omega_c^2} - 1\right]$, ω_c is the beam cyclotron frequency, ω_β is the beam betatron frequency. If one formally assumes that the same condition applies for a toroidal beam, then the modification resulting from toroidal drifts may be readily calculated. In Fig. V-4 a flux surface is shown (dashed lines) along with the corresponding toroidal orbit (solid line). Taking into account the slightly greater distance travelled by the toroidal orbit than the related cylindrical orbit (colinear with the flux surface in Fig. V-4), the condition for a closed orbit becomes the following.

$$f \frac{v_z}{R_0} > \omega^- \qquad \text{V-119}$$

$$\text{where } f = \frac{\sqrt{R_0^2 + (a + \Delta)^2}}{\sqrt{R_0^2 + a^2}}$$

$$\Delta = \rho_{pol}/A$$

$$a = \text{orbit radius}$$

Translating the above into a q limitation results in the inequality given below.

$$q > \frac{1}{f(1+f\varepsilon)} \qquad \text{V-120}$$

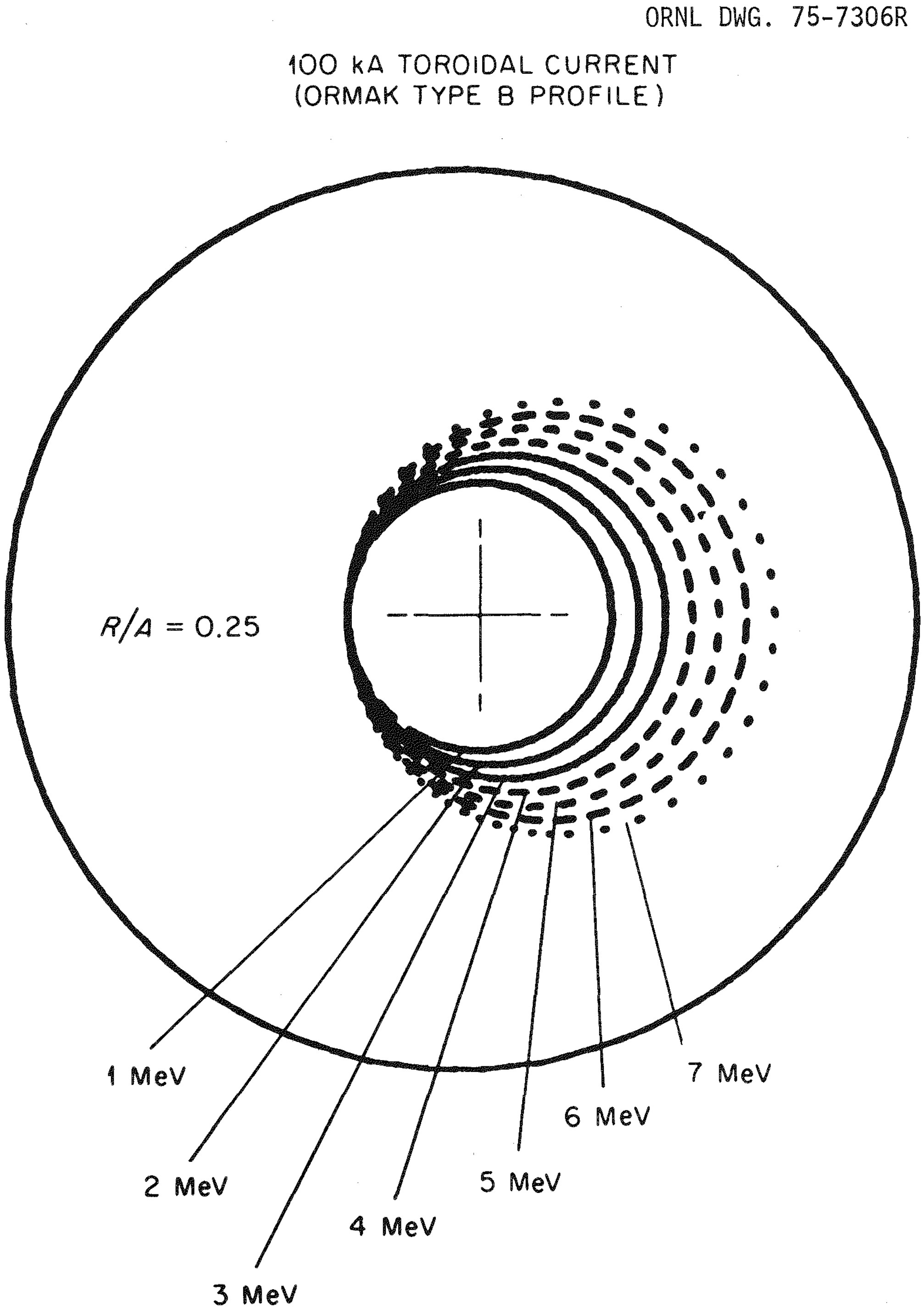

FIGURE V-3

Relativistic Electron Orbits in ORMAK Projected onto a Minor Cross Section - All Orbits are Started Out at the Left-Hand Side on the Equatorial Plane.

ORNL DWG. 75-13729

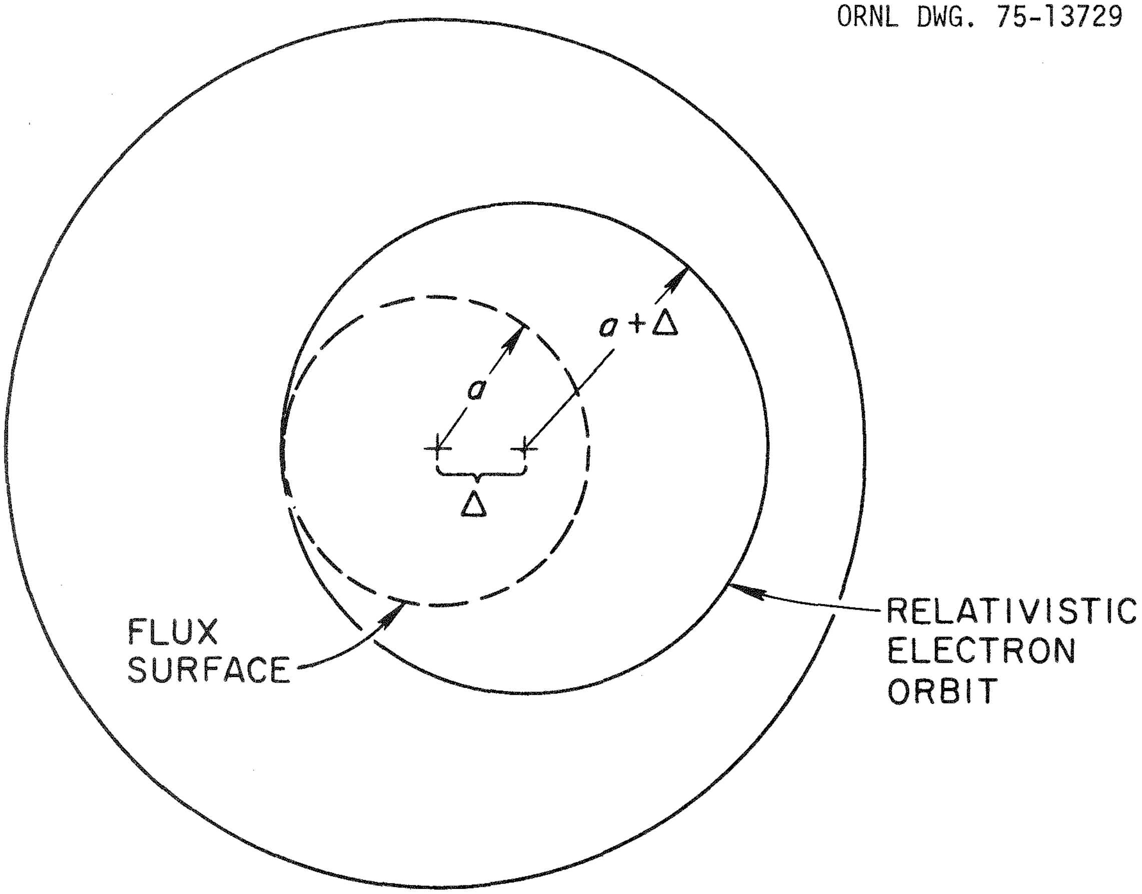

FIGURE V-4

Magnetic Flux Surface and Toroidal Relativistic Electron Orbit.

where $\varepsilon = \gamma mc^2\beta/e\ R_0B_z$

$\beta = v_z/c$

and $f > 1$

It may be noted that for a given toroidal magnetic field and major radius, the above criterion would imply that higher energy beams are required as the total current goes up to maintain a given amount of enhancement in the stability criterion. This is due to the fact that at a fixed energy the orbits become more closely centered on flux surfaces (Δ goes to 0 and f goes to 1) as the toroidal current is raised. The above mechanism thus scales unfavorably since increasing the energy past a certain point will lead to substantial losses from synchrotron radiation. However, it does not scale as unfavorably as the analagous stability enhancement which was found in the cylindrical model by Lee[43].

The presence of poloidal mode coupling becomes apparent when one attempts to integrate over the unperturbed toroidal orbits to obtain perturbed beam currents. As will be recalled from Subsections V.2.B.2 and 3, the perturbed currents involved integrals of the form given below.

$$\int_{-\infty}^{t} dt'\ f(r)\exp\left[i(m\theta + nz/R_0 - \omega t')\right] \qquad \text{V-121}$$

where $(r,\theta,z) = [r(t'),\theta(t'),z(t')]$ are the coordinates of the unperturbed orbits

and $f(r)$ is some function of r (e.g. $E_\theta(r)$, $B_r(r)$,etc.)

In the cylindrical analysis r,θ, and z were given by the following.

$$r = \text{constant}$$
$$\theta = \theta_0 - \omega_- t \qquad \text{V-122}$$
$$z = z_0 + v_z t$$

However, when toroidal orbits are taken into account, the above equations become:

$$r' = \text{constant}$$
$$\theta' = \theta_0' - \omega_- t \qquad \text{V-123}$$
$$z' = z_0' + v_z t$$

where the r,θ,z and r',θ',z' coordinates are shown in Fig. V-5 and are related by the following.

$$\theta = \tan^{-1}\left[\frac{r'\sin\theta'}{\Delta + r'\cos\theta'}\right]$$
$$r = r'\sqrt{1 + \Delta^2/r'^2 + (2\Delta/r')\cos\theta'} \qquad \text{V-124}$$
$$z = z'$$

To first order in Δ/a, the above transformations become as shown below.

$$r \simeq r' + \Delta\cos\theta'$$
$$\sin\theta \simeq \sin\theta' - \frac{\Delta}{r}\sin 2\theta' \qquad \text{V-125}$$
$$\cos\theta \simeq \frac{\Delta}{2r} + \cos\theta' - \frac{\Delta}{2r}\cos 2\theta'$$

Utilizing the above equations, the $e^{im\theta}$ factor in the integrand of equation V-121 becomes the following (in terms of θ').

$$e^{im\theta} = \left[\frac{\Delta}{2r} + e^{i\theta'} - \frac{\Delta}{2r}e^{2i\theta'}\right]^m \qquad \text{V-126}$$

When the above transformation is used in a stability analysis (via an integral like V-121), a coupling will enter in between the various order m modes. This is due to the fact that $e^{im\theta}$ is related to the functions $1, e^{i\theta'}, e^{2i\theta'}, \ldots, e^{2im\theta'}$. For example, $m = 1$ is coupled to $m = 0,1,2$, $m = 2$ is coupled to $m = 0,1,2,3,4$, etc. This fact can greatly complicate an instability analysis and will not be further considered in this work. However, in order to perform a realistic stability calculation for a toroidal relativistic beam where the quantity ρ_{pol}/A is not small compared to the beam radius, it would need to be taken into account.

ORNL DWG. 75-13728

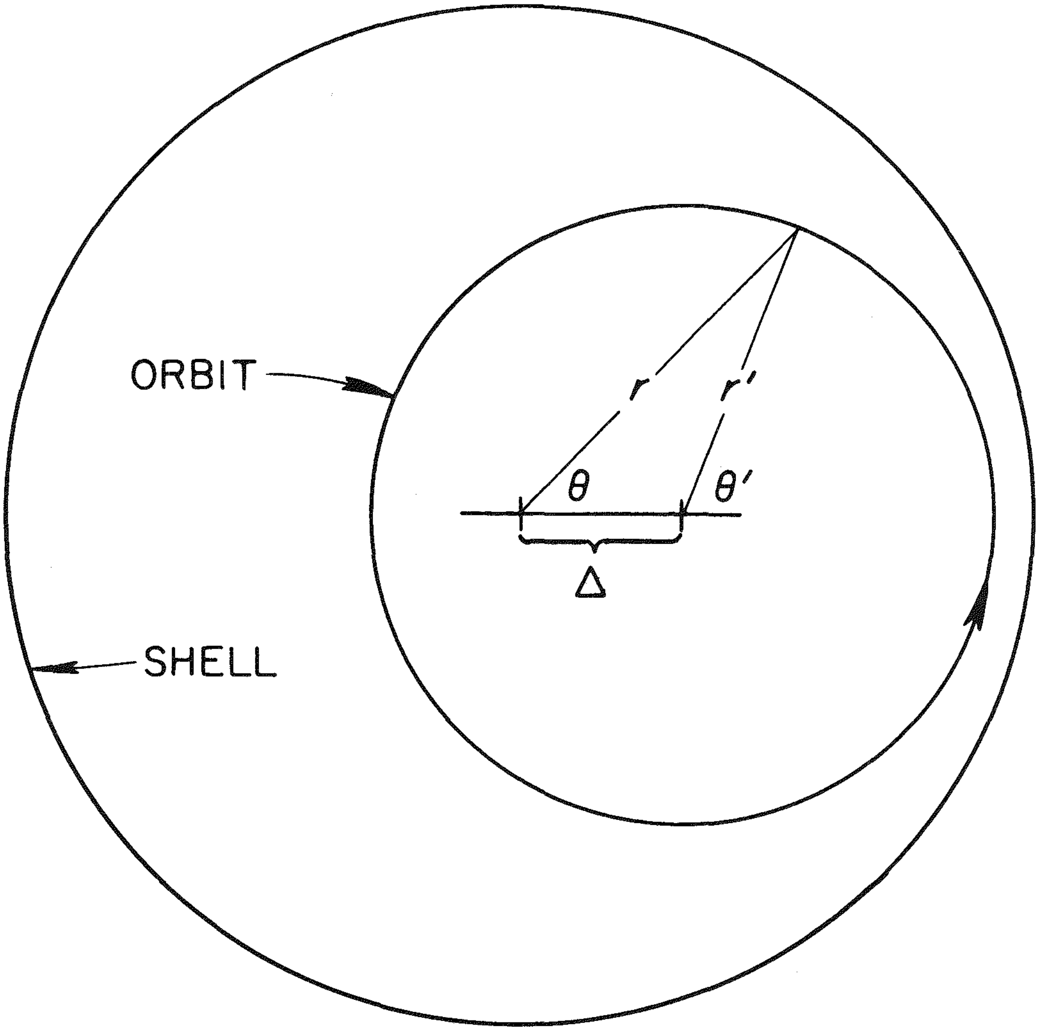

FIGURE V-5

Relation Between r,θ and r′,θ′ Coordinate Systems.

V.2.D. Dispersion Relation

A dispersion relation will now be derived for both a fixed boundary model and a free boundary model. For simplicity, the perturbed beam currents used will be those derived for the fluid model of Subsection V.2.B.2; this derivation could readily be generalized to treat the case of the Vlasov beam model. The derivation will proceed according to the following outline. First, the perturbed currents for the three species present: electrons, ions, beam electrons, will be substituted into the field equations of Subsection V.2.A. Next, these equations are manipulated until two coupled equations for the perturbed fields E_z and B_z are obtained. Finally, a decoupling method is used to solve these equations and a dispersion relation is obtained by requiring the appropriate boundary and jump conditions to be satisfied by B_z and E_z.

Adding up the perturbed current for the three species as given in equations V-77, V-92, and V-93 results in the following perturbed currents.

$$\frac{4\pi J_r}{\omega} = \frac{i\omega_{pi}^2}{\omega^2-\Omega_i^2} E_r - \frac{\omega_{pi}^2}{\omega^2-\Omega_i^2} \frac{\omega}{\Omega_i} E_\theta - \frac{i\omega_{pb}^2\omega_{br}}{\omega\Omega_e} \frac{E_r - \frac{v_z}{c} B_\theta}{\omega - (m+nq)\omega_{br}} \qquad \text{V-127}$$

$$\frac{4\pi J_\theta}{\omega} = \frac{i\omega_{pi}^2}{\omega^2-\Omega_i^2} E_\theta + \frac{\omega_{pi}^2}{\omega^2-\Omega_i^2} \frac{\omega}{\Omega_i} E_r - \frac{i\omega_{pb}^2\omega_{br}}{\omega\Omega_e} \frac{E_\theta + \frac{v_z}{c} B_r}{\omega - (m+nq)\omega_{br}} \qquad \text{V-128}$$

$$\frac{4\pi J_z}{\omega} = \frac{i\omega_{pe}^2}{\omega^2} E_z + \frac{i\omega_{pb}^2}{\omega\gamma^3} \frac{E_z}{\omega - (m+nq)\omega_{br}} \qquad \text{V-129}$$

The field equations V-62 and V-63 are now used for B_r and B_θ; also, the following quantities are defined.

$$Q = \frac{\omega_{br}\omega_{pb}^2}{\omega\Omega_e} \frac{1}{\omega - (m+nq)\omega_{br}} \qquad \text{V-130}$$

$$D = \frac{\omega\omega_{pi}^2}{\Omega_i(\omega^2-\Omega_i^2)} \qquad \text{V-131}$$

$$S = 1 - \frac{\omega_{pi}^2}{\omega^2-\Omega_i^2} \qquad \text{V-132}$$

$$P = 1 - \frac{\omega_{pe}^2}{\omega^2} - \frac{\omega_{pb}^2}{\omega\gamma^3} \frac{1}{\omega - (m+nq)\omega_{br}} \qquad \text{V-133}$$

The perturbed currents V-127 to V-129 may then be written in the form given below.

$$\frac{4\pi i J_r}{\omega} = [S - 1 + (1 - n_{\|})Q]\, E_r - iDE_\theta - iQ\frac{\partial E_z}{\partial \rho} \qquad \text{V-134}$$

$$\frac{4\pi i J_\theta}{\omega} = [S - 1 + (1 - n_{\|})Q]\, E_\theta + iDE_r + Q\frac{m}{\rho}\, E_z \qquad \text{V-135}$$

$$\frac{4\pi i J_z}{\omega} = (P - 1)\, E_z \qquad \text{V-136}$$

The transverse perturbed electric fields, E_r and E_θ, are now obtained in terms of E_z and B_z by substituting J_r and J_θ, as given above, into equation equations V-69 and V-70. It is convenient to define the following quantities.

$$\varepsilon_1 = G^{-1}[S - n_{\|}^2 + (1 - n_{\|})Q] \qquad \text{V-137}$$

$$\varepsilon_2 = G^{-1}D(n_{\|} + Q) \qquad \text{V-138}$$

3

$$\varepsilon_3 = 1 + G^{-1} n_{\parallel}(n_{\parallel} + Q)\ [S - n_{\parallel}^2 + (1 - n_{\parallel})\ Q] \qquad \text{V-139}$$

$$\varepsilon_4 = n_{\parallel} D G^{-1} \qquad \text{V-140}$$

$$G = [S - n_{\parallel}^2 + (1 - n_{\parallel})Q]^2 - D^2 \qquad \text{V-141}$$

E_r and E_θ are then obtained as given below.

$$E_r = \frac{i}{n_{\parallel}}(\varepsilon_3 - 1)\frac{\partial E_z}{\partial \rho} - \frac{m}{\rho}\varepsilon_1 B_z + \frac{\varepsilon_4}{n_{\parallel}}\frac{\partial B_z}{\partial \rho} - \frac{im}{\rho}\varepsilon_2 E_z \qquad \text{V-142}$$

$$E_\theta = -i\varepsilon_1 \frac{\partial B_z}{\partial \rho} - \frac{m}{\rho n_{\parallel}}(\varepsilon_3 - 1)\ E_z + \varepsilon_2 \frac{\partial E_z}{\partial \rho} + \frac{im}{\rho n_{\parallel}}\varepsilon_4 B_z \qquad \text{V-143}$$

Substituting the above equations into equation V-61 results in the following equation. This is the first of the two coupled radial eigenvalue equations.

$$\varepsilon_1 \nabla_\perp^2 B_z + B_z + i\varepsilon_2 \nabla_\perp^2 E_z = 0 \qquad \text{V-144}$$

$$\text{where } \nabla_\perp^2 \equiv \frac{1}{\rho}\frac{d}{d\rho}\left(\rho\frac{d}{d\rho}\right) - \frac{m^2}{\rho^2}$$

Combining equations V-62, V-63, and V-64 with equations V-142 and V-143 for E_r and E_θ then results in the second of the two coupled radial eigenvalue equations involving E_z and B_z.

$$\varepsilon_3 \nabla_\perp^2 E_z + PE_z - i\varepsilon_4 \nabla_\perp^2 B_z = 0 \qquad \text{V-145}$$

In order to examine stability, it is then necessary to find the eigenvalues of the coupled system of equations V-144 and V-145. In order to get these into a convenient form, equation V-144 is first multiplied by $-\varepsilon_3/\varepsilon_2$ and added to V-145; V-145 is then multiplied by $-i\varepsilon_1/\varepsilon_4$ and added to V-144. This results in the two coupled equations given below.

$$(\nabla_{\perp}^2 + T_B^{\,2})\, B_z = T_{BE}^{\,2}\, E_z \qquad \text{V-146}$$

$$(\nabla_{\perp}^2 + T_E^2)\, E_z = T_{EB}^{\,2}\, B_z \qquad \text{V-147}$$

where $T_B^2 = \varepsilon_3/(\varepsilon_1\varepsilon_3 - \varepsilon_2\varepsilon_4)$

$T_E^2 = \varepsilon_1 P/(\varepsilon_1\varepsilon_3 - \varepsilon_2\varepsilon_4)$

$T_{BE}^{\,2} = iP\varepsilon_2/(\varepsilon_1\varepsilon_3 - \varepsilon_2\varepsilon_4)$

$T_{EB}^{\,2} = -i\varepsilon_4/(\varepsilon_1\varepsilon_3 - \varepsilon_2\varepsilon_4)$

Equations V-146 and V-147 are now in a form for which a solution may be obtained. A technique for decoupling these equations is used below which was given in Ref.93 for the normal modes of a plasma filled waveguide. Defining the two functions ψ_1 and ψ_2 as follows:

$$\begin{aligned} \psi_1 &= E_z + Z_1 B_z \\ \psi_2 &= E_z + Z_2 B_z \end{aligned} \qquad \text{V-148}$$

one may write E_z and B_z as given below.

$$E_z = \frac{Z_1\psi_2 - Z_2\psi_1}{Z_1 - Z_2} \qquad \text{V-149}$$

$$B_z = \frac{\psi_1 - \psi_2}{Z_1 - Z_2} \qquad \text{V-150}$$

Equations V-146 and V-147 are then decoupled by substituting the above forms for E_z and B_z and properly choosing the constants Z_1 and Z_2 such that decoupled equations for ψ_1 and ψ_2 result. Straightforward algebra shows that such a choice is given by the following.

$$Z_{1,2} = \frac{T_E^2 - T_B^2}{2T_{BE}^2}\left[1 \pm \sqrt{1 + \frac{4T_{BE}^2\,T_{EB}^2}{(T_E^2 - T_B^2)^2}}\right] \qquad \text{V-151}$$

This results in the two equations given below.

$$(\nabla_\perp^2 + T_1^2)\psi_1 = 0 \qquad \text{V-152}$$

$$(\nabla_\perp^2 + T_2^2)\psi_2 = 0 \qquad \text{V-153}$$

where $T_{1,2}^2 = T_E^2 - Z_{1,2}\,T_{BE}^2$

These are Bessel's equations and have the following solutions.

$$\psi_1 = A_1 J_m(T_1\rho) \qquad \text{V-154}$$

$$\psi_2 = A_2 J_m(T_2\rho) \qquad \text{V-155}$$

A_1 and A_2 are constants. One of these is determined by the boundary conditions.

V.2.D.1. Fixed Boundary Model

In the fixed boundary model, both the beam and plasma extend all the way to the wall and there is no vacuum region in between. For both the fixed boundary and free boundary models, a perfectly conducting wall will be assumed. This is reasonable in relation to tokamak runaway experiments since the time scales for the instabilities are so short (less than 100 μsec) that the liner and shell will appear perfectly conducting. For such a boundary one has the following requirements on the perturbed fields.

$$E_z\,(\rho_a) = E_\theta\,(\rho_a) = B_r\,(\rho_a) = 0 \qquad \text{V-156}$$

where $\rho_a = a\omega/c$

a = shell radius

Setting E_z equal to zero at the boundary (using equations V-149, V-154, and V-155) leads to the equation given below.

$$A_1 = \frac{Z_1}{Z_2}\;A_2\;\frac{J_m(T_2\rho_a)}{J_m(T_1\rho_a)} \qquad \text{V-157}$$

Next, using equation V-143 and setting E_θ equal to zero at $\rho=\rho_a$ leads to the following equation.

$$-i\varepsilon_1\;\frac{\partial B_z}{\partial\rho}\Big|_{r=a} + \varepsilon_2\frac{\partial E_z}{\partial\,\rho}\Big|_{r=a} + \frac{im}{\rho_a n_\parallel}\;\varepsilon_4 B_z\Big|_{r=a} = 0 \qquad \text{V-158}$$

Substituting equations V-154 and V-155 and combining with equation V-157 one obtains the dispersion relation as given below.

$$Z_2T_2(i\varepsilon_1 + \varepsilon_2 Z_1)\,\frac{J_m'(\rho_a T_2)}{J_m(\rho_a T_2)} - Z_1T_1\,(i\varepsilon_1 + \varepsilon_2 Z_2)\,\frac{J_m'(\rho_a T_1)}{J_m(\rho_a T_1)}$$

$$+\,\frac{im\varepsilon_4}{\rho_a n_\parallel}\,(Z_1 - Z_2) = 0 \qquad \text{V-159}$$

V.2.D.2. Free-Boundary Model

In the free boundary beam-plasma model, the beam and plasma extend out to a radius r=a and then a vacuum region is present between r=a and r=b. The boundary conditions on the conducting wall (at r=b) are the same as in the fixed boundary model, i.e. $E_z(r=b) = E_\theta(r=b) = B_r(r=b) = 0^*$.

* Note that from equation V-62, $B_r = \frac{m}{\rho}E_z - n_\parallel E_\theta$, one of this conditions is redundant.

At the plasma-vacuum interface, three jump conditions may be derived from Maxwell's equations and two more from equations V-144 and V-145.

In summary, the two coupled differential equations for the perturbed fields E_z and B_z within the plasma (as derived in Subsection V.2.D) are given by the following.

$$\varepsilon_1 \nabla_\perp^2 B_z + B_z + i\varepsilon_2 \nabla_\perp^2 E_z = 0 \qquad \text{V-160}$$

$$\varepsilon_3 \nabla_\perp^2 E_z + PE_z - i\varepsilon_4 \nabla_\perp^2 B_z = 0 \qquad \text{V-161}$$

The solutions of the above equations are as given below.

$$E_z = (Z_1 - Z_2)^{-1} \left[Z_1 A_2 J_m(T_2\rho) - Z_2 A_1 J_m(T_1\rho)\right] \qquad \text{V-162}$$

$$B_z = (Z_1 - Z_2)^{-1} \left[A_1 J_m(T_1\rho) - A_2 J_m(T_2\rho)\right] \qquad \text{V-163}$$

A_1, A_2 = constants which will be determined

In the vacuum region, the differential equations for E_z and B_z decouple, resulting in the following.

$$\nabla_\perp^2 B_z + (1 - n_\parallel^2) B_z = 0 \qquad \text{V-164}$$

$$\nabla_\perp^2 E_z + (1 - n_\parallel^2) E_z = 0 \qquad \text{V-165}$$

The solutions are given below.

$$E_z = A_3 J_m(\kappa\rho) + A_4 Y_m(\kappa\rho) \qquad \text{V-166}$$

$$B_z = A_5 J_m(\kappa\rho) + A_6 Y_m(\kappa\rho) \qquad \text{V-167}$$

where $\kappa^2 \equiv 1 - n_\parallel^2$

From equations V-162, V-163, V-166, and V-167 it may be seen that there are six undetermined constants, $A_1, A_2, \ldots, A_6$ which will be found from the two conducting shell boundary conditions and the four independent interface jump conditions.

At the conducting wall one has the conditions E_z and E_θ equal zero. The first of these results in the equation given below.

$$A_3 J_m(\kappa\rho_b) + A_4 Y_m(\kappa\rho_b) = 0 \qquad \text{V-168}$$

The second of these may be evaluated by using equation V-66 with $J_\theta=0$ (to give the vacuum result), i.e. $E_\theta = -n_\parallel B_r - iB_z'$. Since B_r is zero at the conducting wall, this results in the following equation.

$$A_5 \, J_m'(\kappa\rho_b) + A_6 \, Y_m'(\kappa\rho_b) = 0 \qquad \text{V-169}$$

At the plasma-vacuum interface, the following three jump conditions may be derived directly from Maxwell's equations by integrating over a small pillbox region at the interface and assuming that the equilibrium magnetic field inside the plasma is equal to that in the vacuum.

$$[B_r(r=a)] = 0$$

$$[E_z(r=a)] = 0 \qquad \text{V-170}$$

$$[E_\theta(r=a)] = 0$$

where [ ] indicates the change in a quantity over the interface. Only two of these conditions are independent due to equation V-62. Requiring the continuity of E_z and E_θ over the interface leads to the following two equations.

$$-A_1 Z_2 J_m(T_1\rho_a) + A_2 Z_1 J_m(T_2\rho_a) - A_3(Z_1-Z_2) J_m(\kappa\rho_a) - A_4(Z_1-Z_2) Y_m(\kappa\rho_a) = 0$$

V-171

$$i(n_\parallel^2 - 1)^{-1} [A_5 J_m(\kappa\rho_a) + A_6 Y_m(\kappa\rho_a)]$$

$$+ \frac{m}{n_\parallel \rho_a} [(n_\parallel^2 - 1)^{-1} + \varepsilon_3] [A_3 J_m(\kappa\rho_a) + A_4 Y_m(\kappa\rho_a)]$$

$$= -i\varepsilon_1(Z_1 - Z_2)^{-1} [A_1 T_1 J_m'(T_1\rho_a) - A_2 T_2 J_m'(T_2\rho_a)] \qquad \text{V-172}$$

$$+ \varepsilon_2(Z_1 - Z_2)^{-1} [Z_1 A_2 T_2 J_m'(T_2\rho_a) - Z_2 T_1 A_1 J_m'(T_1\rho_a)]$$

$$+ \frac{im}{\rho_a n_\parallel} \varepsilon_4 (Z_1 - Z_2)^{-1} [A_1 J_m(T_1\rho_a) - A_2 J_m(T_2\rho_z)]$$

The final two jump conditions are obtained by integrating the differential equations for the perturbed fields E_z and B_z over the interface. In order to do this, it is first convenient to combine equations V-160, V-161, V-164, and V-165 into the following form.

$$[(\varepsilon_1 - 1)H(\rho-\rho_a) + H(\rho-\rho_b)]\nabla_\perp^2 B_z + [n_\parallel^2 H(\rho-\rho_a) + (1 - n_\parallel^2)H(\rho-\rho_b)]B_z$$

$$+ i\varepsilon_2 H(\rho-\rho_a) \nabla_\perp^2 E_z = 0 \qquad \text{V-173}$$

$$[(\varepsilon_3 - 1)H(\rho-\rho_a) + H(\rho-\rho_b)]\nabla_\perp^2 E_z + [(P - 1 + n_\parallel^2)H(\rho-\rho_a) + (1 - n_\parallel^2)H(\rho-\rho_b)]E_z$$

$$- i\varepsilon_4 H(\rho-\rho_a)\nabla_\perp^2 B_z = 0 \qquad \text{V-174}$$

where H = Heaviside step function

Equations V-173 and V-174 are now multiplied by $\rho d\rho$, integrated over the layer from $\rho_a - \varepsilon$ to $\rho_a + \varepsilon$ and then ε is allowed to go to zero. The necessary integrals are given below; X represents either B_z or E_z.

$$\lim_{\varepsilon\to 0} \int_{\rho_a-\varepsilon}^{\rho_a+\varepsilon} \rho d\rho\, H(\rho-\rho_a) \frac{1}{\rho} \frac{\partial}{\partial \rho} \rho \frac{\partial X}{\partial \rho} = -\frac{\rho_a}{2} \frac{\partial X}{\partial \rho} \Big|_{\rho_{\bar{a}}} \qquad \text{V-175}$$

$$\lim_{\varepsilon \to 0} \int_{\rho_a - \varepsilon}^{\rho_a + \varepsilon} \rho d\rho H(\rho - \rho_a) \frac{X}{\rho^2} = 0 \qquad \text{V-176}$$

$$\lim_{\varepsilon \to 0} \int_{\rho_a - \varepsilon}^{\rho_a + \varepsilon} \rho d\rho H(\rho - \rho_a) \frac{1}{\rho} \frac{\partial}{\partial p} p \frac{\partial X}{\partial \rho} = \rho_a \left[X'(\rho_a +) - X'(\rho_a^-)\right] \qquad \text{V-177}$$

$$\lim_{\varepsilon \to 0} \int_{\rho_a - \varepsilon}^{\rho_a + \varepsilon} \rho d\rho H(\rho - \rho_a) X = 0 \qquad \text{V-178}$$

$$\lim_{\varepsilon \to 0} \int_{\rho_a - \varepsilon}^{\rho_a + \varepsilon} \rho d\rho H(\rho - \rho_b) X = 0 \qquad \text{V-179}$$

Thus, the interface integrals of equations V-173 and V-174 result in the following conditions.

$$-\frac{\rho_a}{2} (\varepsilon_1 - 1) B_z' (\rho_a^-) + \rho_a \left[B_z'(\rho_a^+) - B_z' (\rho_a^-)\right] - \frac{i}{2} \varepsilon_2 E_z' (\rho_a^-) = 0 \qquad \text{V-180}$$

$$-\frac{\rho_a}{2} (\varepsilon_3 - 1) E_z' (\rho_a^-) + \rho_a \left[E_z'(\rho_a^+) - E_z' (\rho_a^-)\right] + \frac{i}{2} \varepsilon_4 B_z'(\rho_a^-) = 0 \qquad \text{V-181}$$

Substituting in the field solutions given in equations V-162, V-163, V-166, V-167 gives the two equations given below.

$$\begin{aligned} &-\frac{\rho_a}{2} (\varepsilon_1 - 1) (Z_1 - Z_2)^{-1} \left[A_1 T_1 J_m'(T_1 \rho_a) - A_2 T_2 J_m'(T_2 \rho_a)\right] \\ &+ \rho_a \Big\{ A_5 \kappa J_m'(\kappa \rho_a) + A_6 \kappa Y_m'(\kappa \rho_a) - (Z_1 - Z_2)^{-1} \\ &\times \left[A_1 T_1 J_m'(T_1 \rho_a) - A_2 T_2 J_m'(T_2 \rho_a)\right] \Big\} \qquad \text{V-182} \\ &- \frac{1}{2} \varepsilon_2 (Z_1 - Z_2)^{-1} \left[Z_1 A_2 T_2 J_m'(T_2 \rho_a) - Z_2 A_1 T_1 J_m'(T_1 \rho_a)\right] = 0 \end{aligned}$$

$$\begin{aligned} &- \frac{\rho_a}{2} (\varepsilon_3 - 1)(Z_1 - Z_2)^{-1} [Z_1 A_2 T_2 J'_m(T_2\rho_a) - Z_2 A_1 T_1 J'_m(T_1\rho_a)] \\ &+\rho_a \left\{ A_3 \kappa J'_m(\kappa\rho_a) + A_4 \kappa Y'_m(\kappa\rho_a) - (Z_1 - Z_2)^{-1} [Z_1 A_2 T_2 J'_m(T_2\rho_a) \right. \\ &\quad \left. - Z_2 A_1 T_1 J'_m(T_1\rho_a)] \right\} \\ &+ \frac{i}{2} \varepsilon_4 (Z_1 - Z_2)^{-1} [A_1 T_1 J'_m(T_1\rho_a) - A_2 T_2 J'_m(T_2\rho_a)] = 0 \end{aligned} \tag{V-183}$$

Equations V-168, V-169, V-171, V-172, V-182, V-183 now provide six independent equations for the constants, A_1, A_2, ..., A_6. The dispersion relation is derived by requiring the determinant of the coefficient matrix to be equal to zero. This is given in Appendix C.

V.2.E. Normal Plasma Alfvén Modes

Before examining the unstable spectra (presented in Subsection V.2.F.), the roots of the fixed boundary dispersion relation (equation V-159) will be investigated with the relativistic beam density set equal to zero. It can be shown that in this case only purely real roots are possible. These are simply the Alfvén modes of a cylindrical cavity.

In Figs. V-6 and V-7 roots of the dispersion relation V-159 are plotted as functions of plasma density (at fixed toroidal field) and toroidal field (at fixed plasma density). As may be seen, the frequencies do scale with the Alfvén velocity; they go linearly in magnetic field strength and inversely proportional to the plasma density.

By examining the relative size of the terms in equation V-159 with beam density set equal to zero, an approximate analytic theory can be developed to explain the results displayed in Figs. V-6 and V-7.

ORNL DWG. 75-13735

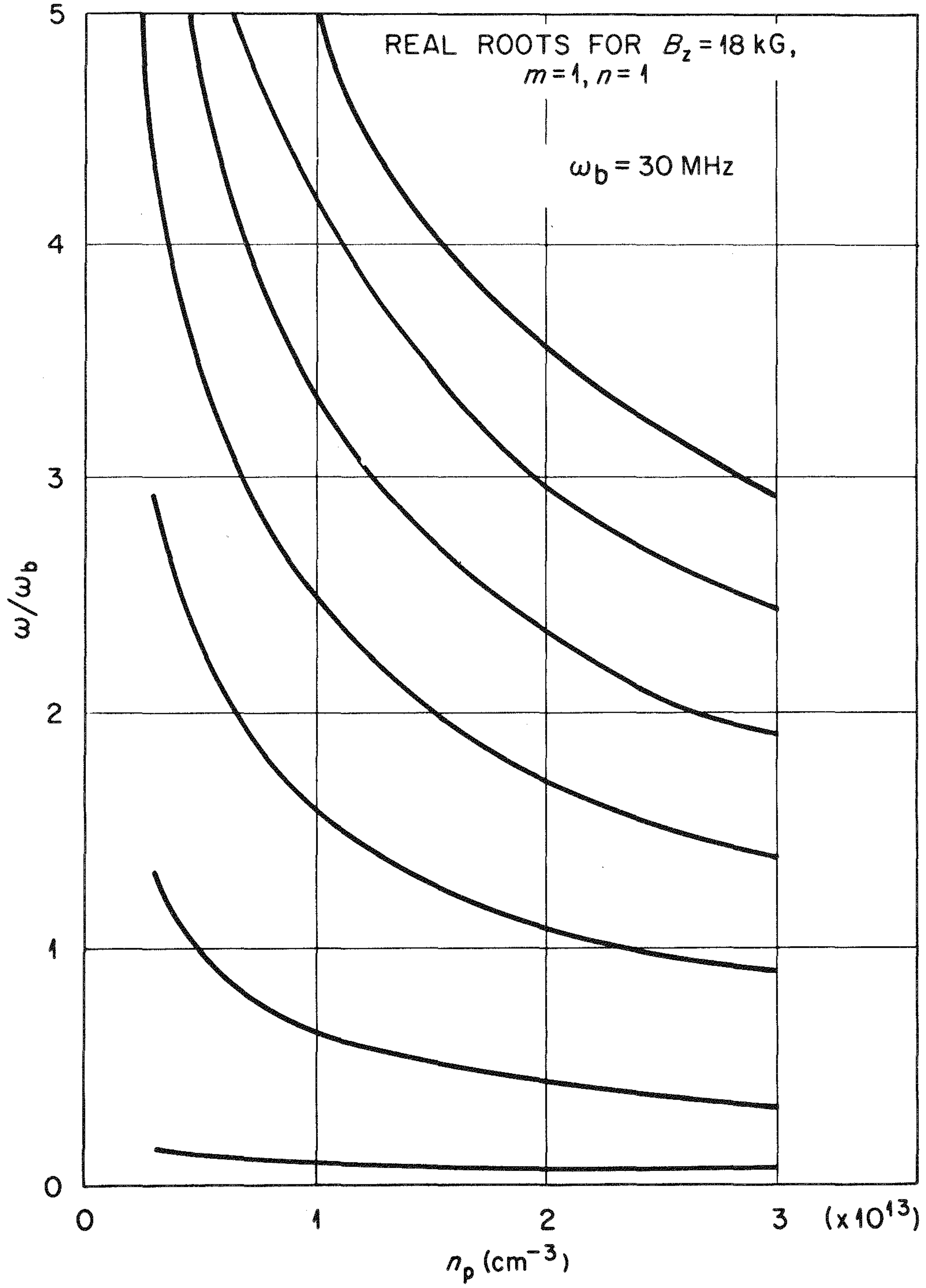

FIGURE V-6

Roots of the Fixed Boundary Dispersion Relation vs. n_p with n_B = 0 and at a Fixed B_z.

ORNL DWG. 75-13736

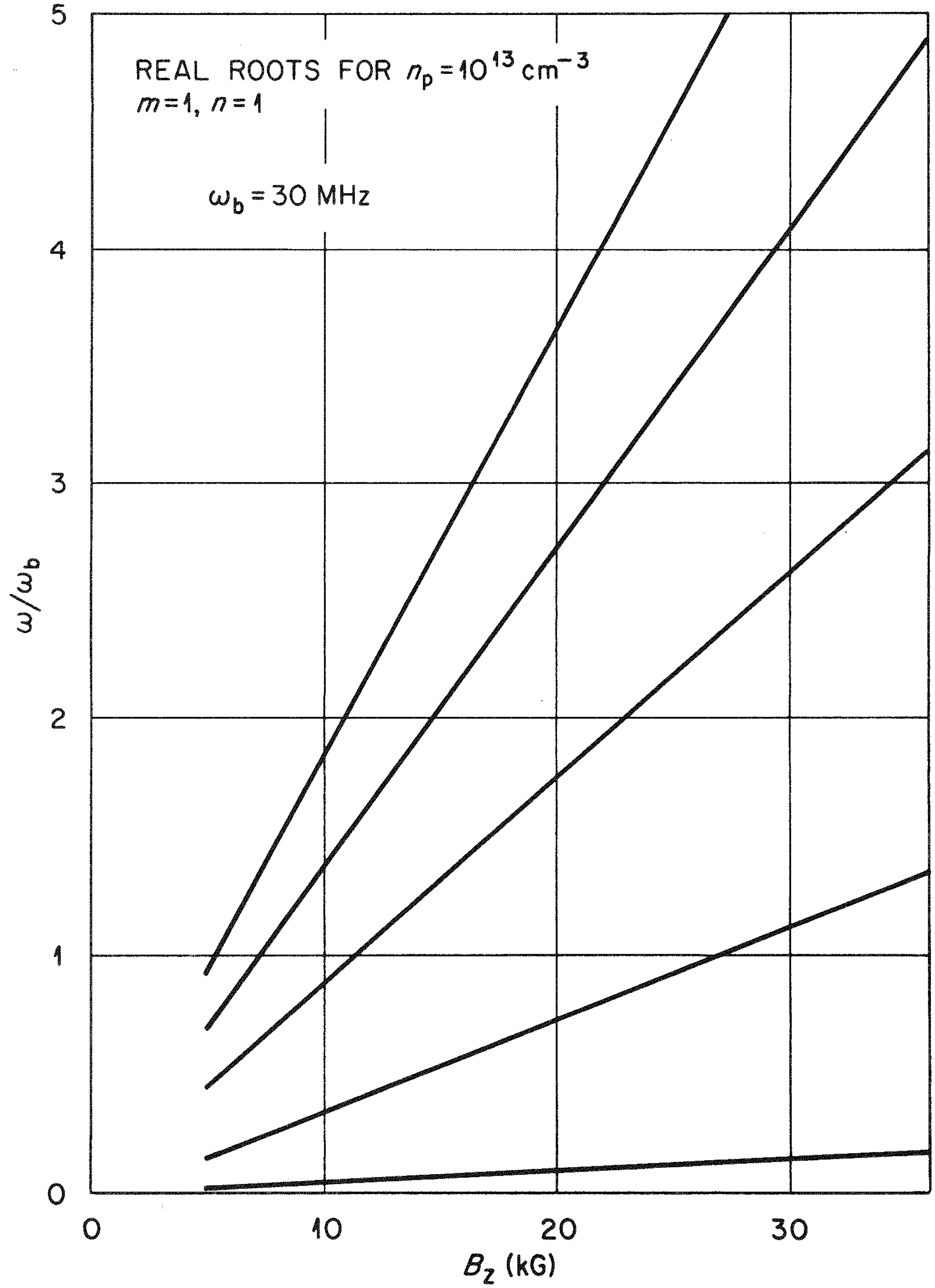

FIGURE V-7

Roots of the Fixed Boundary Dispersion Relation vs. B_z with n_B=0 and at a Fixed n_p.

The exact dispersion relation is given as follows.

$$Z_2\rho_a T_1{}^2 T_2 \frac{J_m'(\rho_a T_2)}{J_m(\rho_a T_2)} - Z_1\rho_a T_1 T_2{}^2 \frac{J_m'(\rho_a T_1)}{J_m(\rho_a T_1)} \qquad \text{V-184}$$

$$+ \frac{DP}{S+Q} m(Z_1 - Z_2) = 0$$

For the frequency range examined here ($\omega \lesssim \omega_{ci}$) and for plasma densities, toroidal fields, and minor radii typical of tokamaks, the first term in the above equation is four to five orders of magnitude less than the other two; also, Z_2 is several orders of magnitude less than Z_1. Thus equation V-184 is adequately approximated by the dispersion relation given below.

$$-\rho_a T_1(S - n_{\|}^2)\, J_m'(\rho_a T_1) + mDJ_m(\rho_a T_1) = 0 \qquad \text{V-185}$$

Also, for the frequency range of interest the following approximations can be made.

$$\begin{aligned} S - n_{\|}^2 &\simeq S \\ T_1{}^2 &\simeq c^2/v_A{}^2 \\ D/S &\simeq -\omega/\Omega_i \end{aligned} \qquad \text{V-186}$$

Defining the following quantities,

$$\begin{aligned} x &= a\omega/v_A \\ \delta &= c/a\omega_{pi} \end{aligned} \qquad \text{V-187}$$

the dispersion relation may be written as given below.

$$J_{m-1}(x) + m\,(\delta - \frac{1}{x})\, J_m(x) = 0 \qquad \text{V-188}$$

The zeros of this equation as a function of δ are plotted in Figs. V-8 and V-9 for m=1 and m=2. Also, zeros of J_{m-1} are plotted using dashed

ORNL DWG. 75-13734

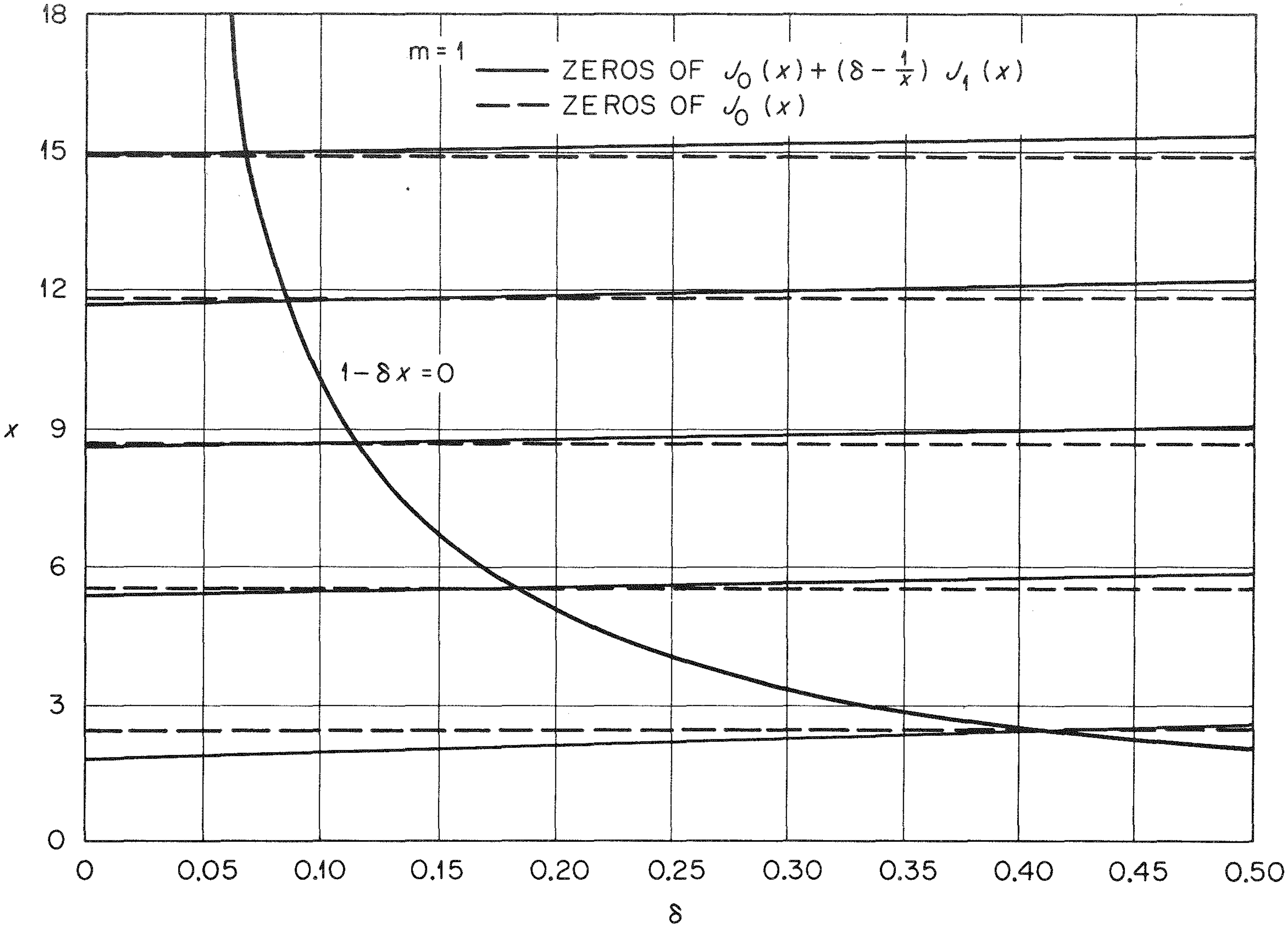

FIGURE V-8

Roots of Equation V-188 vs. δ for m=1

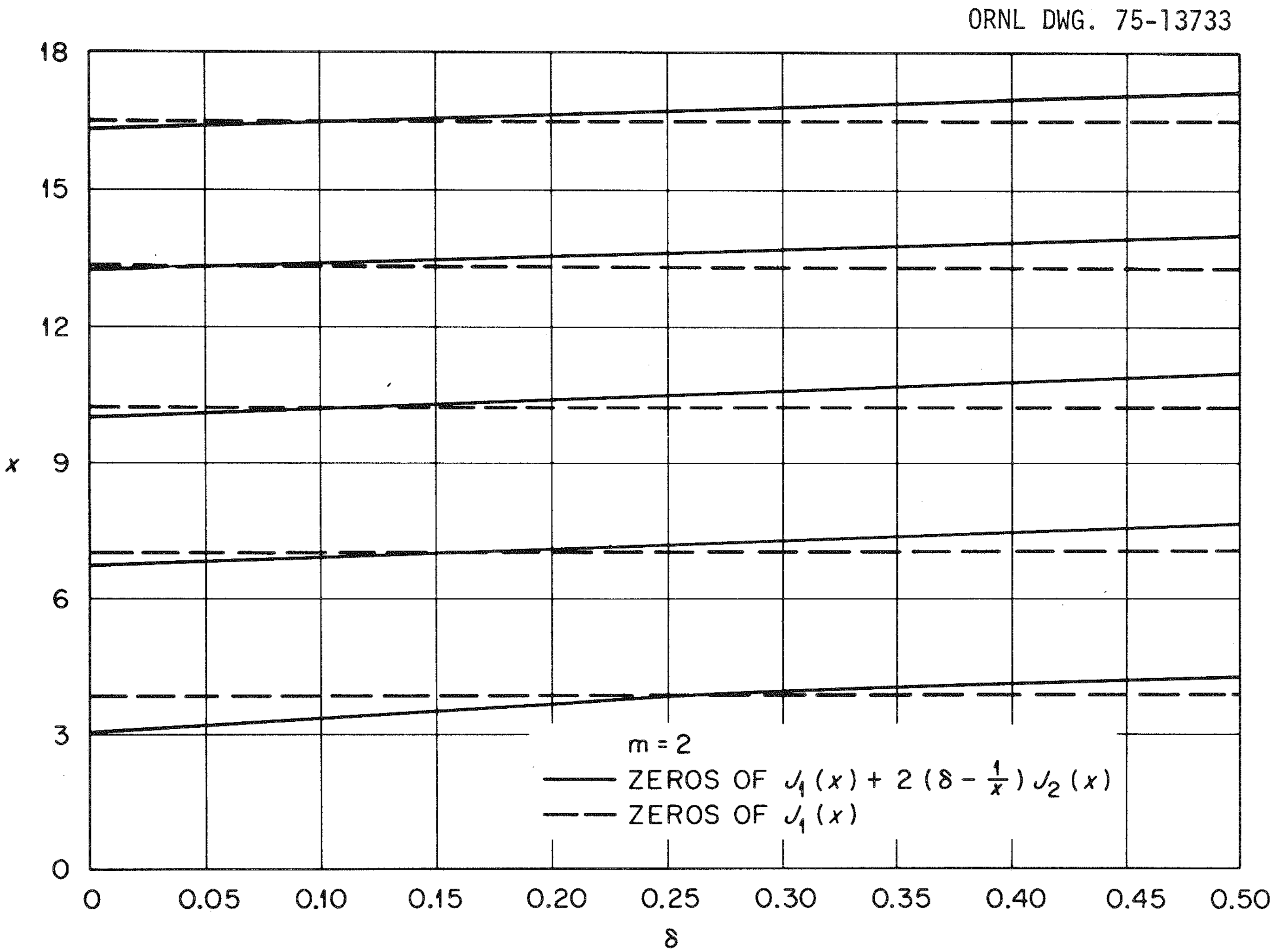

FIGURE V-9

Roots of Equation V-188 vs. δ for m=2 lines. As may be seen, the zeros of equation V-188 do not depend strongly on the parameter δ and are approximately equal to the zeros of J_{m-1}. Thus, the roots of V-188 are roughly given by $\omega \simeq j_{m-1,s} \frac{v_A}{a}$. Using the calculated roots of V-188 (from Figs. V-11 and V-12), the results of Figs. V-6 and V-7 may be reproduced.

V.2.F. Numerical Results for Growth Rates

The unstable spectra have been numerically calculated for the fixed boundary kink mode dispersion relation (equation V-159) over a range of parameters which are typical of tokamak strong runaway regimes. These will be presented in this section and discussed; before examining the dependence on various parameters, a few general remarks will be made on the features of the results. Roots were calculated using the Cauchy root-finding subroutine developed by Beasley and Meier [94]. A technical point with regard to equation V-159 is that a branch cut is present near the low frequency roots due to the square root involved in computing T_1. This can be avoided, however, by noting that the second term in V-159 is an even function of T_1 and thus may be written such that it only depends on T_1^2.

One feature which was seen in all of the growth rate calculations was that the real part of the unstable root was relatively small above where the maximum growth rate (as a function of q) occurred, but then rose to high values for q just below the maximum growth rate. Near where the growth rate went to zero, the real part would become as large as half the ion gyrofrequency. This is interpreted, as was mentioned earlier, as being due to the high frequency with which the relativistic electrons move around the poloidal direction. When this bounce frequency was artificially lowered, the real component of the root became generally less than the growth rate. It is thought that the high transit frequency may be effective in shorting out the growth of instabilities. As may be seen from the results (Figs. V-10 to V-17), whenever the real part of the frequency rose to high values (relative to the ion gyrofrequency) the growth rate fell rapidly to zero.

A second feature which was observed in the calculations was that the first term of the dispersion relation V-159 was always much less (by 4 to 5 orders of magnitude) than the other two. This term may be related to the effects of electron inertia; it would become more significant if the collision frequency of equation V-78 were large relative to ω, i.e. for a resistive plasma. This same term contains the effects of the longitudinal dynamics of the beam electrons; its relative smallness is the basis for the statement which was made in the introduction of this section that such effects were not of importance in the fixed boundary, ideally conducting beam-plasma model.

A final characteristic of the growth rates calculated is that the thresholds do not precisely correspond to rational magnetic surfaces; although, in most cases the maximum growth rate occurs there. This feature is perhaps related to the fact that the beam displacements have been calculated kinetically, by integrating along unperturbed single particle orbits, and thus do not conform exactly to the pitch of the helical field lines.

V.2.F.1. Dependence on Beam Density

In Figs. V-10 and V-11 growth rates and real frequencies are presented as a function of beam density. Densities are chosen such that the beam carries 25%, 50%, and 100% of the total current which is consistent with the q-values and other parameters. In this case ORMAK parameters are used for the major and minor radii and a toroidal field of 15 kG is assumed -- the plasma density is 10^{13} cm^{-3}. As may be seen, the growth rates are higher when the beam carries a larger fraction of the current.

V.2.F.2. Dependence on Beam Energy

In Figs. V-12 to V-15 growth rates and real frequencies are plotted for beam energies of 250 keV, 500 keV, 1 MeV, and 14.5 MeV. The beam is assumed to carry 100% of the current and the toroidal field and plasma density are again 15 kG and 10^{13}cm-3. Fairly slight differences are seen between the 1 MeV and 14.5 MeV cases, but large changes are apparent in going from 250 keV to 500 keV to 1 MeV. Increasing energy seems to shift the growth rate curves to the right on the q-axis, but not to change the shape substantially. This effect is particularly more noticeable for the higher m numbers.

V.2.F.3. Dependence on v_A/c

In Figs. V-16 and V-17 growth rates and real frequencies are plotted for v_A/c=.0576, .0415, and .0345. These correspond to a plasma density of $10^{13}cm^{-3}$ and toroidal fields of 15 kG, 18 kG, and 25 kG, respectively. The beam carries all of the toroidal current and has an energy of 1 MeV. The growth rates scale with v_A/c, as is the case in ideal MHD[81], becoming larger as v_A/c is increased. It is also noted that the upper value of q where the threshold occurs is relatively independent of v_A/c, whereas the lower threshold is not. The lower threshold goes to lower values of q as v_A/c is increased.

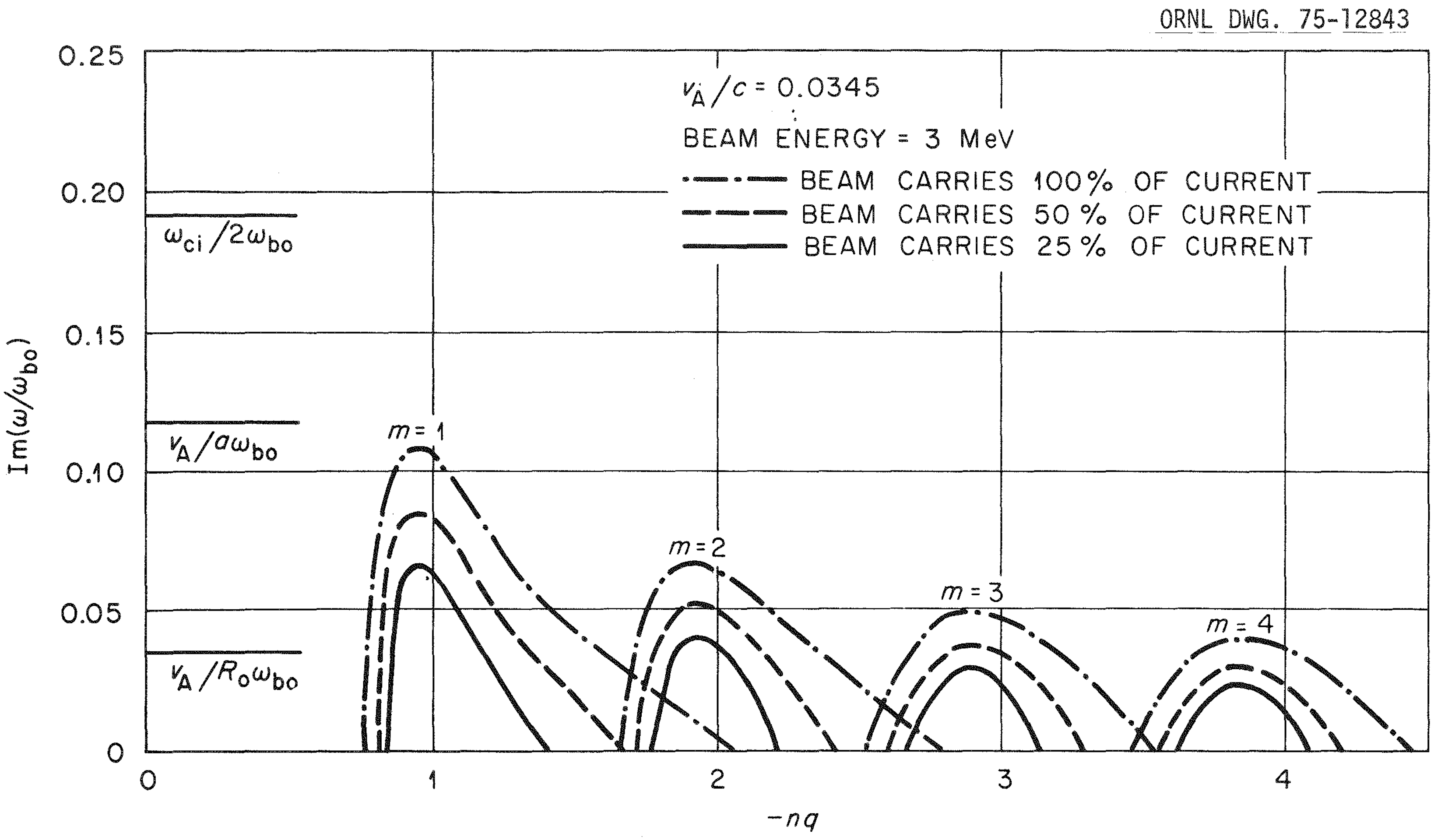

FIGURE V-10

Growth Rates for m = 1,2,3,4; n = -1 kink modes vs. nq and Beam Density for $v_A/c = 0.0345$ and 3 MeV Beam Energy.

ORNL DWG. 75-12810

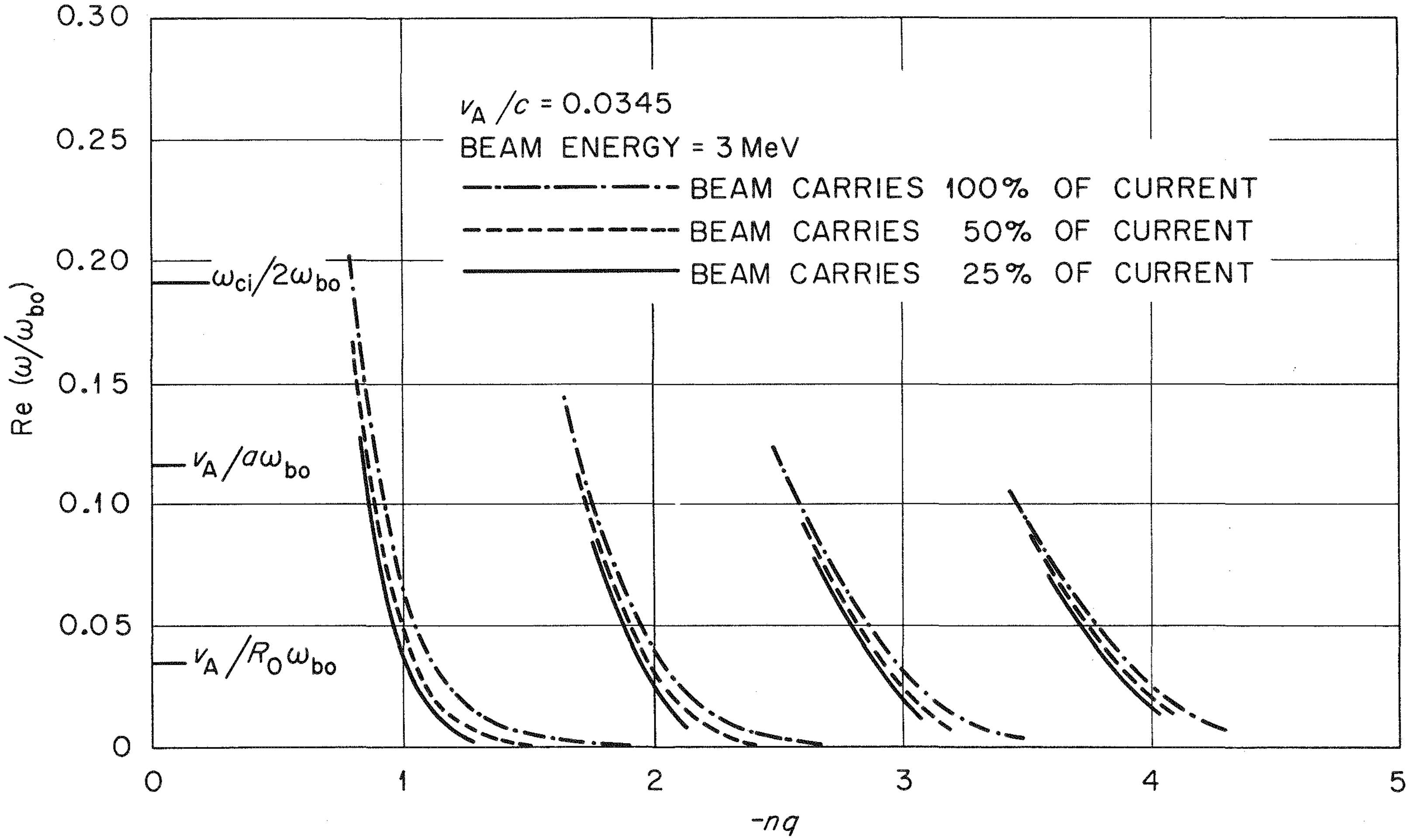

FIGURE V-11

Real Part of the Unstable Roots for m = 1,2,3,4; n = -1 kinks vs. nq and Beam Density for $v_A/c = 0.0345$ and 3 MeV Beam Energy.

ORNL DWG. 75-12806

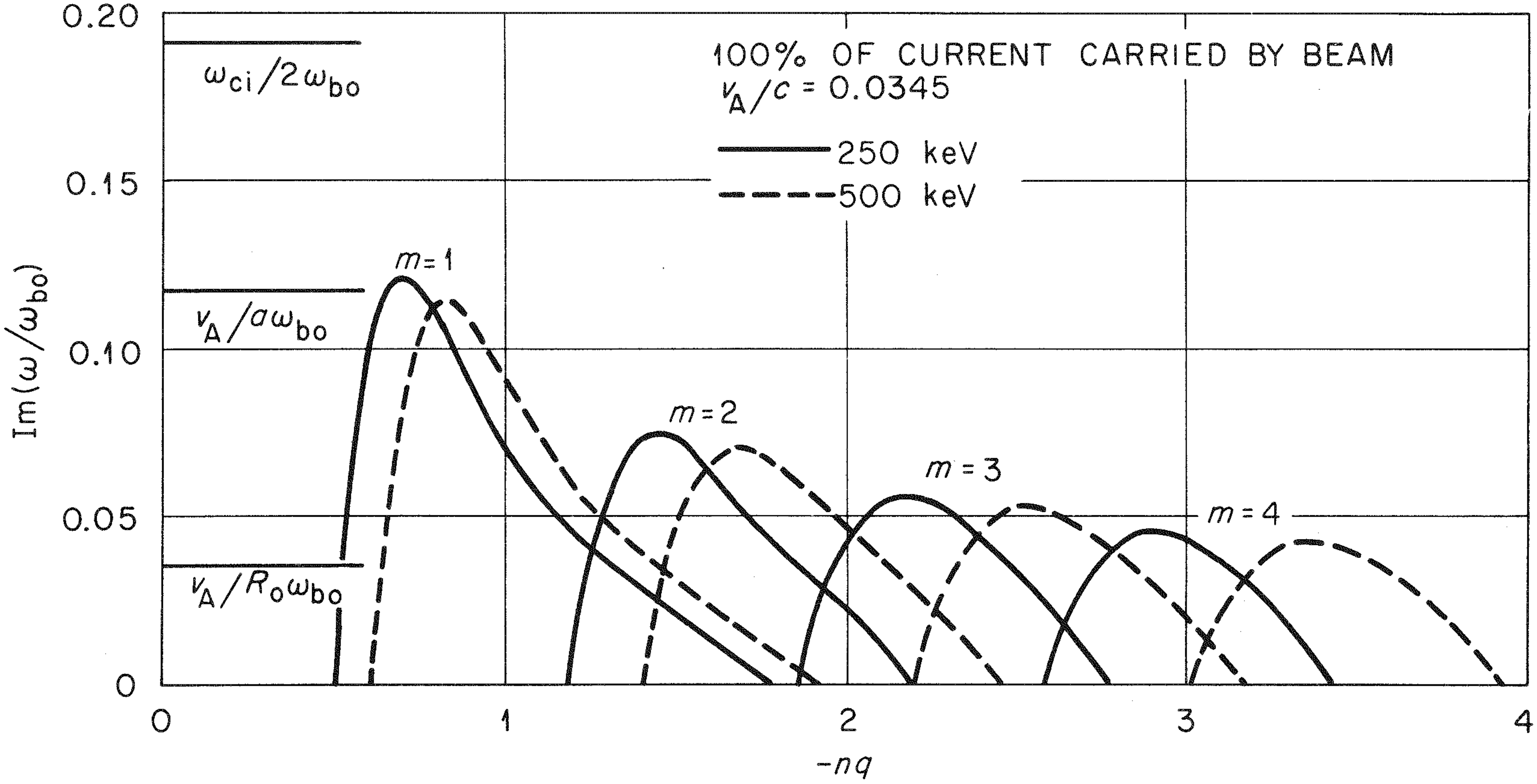

FIGURE V-12

Growth Rates for m = 1,2,3,4; n = -1 kink modes vs. nq and Beam Energy (250,500 keV) for $v_A/c = 0.0345$

ORNL DWG. 75-12807

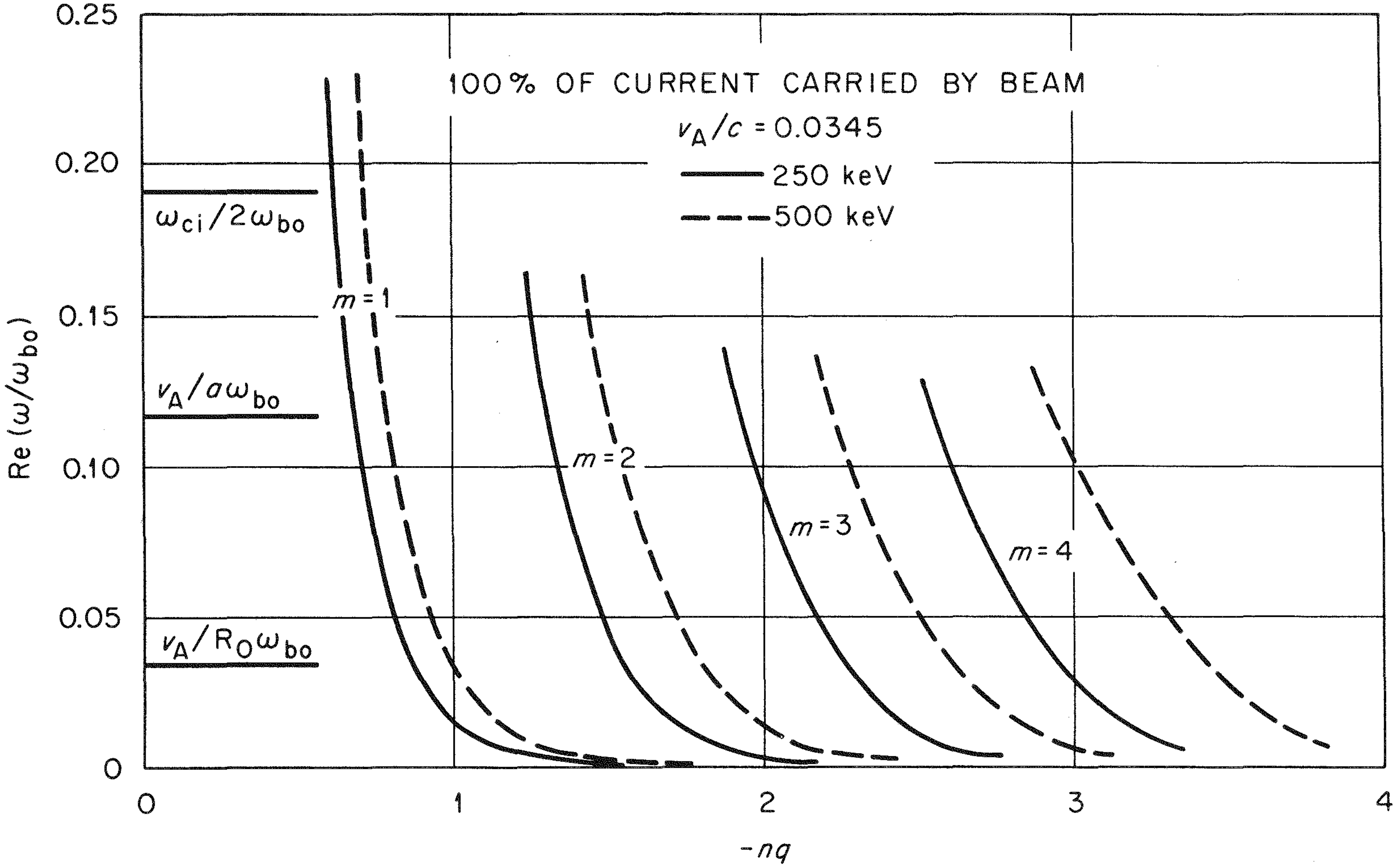

FIGURE V-13

Real Part of the Unstable Roots for m = 1,2,3,4; n = -1 kinks vs. nq and Beam Energy (250,500 keV) for $v_A/c = 0.0345$.

ORNL DWG. 75-12804

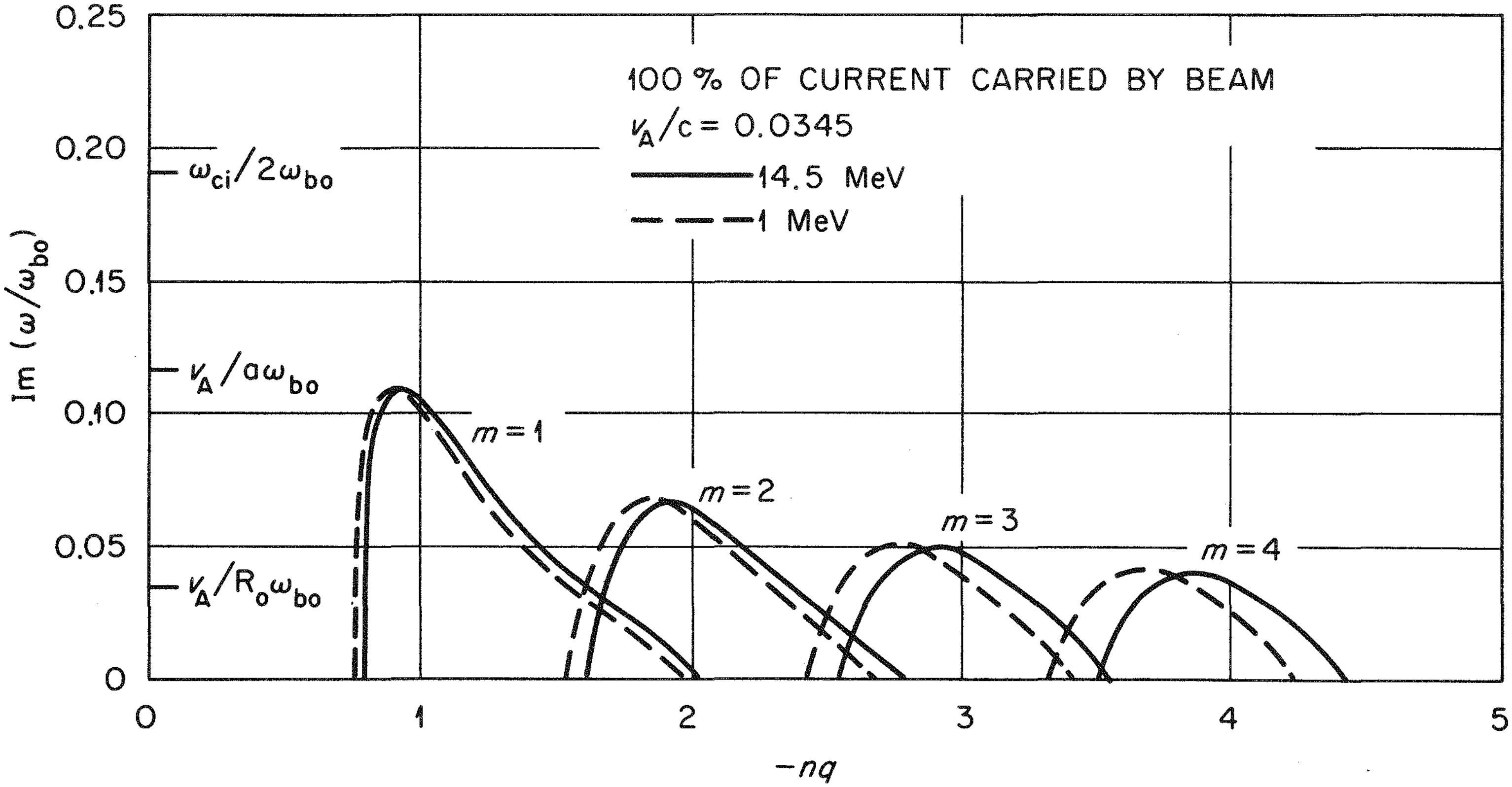

FIGURE V-14

Growth Rates for m = 1,2,3,4; n = -1 kink modes vs. nq and Beam Energy (1,14.5 MeV) for $v_A/c = 0.0345$.

ORNL DWG. 75-12805

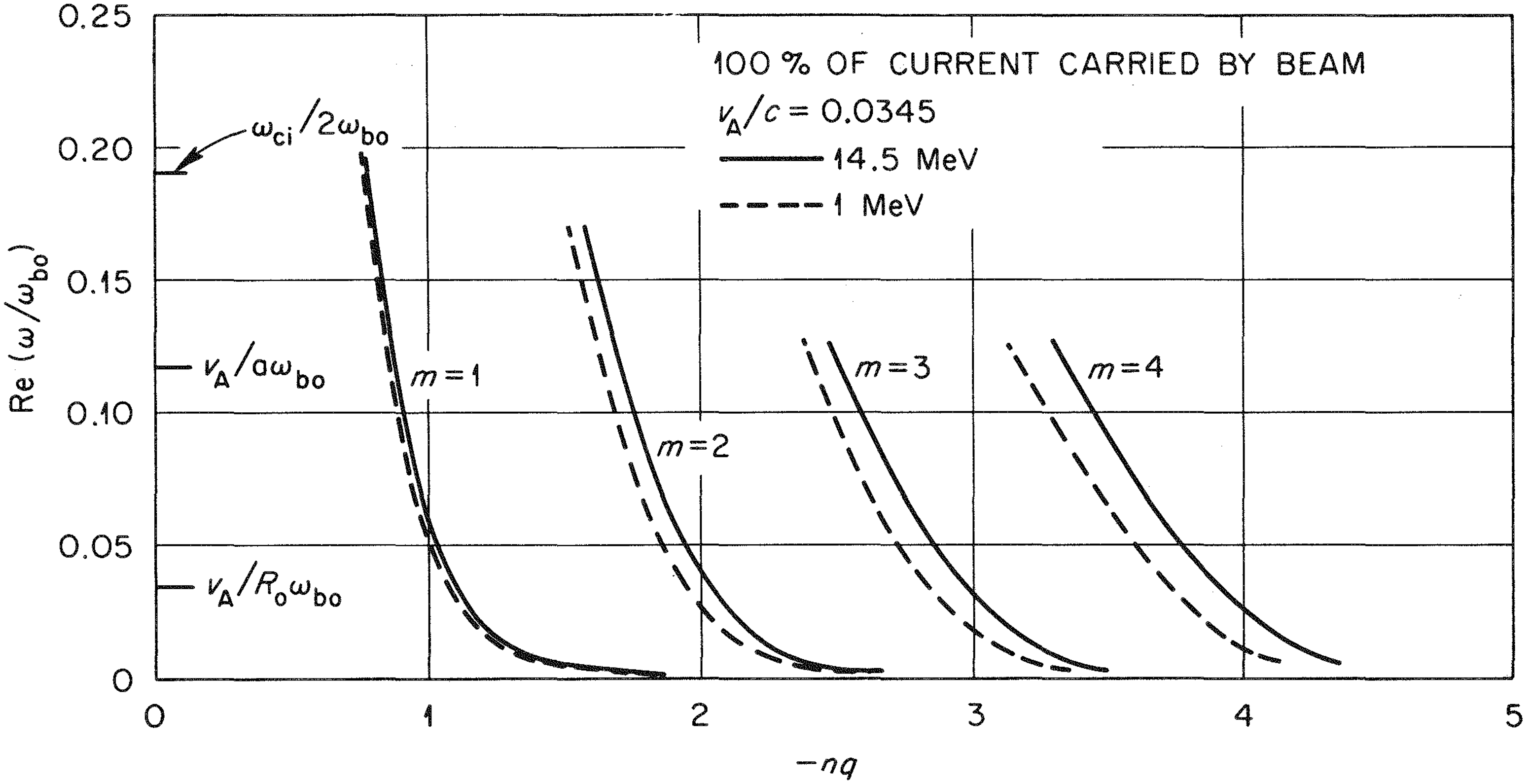

FIGURE V-15

Real Part of the Unstable Roots for m = 1,2,3,4; n = -1 kink modes vs. nq and Beam Energy (1, 14.5 MeV) for $v_A/c = 0.0345$.

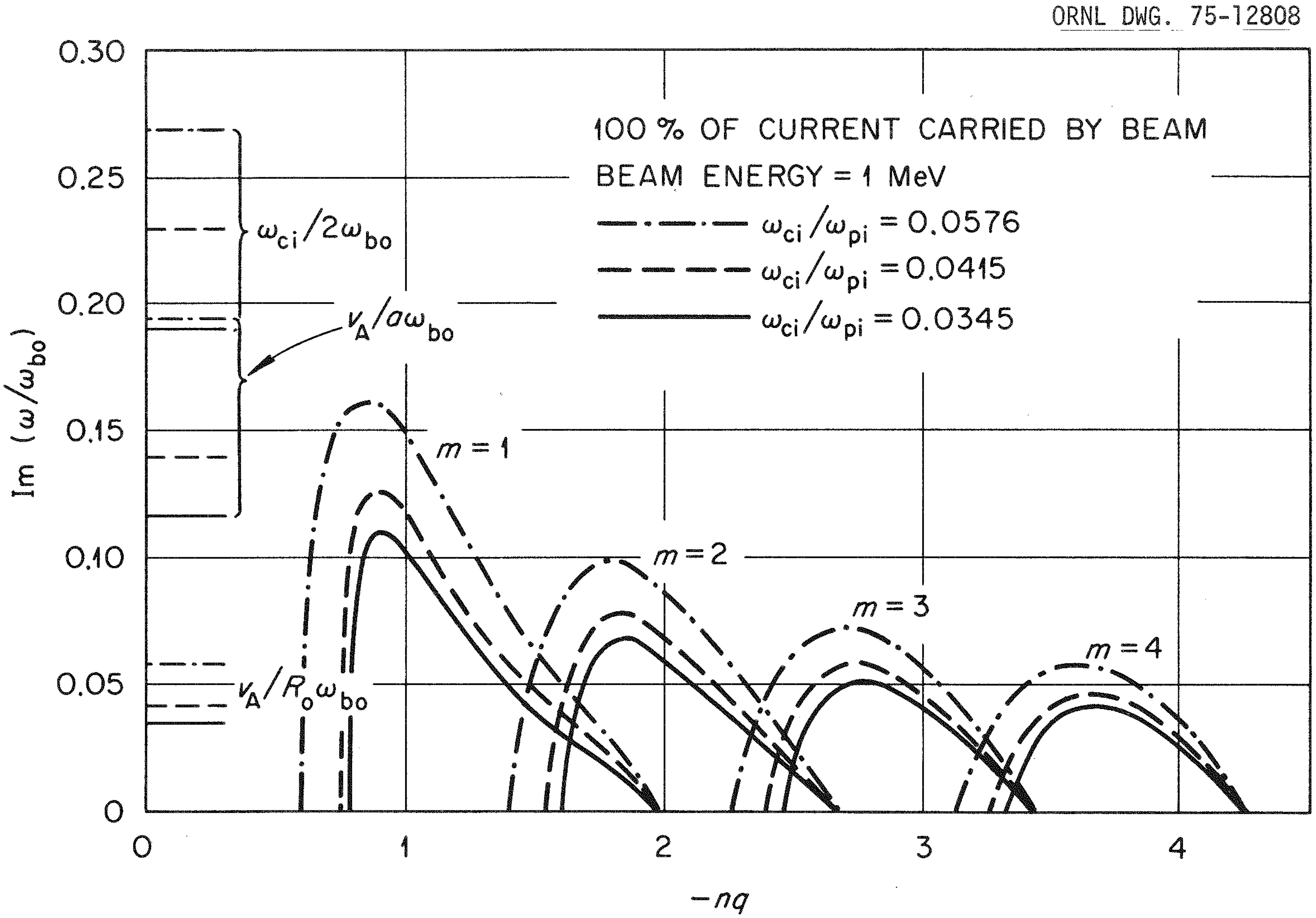

FIGURE V-16

Growth Rates for m = 1,2,3,4; n = -1 kink modes vs. nq and ω_{ci}/ω_{pi} for 1 MeV Beam Energy.

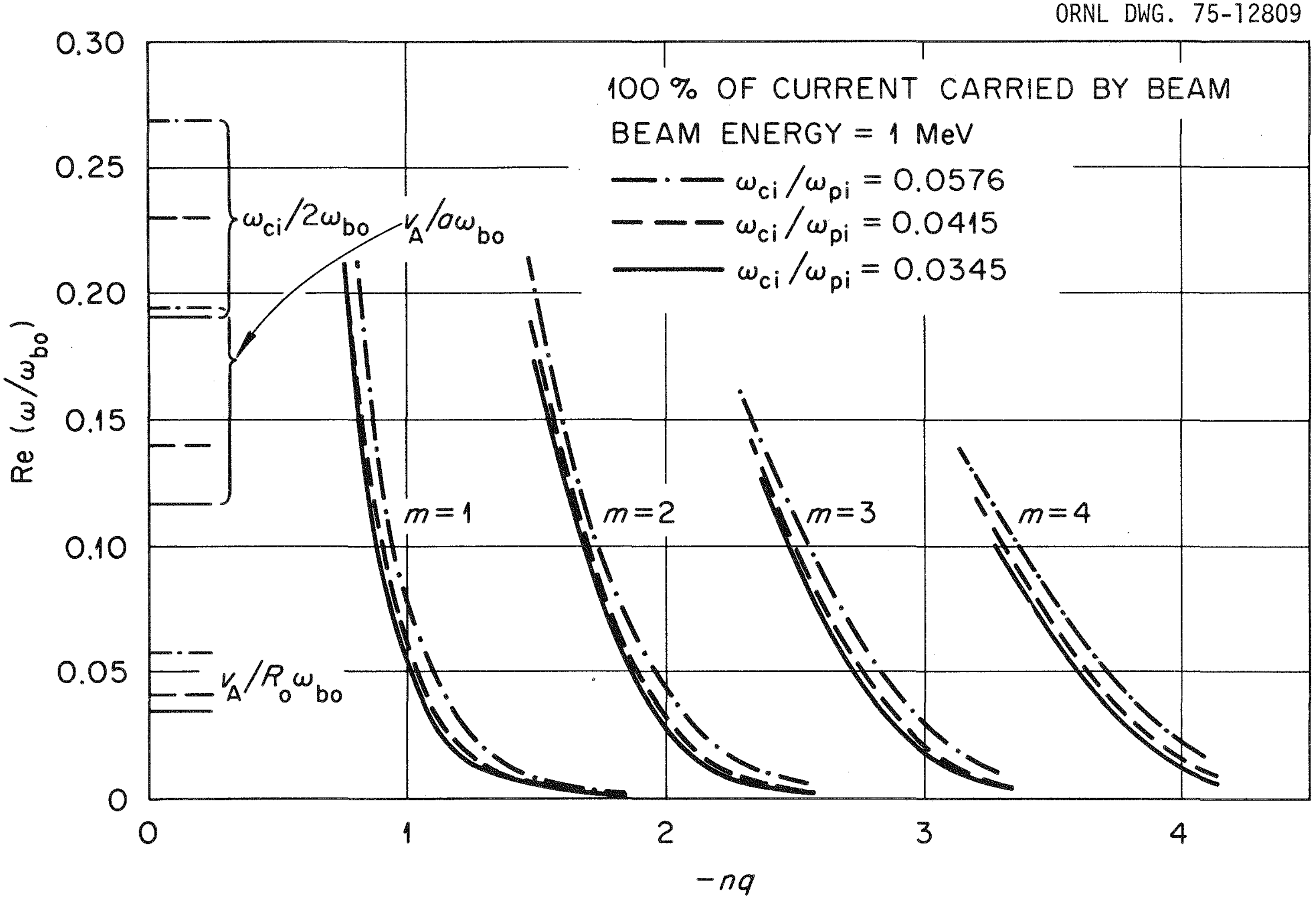

FIGURE V-17

Real Part of the Unstable Roots for m = 1,2,3,4; n = -1 kink modes vs. nq and ω_{ci}/ω_{pi} for 1 MeV Beam Energy.

CHAPTER VI

Summary and Conclusions

The purpose of this work, as discussed in Chapter I, has been to develop theoretical models to explain a number of the salient features of runaways in tokamaks. Specifically, the characteristics of the weak and strong regimes (which were defined in the introductory comments) have been investigated. The areas studied include: parameter modeling, particle confinement, equilibrium, and macroscopic stability.

In Chapter II, a parameter model was presented in relation to strong runaway discharges. The assumptions made there were that the runaways are predominantly formed in the early phase of the discharge and the bulk of the toroidal current is carried within a localized beam (due to the evolution of contained drift surfaces early in the discharge). The gradual acceleration of this beam in the applied Ohmic heating field was treated self-consistently using the relativistic force equation and Ampere's law. The model was then applied to several typical strong runaway discharges from the early operation phase of the ORMAK device, assuming that the bulk of the observed current was carried by runaways. Reasonable fits to the experimental data were obtained for beam densities on the order of $10^{11} cm^{-3}$ and beam radii of 5-6 cm. It should be kept in mind that this treatment represents only a preliminary, approximate model of a strong runaway discharge. A number of effects have been subsequently identified by experimental measurements in this regime which merit further study and inclusion in such a model. These include: gradual loss of runaways from the beam due to poorly-confined orbits, energy loss from synchrotron radiation, deviation of runaway acceleration from free-fall, and proper treatment of the poloidal variation in beam equilibrium properties. Techniques for treating some of these areas were then developed in the remaining work. Single particle orbits and confinement (both in relation to the strong and weak regimes) were analyzed in Chapter III and the beam equilibrium problem was studied in Chapter IV. Keeping in mind the above approximations of the strong runaway model of Chapter II, it was of interest that its prediction of a 5-6 cm beam radius implied the beam was attaining q values (q is the Kruskal-Shafranov safety factor) less than unity without substantial instabilities. This observation, and the experimentally-measured low level of MHD activity in runaway discharges, motivated the stability analysis of Chapter V.

In Chapter III, as mentioned above, the drift orbits of high energy electrons in the tokamak weak and strong runaway regimes were studied. The effect of $\vec{E}\times\vec{B}$ drifts in the strong regime was examined using the drift, density continuity, and Ampere's equations. It was determined that relatively little change occurred in the beam radius or density profile for parameters characteristic of the study of Chapter II. Next, drift orbits were analyzed for the weak runaway regime and a model was developed to explain the hard X-ray dumps which occur near the end of ORMAK type B discharges. The transport of high energy runaways out of the plasma region was found to be largely determined by the presence of the curvature drift term; however, the effects of finite pitch angle (finite gradient drift) on the orbits were also considered. Finally, the change in minor radius of an accelerating electron was examined; it was found to gradually increase as the runaway gained energy. Understanding this effect is of importance in relating the final orbits of these particles - as they intersect the plasma limiter - back to orbit characteristics earlier in the discharge. These considerations are necessary if runaway dumps in tokamaks are to be used for diagnostic purposes.

Next, in Chapter IV, the macroscopic equilibrium properties of toroidal beam-plasma configurations were studied. The basic equations were formulated and two mathematical limitations on their solution were indicated -- the firehose and mirror instability conditions. Some sample finite difference numerical solutions of the equilibirum equation were displayed and compared with analytic equilibrium theories. Also, estimates were made of beta poloidal limitations in toroidal beam-plasma equilibria using a simple force balance. It was found that the presence of a beam can reduce the allowable plasma beta poloidal; however, if the beam current density may be increased arbitrarily, such equilibrium limits can be avoided.

Finally, in Chapter V possible limits on the beam current density due to macroscopic instabilities were explored. The effects of spatial velocity and energy shear on m=1, n=1 kink modes were examined first using a cold, ideal MHD model for the background plasma and a rigid beam model. Only very slight enhancements in the stability boundaries for this mode were found with the inclusion of beam velocity shear.

Next, this model was generalized to allow consideration of several kinetic effects. The influence of perturbed electric fields was included in the beam equation of motion and the differing effective inertias of the beam electrons parallel and perpendicular to the propagation direction were taken into account. A Vlasov treatment of the beam energy spread was developed and the effects of toroidal drifts were discussed. Also, the background plasma model was extended so that frequencies which are not small relative to the ion gyrofrequency could be considered. Numerical calculations of the instability growth rates were made for a fixed boundary model with n=1, m=1,2,3,4; these were examined as a function of beam energy, beam density, and v_A/c. Somewhat larger growth rates were found near the q=1 point than had been previously estimated by Lee [43]. Regions of stability were also present for $q < 1$; near the lower marginal point, the real part of the unstable root was observed to become larger than the growth rate and was usually an appreciable fraction of the ion gyrofrequency. In the author's opinion, this indicates that an MHD approximation (which assumes $\omega << \omega_{ci}$) for the background plasma is simply not adequate for macroscopic modes in runaway-dominated discharges; this is related to the fact that relativistic electrons in present sized tokamaks have large drift frequencies ($\omega_d = c/R_0q \sim \omega_{ci}$) around the minor cross section. It is clear that a thorough study of macroscopic instability modes in toroidal relativistic beam-plasma configurations has only been just begun [43,44]. A number of effects such as beam energy spread and the influence of toroidal curvature drifts which have been touched upon here merit further consideration. Also, as data becomes available from experiments on beam current profiles, inclusion of this feature in the theory would be desirable.

APPENDIX A

Dispersion Relation for Two-Region Sheared Velocity Beam

A dispersion relation will be derived for $\tilde{m} = \pm 1$, $n = 1$ kinks in the following for the two-region sheared velocity beam model. The analysis begins with the perturbed field equation V-24.

$$\left(k^2 r - \frac{\omega^2 r}{v_A^2} + k\tilde{m}\tan\psi\right)\left[\frac{\delta A_\theta}{r} - \frac{1}{r}\frac{\partial}{\partial r} r\frac{\partial}{\partial r}\,\delta A_\theta\right]$$

$$+ (\tilde{m}kr + \tan\psi)\left[\frac{\delta A_\theta \tan\psi}{r^2} - \frac{1}{r}\frac{\partial}{\partial r}\, r\frac{\partial}{\partial r}\,\delta A_\theta \tan\psi\right] \qquad \text{A-1}$$

$$= \frac{2\omega_{\beta 1}^2 (1 - v_{Z2}/v_{Z1})(\varepsilon_1 - \tilde{m}ka_1)^2\, \delta A_\theta(a_1)}{-k^2 v_{Z1}^2 - \tilde{m}\omega_{C1}kv_{Z1} + \omega_{\beta 1}^2}\;\frac{\delta(r - a_1)}{a_1}$$

$$+ \frac{2\omega_{\beta 2}^2 (\varepsilon_2 - \tilde{m}ka_2)^2\, a_2(a_2^2 - a_1^2)^{-1}\, \delta A_\theta(a_2)}{-k^2 v_{Z2}^2 (1 + A_1) - \tilde{m}\omega_{C2}kv_{Z2}(1 + A_2) + \omega_{\beta 2}^2(1 + A_3)}\;\delta(r-a_2)$$

Two jump conditions are obtained on the derivatives of the perturbed field $\delta A_\theta(r)$ by integrating the above equation from $a_1 - \varepsilon$ to $a_1 + \varepsilon$ and from $a_2 - \varepsilon$ to $a_2 + \varepsilon$ and then allowing ε to go to zero. These are given below.

$$-\left(k^2 - \frac{\omega^2}{v_A^2} - \frac{\varepsilon_1 k\tilde{m}}{a_1}\right) a_1^2 \left[\delta A_\theta'(a_{1+}) - \delta A_\theta'(a_{1-})\right]$$

$$+ (\varepsilon_1 - \tilde{m}a_1 k)\left[(\delta A_\theta \tan\psi)'_{a_{1+}} - (\delta A_\theta \tan\psi)'_{a_{1-}}\right] \qquad \text{A-2}$$

$$= \frac{2\omega_{\beta 1}^2 (1 - v_{Z2}/v_{Z1})(\varepsilon_1 - \tilde{m}ka_1)^2\, \delta A_\theta(a_1)/a_1}{-k^2 v_{Z1}^2 - \tilde{m}\omega_{C1}\, kv_{Z1} + \omega_{\beta 1}^2}$$

$$-\left(k^2 - \frac{\omega^2}{v_A^2} - \frac{\varepsilon_2 k\tilde{m}}{a_2}\right) a_2^2 \left[\delta A_\theta'(a_{2+}) - \delta A_\theta'(a_{2-})\right]$$

$$+ (\varepsilon_2 - \tilde{m}a_2 k)\left[(\delta A_\theta \tan\psi)'_{a_{2+}} - (\delta A_\theta \tan\psi)'_{a_{2-}}\right] \qquad \text{A-3}$$

$$= \frac{2\omega_{\beta 2}^{2}\,(\varepsilon_2 - \tilde{m}ka_2)^2\,(a_2^2 - a_1^2)^{-1}\,a_2\,\delta A_\theta(a_2)}{-k^2 v_{Z2}^{2}\,(1+A_1) - \tilde{m}\omega_{C2}kv_{Z2}(1+A_2) + \omega_{\beta 2}^{2}\,(1+A_3)}$$

Here $\delta A_\theta' \,(a_{1+}) = \lim\limits_{\varepsilon\to 0} \frac{\partial}{\partial r}\,(\delta A_\theta)\Big|_{a_1+\varepsilon}$

$\delta A_\theta \,(a_{1-}) = \lim\limits_{\varepsilon\to 0} \frac{\partial}{\partial r}\,(\delta A_\theta)\Big|_{a_1-\varepsilon}$

and similar notation is used at $r = a_2$.

The solution of equation I-1 is given by the following.

$$\delta A_\theta\,(r) = \begin{cases} 1 & 0 < r < a_1 \\[2ex] \dfrac{Dv_A}{4\omega A}\ln\left[\dfrac{r^2+AX^2Y}{r^2+AX\,Y^2}\right] + D' & a_1 < r < a_2 \\[2ex] D''\ln\left[\dfrac{r^2(Y-B) - \varepsilon_2 a_2}{r^2(X-B) - \varepsilon_2 a_2}\cdot\dfrac{(X-B)R^2 - \varepsilon_2 a_2}{(Y-B)R^2 - \varepsilon_2 a_2}\right] & a_2 < r < R \end{cases} \qquad \text{A-4}$$

where D, D', D'' = constants of integration and the following quantities have been defined.

$Y = B + \tilde{m}k + \dfrac{\omega}{v_A}$

$X = B + \tilde{m}k - \dfrac{\omega}{v_A}$

$A = a_1 a_2\,(\varepsilon_2 a_1 - \varepsilon_1 a_2)\,(a_2^2 - a_1^2)^{-1}$

$B = (\varepsilon_1 a_1 - \varepsilon_2 a_2)\,(a_2^2 - a_1^2)^{-1}$

From the above solutions, the derivatives of the perturbed fields near $r=a_1$ and $r=a_2$ may be calculated (for use in equations I-2 and I-3) as given below.

$$(\delta A_\theta)'_{a_{1-}} = 0 \tag{A-5}$$

$$(\delta A_\theta \tan\psi)'_{a_{1-}} = -\varepsilon_1/a_1 \tag{A-6}$$

$$(\delta A_\theta)'_{a_{1+}} = \frac{Da_1XY}{(a_1^2+AX^2Y)\,(a_1^2+AXY^2)} \tag{A-7}$$

$$(\delta A_\theta \tan\psi)'_{a_{1+}} = -\,\frac{a_1D\varepsilon_1XY}{(a_1^2+AX^2Y)\,(a_1^2+AXY^2)} + \left(B - \frac{A}{a_1^2}\right)\left[\frac{Dv_A}{4\omega A}\ln\left(\frac{a_1^2 + AX^2Y}{a_1^2 + AXY^2}\right) + D'\right] \tag{A-8}$$

$$(\delta A_\theta)'_{a_{2-}} = \frac{a_2DXY}{(a_2^2+AX^2Y)\,(a_2^2+AXY^2)} \tag{A-9}$$

$$(\delta A_\theta \tan\psi)'_{a_{2-}} = \frac{-a_2D\varepsilon_2XY}{(a_2^2+AX^2Y)\,(a_2^2+AXY^2)} + \left(B - \frac{A}{a_2^2}\right)\left[\frac{Dv_A}{4\omega A}\ln\left(\frac{a_2^2+AX^2Y}{a_2^2+AXY^2}\right) + D'\right] \tag{A-10}$$

$$(\delta A_\theta)'_{a_{2+}} = \frac{-2\tilde{m}k\varepsilon_2D''}{[a_2(Y-B)-\varepsilon_2]\,[a_2(X-B)-\varepsilon_2]} \tag{A-11}$$

$$(\delta A_\theta \tan\psi)'_{a_{2+}} = \frac{2\tilde{m}k\varepsilon_2^2D''}{[a_2(Y-B)-\varepsilon_2]\,[a_2(X-B)-\varepsilon_2]} + \frac{\varepsilon_2}{a_2}\,D''\ln\left\{\frac{a_2(Y-B)-\varepsilon_2}{a_2(X-B)-\varepsilon_2}\cdot\frac{(X-B)R^2-\varepsilon_2a_2}{(Y-B)R^2-\varepsilon_2a_2}\right\} \tag{A-12}$$

Using the condition that δA_θ must be continuous at $r=a_1$ and a_2, one may express the two constants D' and D'' in terms of D.

$$D' = 1 - \frac{Dv_a}{4A\omega} \ln \left(\frac{a_1^2 + AX^2Y}{a_1^2 + AXY^2} \right) \tag{A-13}$$

$$D'' = \left\{ \ln \left[\frac{(Y-B)a_2-\varepsilon_2}{(X-B)a_2-\varepsilon_2} \cdot \frac{(X-B)R^2-\varepsilon_2 a_2}{(Y-B)R^2-\varepsilon_2 a_2} \right] \right\}^{-1}$$
$$\text{x} \left\{ 1 + \frac{Dv_A}{4A\omega} \ln \left[\frac{a_2^2 + AX^2Y}{a_2^2 + AXY^2} \cdot \frac{a_1^2 + AXY^2}{a_1^2 + AX^2Y} \right] \right\} \tag{A-14}$$

Substituting equations I-5 through I-8 into the first jump condition (equation I-2) gives the following solution for the constant D.

$$D = \frac{(a_1^2 + AX^2Y)\ (a_1^2 + AXY^2)}{a_1^2XY \left[-a_1^2k^2 + a_1^2\omega^2/v_A{}^2 + 2\tilde{m}ka_1\varepsilon_1 - \varepsilon_1^2 \right]}$$
$$\text{x} \left\{ \frac{2\omega_{\beta 1}^2\ (1 - v_{Z2}/v_{Z1})\ (\varepsilon_1 - \tilde{m}ka_1)^2}{-k^2v_{Z1}^2 - \tilde{m}\omega_{C1}kv_{Z1} + \omega_{\beta 1}^2} - (\varepsilon_1 - \tilde{m}a_1k)\ (\varepsilon_1 + Ba_1 - \frac{A}{a_1}) \right\} \tag{A-15}$$

Finally, using equations I-9 through I-12 in the second jump condition (equation I-3) and employing equations I-13 to I-16, a dispersion relation may be obtained relating ω and k.

$$- (k^2 - \frac{\omega^2}{v_A{}^2} - \frac{\varepsilon_2 k\tilde{m}}{a_2})\ a_2^2\ T_1 + (\varepsilon_2 - \tilde{m}a_2k)T_2$$
$$= \frac{2\omega_{\beta 2}^2\ (\varepsilon_2 - mka_2)^2\ a_2(a_2^2 - a_1^2)\ D''\ \ln E}{-k^2v_{Z2}^2(1+A_1)\ -\tilde{m}\omega_{C2}kv_{Z2}(1+A_2)+\omega_{\beta 2}^2\ (1+A_3)} \tag{A-16}$$

where the following quantities have been defined.

$$T_1 = - \frac{2\tilde{m}k\varepsilon_2 D''}{[a_2(Y-B)-\varepsilon_2]\ [a_2(X-B)-\varepsilon_2]} - \frac{a_2 DXY}{(a_2^2+AX^2Y)\ (a_2^2+AXY^2)}$$

$$T_2 = \frac{2\tilde{m}k\varepsilon_2^2 D''}{[a_2(Y-B)-\varepsilon_2]\ [a_2(X-B)-\varepsilon_2]} + \frac{\varepsilon_2}{a_2} D'' \ln E + D'$$

$$+ \frac{Da_2\varepsilon_2 XY}{(a_2^2+AX^2Y)\ (a_2^2+AXY^2)}$$

$$E = \frac{a_2(Y-B)-\varepsilon_2}{a_2(X-B)-\varepsilon_2} \cdot \frac{(X-B)R^2-\varepsilon_2 a_2}{(Y-B)R^2-\varepsilon_2 a_2}$$

APPENDIX B

Perturbed Current Integrals for Vlasov Beam Model

The three momentum space integrals used in the perturbed currents of the Vlasov beam model (Equations V-116 to V-118) are given below.

$$I_1 = \int_{\gamma_0}^{\gamma_m} \frac{d\gamma}{\gamma} \left[\omega - \omega_{br}(nq+M) - \varepsilon m\omega_{br}\gamma\right]^{-1} \qquad \text{B-1}$$

$$I_2 = \int_{\gamma_0}^{\gamma_m} \frac{d\gamma}{\gamma^3} \left[\omega - \omega_{br}(nq+m) - \varepsilon m\omega_{br}\gamma\right]^{-1} \qquad \text{B-2}$$

$$I_3 = \int_{\gamma_0}^{\gamma_m} \gamma d\gamma \left[\omega - \omega_{br}(nq+m) - \varepsilon m\omega_{br}\gamma\right]^{-1} \qquad \text{B-3}$$

where $\varepsilon = 2\omega_{br}/\Omega e$

Evaluating these integrals (for example, see ref. 95, pgs. 59-60) leads to the following.

$$I_1 = - \left[\omega - \omega_{br}(nq+m)\right]^{-1} \ln\left\{\frac{\gamma_0}{\gamma_m} \frac{\omega - \omega_{br}(nq+m) - \varepsilon m\omega_{br}\gamma_m}{\omega - \omega_{br}(nq+m) - \varepsilon m\omega_{br}\gamma_0}\right\} \qquad \text{B-4}$$

$$I_2 = \left[\omega - \omega_{br}(nq+m)\right]^{-1} \left\{\frac{1}{2}\left(\frac{1}{\gamma_0^2} - \frac{1}{\gamma_m^2}\right) + \frac{\varepsilon m\omega_{br}}{\omega - \omega_{br}(nq+m)}\left(\frac{1}{\gamma_0} - \frac{1}{\gamma_m}\right)\right\}$$

$$- \frac{\varepsilon^2 m^2 \omega_{br}^2}{\left[\omega - \omega_{br}(nq+m)\right]^3} \ln\left[\frac{\gamma_0}{\gamma_m} \frac{\omega - \omega_{br}(nq+m) - \varepsilon\omega_{br} m\gamma_m}{\omega - \omega_{br}(nq+m) - \varepsilon\omega_{br} m\gamma_0}\right] \qquad \text{B-5}$$

$$I_3 = \frac{\gamma_0 - \gamma_m}{\varepsilon m\omega_{br}} - \frac{\omega - \omega_{br}(nq+m)}{\varepsilon^2 m^2 \omega_{br}^2} \ln\left[\frac{\omega - \omega_{br}(nq+m) - \varepsilon\omega_{br} m\gamma_m}{\omega - \omega_{br}(nq+m) - \varepsilon\omega_{br} m\gamma_0}\right] \qquad \text{B-6}$$

APPENDIX C

Free Boundary Beam-Plasma Dispersion Relation

The following are the coefficients of $A_1, A_2, \ldots, A_6$ in equations V-168, V-169, V-171, V-172, V-182, and V-183.

$$C_1 = Jm\ (\kappa\rho_b) \tag{C-1}$$

$$C_2 = Ym\ (\kappa\rho_b) \tag{C-2}$$

$$C_3 = J\acute{m}\ (\kappa\rho_b) \tag{C-3}$$

$$C_4 = Y\acute{m}\ (\kappa\rho_b) \tag{C-4}$$

$$C_5 = -Z_2 Jm(T_1\rho_a) \tag{C-5}$$

$$C_6 = Z_1 Jm(T_2\rho_a) \tag{C-6}$$

$$C_7 = (Z_2-Z_1) Jm\ (\kappa\rho_a) \tag{C-7}$$

$$C_8 = (Z_2-Z_1) Ym\ (\kappa\rho_a) \tag{C-8}$$

$$C_9 = (Z_1-Z_2)^{-1}\ J\acute{m}(T_1\rho_a)\left[-i\varepsilon_1 T_1 - \varepsilon_2 Z_2 T_1 + \frac{im}{\rho_a n_\parallel}\ \frac{Jm(T_1\rho_a)}{J\acute{m}(T_1\rho_a)}\right] \tag{C-9}$$

$$C_{10} = (Z_1-Z_2)^{-1}\ J\acute{m}(T_2\rho_a)\left[i\varepsilon_1 T_2 + \varepsilon_2 Z_1 T_2 - \frac{im}{\rho_a n_\parallel}\ \varepsilon_4 Jm(T_2\rho_a)\right] \tag{C-10}$$

$$C_{11} = -\frac{m}{n_\parallel \rho_a}\left(\varepsilon_3 + \frac{1}{n_\parallel^2-1}\right) Jm\ (\kappa\rho_a) \tag{C-11}$$

$$C_{12} = -\frac{m}{n_\parallel \rho_a}\left(\varepsilon_3 + \frac{1}{n_\parallel^2-1}\right) Ym\ (\kappa\rho_a) \tag{C-12}$$

$$C_{13} = \frac{i}{1-n_\parallel^2}\ Jm\ (\kappa\rho_a) \tag{C-13}$$

$$C_{14} = \frac{i}{1-n_\parallel^2}\ Ym\ (\kappa\rho_a) \tag{C-14}$$

$$C_{15} = T_1 J\acute{m}(T_1\rho_a)\ (Z_1-Z_2)^{-1}\left[-\frac{\rho_a}{2}(\varepsilon_1-1) - \rho_a + \frac{i}{2}\varepsilon_2 Z_2\right] \tag{C-15}$$

$$C_{16} = T_2 J\acute{m}(T_2\rho_a)\ (Z_1-Z_2)^{-1}\left[\frac{\rho_a}{2}(\varepsilon_1-1) + \rho_a - \frac{i}{2}\varepsilon_2 Z_1\right] \tag{C-16}$$

$$C_{17} = \rho_a \, \kappa \, J\acute{m} \, (\kappa\rho_a) \qquad \text{C-17}$$

$$C_{18} = \rho_a \, \kappa \, Y\acute{m} \, (\kappa\rho_a) \qquad \text{C-18}$$

$$C_{19} = T_1 J\acute{m}(T_1\rho_a) \, (Z_1 - Z_2)^{-1} \left[\frac{\rho_a}{2} \, (\varepsilon_3 - 1) Z_2 + \rho_a Z_2 + \frac{i}{2} \, \varepsilon_4 \right] \qquad \text{C-19}$$

$$C_{20} = T_2 J\acute{m}(T_2\rho_a) \, (Z_1 - Z_2)^{-1} \left[-\frac{\rho_a}{2} \, (\varepsilon_3 - 1) Z_1 - \rho_a Z_1 - \frac{i}{2} \, \varepsilon_4 \right] \qquad \text{C-20}$$

$$C_{21} = \rho_a \, \kappa \, J\acute{m} \, (\kappa\rho_a) \qquad \text{C-21}$$

$$C_{22} = \rho_a \, \kappa \, Y\acute{m} \, (\kappa\rho_a) \qquad \text{C-22}$$

In terms of the above quantities, equations V-168, V-169, V-171, V-172, V-182, and V-183 may be expressed as follows.

$$\begin{bmatrix} 0 & 0 & C_1 & C_2 & 0 & 0 \\ 0 & 0 & 0 & 0 & C_3 & C_4 \\ C_5 & C_6 & C_7 & C_8 & 0 & 0 \\ C_9 & C_{10} & C_{11} & C_{12} & C_{13} & C_{14} \\ C_{15} & C_{16} & 0 & 0 & C_{17} & C_{18} \\ C_{19} & C_{20} & C_{21} & C_{22} & 0 & 0 \end{bmatrix} \begin{bmatrix} A_1 \\ A_2 \\ A_3 \\ A_4 \\ A_5 \\ A_6 \end{bmatrix} = 0 \qquad \text{C-23}$$

A free boundary dispersion relation is then obtained by setting the determinant of the coefficient matrix equal to zero.

REFERENCES

1. C.T.R. Wilson, Proc. Camb. Phil. Soc. 22 (1925) 534.

2. A. S. Eddington, The Internal Constitution of the Stars, Cambridge Univ. Press, 1926.

3. R. G. Giovanelli, Phil. Mag. 40 (1949) 206.

4. L. A. Artsimovich, Nuclear Fusion 12 (1972) 215.

5. H. P. Furth, Nuclear Fusion 15 (1975) 487.

6. J. A. Rome, ORNL-TM-3880 (1972).

7. D. A. Spong, J. F. Clarke, J. A. Rome, T. Kammash, Nuclear Fusion 14 (1974) 397.

8. H. Knoepfel, D. A. Spong, S. J. Zweben, Seventh European Conf. on Controlled Fusion and Plasma Physics, Vol. 1, Lusanne (Sept., 1975).

9. S. von Goeler, W. Stodiek, Fifth European Conf. on Controlled Fusion and Plasma Physics, Grenoble 1 (1972) 2; also S. von Goeler, W. Stodiek, et al., Third International Symposium on Toroidal Confinement, Garching, Germany, paper B25, 1973.

10. L. Pieroni and S. E. Segre, Phys. Rev. Lett. 34 (1975) 928.

11. P. Chrisman, J. F. Clarke, J. A. Rome, ORNL-TM-4501 (1974); also see J. M. Finn, Nuclear Fusion 15 (1975) 845.

12. J. D. Strachan, R. L. Dewar, Plasma Physics and Controlled Nuclear Fusion Research, Proc. of Fifth Int. Conf., Tokyo, Japan, paper IAEA CN 33/A8/11.

13. A. C. England, ORMAK Tech. memo, "Progress Report on Hard X-ray Diagnostics" (1973).

14. H. Knoepfel, D. A. Spong, S. J. Zweben, Bulletin of the American Phys. Soc. 20 (1975) 1300.

15. V. S. Vlasenkov, et al., Nuclear Fusion 13 (1973) 509.

16. V. V. Alikaev, et al., MATT-TRANS-111, April, 1973.

17. J. Tachon, et al., Plasma Physics and Controlled Fusion Research, Proc. Fifth Int. Conf., Tokyo, Japan, paper IAEA CN 33/A6-2.

18. B. Coppi, H. Knoepfel, R. Pozzoli, MIT Plasma Research Report 745 (June, 1974).

19. C. W. Hartman, Phys. Rev. Lett. 26 (1971) 826.

20. D. A. Spong, J. F. Clarke, ORNL-TM-4512 (1974).

21. G. Miyamoto, et al., Proc. of the Second United Nations Conf. on the Peaceful Uses of Atomic Energy (United Nations, Geneva, 1958), 32, 308.

22. D. Finklestein, ibid. 32, 446.

23. G. I. Budker, "Relativistic Stabilized Electron Beam", CERN, Symposium on High Energy Accelerators and Meson Physics, Vol. I. Geneva (1956).

24. A. Mohri, et al., Phys. Rev. Lett. 34 (1975) 574.

25. J. Benford, B. Ecker, V. Bailey, Phys. Rev. Lett. 33 (1974) 574.

26. P. Gilad, B. R. Kusse, T. R. Lockner, Phys. Rev. Lett. 33 (1974) 1275.

27. D. W. Swain, P. A. Miller, M. M. Widner, SAND 75-0214 (June, 1975).

28. T. K. Kammash, Fusion Reactor Physics (1975) Ann Arbor Science.

29. S. Zweben, H. E. Knoepfel, D. A. Spong, Bulletin of the American Phys. Soc. 20 (1975) 1300.

30. A. T. Altyntsev, et al., Zh.ETF Pis. Red. 13 (1971) 197 [JETP Lett. 13 (1971) 139], and Proc. of the Fourth Int. Conf. on Plasma Physics and Controlled Nuclear Fusion Research, Madison, Wisconsink (1971) 2, 309.

31. P. A. Miller and G. W. Kuswa, Phys. Rev. Lett. 30 (1973) 958.

32. C. A. Kapetanakos, D. A. Hammer, Appl. Phys. Lett. 23 (1973) 17.

33. P. Korn, et al., Phys. Rev. Lett. 31 (1973) 579; also J. Appl. Phys. 44 (1973) 4946.

34. Yu. I. Abrashitov, et al., Zh.ETF Pis. Red. 18 (1973) 675 [JETP Lett. 18 (1973) 395].

35. D. Prono, et al., Phys. Rev. Lett. 35 (1975) 438.

36. A. E. Costly, et al., Phys. Rev. Lett. 33 (1974) 758.

37. Al Trivelpiece, private communication.

38. R. Motley, et al., MATT-43 (1960).

39. R. Motley, et al., Plasma Physics 3 (1961) 17.

40. W. Bernstein, et al., Phys. of Fluids 1 (1958) 430.

41. W. Stodiek, D. W. Grove, MATT-Q-20 (1962) 50.

42. H. Knoepfel, S. Zweben, Phys. Rev. Lett. 35 (1975) 1340.

43. E. P. Lee, Phys. of Fluids 16 (1973) 1072.

44. R. Lovelace, Cornell Univ. Lab. of Plasma Studies, Report No. 162 (1975).

45. E. R. Harrison, Plasma Physics 1 (1960) 105.

46. E. R. Harrison, Plasma Physics 4 (1962) 7.

47. H. Dreicer, Phys. Rev. 115 (1959) 238, and 117 (1960) 329.

48. M. Kruskal, I. B. Bernstein, MATT-Q-20 (1960) 174.

49. M. Kruskal, I. B. Bernstein, MATT-226 (1963).

50. M. Kruskal, I. B. Bernstein, Phys. of Fluids 7 (1964) 407.

51. A. V. Gurevich, JETP 11 (1960) 85.

52. A. V. Gurevich, JETP 12 (1961) 904.

53. A. V. Gurevich, Yu. N. Zhivlyuk, JETP 22 (1966) 153.

54. A. N. Lebedev, JETP 21 (1965) 931.

55. R. M. Kulsrud, Y. C. Sun, et al., Phys. Rev. Lett. 31 (1973) 690.

56. J. W. Connor, R. J. Hastie, Nuclear Fusion 15 (1975) 415.

57. Yu. L. Klimontovich, The Statistical Theory of Non-Equilibrium Processes in a Plasma, The MIT Press, Cambridge, Mass. (1967).

58. V. S. Mukhovatov, V. D. Shafranov, Nuclear Fusion 11 (1971) 605.

59. E. Ott, R. N. Sudan, Phys, of Fluids 14 (1971) 1226.

60. A. Mondelli, E. Ott, Phys, of Fluids 17 (1974) 1017.

61. T. G. Northrup, The Adiabatic Motion of Charged Particles, Interscience Pub. (1963) New York.

62. N. N. Bogolyubov, Yu. A. Mitropol'skii, Asymptotic Methods in the Theory of Nonlinear Oscillations (1958).

63. I. B. Bernstein, Advances in Plasma Physics 4, ed's. Simon, Thompson, pg. 311.

64. A. I. Morozov, L. S. Solovev, Doklady 128 (1959) 506.

65. A. A. Galeev, R. Z. Sagdeev, Soviet Phys. JETP 26 (1968) 233.

66. Georg Knorr, Phys, of Fluids 8 (1965) 1334.

67. L. A. Berry, J. D. Callen, J. F. Clarke, et al., Fifth IAEA Conf. on Plasma Physics and Controlled Nuclear Fusion Research (1974), Tokyo, Japan, paper IAEA-CN-33/A 5-1.

68. Private communication, James D. Callen.

69. K. T. Tsang, E. A. Frieman, ORNL-TM-4948 (1975).

70. R. J. Colchin, ORMAK Technical Memo 103, "In Search of the ORMAK Plasma".

71. J. M. Greene, J. L. Johnson, K. E. Weimer, Phys. of Fluids 14 (1971) 671.

72. V. D. Shafranov, Reviews of Plasma Physics, ed. by M. A. Leontovich (Consultants Bureau, New York, 1966) 2 103.

73. V. D. Shafranov, V. S. Mukhovatov, Nuclear Fusion 11 (1971) 605.

74. H. P. Zehrfeld, B. J. Green, Phys. Rev. Lett. 23 (1969) 961.

75. H. P. Zehrfeld, B. J. Green, Nuclear Fusion 12 (1972) 569.

76. B. J. Green, H. P. Zehrfeld, Nuclear Fusion 13 (1973) 750.

77. C. L. Hedrick, G. E. Guest, D. B. Nelson, ORNL-TM-4076 (1973).

78. H. Grad, Magneto-Fluid and Plasma Dynamics, Symposia in Applied Mathematics (American Mathematical Society, 1967) 18 162.

79. J. Killeen, K. J. Whiteman, Phys. of Fluids, 9 (1966) 1846.

80. J. D. Callen, R. A. Dory, Phys. of Fluids 15 (1972) 1523.

81. V. D. Shafvanov, Soviet Physics - Tech. Physics 15 (1970) 175.

82. L. A. Artsimovich, Controlled Thermonuclear Reactions, New York, Gordon and Breach Science Pub. (1964).

83. J. Tachon, Proc. of the Annual Meeting on Theoretical Aspects of Controlled Thermonuclear Research, Arlington, Va. (1975).

84. S. von Goeler, W. Stodiek, N. Sauthoff, Phys. Rev. Lett. 33 (1974) 1201; S. von Goeler, et al., Princeton Plasma Physics Lab. Report MATT-1060 (1974).

85. Status and Objectives of Tokamak Systems for Fusion Research, WASH-1295, UC-20.

86. V. A. Vershkov, et al., Kurchatov Inst. Preprint IAE-2241 (1973), MATT-TRANS-113 (1973).

87. M. N. Rosenbluth, Phys. of Fluids 3 (1960) 932.

88. R. C. Mjolsness, et al., Phys. of Fluids 6 (1962) 1741; Phys. of Fluids 6 (1962) 1730.

89. S. Weinberg, J. of Math. Phys. 5 (1964) 1371; J. of Math. Phys. 8 (1967) 614.

90. E. P. Lee, "Hose Theory", UCRL-16268 (1973).

91. G. E. Guest, C. L. Hedrick, D. B. Nelson, Phys. of Fluids 18 (1975) 871.

92. J. D. Jackson, Classical Electrodynamics, John Wiley and Sons, Inc., New York (1962).

93. C. C. Johnson, Field and Wave Electrodynamics, McGraw-Hill, Inc., New York (1965).

94. C. O. Beasley, Jr., H. K. Meier, ORNL-TM-4588 (1974).

INTERNAL DISTRIBUTION

1-3.	Lab Records
4-5.	Central Research Library
6.	Y-12 Document Reference
7.	Thermonuclear Library
8.	ORNL Patent Office
9.	J. D. Callen
10.	D. G. McAlees
11.	R. A. Dory
12.	G. G. Kelley
13.	J. F. Clarke
14.	O. B. Morgan
15.	Lab Records - RC
16.	Research & Technical Support Div., (ORO) ERDA
17.	M. W. Rosenthal
18-57.	D. A. Spong

EXTERNAL DISTRIBUTION

58. Plasma Physics Library, Plasma Physics Laboratory, Princeton University, Forrestal Campus, P. O. Box 451, Princeton, NJ 08540

59. Controlled Thermonuclear Research Library, Lawrence Livermore Laboratory, P. O. Box 808, Livermore, CA 94550

60. Q Division Library, c/o F. L. Ribe, Los Alamos Scientific Laboratory, P. O. Box 1663, Los Alamos, NM 87544

61. Controlled Thermonuclear Research Library, c/o Weston M. Stacey, Jr., Argonne National Laboratory, 9700 S. Cass Ave., Argonne, IL 60439

62. Librarian, Culham Laboratory, U.K. Atomic Energy Authority, Abingdon, Oxon, OX14, 3DB, United Kingdom

63. Ruth Lengye, Bibliothek, Max Planck Institut fur Plasmaphysik, 8046 Garching be Munchen, Federal Republic of Germany

64. Library, Centre de Recherches en Physique des Plasma, 21 Avenue des Bains, 1007 Lausanne, Switzerland

65. A. M. Dupas, Documentation S.I.G.N., Department de La Physique du Plasma, Et de La Fusion Controlee, Association EURATOM-CEA, Sur La Fusion, Centre D-Etudes Nucleaires, BP 85 Centre Du TRI 38041 Grenoble Cedex (FRANCE)

66. Bibliotheque, Service du Confinement des Plasmas, C.E.A., B.P. No. 6, 92, Fontenay-Zux-Roses (Seine) FRANCE

67. Library, International Centre for Theoretical Physics, Trieste, ITALY

68. Library, Laboratorio Gas Ionizati, Frascatti, ITALY

69. V. E. Ivanov, Physical-Technical Institute of the Ukranian Academy of Sciences Sukhumi, U.S.S.R.

70. M. S. Rabinovich, Lebedev Institute of Physics, Academy of Sciences of the U.S.S.R., Leninsky Prospect 53, Moscow, U.S.S.R.

71. Thermonuclear Library, Kurchatov Institute of Atomic Energy, 46 Ulitsa Kurchatova, P. O. Box 3402, Moscow, U.S.S.R.

72. Library, Institute for Plasma Physics, Nagoya University, Nagoya, JAPAN 464

73. Library, FOM-Institut voor Plasma-Fysica, Rijnhuizen, Jutphaas, NETHERLANDS

74. Plasma Physics Group, Department of Engineering Physics, Australian National University, P. O. Box 4, Canberra A.C.T. 2600 AUSTRALIA

75. Thermonuclear Library, Japan Atomic Energy Research Institute, Tokai, Naka, Ibaraki, JAPAN

76. CTR Reading Room, c/o Prof. Dieter J. Sigmar, Room 37-391, M.I.T., Cambridge, MA 02139

77. CTR Reading Room, c/o Prof. D. W. Kerst, Dept. of Physics, Sterling Hall, Univ. of Wisconsin, Madison, WI 53706

78. CTR Reading Room, c/o Prof. I. B. Berstein, Yale University, New Haven, Conn. 06510

79. Center for Plasma Physics and Thermonuclear Research, Univ. of Texas, Physics Building 330, Austin, TX 78712

80. CTR Reading Room, c/o Prof. B. D. Fried, Physics Dept., Univ. of California, Los Angeles, CA 90024

81. Magneto-Fluid-Dynamics Library, Courant Inst. of Math. Science, New York Univ., 251 Mercer St., New York, NY 10012

82. CTR Reading Room, c/o Prof. Alvin W. Trivelpiece, Dept. of Physics & Astronomy, Univ. of Maryland, College Park, MD 20742

83. CTR Reading Room, c/o Dr. Ravi N. Sudan, Phillips Hall, Cornell Univ., Ithaca, NY 18450

84. Prof. Marshall N. Rosenbluth, Institute for Advanced Study,
Princeton, NJ 08540

85. CTR Reading Room, c/o Prof. Roy Gould, California Inst. of Tech.,
Pasadena, CA 91103

86. Dr. Nicholas A. Krall, Science Applications, Inc., P. O. Box 2354,
1200 Prospect St. La Jolla, CA 92037

87. CTR Reading Room, c/o Dr. Jay P. Boris, Plasma Physics, Naval
Research Laboratory, Washington, DC 20390

88. CTR Library, General Atomic Co., P. O. Box 81608, San Diego,
CA 92138

89. CTR Library, c/o Dr. Alan F. Haught, United Technologies Research
Labs. East Hartford, Conn. 06108

90. Dr. Robert E. Price, Division of Controlled Thermonuclear Research,
U. S. Energy Research and Development Administration, Washington,
DC 20545

91. Dr. Bennett Miller, Division of Controlled Thermonuclear Research,
U. S. Energy Research and Development Administration, Washington,
DC 20545

92. Dr. Arthur Sleeper, Division of Controlled Thermonuclear Research,
U. S. Energy Research and Development Administration, Washington,
DC 20545

93. Dr. Paul H. Rutherford, Princeton Plasma Physics Lab., Princeton
University, Princeton, NJ 08540

94. Dr. L. D. Pearlstein, L-388, Lawrence Livermore Laboratory,
P. O. Box 808, Livermore, CA 94550

95. Dr. J. P. Friedberg, Los Alamos Scientific Laboratory, Los Alamos,
NM 87544

96. Dr. Gareth E. Guest, General Atomic Co., P. O. Box 81608,
San Diego, CA 92168

97. Dr. V. D. Shafranov, I.V. Kurchatov Inst. of Atomic Energy,
46 Ulitsa Kurchatov, P. O. Box 3402, Moscow, U.S.S.R.

98. Dr. Harold Grad, Courant Inst. of Math. Sci., New York Univ.,
251 Mercer St., New York, NY 10012

99. Prof. Bruno Coppi, Dept. of Physics, M.I.T., Cambridge, Mass.
02139

100. Dr. Harold P. Furth, Princeton Plasma Physics Lab., Princeton Univ., P. O. Box 451, Princeton, NJ 08540

101-127. Technical Information Center, ERDA